

Experimental Tests of QCD and Fragmentation Models in Electron-Positron Annihilation

Thesis by
Howard D. Stone

In Partial Fulfilment of the Requirements
for the Degree of
Doctor of Philosophy

California Institute of Technology
Pasadena, California

1988
(submitted October 5, 1987)

Acknowledgements

The data used in this study were accumulated over a period of eight years by the MARK J collaboration. I thank all the members of the MARK J collaboration, students (past and present), technical staff, post-docs and professors for their efforts in collecting the data, taking shifts, and building, maintaining and calibrating the detector.

The analysis presented here is a continuation of earlier work by Mike Capell, Dorothee Hueser-Teuchert, Greg Swider, Lluís Garrido, Mourad Dhina, Ren-Yuan Zhu and Bob Clare. Without the prior work of these people, this study would not have been possible, and I thank them for having laid the foundations on which this study stands.

My thesis advisor, Prof. Harvey Newman, has taught me many things over the past five years, and I thank him for having taken the time to impart some of his knowledge to me. While at DESY, I also benefited from discussions with Prof. Min Chen, Prof. Albrecht Boehm and Dr. Illias Mirza, and I thank them for the time they spent with me. I would also like to acknowledge the efforts of Prof. Ting, without which neither the detector, nor the collaboration, would have come into being.

Duncan Morris and Tom Gottschalk were very helpful in explaining some details of the subject to me, and many useful discussions with them are gratefully acknowledged.

I thank all my friends, who have made the years spent working on this study happy ones. Fortunately, they are too numerous to mention by name – but they know who they are.

I would like to take this opportunity to thank the people of England, Germany and The United States¹ for making this study possible through their support of the Universities and High Energy Physics research.

Finally, I thank my family, for it is they who have paid the highest price for my education. This thesis is dedicated to them.

¹Support for this research was partially provided through a Department of Energy Contract; DE-AC03-81-ER40050.

Abstract

This thesis presents a detailed study of the hadronic data obtained with the MARK J detector from e^+e^- annihilation. The predictions of several new combinations of Monte Carlo parton generators and fragmentation schemes have been tuned and compared directly to the data.

A study, performed in the limit of perfect detector resolution and efficiency, has shown that the string effect, which some groups claimed to have observed, cannot be attributed to soft gluon coherence effects occurring at the soft perturbative stage of the event evolution.

It is found that all the fragmentation schemes employing the string formalism are unable to correctly describe the form of the Thrust and Energy-Energy Correlation distributions obtained with the high energy data above 40 GeV center-of-mass energy. The problems encountered have their origins in the modelling of the fragmentation process rather than in the perturbative QCD aspects of the models. All the models investigated, however, are capable of describing a broad range of distributions at the lower center-of-mass energies.

No evidence for the presence of the string effect has been found in the MARK J data.

The new fragmentation models have been used to extract values for the strong coupling constant from the data. The systematic uncertainties assigned to previous α_s measurements have been re-assessed in the light of this study, and it has been found that previous error assignments require no adjustment.

A recent 2nd order calculation for the three-jet partial cross section has been investigated and converted into a form where it can be directly compared to previous calculations. The calculations are found to be in excellent agreement, and it is concluded that the systematic errors that should be assigned to α_s measurements due to theoretical uncertainties are negligible.

Motivated by the observation of an excess number of low thrust inclusive muon events at the highest PETRA energies, the MARK J hadronic data above 46.3 GeV has been compared to a lower energy data sample. The presence of new phenomena in the highest energy hadronic data has been ruled out at the level of available statistics.

A brief study of the characteristics to be expected at LEP energies for events originating in the production of top quarks has been made, and a method for isolating a top-enriched sample has been investigated.

But I desire to point out that this seems to be one of the many cases in which the admitted accuracy of mathematical processes is allowed to throw a wholly inadmissible appearance of authority over the results obtained by them. Mathematics may be compared to a mill of exquisite workmanship, which grinds you stuff of any degree of fineness; but, nevertheless, what you get out depends on what you put in; and as the grandest mill in the world will not extract wheat-flour from peascods, so pages of formulae will not get a definite result out of loose data.

19th February. 1869

— From an address delivered to the Geological Society of London by T.H. Huxley defending the geological age of the earth against a much younger age derived by William Thomson^a (later Lord Kelvin). Thomson had applied the theory of heat conduction to the cooling of the earth and concluded that it was much younger than previous estimates, which had been based on the rate of erosion of material from The White Cliffs of Dover. Thomson had not known about the generation of heat in the earth's interior by radioactivity.

^aTaken from P.T. Landsberg's *The Enigma of Time*.
Adam Hilger Ltd, Bristol. 1985.

Contents

1	Introduction	1
2	Description of the Experiment	7
2.1	The PETRA e^+e^- Storage Ring	7
2.2	The MARK J Detector	10
2.3	Description of Detector Elements	13
2.3.1	The Vertex Detector	13
2.3.2	The Calorimeters	14
2.3.3	The Muon Spectrometer	16
2.3.4	The Data Acquisition System and Trigger	16
2.3.5	Offline Analysis and Calibration	18
2.4	The Event Selection	27
2.5	The Hadron Data Set	30
3	Theoretical Outline: e^+e^- Annihilation into Quarks and Gluons	33
3.1	An Overview of $e^+e^- \rightarrow$ Hadrons in the Standard Model	33
3.2	The Initial State	37
3.3	The Hadronic Final State	41
3.3.1	QCD: Running Coupling Constants and Asymptotic Freedom	41
3.3.2	The Importance of Second Order Terms in The Determination of α_s	47
3.3.3	Screening and Antiscreening in QED and QCD	47
3.4	Perturbative QCD Predictions	48
3.4.1	The Total Cross Section for $e^+e^- \rightarrow$ Hadrons	48
3.4.2	Jet Cross Sections in $e^+e^- \rightarrow$ Hadrons	52
3.5	Leading logarithmic QCD	57
3.5.1	Color Coherence in LLA Showers	60
4	Theoretical Outline: Fragmentation Models	62
4.1	Overview of The Fragmentation Process	62
4.2	Independent Jet Fragmentation	66
4.2.1	The Field-Feynman Model and its Variants	66
4.3	String Fragmentation Models	70
4.3.1	String Fragmentation: Ingredients	70
4.4	The LUND Models	74

4.5	The Caltech-II Model	76
4.6	Cluster Models	79
4.7	Phenomenological Consequences of the Models	81
5	Model Comparisons at the Parton and Raw Track Level	83
5.1	Comparison of the ERT/Ali/Zhu Calculation with that of Gottschalk and Shatz	83
5.2	Investigation into the Phenomonological Relevance of Gluon Coherence	88
5.3	Discussion	93
6	Tuning the Model Parameters	95
6.1	The Detector Simulation	95
6.2	The Basic Model Parameters	103
6.3	Definition of the Shape Variables Used for Parameter Determination .	104
6.4	The Approach to the Fitting Problem	108
6.5	Tuning the Ali Model Parameters	109
6.6	Tuning the LUND Model Parameters	111
6.6.1	The Transverse Momentum Parameter in LundV4.3	111
6.6.2	Tuning the Parameters in LundV6.3	112
6.7	Tuning the Caltech Model Parameters	119
6.7.1	The Parameters of CIT2-FME	119
6.7.2	The Parameters of CIT2-DLLA	123
7	Comparisons with Data	129
7.1	General Considerations	129
7.2	Comparisous at 35 GeV and 44 GeV	130
7.3	Comparisons at Low Energy	138
7.4	Discussion	145
7.4.1	The String Effect	146
7.4.2	Comparison with Other Studies	149
7.5	The Role of Transverse Momentum in String Models	150
7.5.1	Conclusions	157
8	Comment on Systematic Errors Assigned to α_s Measurements	159
8.1	General Considerations	159
8.2	The Determination of α_s	162
8.3	Discussion	169
9	The Highest Energy Data from PETRA	174
9.1	Introduction	174
9.2	A Comparison Between the High-Energy Data and a Control Data Set at 44 GeV	175
9.3	Comparisons with the Multidimensional Discriminant Function	183
9.4	Discussion	185

10 Top Production in e^+e^- Annihilation at LEP Energies	189
10.1 Introduction	189
10.2 The Effect of Top on the Hadronic Cross Section	191
10.3 The Effect of Top on the Inclusive Lepton Rate	198
10.4 The Effect of Top on the Event Topologies: All Events	199
10.5 Event Topologies: Inclusive Muon Events	204
10.6 Isolating a Top-enriched Hadron Sample	207
11 Conclusions	212
11.1 Summary	212
11.1.1 Results	213
11.2 Looking to the Future	215
A Static Quarks and Flavor	217
A.1 Static Quarks and Color	222
A.2 Dynamic Quarks and QCD	223
B The Recombination Dependence of the Three-jet Cross Section	226
C Model Comparisons: Plots	233
D α_s values extracted with the FKSS calculation	262

List of Figures

2.1	The layout of the DESY site	8
2.2	Integrated luminosity taken by the MARK J detector	9
2.3	The MARK J detector, side view	10
2.4	The MARK J detector, end on view	11
2.5	The structure of the MARK J detector	12
2.6	Reconstruction of particle trajectories with the vertex detector	14
2.7	Reconstruction of the event Z-position with the vertex detector	15
2.8	The MARK J trigger logic.	19
2.9	Method of Z-position reconstruction for counters	21
2.10	Z-position reconstruction of hits for A and C counters	23
2.11	The run-to-run variation in the counter attenuation length	26
2.12	The physics background processes	27
2.13	Computer reconstruction of a typical hadronic event in the MARK J detector	30
2.14	The visible energy in the detector at 35 and 44 GeV	31
3.1	Schematic diagram showing the development of a hadronic final state in e^+e^- annihilation	35
3.2	Initial state radiative corrections to $e^+e^- \rightarrow$ hadrons	38
3.3	The relative production probabilities for charge 1/3 and 2/3 quarks versus Q^2	40
3.4	Loop diagrams contributing to the photon propagator in QED	42
3.5	Diagrams contributing to the electron self-energy in QED	43
3.6	Loop diagrams that modify the bare QCD coupling	45
3.7	Zeroth order diagram for the calculation of the total cross section	49
3.8	QCD diagrams leading to the 1 st order modification of the total cross section for $e^+e^- \rightarrow$ hadrons	50
3.9	QCD loop diagrams leading to the 1 st order modification of the total cross section for $e^+e^- \rightarrow$ hadrons	50
3.10	2 nd order diagrams contributing to the calculation of the 3-jet cross section	53
3.11	Loop diagrams involved in the calculation of the 3-jet cross section	54
3.12	A leading logarithmic parton shower developing from $e^+e^- \rightarrow$ hadrons	58
3.13	The basic elements of a leading logarithmic parton shower	59

4.1	Schematic diagram showing the breakup of a QCD color flux tube . . .	64
4.2	Schematic diagram showing the fragmentation of an energetic quark in the Field-Feynman model	66
4.3	The yo-yo mode for a quark-antiquark pair connected by a string . . .	71
4.4	Schematic view of the mechanism of color screening in the string picture of fragmentation	71
4.5	The representation of gluons as kinks on the strings in the string picture of fragmentation	72
4.6	The color flow in an e^+e^- annihilation event	73
4.7	The string effect in the fragmentation of a three-jet system	82
5.1	The parton level Thrust for three-jet events from the GS calculation compared to the same from the ERT/Ali/Zhu calculation	88
5.2	Analytic results showing the presence of the string effect in angle-ordered LLA QCD	90
5.3	The energy flow around the thrust axis for Caltech-I LLA partons, showing the effect of angle ordering	92
5.4	The energy flow around the thrust axis for events generated with the Caltech-I LLA package and fragmented with the Caltech-II fragmentation scheme, showing the effect of angle ordering	92
5.5	The energy flow around the thrust axis for events generated with the BIGWIG V3.0 package for two different LLA shower termination parameter values	94
6.1	The energy-loss fraction for the A, B and C counters, as used by the detector simulation	97
6.2	The total energy fraction deposited in the detector at 35 and 44 GeV	99
6.3	The missing z-direction energy fraction deposited in the detector at 35 and 44 GeV	100
6.4	The missing transverse energy fraction seen in the detector at 35 and 44 GeV	100
6.5	The total energy fraction deposited in the detector at 35 GeV by various processes	101
6.6	The energy imbalance in the detector for hadron and tau events at 35 GeV	102
6.7	The coordinate system used to define the event plane	105
6.8	Calculation of the Energy-Energy correlation function	107
6.9	Determination of the σ_q parameter for the Ali Monte Carlo	110
6.10	The predictions for O_N and T_N from the Ali MC for several σ_q parameter values	111
6.11	Determination of the σ_q parameter for the LundV4.3 Monte Carlo . .	112
6.12	The predictions for O_N and T_N from the LundV4.3 MC for several σ_q parameter values	113
6.13	The form of the LundV6.3 fragmentation function	114
6.14	The results of varying the parameters of the LundV6.3 model	116

6.15	χ^2 contours obtained by comparing the predictions of the LundV6.3 model for Σ_A to the data	117
6.16	χ^2 contours obtained by comparing the predictions of the LundV6.3 model for T_N to the data	118
6.17	χ^2 contours obtained by comparing the predictions of the CIT2-FME model for narrow-side Thrust to the data	121
6.18	χ^2 contours obtained by comparing the predictions of the CIT2-FME model for broad-side Thrust to the data	122
6.19	χ^2 for the comparison of CIT2-DLLA with the data	125
6.20	The sensitivity of hard-QCD sensitive variables to variation of the ρ parameter in the CIT2-DLLA model	127
6.21	Comparison of the CIT2-DLLA model prediction for Σ with the data at 35 GeV	128
7.1	Comparison of the Ali model predictions for Thrust at 35 and 44 GeV with the data	131
7.2	Comparison of the LundV4.3 model predictions for Thrust at 35 and 44 GeV	132
7.3	Comparison of the LundV6.3 model predictions for Thrust at 35 and 44 GeV	132
7.4	Comparison of the CIT2-FME model predictions for Thrust at 35 and 44 GeV	133
7.5	Comparison of the CIT2-DLLA model predictions for Thrust at 35 and 44 GeV	133
7.6	Comparison of the Ali model predictions for Σ at 35 and 44 GeV	135
7.7	Comparison of the LundV4.3 model predictions for Σ at 35 and 44 GeV	135
7.8	Comparison of the LundV6.3 model predictions for Σ at 35 and 44 GeV	136
7.9	Comparison of the CIT2-FME model predictions for Σ at 35 and 44 GeV	136
7.10	Comparison of the CIT2-DLLA model predictions for Σ at 35 and 44 GeV	137
7.11	Comparison of the Ali model predictions for the energy flow at 35 and 44 GeV	139
7.12	Comparison of the LundV4.3 model predictions for the energy flow at 35 and 44 GeV	139
7.13	Comparison of the LundV6.3 model predictions for the energy flow at 35 and 44 GeV	140
7.14	Comparison of the CIT2-FME model predictions for the energy flow at 35 and 44 GeV	140
7.15	Comparison of the CIT2-DLLA model predictions for the energy flow at 35 and 44 GeV	141

7.16	Comparison of the CIT2-DLLA and CIT2-FME model predictions for the Thrust at 14 GeV	142
7.17	Comparison of the Ali model predictions for the Thrust and Σ at 22 GeV	142
7.18	Comparison of the LundV4.3 model predictions for the Thrust and Σ at 22 GeV	143
7.19	Comparison of the LundV6.3 model predictions for the Thrust and Σ at 22 GeV	143
7.20	Comparison of the CIT2-FME model predictions for the Thrust and Σ at 22 GeV	144
7.21	Comparison of the CIT2-DLLA model predictions for the Thrust and Σ at 22 GeV	144
7.22	Comparison of the Ali model predictions for the flower plot for two different σ_q values	147
7.23	Comparison of the LundV6.3 model predictions for the flower plot for two different σ_q values	148
7.24	Comparison of the modified CIT2-FME model predictions for Thrust at 35 and 44 GeV with the data	152
7.25	Comparison of the modified CIT2-FME model predictions for Σ at 35 and 44 GeV with the data	153
7.26	Comparison of the modified CIT2-FME model predictions for the energy flow at 35 and 44 GeV with the data	154
7.27	Comparison of the second modified CIT2-FME model predictions for Thrust at 35 and 44 GeV with the data	155
7.28	Comparison of the second modified CIT2-FME model predictions for Σ at 35 and 44 GeV with the data	156
7.29	Comparison of the second modified CIT2-FME model predictions for the energy flow at 35 and 44 GeV with the data	156
8.1	The insensitivity of Σ to the event selection criteria	163
8.2	The insensitivity of Σ and Σ_A to poor Z-position reconstruction in the events	164
8.3	The prediction of the Ali model for Σ_A and O_B for $\alpha_s = 0.11$	166
8.4	The prediction of the LundV4.3 model for Σ_A and O_B for $\alpha_s = 0.15$	166
8.5	The prediction of the LundV6.3 model for Σ_A and O_B for $\alpha_s = 0.15$	167
8.6	The prediction of the CIT2-FME model for Σ_A and O_B for $\alpha_s = 0.16$	169
8.7	Comparison of α_s values obtained in e^+e^- annihilations	173
9.1	Comparison between the high energy data and the Monte Carlo, including top production, for Thrust	176
9.2	The Thrust and Sphericity distributions for the high energy data.	178
9.3	The distributions in the first and second Fox-Wolfram event moments for the high energy data.	178
9.4	The distributions in the third and fourth Fox-Wolfram event moments for the high energy data.	179

9.5	Illustration of the idea behind the multidimensional discriminant analysis	184
9.6	The separation of top events from background events obtained by the multidimensional discriminant analysis at PETRA energies	186
9.7	Comparison between the high energy data sample and the control data sample with a multidimensional discriminant function.	187
10.1	R as a function of E_{cm} for various Top quark masses	193
10.2	R at the pole as a function of E_{cm} for various Top quark masses	194
10.3	The flavor composition of the events	198
10.4	The μ -inclusive event rate on passing a Top-production threshold at 60 GeV	200
10.5	The prediction for Thrust at the Z^0 pole with, and without, Top production	201
10.6	The prediction for Sphericity at the Z^0 pole with, and without, Top production	202
10.7	The prediction for Oblateness at the Z^0 pole with, and without, Top production	202
10.8	The prediction for H_4 at the Z^0 pole with, and without, Top production	203
10.9	Predicted Oblateness for events $t\bar{t} \rightarrow V^0 \rightarrow ggg(\gamma)$	204
10.10	The degree of isolation of muons in Top, u, d, s, c and b inclusive muon events	205
10.11	The amount of energy within a cone of 1/2-opening angle $\cos(\delta_{1/2})=0.70$ centred on the muon direction for inclusive muon events	206
10.12	The energy flow with respect to the muon direction for Top containing events	207
10.13	The distributions of Top events and the background obtained with a multidimensional discriminant function	208
A.1	Diagrams involved in the calculation of $\pi^0 \rightarrow 2\gamma$	223
B.1	The effect of combining partons at random within the minimum invariant mass cut scheme	230
C.1	Comparison of the Ali model predictions for T_N at 35 and 44 GeV	234
C.2	Comparison of the LundV4.3 model predictions for T_N at 35 and 44 GeV	234
C.3	Comparison of the LundV6.3 model predictions for T_N at 35 and 44 GeV	235
C.4	Comparison of the CIT2-FME model predictions for T_N at 35 and 44 GeV	235
C.5	Comparison of the CIT2-DLLA model predictions for T_N at 35 and 44 GeV	236
C.6	Comparison of the Ali model predictions for T_B at 35 and 44 GeV	236

C.7	Comparison of the LundV4.3 model predictions for T_B at 35 and 44 GeV	237
C.8	Comparison of the LundV6.3 model predictions for T_B at 35 and 44 GeV	237
C.9	Comparison of the CIT2-FME model predictions for T_B at 35 and 44 GeV	238
C.10	Comparison of the CIT2-DLLA model predictions for T_B at 35 and 44 GeV	238
C.11	Comparison of the Ali model predictions for M at 35 and 44 GeV	239
C.12	Comparison of the LundV4.3 model predictions for M at 35 and 44 GeV	239
C.13	Comparison of the LundV6.3 model predictions for M at 35 and 44 GeV	240
C.14	Comparison of the CIT2-FME model predictions for M at 35 and 44 GeV	240
C.15	Comparison of the CIT2-DLLA model predictions for M at 35 and 44 GeV	241
C.16	Comparison of the Ali model predictions for M_N at 35 and 44 GeV	241
C.17	Comparison of the LundV4.3 model predictions for M_N at 35 and 44 GeV	242
C.18	Comparison of the LundV6.3 model predictions for M_N at 35 and 44 GeV	242
C.19	Comparison of the CIT2-FME model predictions for M_N at 35 and 44 GeV	243
C.20	Comparison of the CIT2-DLLA model predictions for M_N at 35 and 44 GeV	243
C.21	Comparison of the Ali model predictions for M_B at 35 and 44 GeV	244
C.22	Comparison of the LundV4.3 model predictions for M_B at 35 and 44 GeV	244
C.23	Comparison of the LundV6.3 model predictions for M_B at 35 and 44 GeV	245
C.24	Comparison of the CIT2-FME model predictions for M_B at 35 and 44 GeV	245
C.25	Comparison of the CIT2-DLLA model predictions for M_B at 35 and 44 GeV	246
C.26	Comparison of the Ali model predictions for m at 35 and 44 GeV	246
C.27	Comparison of the LundV4.3 model predictions for m at 35 and 44 GeV	247
C.28	Comparison of the LundV6.3 model predictions for m at 35 and 44 GeV	247
C.29	Comparison of the CIT2-FME model predictions for m at 35 and 44 GeV	248
C.30	Comparison of the CIT2-DLLA model predictions for m at 35 and 44 GeV	248

C.31	Comparison of the Ali model predictions for m_N at 35 and 44 GeV	249
C.32	Comparison of the LundV4.3 model predictions for m_N at 35 and 44 GeV	249
C.33	Comparison of the LundV6.3 model predictions for m_N at 35 and 44 GeV	250
C.34	Comparison of the CIT2-FME model predictions for m_N at 35 and 44 GeV	250
C.35	Comparison of the CIT2-DLLA model predictions for m_N at 35 and 44 GeV	251
C.36	Comparison of the Ali model predictions for m_B at 35 and 44 GeV	251
C.37	Comparison of the LundV4.3 model predictions for m_B at 35 and 44 GeV	252
C.38	Comparison of the LundV6.3 model predictions for m_B at 35 and 44 GeV	252
C.39	Comparison of the CIT2-FME model predictions for m_B at 35 and 44 GeV	253
C.40	Comparison of the CIT2-DLLA model predictions for m_B at 35 and 44 GeV	253
C.41	Comparison of the Ali model predictions for O at 35 and 44 GeV	254
C.42	Comparison of the LundV4.3 model predictions for O at 35 and 44 GeV	254
C.43	Comparison of the LundV6.3 model predictions for O at 35 and 44 GeV	255
C.44	Comparison of the CIT2-FME model predictions for O at 35 and 44 GeV	255
C.45	Comparison of the CIT2-DLLA model predictions for O at 35 and 44 GeV	256
C.46	Comparison of the Ali model predictions for O_N at 35 and 44 GeV	256
C.47	Comparison of the LundV4.3 model predictions for O_N at 35 and 44 GeV	257
C.48	Comparison of the LundV6.3 model predictions for O_N at 35 and 44 GeV	257
C.49	Comparison of the CIT2-FME model predictions for O_N at 35 and 44 GeV	258
C.50	Comparison of the CIT2-DLLA model predictions for O_N at 35 and 44 GeV	258
C.51	Comparison of the Ali model predictions for O_B at 35 and 44 GeV	259
C.52	Comparison of the LundV4.3 model predictions for O_B at 35 and 44 GeV	259
C.53	Comparison of the LundV6.3 model predictions for O_B at 35 and 44 GeV	260
C.54	Comparison of the CIT2-FME model predictions for O_B at 35 and 44 GeV	260

C.55 Comparison of the CIT2-DLLA model predictions for O_B at 35 and 44 GeV	261
D.1 Comparison of α_s values obtained in e^+e^- annihilations	263

List of Tables

2.1	Summary of the MARK J hadron data	31
2.2	The detector energy containment and resolution	32
4.1	The models used in this study	64
5.1	The GS calculation compared to the ERT/Ali/Zhu calculation for $Y_{c,DD}=0.02$	85
5.2	The GS calculation compared to the ERT/Ali/Zhu calculation for $Y_{c,DD}=0.03$	85
5.3	The GS calculation compared to the ERT/Ali/Zhu calculation for $Y_{c,DD}=0.04$	86
5.4	The GS calculation compared to the ERT/Ali/Zhu calculation for $Y_{c,DD}=0.05$	86
5.5	The GS calculation compared to the ERT/Ali/Zhu calculation for $Y_{c,DD}=0.02$ and $Y_{c,FFS}=10^{-5}$	87
6.1	Example of an energy loss look-up table used by the detector simulation	96
6.2	Example of an r.m.s. deviation in energy loss look-up table used by the detector simulation	97
6.3	The detector acceptance for hadrons	102
6.4	The model parameters considered variable in this study	103
6.5	The mean values of some distribution predicted by the CIT2-DLLA model combination	124
6.6	The variation in the hard-QCD sensitive variables with changes in Λ_{LLA} for CIT2-DLLA	126
7.1	The effect of adding transverse momentum to the CIT2-FME model combination	152
8.1	α_s obtained from the Ali model, with various values of σ_q	165
8.2	The values of α_s obtained from the LundV4.3 model, with various values of σ_q	165
8.3	The values of α_s obtained from the LundV6.3 model, with various values of σ_q	167
8.4	The values of α_s obtained from the CIT2-FME model, with various values of ρ	168

8.5	Summary of α_s measurements in e^+e^- annihilation	172
9.1	The cuts used to search for top in the high energy data	180
9.2	The significance of the discrepancies in the high energy data from counting events	180
9.3	The significance of the discrepancies in the high energy data from a χ^2 comparison	180
9.4	The significance of the discrepancies in the high energy data from a Kolmogorov-Smirnov comparison	181
9.5	The significance of the discrepancies in the high energy data from counting events in scatter plot regions	181
9.6	The coefficients of the discriminant function used to investigate the high energy data	185
10.1	The total cross section and R for $M_t = 30.0$ GeV	195
10.2	The total cross section and R for $M_t = 47.0$ GeV with radiative corrections included	196
10.3	The total cross section and R for $M_t = 47.0$ GeV with radiative corrections omitted	197
10.4	Inclusive Lepton rates as a function of the available center-of-mass energy	199
10.5	The coefficients of the discriminant function for selecting a Top containing hadron sample	207
10.6	The quark content of events selected by cutting on a multidimensional discriminant function	208
B.1	Summary of the recombination schemes recently investigated by Gutbrod <i>et al.</i>	228
B.2	Comparison of the ERT/Ali/Zhu and GS calculation for $Y_{c,DD}=0.02$ with random-parton recombination	231
B.3	Comparison of the ERT/Ali/Zhu and GS calculation for $Y_{c,DD}=0.03$ with random-parton recombination	231
B.4	Comparison of the ERT/Ali/Zhu and GS calculation for $Y_{c,DD}=0.04$ with random-parton recombination	231
B.5	Comparison of the ERT/Ali/Zhu and GS calculation for $Y_{c,DD}=0.05$ with random-parton recombination	232
D.1	Summary of α_s measurements in e^+e^- annihilation	262

Chapter 1

Introduction

This thesis is concerned with the study of the strong interaction based on the analysis of hadronic final states in e^+e^- annihilation. The present theory of the strong interaction is Quantum Chromodynamics, or QCD, which is a field theory describing the interaction between quarks and gluons. A brief review of the discovery of quarks as the fundamental constituents of strongly interacting particles, the mounting evidence for their existence obtained over the last 25 years, and an introduction to the ideas underlying QCD may be found in Appendix A, and the references given there.

The data used in this study were accumulated with the MARK J detector at the PETRA e^+e^- storage ring in Hamburg, West Germany [1,2]. The principal physics process leading to hadronic jet events is:

$$e^+e^- \rightarrow \gamma^* \rightarrow q\bar{q}, \quad (1.1)$$

where the subsequent evolution of the final $q\bar{q}$ state is described by QCD. The first clear evidence for the occurrence of the process (1.1) was obtained in 1974 at the SPEAR storage ring, where it was found that hadrons emerging from the interaction point were collimated into two narrow jet-like regions [3,4]. Further, it was found that the angular distribution of the jet directions with respect to the incoming electron and positron beams was consistent with the production of two spin-1/2

particles [4]. It was soon established that hadron production in e^+e^- annihilation takes place through the decay of a virtual photon (γ^* in Eqn. 1.1) into a quark-antiquark pair. It was also determined that the initial directions of the quark and antiquark are, at least partially, preserved by the final hadron directions.

Within the first few months of operation of PETRA, the predominance of jet production became clear, and the increased collimation of the jets with rising center-of-mass energy was established. The SPEAR results were, therefore, fully confirmed [5,6,7,8,9]. The first few months of operation at PETRA also revealed the existence of events containing three collimated jets [8,10,11,12,13]. This was attributed to the hard bremsstrahlung of a gluon by the quark or antiquark, i.e.,

$$e^+e^- \rightarrow q\bar{q}g. \quad (1.2)$$

This observation was the first experimental evidence for the existence of gluons, and, hence, provided strong experimental support for QCD as a viable candidate theory of the strong interaction. At the present time, there is also evidence for the production of events originating in the process:

$$e^+e^- \rightarrow q\bar{q}gg, \quad (1.3)$$

which are observed as four collimated jets of particles in the detector [14,15].

Since the discovery of gluons, a major effort has been made to determine the magnitude of their coupling to quarks and antiquarks. This coupling, α_s , is one of only four fundamental coupling constants in nature [16,17]. The first *correct* determinations of α_s were made over the period 1980-1983 by the MARK J and PLUTO collaborations [18,19]¹. Other determinations from this period were found to be in disagreement with the MARK J measurement, and questions were raised about the feasibility of measuring α_s in e^+e^- data [17,20,21,22,23,24,25,26]. Detailed analyses made during the period 1983-1987 by R. Zhu and others [25,27,28,29] showed

¹Although the PLUTO result was published later than the MARK J result, both groups performed their analyses during the same period.

that the origin of the discrepancies could be traced to approximations made in the theoretical calculations used in the analyses, to the use of improper experimental observables, or to certain details within the fragmentation models used. By the 1987 Hamburg conference, however, all groups were within reasonable agreement with the 1983 MARK J second order result, and with each other.

Throughout the controversy over the measurement of α_s , it became increasingly clear that one of the main obstacles to be overcome in relating e^+e^- hadronic data to the underlying theory of QCD was the lack of understanding of the mechanism by which the quarks and gluons ‘fragment’ into the finally observed hadrons [25].

In recent years a number of models have been proposed to describe the fragmentation process in e^+e^- annihilation data [30,31,32,33,34,35,36,37,38,39,40]. The principal aim of this thesis is to compare the predictions from some of these models to the MARK J data and attempt to discriminate between the various models. Clearly, if one of the fragmentation models can be deemed incapable of describing the data, then α_s values which have been extracted with that model can be ignored when estimating the systematic error to be assigned to α_s .

In particular, attention has recently been focused on the differences between the so-called ‘string fragmentation’ models and the earlier ‘independent jet’ models. The main difference between the models is thought to arise in the region between the jets due to the quark and the antiquark. Some experiments have claimed to have seen this effect through their measurements of the number density of particles observed in this region [41,42,43,44,45,46,47]. Due to the calorimetric nature of the MARK J detector, it is not possible to investigate the particle densities in the region of interest. However, the ‘density of energy flow’ is well measured by the MARK J, and the various model predictions for this quantity have been examined in the regions between the jets.

Much of the controversy over the early α_s values revolved around the perturbative

QCD calculations being used to give the QCD prediction for the three-jet partial cross section. Recently, a new and independent calculation for the three-jet partial cross section has been made [48]. In this study the results of this calculation have been converted into a form suitable for comparison to the original calculation of Ellis, Ross and Terrano² [50]. The results of this comparison indicate that the perturbative aspects of the theory are now understood, even if their applicability is limited. A summary of a short investigation into one aspect of relating the results of the perturbative QCD calculations to the experimentally observed jet configurations is presented in an appendix.

The α_s values extracted from the data using different fragmentation models are compared to each other and to the previously obtained values. Since the overwhelmingly dominant systematic errors assigned to α_s measurements come from the choice of the fragmentation model used in the measurement, the results of this study can be used to check the magnitudes of the previously assigned systematic errors [51].

At the highest energies at which PETRA operated, the MARK J inclusive muon analysis detected an excess of events having unique and rare topologies. The observed event configurations pointed to the possibility of new heavy particle production [52]. This observation was later confirmed by the JADE collaboration [53]. Since this is a possible signal for the onset of new physics, a detailed analysis of the highest energy hadronic data has been made with the specific aim of detecting any departures from expected behavior.

The data taken by the MARK J detector covers the entire energy range available at PETRA, from 12 GeV to 46.78 GeV in the center-of-mass. There are two large data sets at 35 GeV and at 44 GeV. The large data set at 44 GeV has not previously been studied. The MARK J detector is, essentially, a calorimeter covering 94% of

²Over the last five years, it has become recognized that this calculation, and that performed by Vermaseren *et al.* [49], were the only correct calculations among those originally presented in 1980 and 1981.

the available solid angle, and the data used in this study are derived from this calorimetric information [1,2]. The hadronic data used in this study are selected from background events, arising from the two photon ($e^+e^- \rightarrow e^+e^- + \text{hadrons}$) and from $\tau^+\tau^-$ production, through the use of cuts on the energy distributions measured in the calorimeters as well as other criteria. The data sample used for this study comes purely from the e^+e^- annihilation processes shown in Eqns. (1.1), (1.2) and (1.3), with a contamination from other sources of, at most, a few percent [27].

The basic outline of the thesis is as follows. In Chapter 2 the experimental apparatus is described in detail, with particular emphasis on those detector elements used to identify hadronic events and measure the energies and directions of the hadrons. The offline data reduction procedures and event reconstruction are also described, sources of measurement error are pointed out and discussed, and the final hadron data sample is described. In Chapter 3 the aspects of perturbative calculations, which are relevant to the later parts of the study, are described, and the predictions of QCD pertinent to the e^+e^- annihilation data are outlined. The various fragmentation models which are used to relate the predictions described in Chapter 3 to the measured data are described in Chapter 4, and the possibility of experimentally distinguishing between the models is discussed. In Chapter 5, the existing $O(\alpha_s^2)$ calculation used by the MARK J collaboration [27] is compared to a more recent calculation by Gottschalk and Shatz [48], and certain aspects of the fragmentation models are contrasted with each other for the case of a perfect detector. A discussion of the possible recombination dependence³, which is encountered in the 2nd order perturbative QCD calculations, is relegated to Appendix B. In Chapter 6 the detector simulation program that connects the model predictions for a perfect detector (so called ‘raw track’ predictions) to predictions for hits in

³A dependence of the final state jet topologies on the way soft, or collinear, partons are recombined.

the actual detector is described. Also in Chapter 6, the methods used to adjust the free parameters occurring in the models so that their predictions can be compared to the data are described. In Chapter 7 the model predictions are compared to the data, and detailed comparisons are made to the two large data sets at 35 and 44 GeV. Many of the plots for this discussion have been collected in Appendix C. In the light of the data, the string effect is discussed and the results of this study are compared to existing results. The fragmentation model dependence of α_s is discussed in Chapter 8, and earlier α_s studies are reviewed in the light of this analysis. Chapter 9 contains a detailed comparison between the highest energy hadronic data sample and a control data set at 44 GeV. It is found that, in spite of the observations made in the inclusive muon channel, no new physics is evident in the shapes of hadronic events above 46.3 GeV. Chapter 10 contains the results of a brief study of simulated jet events at higher energies, with emphasis on observing top production at LEP/SLC energies. Finally, in Chapter 11 the main results obtained are reviewed, the conclusions of this work are presented, and suggestions are made for future work.

Chapter 2

Description of the Experiment

2.1 The PETRA e^+e^- Storage Ring

The PETRA (Positron-Electron Tandem Ring Accelerator) storage ring in Hamburg operated from 1978 to 1986¹. It was the world's highest energy electron-positron storage ring and covered the center-of-mass energy range from 12 to 46.8 GeV. The accelerator is housed in a 2.3 kilometer tunnel and consists of eight straight and eight identical curved sections. Four of the straight sections are occupied by R.F. cavities that accelerate the beams. The remaining, shorter straight sections are occupied by the experiments. The MARK J experiment was located at one of the four interaction regions, and it is the data accumulated with this detector that is the subject of this study.

The general layout of the accelerators at the laboratory is shown in Figure 2.1. Initially, electrons are accelerated in LINAC I to 50 MeV prior to injection into the DESY synchrotron. Positrons are obtained through bremsstrahlung and conversion of 150 MeV electrons on a copper, lead or tungsten target. The positrons are then accelerated to 400 MeV in LINAC II and injected into a 'positron accumulating ring' (PIA). Positrons are accumulated until a sufficient number to 'fill' PETRA have

¹It is now being converted to serve as an injector for the HERA ep collider. The TRISTAN storage ring in Japan superseded PETRA as the highest energy e^+e^- storage ring in early 1987, and data is now being accumulated there at 52 GeV in the center-of-mass

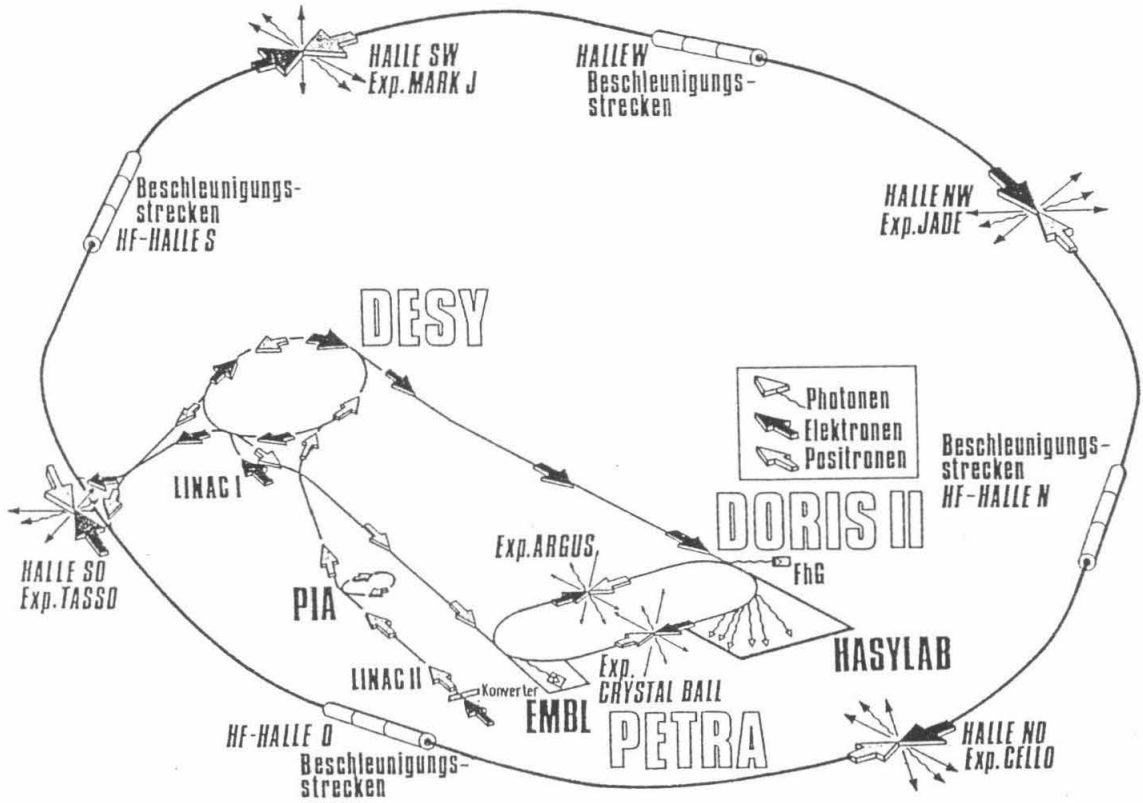


Figure 2.1 Layout of the accelerators at the DESY site.

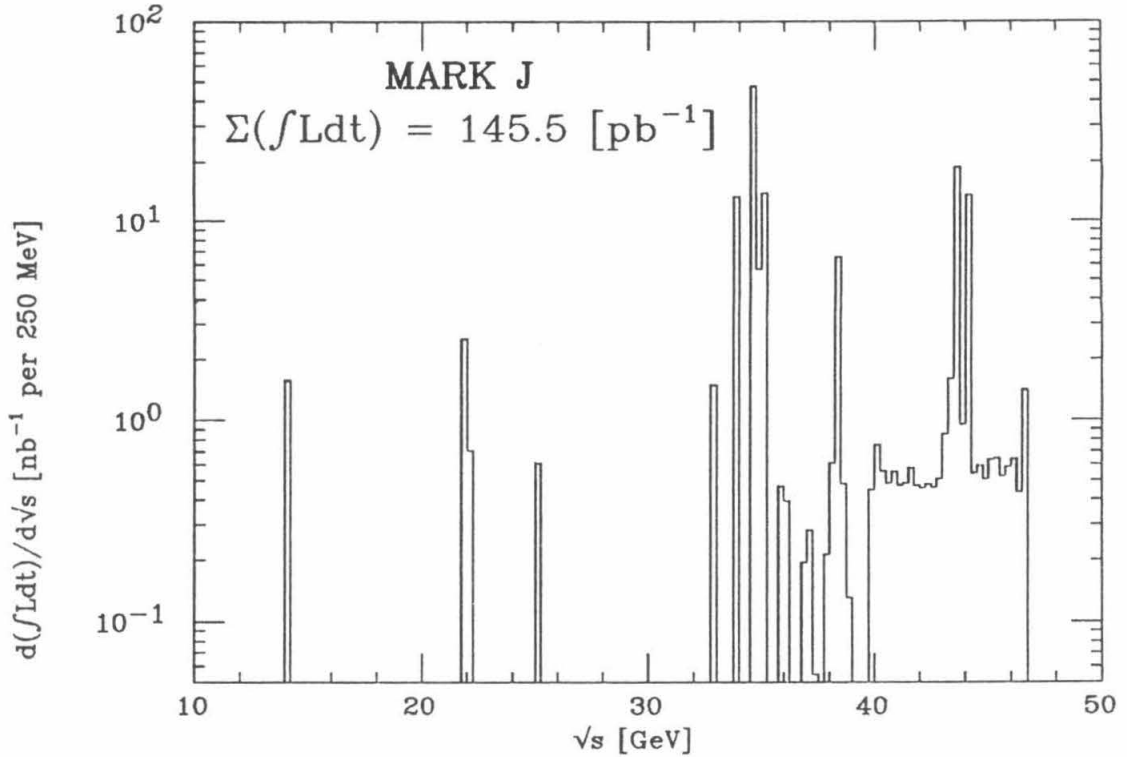


Figure 2.2 The integrated luminosity taken by the MARK J as a function of the available energy in the centre of mass.

been collected. At this point they too are injected into DESY. Both positrons and electrons are accelerated to 7 GeV in DESY for injection into PETRA as counter-rotating beams that are further accelerated to the desired energy. The maximum energy that PETRA attained was 23.4 GeV per beam. Each beam contains two bunches, each of which consists of $1 - 2 \times 10^{11}$ particles, corresponding to a current of 2 to 4 mA/bunch. The bunches are focused to collide at the centers of the detectors every $3.84 \mu\text{sec}$. At the interaction points the bunches are typically 0.5 mm wide, 0.05 mm high, and 10 mm long. The integrated luminosity collected by the MARK J detector over its lifetime is shown in Figure 2.2 as a function of the center of mass energy.

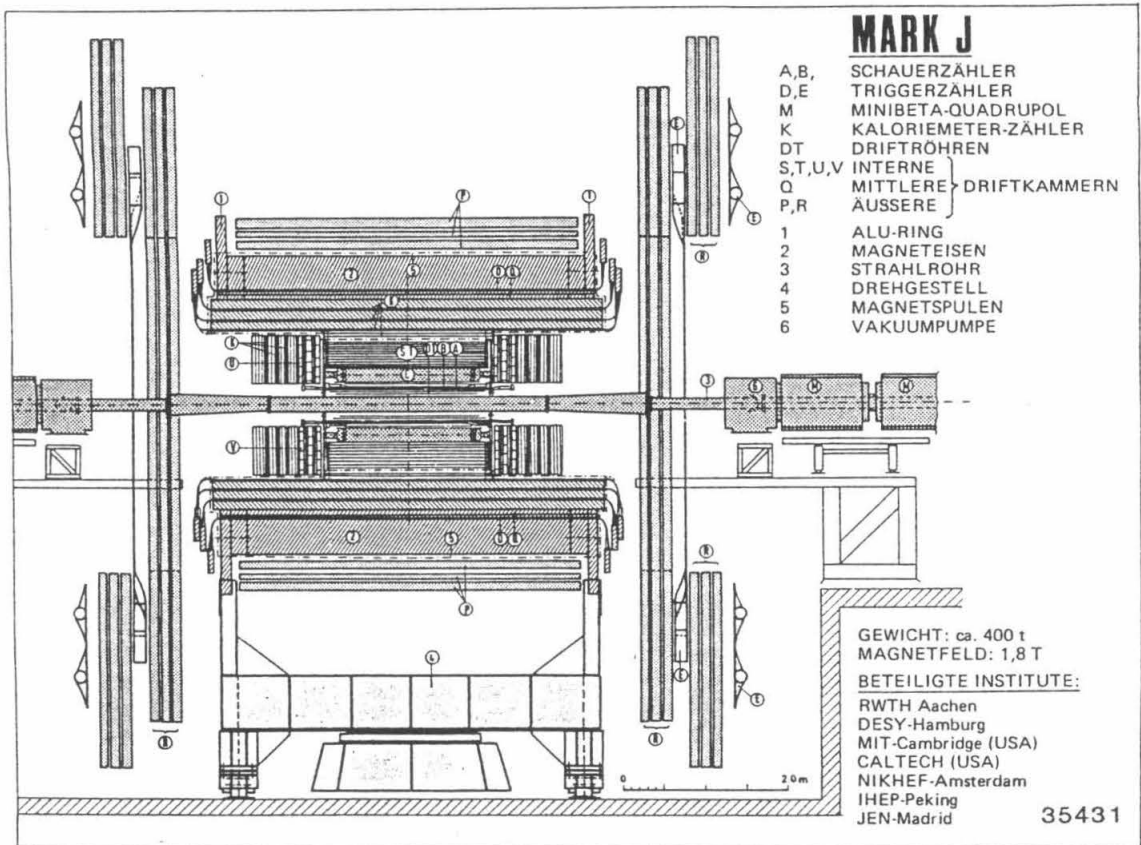
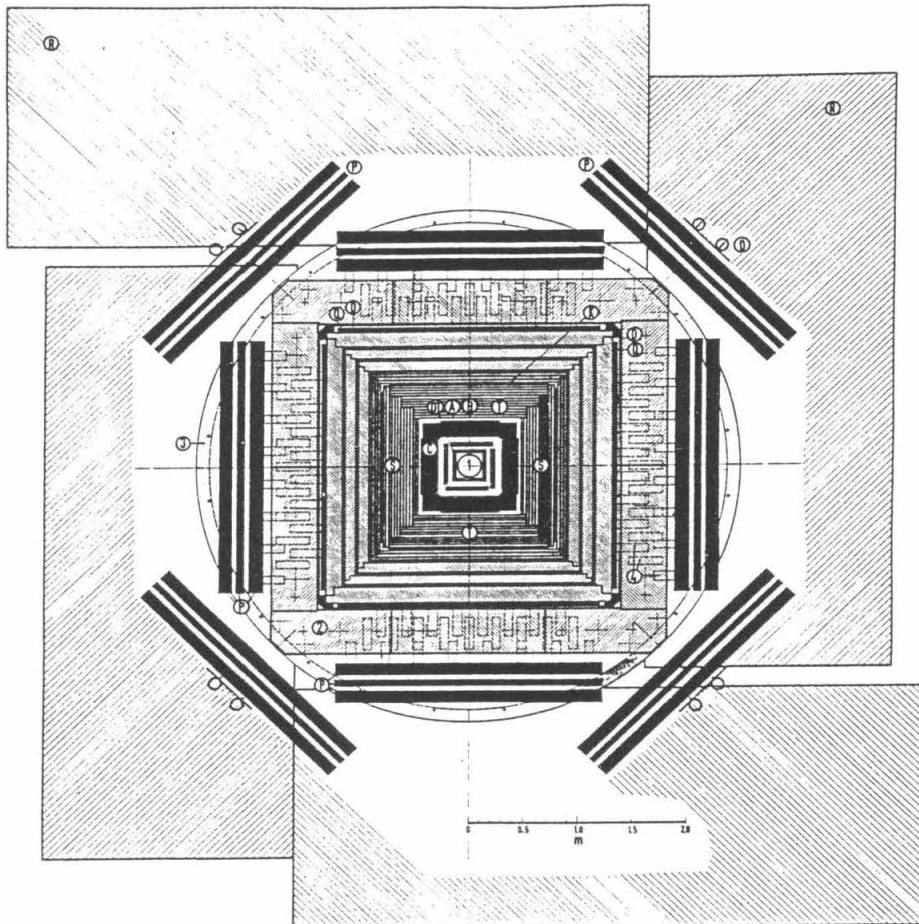


Figure 2.3 The MARK J detector seen side-on.

2.2 The MARK J Detector

The MARK J detector is shown in Figures 2.3 and 2.4. The layer structure of the MARK J detector as seen by a particle emerging from the interaction region perpendicular to the beams is shown in Figure 2.5. As the particles emerge from the interaction point and traverse the detector, they first pass through the 4 mm thick aluminum beam pipe. This is followed by a vertex detector (comprised of drift tubes) and the electromagnetic calorimeter, which consists of three layers of lead scintillation counters (shown as A,B and C in the figures). The electromagnetic calorimeter is surrounded by the inner drift-chambers of the muon spectrometer (S,T). Additional energy measurements for hadrons are made in the 4 layers of scin-

MARK J - DETEKTOR
(Querschnitt)



- Ⓐ Ⓑ Ⓒ SHOWER COUNTERS
- Ⓘ TRIGGER COUNTERS
- Ⓜ DRIFT TUBES
- Ⓛ DRIFT CHAMBERS, MEDIAN
- Ⓟ Ⓠ DRIFT CHAMBERS, OUTER
- Ⓡ Ⓢ DRIFT CHAMBERS, INNER

- ① BEAM PIPE
- ② MAGNET IRON
- ③ AL - RING
- ④ MULTIPLIERS

PARTICIPANTS:

- RWTH - Aachen
- DESY - Hamburg
- MIT - Cambridge
- NIKHEF - Amsterdam
- HEPI - Peking
- JEN - Madrid
- CALTECH - Pasadena

WEIGHT (total) : ~ 400 t
MAGNETIC FIELD: 1.8 T

Figure 2.4 The MARK J detector seen end-on.

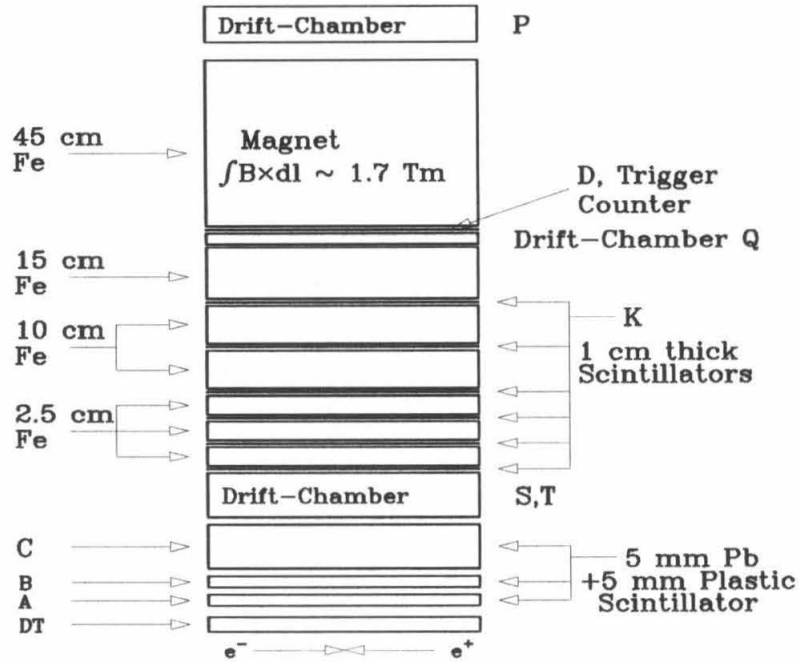


Figure 2.5 The detector elements as they would be seen by a particle crossing perpendicular to the beamline.

tillation counters (K) embedded in the magnetized iron of the muon spectrometer. Particles that pass through the iron are detected by drift-chambers halfway through the iron (Q) and by two large drift-chambers outside the magnet (P,R). Cosmic ray rejection is provided by time-of-flight scintillation counters situated immediately above the Q chambers. Apart from some small gaps in the four corners, the detector covers the entire azimuthal angle ϕ around the beamline and the calorimeters cover the polar range $\theta = 12^\circ$ to 168° . The detector is described in detail in two earlier papers by the collaboration, and the interested reader is referred to these papers [1,2]. We shall omit a detailed discussion of detector elements that are not directly relevant to the hadron data.

2.3 Description of Detector Elements

2.3.1 The Vertex Detector

The vertex detector is used in this analysis to reconstruct the vertex of the event. It also provides information that is used to reject beam gas events and to distinguish high energy photons from jets containing charged particles. This subsystem of the detector consists of 2616 drift tubes arranged in four layers and deployed perpendicular to the beampipe, so that the coordinate along the beam direction is measured. Each tube is made from an aluminum cylinder 1 cm in diameter, 30 cm in length, and 0.2 mm thick. The aluminum cylinder is kept at ground potential while a 0.04 mm diameter tungsten readout wire, running along the center of the tube, is kept at 1950 Volts. The tubes are filled with 60% argon and 40% ethane, a mixture for which the electron drift velocity is 5 cm/ μ s. The distance of closest approach from the readout wire of a particle that passes through a tube is found from the difference in arrival times between the readout signal and a reference signal. The resolution on this time measurement, together with the systematic errors due to positioning the drift tube modules, leads to a distance resolution of 270 μ m (r.m.s.). The entire array covers the full azimuthal angle apart from gaps of 7° degrees in the corners and extends from 10° to 170° in θ , the polar angle with respect to the beam. Complete details of the vertex detector can be found in Reference [54].

The event vertex is reconstructed by performing a least squares fit to find a straight line that is tangent to imagined circles around sense wires, having radii corresponding to the distance of the hit from the wire, as indicated in Figure 2.6. At least 4 hits are required for fitting each track, and the fit is performed with the constraint that the tracks all extrapolate to a common vertex on the beamline. In Figure 2.7 the reconstructed vertices for events at E_{cm} of 35 and 44 GeV are shown

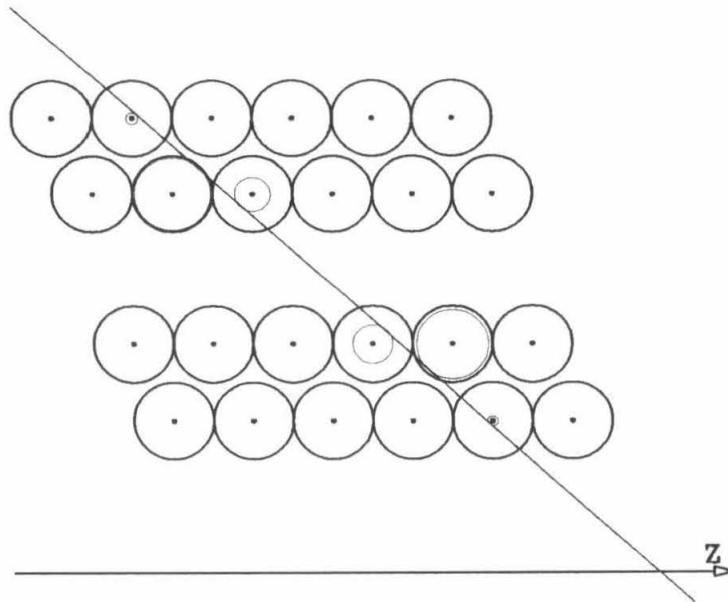


Figure 2.6 The method by which particle trajectories are reconstructed with the vertex drift tube array information.

together with Gaussian fits. The widths of the distributions reflect the longitudinal bunch length of the beams in PETRA. The absence of any constant tails on either side of the peaks shows that the data is free of cosmic-ray or beam-gas backgrounds. The fitted central peak is at $Z=0.816\pm 0.007$ cm for the 35 GeV data and at $Z=0.103\pm 0.009$ cm for the 44 GeV data.

2.3.2 The Calorimeters

Immediately outside the vertex detector are the three layers of scintillation counters that comprise the electromagnetic calorimeter. All the counters are constructed from 5 mm thick pieces of scintillator (read-out from both ends with photomultiplier tubes) alternated with lead plates of equal thickness. The three layers (A,B and C) are 2 m, 1.42 m, and 1.44 m in length respectively. One layer of scintillator together with one plate of lead provides one radiation length at normal incidence. The counters are arranged so that at normal incidence these layers are 3, 3 and

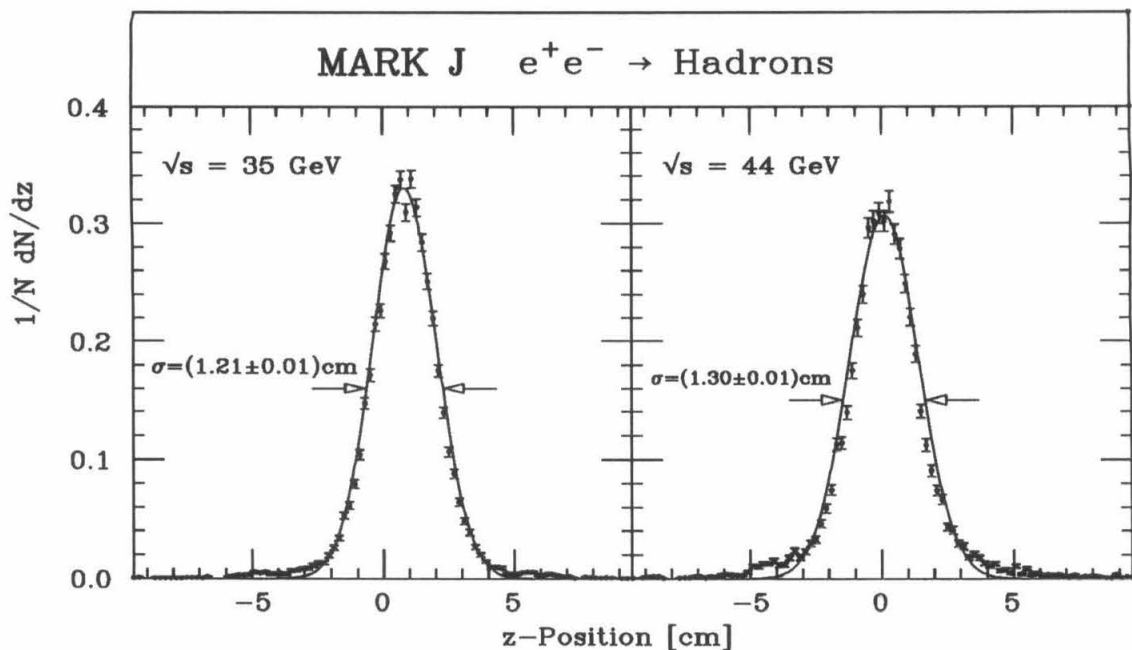


Figure 2.7 Reconstruction of e^+e^- interaction point along the beamline from the vertex drift tube array information.

12 radiation lengths thick for the A, B and C counters respectively, or a total of 1 absorption length. The A layer contains 20 shower counters providing coverage over the full angular range in ϕ and from 12° to 168° in θ . Surrounding the A counters, but off-set slightly in ϕ , are the 24 B counters extending from 16° to 164° in θ and, again, covering the full range in ϕ . The C counters, of which there are 16, are also off-set slightly in ϕ and provide additional coverage in the range $\theta = 26^\circ$ to 154° . For a typical hadronic event, the observed total energy deposited in the detector is shared between the hadron calorimeter, 25%, and the electromagnetic calorimeter, 75%, of which 35% is deposited in the A counters, 15% in the B counters and 25% in the C counters. The energy sharing between the counter planes as a fraction of the available center-of-mass energy is: 32% for the A counters, 13% for the B counters, 20% for the C counters and 22% for the K counters. The resolution of this calorimeter is $\frac{\sigma(E)}{E} = 7\%$ r.m.s. for a 17 GeV electron.

The hadron calorimeter consists of 192 scintillation counters (K), instrumented

with a photomultiplier tube at one end, and interleaved with magnetized iron slabs ranging in thickness from 2.5 cm to 15 cm. The counters are arranged in four layers, the inner layers extending in ϕ from 43° to 137° , and the outer from 26° to 154° . The counters cover the full ϕ range with the exception of some 4° regions in the corners.

2.3.3 The Muon Spectrometer

The inner drift-chambers of the muon spectrometer are arranged in twelve planes outside the C counters. The momenta of the muons are analyzed by the magnetized iron, in which a magnetic field of 1.7 Tesla is maintained. The magnet is 5.4 hadronic interaction lengths thick and also serves as a muon filter, i.e., muons are identified by their ability to penetrate the magnet. The trajectories of muons penetrating the magnet are measured in twelve planes of drift-chambers outside the magnet and in two planes located halfway through the magnet. The drift-chambers all consist of 10 cm cells formed by field-shaping I-beams [55]. Each cell has a position resolution of 0.4 mm for normally incident tracks. The momenta of the muons is obtained by comparing their directions before traversing the magnet to their directions as measured in the outer drift-chambers. Two sets of outer scintillation counter arrays, the D and E counters, are situated in planes in front of and behind (D') the outer muon chambers. These counters are used for triggering on muon events and also provide extremely effective cosmic-ray rejection through timing information.

2.3.4 The Data Acquisition System and Trigger

The information from the detector is read-in with a PDP-11/55 computer that interfaces to two CAMAC branches through two microprogrammable branch drivers

(MBDs). The MBDs are capable of adding, subtracting and performing logical operations. They are used for making fast trigger decisions and are operated in a manner such that the PDP does not read in the data unless a trigger is accepted. One of the CAMAC branches is used exclusively for monitoring the experiment, reading in the high voltages of the counter power supplies, recording counter rates, and reading in various data provided by PETRA. The second CAMAC branch is used to read in the data from the counter ADCs² and TDCs³ and the drift-chamber TDCs.

The trigger is arranged in three stages. The first stage is a fast trigger generated from hit information in the A, B, C and D counters. The hadron trigger requires a signal from this stage of the trigger indicating that at least three A and three B counters were hit, and that there were at least two coincidences between hits in opposite quadrants of the A, B or C counter arrays. This signal requires about 150 ns to be generated and, on being sent, initiates the analog to digital conversions of the signals from the detector components, a process that requires about 100 μ s. The trigger rate after this first stage is typically 300 Hz.

The second stage trigger performs a fast energy sum of the counter hits in the detector. This trigger starts upon receiving a signal from the first stage trigger that indicates a hadron, inclusive muon or Bhabha event. Signals from all the A, B and C counters are fed to three linear fan-in modules where they are summed, attenuated and fed into a further linear fan-in. The attenuation is adjusted so as to allow different weights for the different counter arrays. The signal from the final fan-in represents, in a broad sense, the analog sum of all the hits in the inner counters. This signal is fed into an integrator to find the total charge in the pulse, and the output from the integrator is sent to a discriminator. The signal from this discriminator

²Analog to Digital Converters

³Time to Digital Converters

provides a ‘total energy trigger’. By adjusting the threshold of the discriminator, the ‘threshold energy’ for the detector can be adjusted. For the hadron trigger this ‘threshold energy’ is $1/12^{\text{th}}$ of the available center of mass energy. The generation of the total energy trigger takes about 500 ns and the trigger rate after this stage of the trigger is typically 5 Hz.

The third stage of the trigger is an on-line selection performed by the software running on the data taking MBD. For events that passed the first stage hadron trigger and that generated an above-threshold total energy signal, the MBD performs the following operations. First, the ADC values from the A, B and C counters are read in. The energy deposited in the inner calorimeter is summed and, if larger than $1/12$ of the center-of-mass energy, the K counter ADC values are read-in, otherwise, the electronics are cleared and reset for the next beam crossing. The total energy in the detector is then calculated: a hadron ‘trigger’ requires that this sum is at least $1/6^{\text{th}}$ of the available center-of-mass energy. Next, the energy deposited in the separate quadrants of the whole detector is calculated, and the requirement that the energy imbalance be less than 25% of the center-of-mass energy is imposed. If all of the above criteria are met, the MBD then passes the event to the PDP-11 with the hadron trigger word set. Otherwise it clears the electronics and resets the CAMAC for the next trigger. The PDP-11 writes events passed to it onto magnetic tape for further analysis. The rate at which events are written to tape is about one event per second, and the resulting deadtime is about 5%. The logic diagram for the trigger is shown in Figure 2.8.

2.3.5 Offline Analysis and Calibration

The information written to tape consists of the digitized hit pulse height data from the counters and the digitized timing data from the muon and vertex drift tubes. The offline analysis chain serves to reconstruct the event as far as is possible

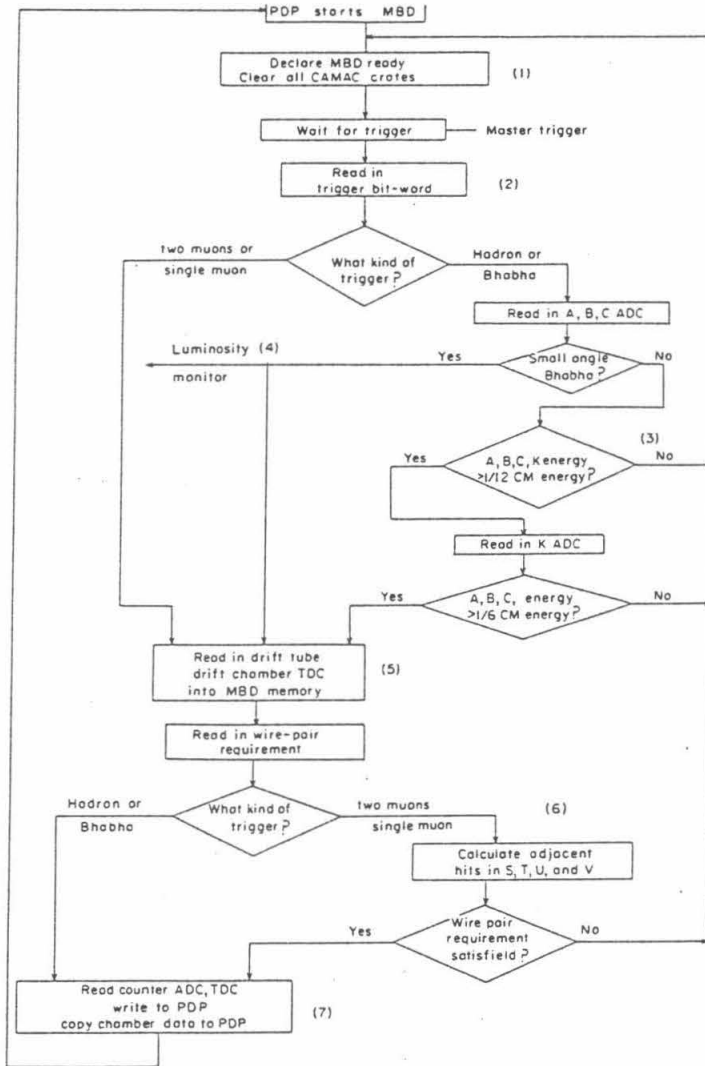


Figure 2.8 The trigger logic diagram for the data taking system and MBD program

from this data. This reconstruction depends on the analysis software and on the detector calibration. We are principally interested in the hadron event reconstruction, which is in the form of energy deposits in the various layers of the detector, and so we will limit the discussion to this aspect of the analysis.

Offline Analysis

The ADC and TDC information from the A, B and C counters is used to determine the θ position of a hit in the counter, while the ϕ position of the counter corresponds to ϕ of the hit. For the inner counters (A, B and C) the photomultiplier tubes (PMT's) on each end of the counter are instrumented with ADCs and TDCs from which the Z-position of the hit is reconstructed. The discussion below is intended to be a brief synopsis of the analysis chain, and we omit a protracted discussion of the many (small) corrections that are applied to the raw data.

For each counter the ADC pedestal, T_0 , gain, light propagation velocity and G-factor are stored in a calibration file (T_0 is the time of flight for a particle to go from the vertex to the middle of the counter, and the G-factor is the gain factor applied to the raw PMT signal). The propagation time of the light arriving at the PMT is calculated according to Eqn. (2.1) where the function $F_i(ADC)$ takes into account the timeskew that results when the pulse height of the signal from the PMT is discriminated prior to being sent to the TDC. In Eqn. (2.1) the subscripts refer to the quantities for each end of the counter:

$$T_i = (T_{TDC,i} - T_0)F_i(ADC). \quad (2.1)$$

A Z-position is obtained from the timing information by comparing the arrival times of the light at each end of the counter. Referring to Figure 2.9, the Z-position is given by the expression in Eqn. (2.2) below, in which V is the light propagation

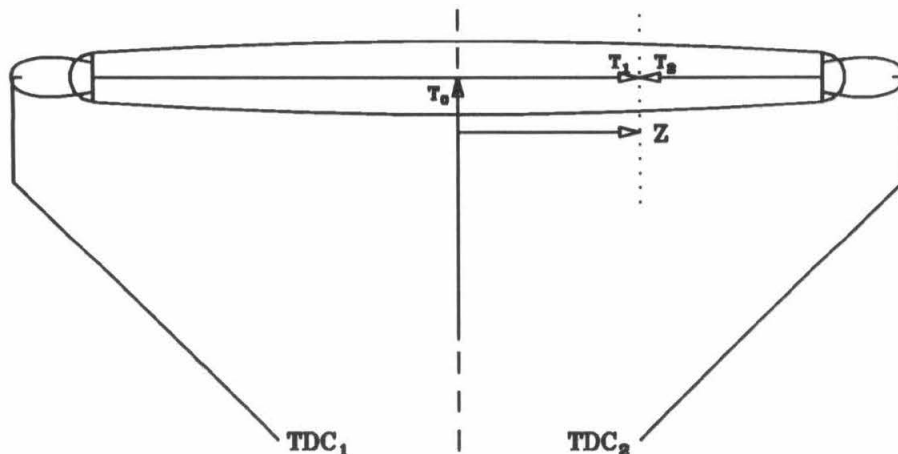


Figure 2.9 The method used to reconstruct the Z-position of a counter hit from counter TDC information

velocity in the counter:

$$Z_{TDC} = \frac{V}{2}(T_2 - T_1). \quad (2.2)$$

Next, the energy of a counter hit, E_i , is determined from the raw ADC value measured by each PMT from:

$$E_i = ADC_{Ch,i} Gain_i G_{fac,i}, \quad (2.3)$$

where $Gain_i$ is the PMT gain and $G_{fac,i}$ is an adjustable correction determined by the calibration procedure (see below). By comparing the pulse height of the PMT signal from each end of the hit counter, the ADC information also yields a Z-position. The magnitude of the ADC value from each end of the counter depends on the attenuation of the hit as the light propagates along the counter. The Z-position can be related to the ratio of the hit magnitude at each end of the counter and the

attenuation length of the counter (Λ) through Eqn. (2.4):

$$Z_{ADC} = \frac{1}{2} \Lambda \ln\left(\frac{E_1}{E_2}\right). \quad (2.4)$$

For the C counters the TDCs are inferior to the ADCs in determining the Z-position, so the Z value used in the analysis is always Z_{ADC} . For the A or B counters the final value taken for the Z-position and used in the analysis is normally determined from the two values above by taking a weighted average, as indicated in Eqn. (2.5):

$$Z = \frac{W_{ADC} Z_{ADC} + W_{TDC} Z_{TDC}}{W_{ADC} + W_{TDC}}. \quad (2.5)$$

The weights, W_{ADC} and W_{TDC} , that are used are optimized by the calibration described below for each run to give the best resolution on the reconstructed position. Typical values are $W_{ADC} \approx W_{TDC} \approx 0.5$. The circumstances under which the final Z-position is not given by Eqn. (2.5) are the following:

- One or both ADCs are saturated. Then $Z = Z_{TDC}$.
- The timing of the hits, T_i , are outside some bound. Then $Z = Z_{ADC}$.
- The quantity $Z_{ADC} - Z_{TDC}$ is outside some bound. Then $Z = Z_{ADC}$.
- Z_{ADC} or Z_{TDC} are greater than the counter length. Then Z is set to half the counter length.

In Figure 2.10 the Z-position calculated from the ADC information is histogrammed against that obtained from the timing information for the A and C counters at 44 GeV E_{cm} . The figure shows contours obtained by normalizing each histogram to have the same peak value at $Z_{TDC} = Z_{ADC} = 0.$, and the contours shown are for values 0.1, 0.2, 0.3 and 0.4 times the value at this peak. It is clear from the figure that the main contribution to the optimized Z-position for the C counters comes from the ADC data, while for the A counters (and B counters) the ADCs and TDCs

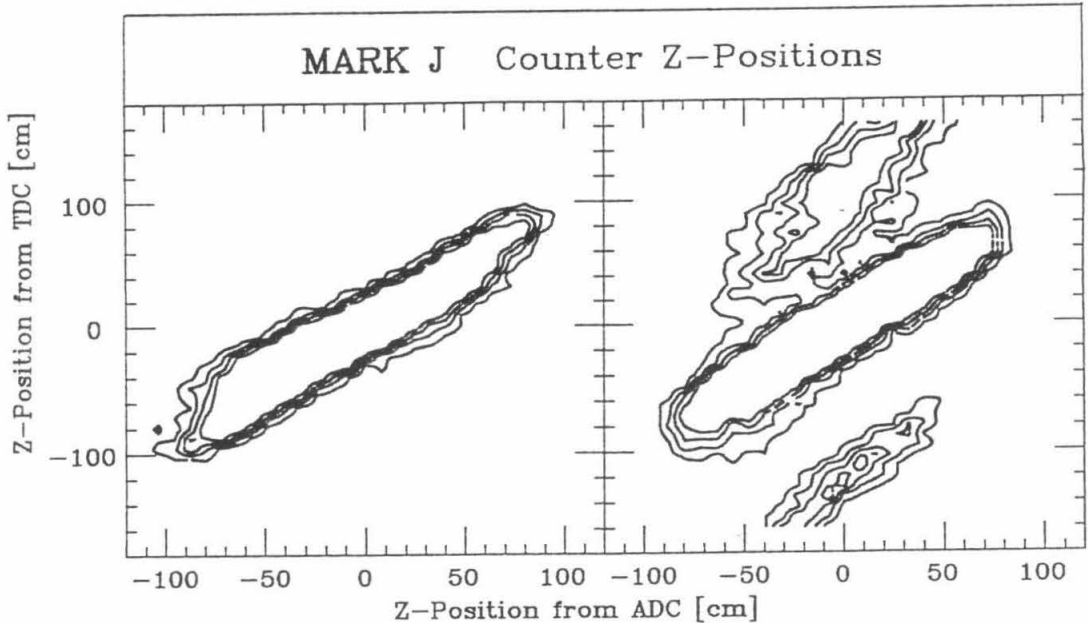


Figure 2.10 The Z-position reconstruction for hits in the A and C counters as determined from timing and pulse-height data

contribute about equally. The side-bands, seen in the figure for the C counters, are caused by soft hits due to synchrotron radiation that are registered in the C counter TDCs but not in the high threshold TDCs that instrument the A and B counters.

The counters in the outer calorimeter (K) are instrumented on one end only. Consequently, the Z-position for these counters is determined from the timing information alone according to:

$$Z = [(T_{TDC} - T_0)F(ADC)]V. \quad (2.6)$$

The final Z-position that is used in the analysis for the K counters is arrived at by comparing ‘counter-tracks’, obtained by applying a track finding algorithm to the counter hits, to hits in the S and T chambers of the inner muon spectrometer. If a track constructed from the K counter-hit can be extrapolated to a cluster of hits in the S and T chambers (so-called STBLOBS), then the Z-positions in the K counter planes are taken as lying on that track. In cases where there is no track pointing to a STBLOB, the K counter hit is moved so that it coincides with the nearest

STBLOB, and this Z-position is used in the subsequent analysis.

The next stage in the analysis of the data is the calculation of the energy to be assigned to each counter hit. For counters that are equipped with a PMT at each end, the total counter energy is taken as the weighted sum of the hit energy as determined by each PMT. The total counter energy for a two-tube counter is then given by Eqn. (2.7), where the subscripts refer to the ends of the counter, W_1 and W_2 are weighting factors determined by the calibration, and l is one half of the counter length:

$$E_{Tot} = \frac{e^{l/2\Lambda}(E_1W_1e^{-Z/\Lambda} + E_2W_2e^{Z/\Lambda})}{W_1 + W_2}. \quad (2.7)$$

This expression is used for the A, B and C counters. For the K counters however, the quality of the Z-position reconstruction that can be obtained from one PMT rules out the possibility of applying corrections for light attenuation as is done in Eqn. (2.7). The expression Eqn. (2.3) is thus used as it stands.

The Calibration Procedure

In order for the analysis outlined in the previous section to work, it is necessary for the detector to be calibrated regularly: G-factors, counter gains and attenuation lengths must be updated every week or so. The calibration is performed by making use of cosmic-ray muons and Bhabha events, because these are particularly simple events whose interaction with the detector is very well understood. We shall discuss the offline calibration procedure and refer the reader elsewhere for a discussion of the on-line calibration of T_0 for each counter and the calibration of drift tubes and chambers [56].

The gain-factors, G_{fac} , for the counters are calibrated from data obtained with minimum ionizing cosmic-ray data. Using data taken with a special cosmic-ray trigger, θ and ϕ for the cosmic-ray muon trajectories are determined from hits in the

D counters and Q chambers. The ADC values for the counters can then be corrected to yield the values expected for normally incident minimum ionizing particles. In addition, the Q chambers yield a Z-position for the muon hit in each counter. A plot of the mean ADC channel versus Z-position of the hit can be fit to a function of the form

$$\langle ADC \rangle = C_0 \text{Exp}\left(-\frac{Z - \frac{l}{2}}{\Lambda}\right) \quad (2.8)$$

which yields the attenuation length of the counter for use in the Z_{ADC} calculation above. C_0 here corresponds to the ADC channel fired by a hit in the middle of the counter.

As described above, the Z-position reconstruction on hits in the A, B and C counters depends on the light propagation velocity in the counters as well as the PMT gains and the counter T_0 's. These quantities are calibrated using Bhabha events and the vertex drift tube arrays. The quantities Z_{ADC} and Z_{TDC} calculated as above are plotted against the Z-positions which are obtained by extrapolating from the drift tube tracks, Z_{Tub} . The T_0 's, PMT gains and light propagation velocities are then adjusted so as to minimize the differences $Z_{Tub} - Z_{ADC}$ and $Z_{Tub} - Z_{TDC}$ over the whole counter length. Typically, the Z-position of the extrapolated drift tube track and the Z-position determined from the counter-hit data agree to within 14 mm for the A counters and 16 mm for the B counters. The systematic variation in the attenuation lengths ascribed to each counter by the calibration procedure is typically small. The attenuation lengths, in cm^{-1} , determined for the A counters are shown in Figure 2.11 as a function of the run number. The period covered in the plots is October 1983 to June 1985, and covers a data taking period when PETRA was operating at 44 GeV. It can be seen that the detector response is quite stable, in spite of varying beam-background levels.

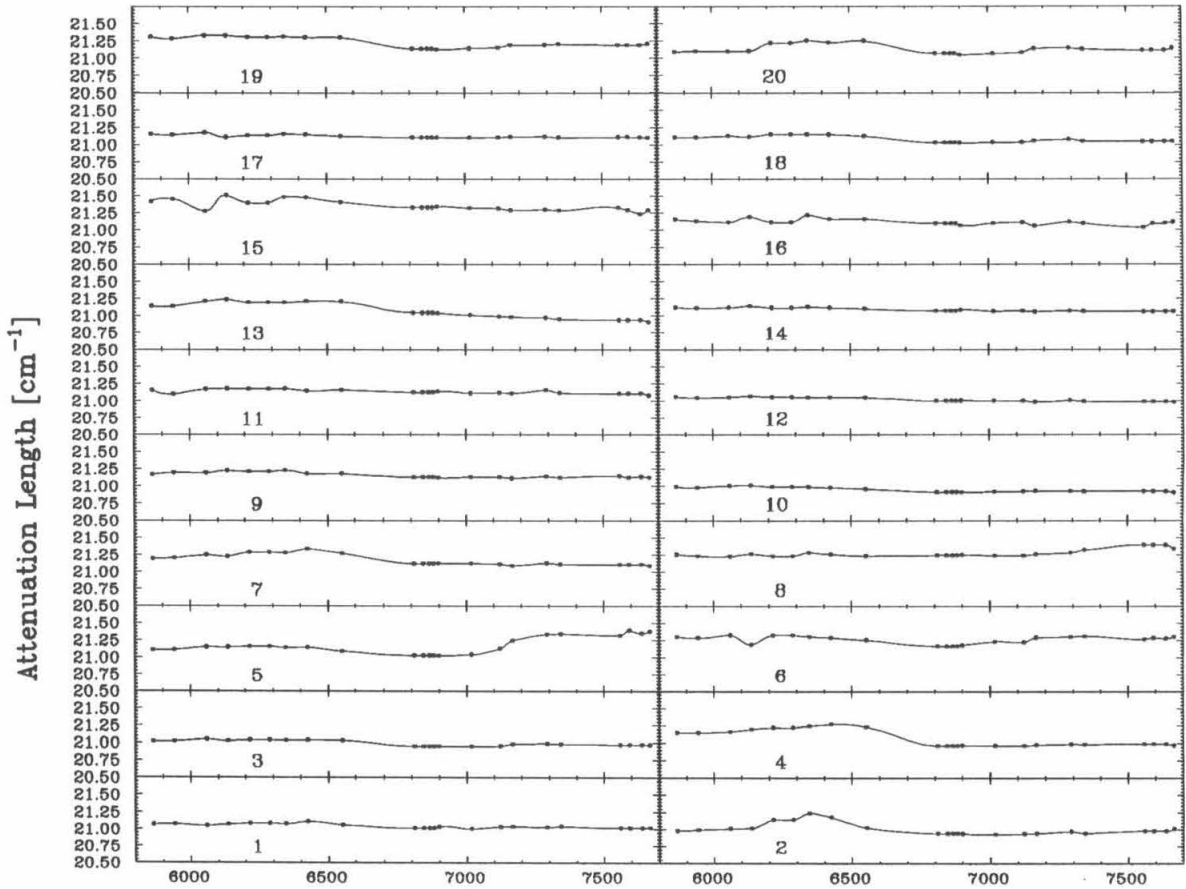


Figure 2.11 The run-to-run variation in the attenuation lengths, obtained by the calibration procedure, for the 20 counters of the A counter array. The attenuation lengths are given in cm^{-1}

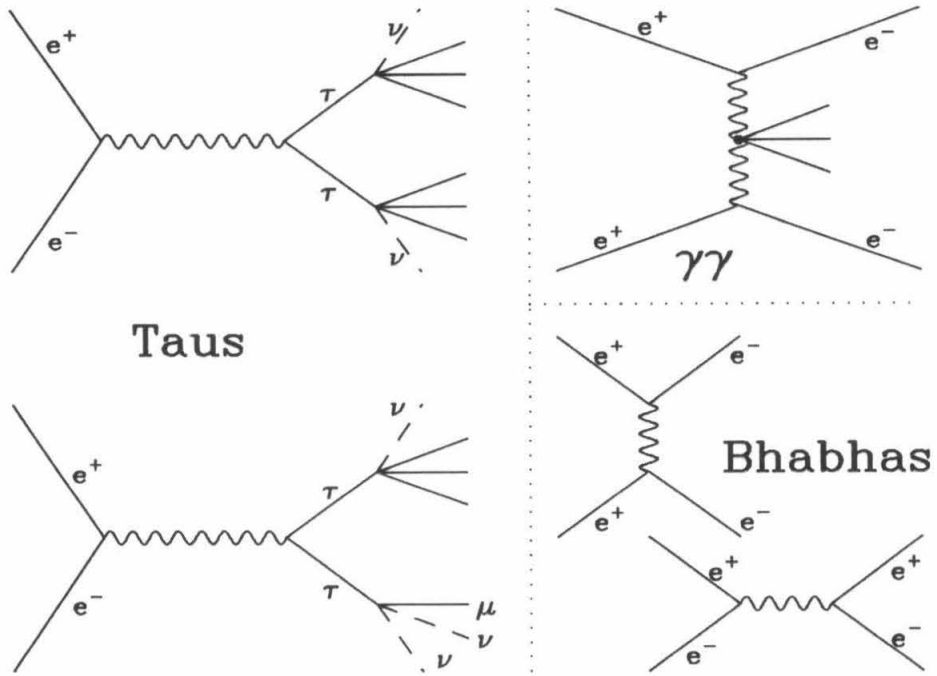


Figure 2.12 The main physics background processes to the one-photon exchange channel.

2.4 The Event Selection

The information written to tape by the data taking system contains events that are of physics interest mixed with background events. The offline analysis outlined above is performed within a series of computer programs whose main function is the separation of the hadron events from the background. Most of the background comes from low-energy hits that trigger the detector, from synchrotron radiation and particles lost from the beams that shower up and downstream of the apparatus. The main physics backgrounds are hadrons produced by τ decay, hadrons originating in the two-photon process $e^+e^- \rightarrow e^+e^- + \text{hadrons}$, and Bhabha scattered electrons appearing in the detector. These backgrounds are illustrated in Figure 2.12. These event selection programs are called the 'hadron filter', and they operate on the data in three stages.

For the hadron selection the first stage filter rejects events that are obviously miss-timed with respect to the beam-crossing time. This eliminates triggers caused by synchrotron radiation and cosmic-rays. Events that have less than 30% of the available center-of-mass energy deposited in the detector, as calculated by a fast algorithm, are rejected, as are events which deposit all their energy in one quadrant of the detector. The data that pass this stage of the filter consist mainly of hadron and Bhabha events. 40% of the original data is rejected as background by this stage.

The second stage filter makes use of the full energy calculation described above and requires that the events have at least 35% of the available center-of-mass energy. This filter also requires that the energy is balanced to within 60% of the observed energy in the directions along and perpendicular to the beam. This eliminates most of the beam gas events, two-photon events and events that have an energetic photon in the initial state. The drift tube vertex is required to be within 10 cm of the interaction point at this stage. The events that pass these cuts are sorted by a pattern recognition algorithm into categories containing events that are labeled as 'definitely Bhabhas', 'definitely hadrons' or 'unresolved'. Typically, the 'unresolved' category comprises 20% of the data at this stage, and of this, 50% is eventually rejected by the third stage of the filter.

The third stage of the filtering is performed by scanning the ambiguous events from stage two at an interactive graphics terminal. Bhabha events can be recognized by the large energies deposited in the inner calorimeters. The remaining backgrounds are identified by examining the drift tube hits in the vertex array or by examining the shower development in the layers of the calorimeters. Typically, a hadron event will have many (around 10) tracks in the inner vertex drift tube array pointing at the interaction point, and significant energy deposited in the outer calorimeter planes. Events due to tau pair production are recognized by the missing momentum carried off by the neutrinos and by two very narrow jets in the detector.

Taus can also be recognized when one of the taus decays leptonically into an electron and the other into hadrons. This is seen as a narrow jet opposite to a large hit in the inner calorimeter. Typical tau events have few drift tube tracks. Events from the two photon process channel are recognized by the presence of electromagnetic activity due to the tagged electron(s), or where one, or both, of the electrons go down the beampipe by the missing total energy in the event. Cosmic-ray events are easily rejected on the basis of timing information provided by the D counters, and electron-beam gas events are recognized by the large energy imbalance and the vertex reconstruction being off-center. In Figure 2.13 a typical hadron event is shown, as reconstructed by the scanning program, at a center-of-mass energy of 46 GeV. Note that the event is well contained in the detector. This particular event shows a measured energy of 46.72 GeV, and the event is well balanced (the energy imbalance for this event is 2.6, 1.2 and 2.2 GeV in the x, y and z directions).

The events that pass the three stages of the hadron filter are passed to the analysis routines. Events are selected from this sample by further demanding that 50% of the center-of-mass energy is visible in the detector, that the energy of the events is balanced to within 60%, that there are at least four drift tube tracks pointing to the vertex and that there are less than three hundred hit drift tubes. The analysis program calculates the thrust, oblateness and other physics quantities of the events and writes a compressed data set, called a 'dst'. The purity of the sample in the 'dst' is estimated by Monte Carlo calculations to be better than 94%, with the main contamination coming from two photon (1.3%) and tau events (4.5%). Further cuts are applied to the events in the 'dst' depending on the physics objectives of the analysis being performed. For most of the analysis performed in this study, the energy cut is raised to 70% of the available center-of-mass energy, and the energy balance cut is tightened to 50%. With these cuts, backgrounds are negligible. The observed energy in the detector for the 35 GeV and 44 GeV dst

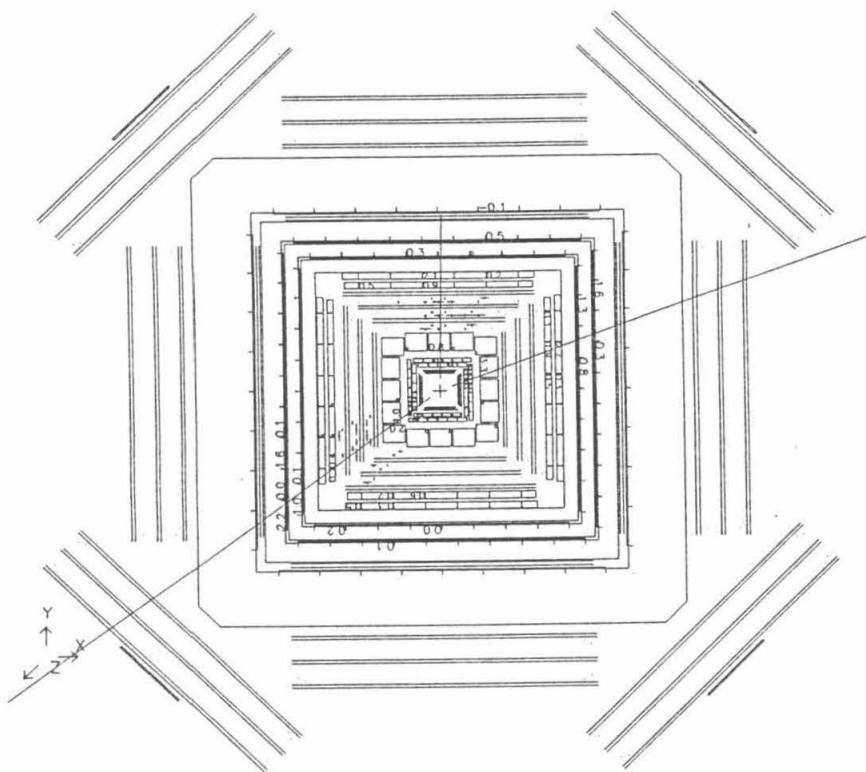


Figure 2.13 A computer reconstructed view of a typical hadron event at 46.0 GeV in the MARK J detector

data sets are shown in Figure 2.14 where the tail of the two-photon distribution can be seen as a rise at low E_{vis}/E_{beam} . It is apparent from the figure that the visible energy cut at 70% is very effective in eliminating the two photon contamination.

The analysis program also constructs energy vectors that point in the direction of a hit in the detector and have a magnitude equal to the energy that was deposited in the hit. The thrust and other event variables are calculated from these energy vectors.

2.5 The Hadron Data Set

Although the bulk of the MARK J hadron data were taken at a center-of-mass energy of 35 GeV, there is a large amount of data at 44 GeV and several smaller data

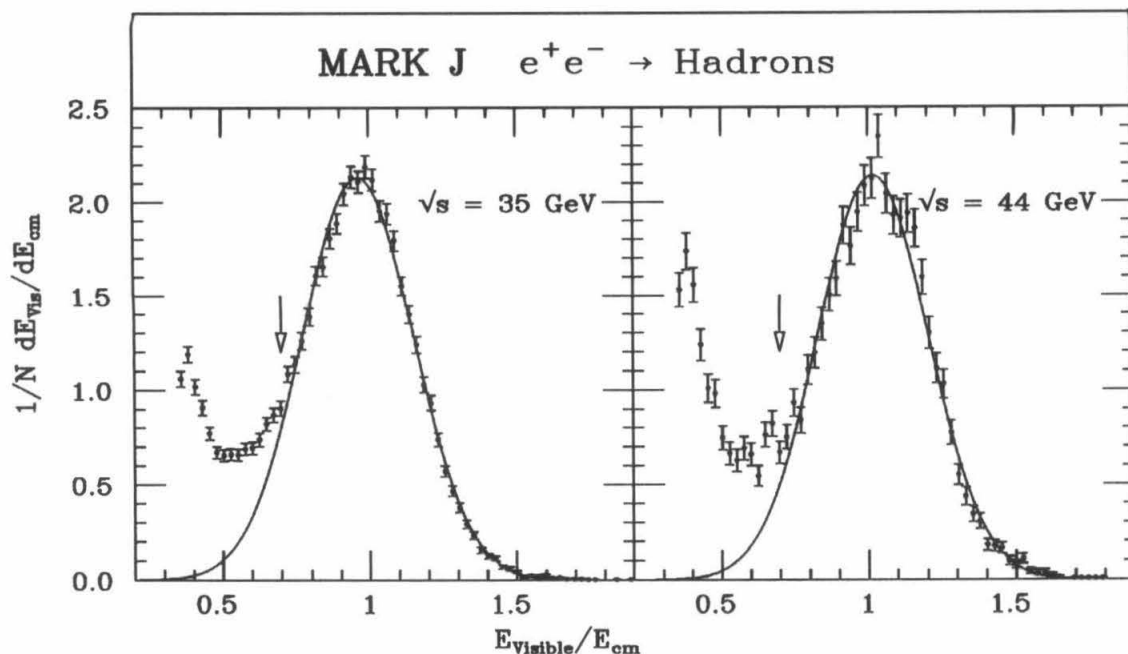


Figure 2.14 The observed visible energy distributions in the detector for available center-of-mass energies 35 GeV and 44 GeV. The curves are the results of a Gaussian fit to the data having $E_{Visible}/E_{cm} > 0.7$

sets at various other energies. The data set is summarized in Table 2.5 where the number of hadron events in eight standard energy groupings is given as a function of the selection cut criteria. The notation here is: visible energy cut/transverse energy balance cut/longitudinal energy balance cut. The energy balance cuts are expressed as a percentage of the observed energy in the detector while the visible energy cut is expressed as a percentage of the available center-of-mass energy.

Sample	13-16	20-24	24-33	33-36	36-39	39-43	43-45	> 45
$\langle E \rangle$ [GeV]	14.03	22.00	30.00	34.62	38.11	41.29	43.85	46.06
50/50/50	2619	2247	1674	26684	2578	1567	8066	1252
60/50/50	2471	2138	1579	25171	2432	1480	7637	1195
70/50/50	2207	1947	1447	23323	2285	1381	7184	1134
50/60/60	2721	2316	1716	27484	2623	1612	8331	1287
60/60/60	2549	2186	1613	25766	2465	1509	7825	1222
70/60/60	2270	1979	1465	23683	2308	1403	7309	1156

Table 2.1 The MARK J hadron data

Sample	13-16	20-24	24-33	33-36
$\frac{E_0}{\sqrt{s}}$	0.916 ± 0.014	0.920 ± 0.009	0.922 ± 0.006	0.961 ± 0.002
$\frac{\sigma_0}{\sqrt{s}}$	23.1 ± 0.8	19.3 ± 0.8	18.6 ± 0.5	18.7 ± 0.2
Sample	36-39	39-43	43-45	> 45
$\frac{E_0}{\sqrt{s}}$	0.993 ± 0.005	0.978 ± 0.011	1.016 ± 0.004	1.021 ± 0.010
$\frac{\sigma_0}{\sqrt{s}}$	20.03 ± 0.8	19.1 ± 0.6	18.7 ± 0.3	18.3 ± 0.1

Table 2.2 The detector energy containment and resolution versus the center-of-mass energy

The data were collected over the lifetime of the experiment, and so, one must be concerned about possible changes in detector response due to the ageing of scintillator and other effects. These effects are, in principle, compensated for by the calibration procedure described above. The most obvious effect of miscalibration or detector deterioration is a degradation of the energy resolution of the detector. By performing frequent calibrations it has been possible to maintain the energy resolution of the detector at $\sigma_0 = \frac{\Delta E_{Vis}}{E_{Vis}} \simeq 19\%$, nearly independent of \sqrt{s} . This is illustrated by the data given in Table 2.5, where the energy resolution of the detector is seen to be independent of the available center-of-mass energy. The table also lists the average fraction of the center-of-mass energy that the detector observed, E_0 . It is clear that the amount of energy leakage out of the detector is roughly constant over the whole PETRA energy range. The figures given in the tables are for the cuts 60/50/50, where the notation has been described above. From Figure 2.14 it will be evident that these numbers are slightly cut-dependent.

Chapter 3

Theoretical Outline: e^+e^- Annihilation into Quarks and Gluons

3.1 An Overview of $e^+e^- \rightarrow$ Hadrons in the Standard Model

The currently accepted view of the interactions of particles is embodied in the so-called ‘Standard Model’, which consists of QCD together with the Glashow-Weinberg-Salam (GWS) model. For the original literature concerning the GWS model, see references [57,58,59,60], and for review articles see references [61,62,63]. The GWS model addresses the electromagnetic and weak interactions. At low energies it is essentially just QED, while at energies comparable with the masses of the W^\pm and Z^0 , the model presents a unified treatment of both electromagnetic and weak phenomena. Both the QCD and electroweak sectors of the standard model are written in a Lagrangian formalism. Despite the fact that in both QCD and the GWS theory, the Lagrangian is known, it turns out that calculations can only be made within the framework of perturbation theory, and consequently, only approximate solutions can be obtained. The solutions are obtained in the form of a perturbative series and are only meaningful when the series converges rapidly. Asso-

ciated with each term in the series are Feynman diagrams, which provide a graphical picture of the interactions occurring within the theory at the order of perturbation theory being considered. As one goes to higher orders in the perturbation series, the permissible interactions that must be considered become more numerous, and the Feynman diagrams more difficult to calculate. The perturbation series is an approximate expansion of the true solution to the theory in the coupling constant. Since the convergence of the perturbation series is determined by the size of the coupling constant, the formalism only works when the coupling constant is smaller than unity, so that the diagrams for the first few terms of the series are all that need be calculated. In the electroweak interaction the coupling constant has all the properties required to make a perturbation series treatment applicable. The strong interaction coupling constant, however, becomes large as one proceeds to low Q^2 , and the perturbative treatment breaks down; the theory becomes non-perturbative in the low- Q^2 region.

The development of a hadronic final state system in e^+e^- annihilation is represented schematically in Figure 3.1. The system is shown passing from a process involving high- Q^2 (high momentum transfer squared) phenomena into one involving low Q^2 phenomenon, on going from left to right in the figure.

Figure 3.1 can be divided into five distinct regions. The left-most region contains the initial state: the virtual photon, the virtual Z^0 and possibly an initial state radiative photon. It is well-described by QED and the GSW model. In the second region the virtual photon or Z^0 decays into a quark-antiquark system, a process that is essentially the reverse of the initial e^+e^- annihilation and is also well described by QED and the GWS model. By now the system consists of a highly energetic quark and its antiquark. One might hope that it would be possible to directly observe these particles in an experiment and study their production mechanisms and properties directly, but this is not the case. These particles carry color and so

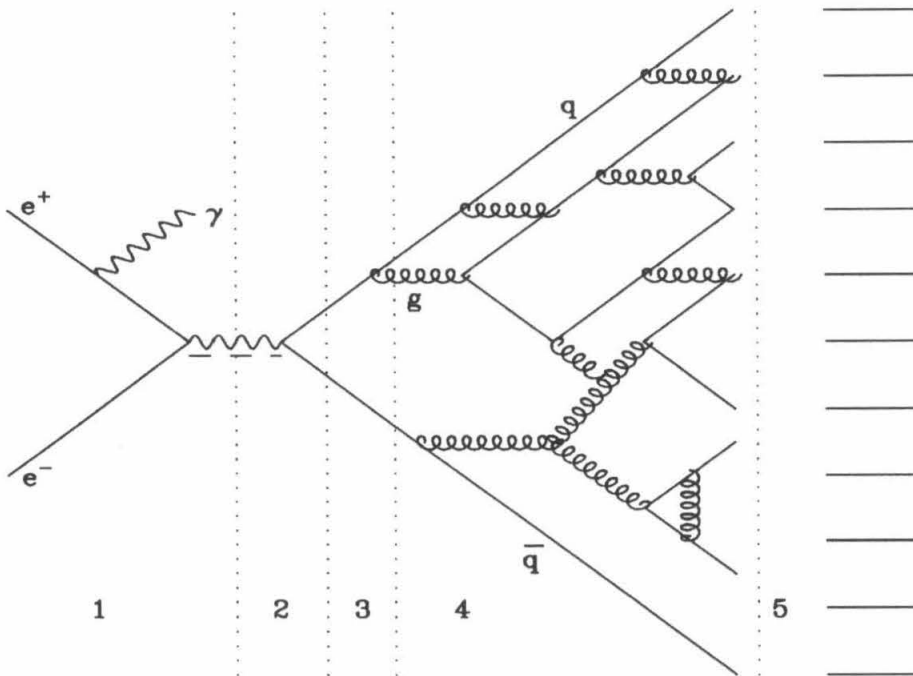


Figure 3.1 Schematic diagram showing the development of a hadronic final state in e^+e^- annihilation. The Q^2 's involved at each stage decrease on going from left to right across the figure.

are not directly observable. What happens instead, is that the quark and antiquark ‘dress’ themselves with other quarks and gluons to form hadrons. This dressing is shown in regions three to five in the figure. At all these stages QCD is involved.

The initial stage of the dressing takes place at relatively high Q^2 and is shown in the figure as the radiation of a gluon by the ‘upper’ quark. At this point there are three particles in the final state and the Q^2 ’s are still relatively high. In this regime it is possible to perform limited calculations within the context of QCD – this is the perturbative region.

By the next stage the gluon has coupled to a quark-antiquark pair, and the initial antiquark has also radiated a gluon. There are now five particles in the final state (ignoring any initial state radiated photons), and the various Q^2 ’s of the particles in the system have been reduced by an appreciable factor. The system is by now hopelessly non-calculable, at least in terms of a full perturbative calculation. The Q^2 ’s appearing at the vertices in the diagram are now small and the coupling constant associated with each vertex is large. Perturbation expansions break down at this point, and the system has passed into the non-perturbative region.

At this stage the system is described as a ‘parton shower’, where this term is intended to indicate the rapid increase in complexity that results as the system evolves further. By the end of the parton shower, the initial, energetic, quark and antiquark have been reduced to a large number of low energy quarks and gluons, all of which have energies comparable to the masses of hadrons.

The system now goes through a process called pre-confinement, in which the quarks and gluons aggregate into clusters so that each cluster carries a net color charge of zero. These colorless clusters then decay into smaller units that are associated with physically observed hadrons. The complete process by which the partons are converted into final-state hadrons is known as ‘fragmentation’.

The whole process of fragmentation cannot be attacked with any solid theoretical

techniques. Instead, the problem is approached through the use of models that are ‘motivated’ by intuitive interpretations of the theory. These models ultimately resort to straight-forward parameterizations of experimental data when even the intuitive approach fails (e.g., in the very low Q^2 region).

In order to examine the theory, it is necessary to compare its predictions with experimental data. Clearly, since we cannot observe the partons involved in QCD processes, it is necessary to relate the processes occurring at early stages of the development of the final state in Figure 3.1 to the hadrons that are finally observed. This is accomplished through the application of an idea that has come to be known as ‘factorization’. The intermediate stages shown in Figure 3.1 are each thought of as taking place with probabilities that can be treated independently of each other and then multiplied at the end to yield a total probability for the occurrence of a particular final state. Factorization makes it possible to calculate the outcome of e^+e^- annihilation into hadrons on a statistical basis, by performing Monte Carlo calculations [64]. These calculations treat each region in Figure 3.1 independently, according to the theory or model that is most applicable to the region at hand, and the results of these separate calculations are then combined to yield a prediction that can be compared to the measured distribution of the final states.

In the remainder of this chapter, the aspects of the theories mentioned above that are of relevance in the later chapters of the thesis are outlined. A discussion of the various models employed to relate the theories to the observations is postponed until the next chapter.

3.2 The Initial State

Unlike the situation that occurs in hadron-hadron scattering, the process $e^+e^- \rightarrow$ hadrons has a particularly simple initial state that involves only two point-like particles and, possibly, an initial state radiative photon. The probability of a photon

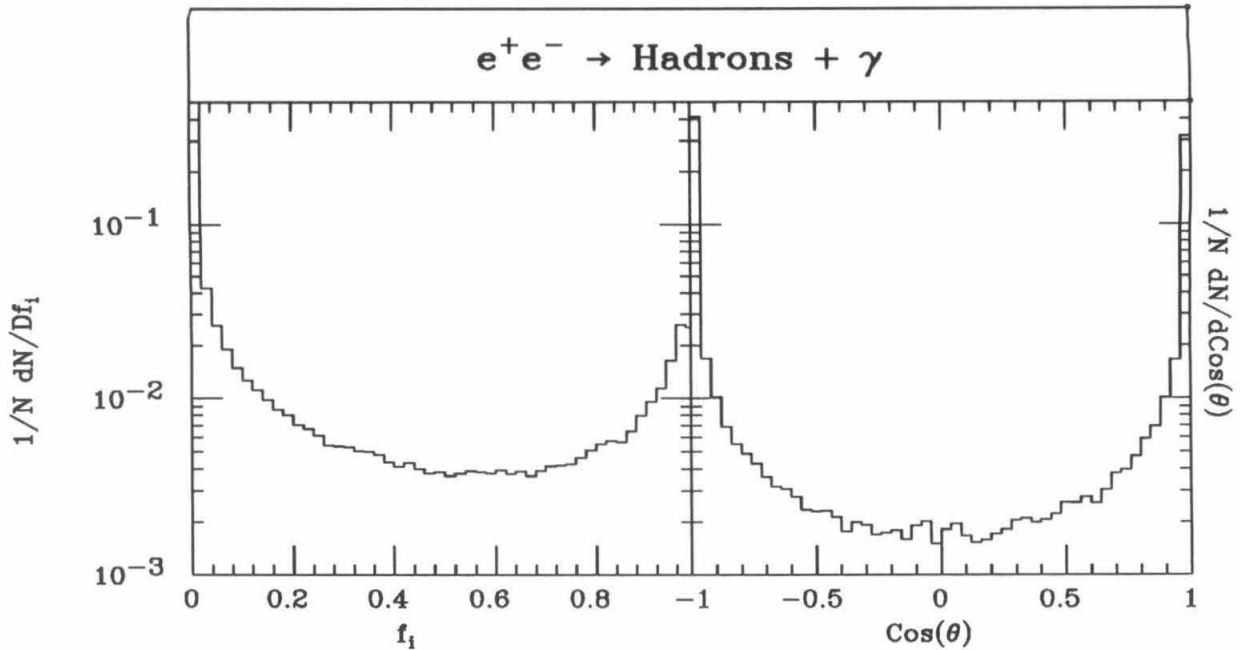


Figure 3.2 The probability of an initial state radiative photon having energy $f_i E_{beam}$ being emitted into the initial state, and the angular distribution of radiative photons with respect to the beamline.

of a given energy being radiated into the initial state is given by QED, and in this work a calculation to order α^3 is used to take this process into account [65,66,67]. The effect of the radiative photon is to reduce the actual center-of-mass energy at which the hadronic system is produced and to confuse the experimental situation in cases where the photon appears in the final state and mimics a hadronic final state particle. The cross section for bremsstrahlung of a photon from one of the initial state particles diverges as the angle between the photon and the electron, or positron, goes to zero, or as the photon energy becomes small. As a result most of the hard initial state photons pass down the beam pipe and are not detected. The cross section for emission of an initial state radiative photon having an energy fraction f_i of the beam energy, and for a photon making an angle θ_i with respect to the beampipe, are shown in Figure 3.2. In order to regulate the infinities in the cross section, a kinematic cut on the photon energy is applied: we use a cut-off in the photon energy at 99% of the beam energy throughout this study.

At PETRA energies the total cross section for e^+e^- annihilation into hadrons is modified from the quark parton model expression, given in Eqn. (A.3), by the inclusion of the interference of virtual Z^0 's with the annihilation photon. This modifies the cross section at momentum transfer $s = Q^2$ to an expression of the form :

$$\frac{\sigma_{EW}(e^+e^- \rightarrow (\gamma^*, Z^0) \rightarrow \text{hadrons})}{\sigma_{QED}(e^+e^- \rightarrow \mu^+\mu^-)} = N_c \sum_i [Q_i^2 + 2Q_i \Re(\chi) g_v^e g_v^i + |\chi|^2 s^2 (g_v^{e2} + g_a^{e2})(g_v^{i2} + g_a^{i2})] \frac{\beta_i(3-\beta_i^2)}{2}$$

where,

$$\begin{aligned} \chi &= \frac{1}{4 \sin^2 \theta_W \cos^2 \theta_W} \frac{s}{(s - M_{Z^0}^2 + i M_{Z^0} \Gamma_Z)} \\ g_v^i &= T_{3L}^i - 2Q_i \sin^2 \theta_W \\ g_a^i &= T_{3L}^i \\ T_{3L}^i &= \begin{cases} +\frac{1}{2} & \text{for } i = u, c \\ -\frac{1}{2} & \text{for } i = d, s, b. \end{cases} \end{aligned} \quad (3.1)$$

In this expression θ_W is the Weinberg angle and is a parameter of the electroweak part of the standard model. g_v^i and g_a^i are the the weak vector and axial couplings of the i^{th} quark flavor, which are determined by the value of the third component of the left-handed weak isospin T_{3L}^i , and the mixing angle θ_W , as indicated. The expression containing the β s is a kinematic factor that goes to 1 at energies well above the production thresholds of the quarks. A close look at Eqn. (3.1) reveals that the contributions to R are governed by terms that depend on the value of T_{3L}^i for the quarks, and that, further, these terms have magnitudes that are energy dependent. One consequence of this is that the electroweak effects modify the fractional contribution to R from each quark type as one goes to higher energy. The effect is of relevance when extrapolating our results to TRISTAN and LEP energies, and so, has been included in the Monte Carlo calculations. The production probabilities for charge 1/3 quarks, $R_{\frac{1}{3}}$, and for charge 2/3 quarks, $R_{\frac{2}{3}}$, can be written as follows:

$$\begin{aligned} R_{\frac{1}{3}} &= \frac{1}{9} + \frac{1}{6} g g_{\frac{1}{3}} P_{Z^0} + \frac{1}{16} (1 + g^2) (1 + g_{\frac{1}{3}}^2) P'_{Z^0} \\ R_{\frac{2}{3}} &= \frac{4}{9} - \frac{1}{3} g g_{\frac{2}{3}} P_{Z^0} + \frac{1}{16} (1 + g^2) (1 + g_{\frac{2}{3}}^2) P'_{Z^0} \end{aligned} \quad (3.2)$$

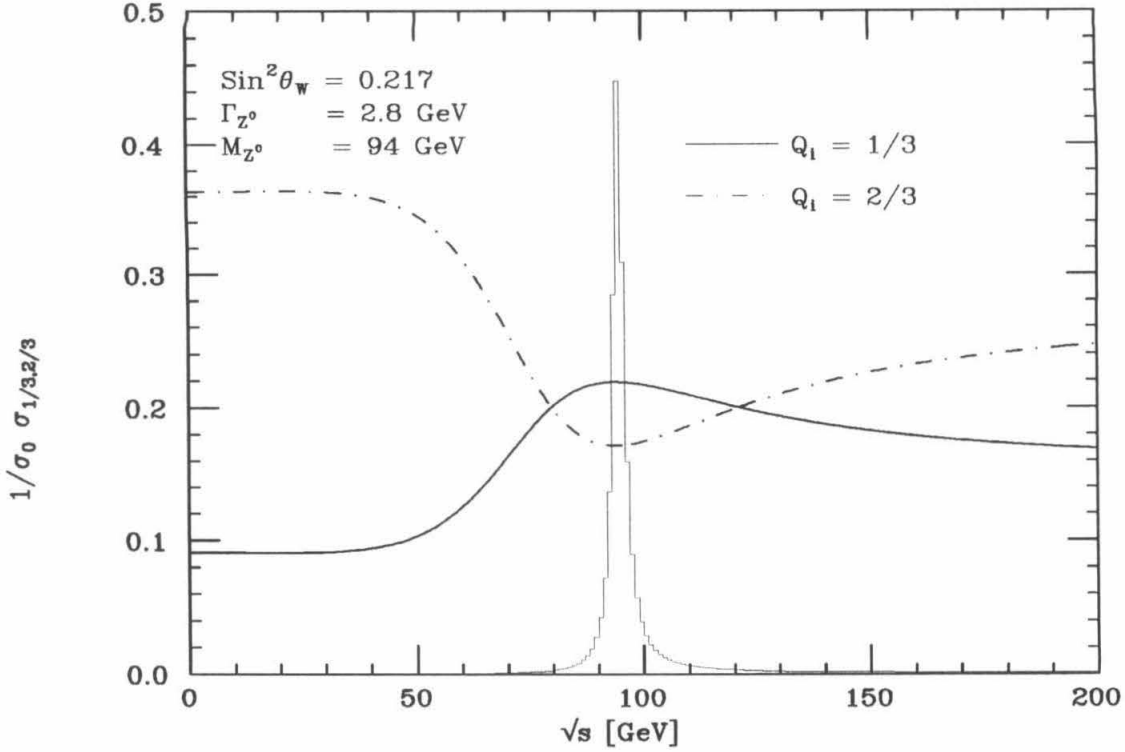


Figure 3.3 $R_{\frac{1}{3}}$ and $R_{\frac{2}{3}}$ as a function of the available center-of-mass energy. Also shown is the Z^0 pole

where,

$$\begin{aligned}
 g &= -1 + 4 \sin^2 \theta_W \\
 g_{\frac{1}{3}} &= -1 + \frac{4}{3} \sin^2 \theta_W \\
 g_{\frac{2}{3}} &= 1 - \frac{8}{3} \sin^2 \theta_W \\
 P_{Z^0} &= \frac{1.81 \times 10^{-4} s M_{Z^0}^2 (s - M_{Z^0}^2)}{(s - M_{Z^0}^2)^2 + M_{Z^0}^2 \Gamma_{Z^0}^2} \\
 P'_{Z^0} &= \frac{3.28 \times 10^{-8} s^2 M_{Z^0}^4}{(s - M_{Z^0}^2)^2 + M_{Z^0}^2 \Gamma_{Z^0}^2}.
 \end{aligned}$$

In Figure 3.3 these production probabilities are shown as a function of the center-of-mass energy. Also shown is the Z^0 pole. It can be seen from the figure, that the effect of electroweak interference is expected to become noticeable at TRISTAN energies, but that at PETRA energies the effect is minimal. The initial state radiative corrections further mask the effect and attempts to see the prediction of Eqn. (3.2) in the data used for this study have failed. The extent to which these effects modify the model predictions will be discussed in Chapter 9.

3.3 The Hadronic Final State

The early stages in the evolution of the hadronic final state shown in Figure 3.1 take place at high Q^2 and may be treated by perturbative QCD calculations. As pointed out earlier, the type of calculation that modern theoretical technology is capable of handling is very limited, and for systems involving more than four quarks and gluons approximate methods have to be employed. The remainder of this chapter is devoted to a discussion of the theory of QCD and the calculations that are presently possible within the theory.

3.3.1 QCD: Running Coupling Constants and Asymptotic Freedom

As outlined in Appendix A, QCD is a field theory based on invariance under local $SU(3)$ color transformations. The theory describes the interaction of color triplet quarks through the exchange of color octet gluons. The color singlet gluon combination is symmetric and colorless, so it does not enter into the theory, and so, we are left with eight gluon fields. The theory is written in terms of a Lagrangian of the form:

$$L_{\text{QCD}} = -\frac{1}{4} \sum_{i=1}^8 G_{\mu\nu}^i G^{i\mu\nu} + \sum_{\text{flavors}} \bar{q}(i\gamma^\mu(\partial_\mu - igA_\mu) - m)q. \quad (3.3)$$

In this equation g is the strong coupling constant, q is the quark wavefunction and $G_{\mu\nu}$ is the field tensor, which is defined in terms of the potential A_μ by

$$G_{\mu\nu} = \partial_\mu A_\nu - \partial_\nu A_\mu - ig[A_\mu, A_\nu]. \quad (3.4)$$

A_μ has the color space decomposition

$$A_\mu = \sum_{i=1}^8 A_\mu^i \frac{\lambda^i}{2}. \quad (3.5)$$

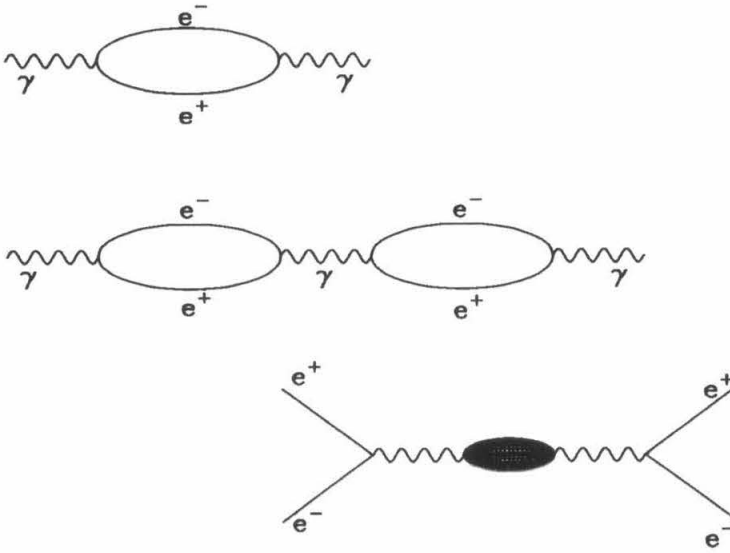


Figure 3.4 QED loop diagrams that modify the lowest order photon propagator.

The commutator term in Eqn. (3.4) introduces self-couplings for the gauge fields because the commutation relations for $SU(3)$,

$$\left[\frac{\lambda_i}{2}, \frac{\lambda_j}{2} \right] = i f^{ijk} \frac{\lambda_k}{2}, \quad (3.6)$$

involve non-zero structure constants f^{ijk} . In the QED Lagrangian there is no photon self-coupling term analogous to the gluon self-coupling term appearing in the QCD Lagrangian above. It is this difference that makes QCD an asymptotically free theory while QED is not [68]. The mechanism linking the gluon self-coupling to asymptotic freedom is best understood by first examining the example of QED.

In QED the photon propagator is modified by the inclusion of loop diagrams as shown in Figure 3.4. When these diagrams are evaluated, they lead to expressions containing infinite terms. Evaluation of the diagram containing one loop, for example, gives rise to an expression for the photon propagator that includes a finite term and a divergent term. The divergent term can be dealt with by absorbing it into the electromagnetic coupling constant appearing in the QED Lagrangian. The

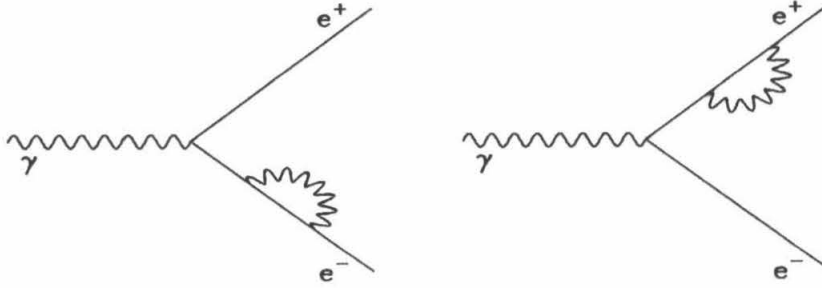


Figure 3.5 Loop diagrams that modify the bare electron mass in QED

coupling constant in the Lagrangian is then rescaled such that:

$$e_0 = e \left[1 - \frac{e}{12\pi^2} \ln\left(\frac{M^2}{m^2}\right) \right], \quad (3.7)$$

where m is the electron mass and M is a mass cut-off. The rescaled coupling that now appears in the Lagrangian, e_0 , is known as the ‘bare’ coupling constant and e is the physical coupling. The loop diagrams shown in Figure 3.4 are not the only diagrams that lead to divergent terms when evaluated; the diagrams shown in Figure 3.5 also lead to infinities. In the case of the diagrams in Figure 3.5, the divergent terms can be absorbed into the electron mass appearing in the Lagrangian. When the divergent terms that arise in the calculation of the diagrams of a theory can all be absorbed into bare quantities appearing in the Lagrangian, in a fashion that leaves the form of the Lagrangian unchanged, the theory is said to be renormalizable. QED, QCD and the GWS model are all renormalizable theories.

The bare quantities appearing in the Lagrangian are not the quantities that appear in nature. A measurement of the electric charge in the laboratory, for example, is a measurement of e in Eqn. (3.7), not of e_0 . The charge that one measures in the laboratory includes contributions to e_0 from all the diagrams it is possible to draw

according to the rules implied by the QED Lagrangian. Diagrammatically, the sum of all possible contributions is drawn as a filled-in loop, and this is what the bottom diagram in Figure 3.4 attempts to show. Divergent terms from these diagrams will have conspired to cancel the divergences that appear in the bare charge, e_0 - in the parlance of field theory the bare charge is renormalized to yield the physical charge. A similar mechanism can be applied to make sure that the theory yields a finite physical mass for the electron, despite the appearance of infinities in the bare mass due to the diagrams of Figure 3.5. It turns out, due to the existence of relationships known as Ward identities, that the only diagrams that contribute to the renormalization of the coupling constant are the loop diagrams of Figure 3.4.

The expression Eqn. (3.7), which is derived in the one-loop approximation, may be expressed in terms of the square of the momentum carried by the virtual photon, Q^2 . Differentiation of this expression, with respect to Q^2 , eliminates the (constant) bare charge from the expression and yields a differential equation relating the physical coupling to the Q^2 ,

$$Q^2 \frac{\partial e}{\partial(Q^2)} = \frac{e^3}{12\pi^2}. \quad (3.8)$$

The solution of this equation is:

$$e^2(Q^2) = \frac{e^2(Q_0^2)}{1 - \frac{e^2(Q_0^2)}{6\pi^2} \ln\left(\frac{Q^2}{Q_0^2}\right)}, \quad (3.9)$$

where $e^2(Q_0^2)$ has arisen as the constant of integration and reflects the value of the coupling at some reference $Q^2 = Q_0^2$. Eqn. (3.9) shows how the strength of the coupling constant varies with the Q^2 of the probe being used to investigate the interaction: it is said to show how the coupling constant ‘runs’. Eqn. (3.9) shows that in QED the strength of the coupling increases with Q^2 , corresponding to the interaction between two electric charges becoming stronger as they approach each other.

When the discussion above is followed through for the case of QCD, the role

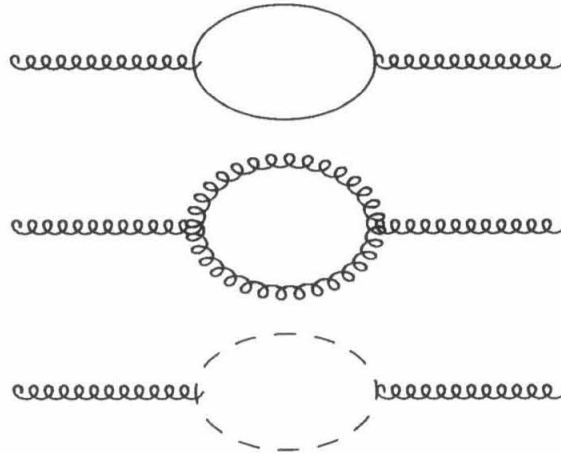


Figure 3.6 Loop diagrams that renormalize the bare QCD coupling constant in the QCD Lagrangian

of the gluon self-coupling alters the situation completely. Again, due to the Ward identities, only loop diagrams in the propagator need to be considered, and at the level of the one-loop approximation for QCD, only the diagrams shown in Figure 3.6 need be included. The presence of the gluon self-coupling has introduced gluon loop diagrams. The situation in QCD is further complicated by the presence of the ghost diagrams shown containing a dashed-line loop in the figure. The ghosts are particles that are allowed by the QCD Lagrangian to appear internally in a diagram, but that may never form an external line. They are needed to preserve the unitarity of the theory, but should not be regarded as anything more than mathematical artifacts. In fact, the ghost loop diagrams shown in the above figure can be made to vanish by an appropriate choice of gauge. Evaluation of the loops shown in Figure 3.6 leads to divergences that must be absorbed into the coupling constant appearing in the Lagrangian. Diagrams similar to those that renormalize the electron mass in QED also arise in QCD, and the bare quark masses are altered in the theory. It turns out

that the QCD Lagrangian can also be rewritten in its original form and that QCD is thus a renormalizable theory in the same sense as QED.

The calculations leading to the QED result of Eqn. (3.9) can be followed through for the QCD case, and the resulting expression is:

$$\alpha_s(Q^2) = \frac{\alpha_s(Q_0^2)}{1 + \left(\frac{\alpha_s(Q_0^2)}{12\pi^2}\right)(33 - 2N_f) \ln\left(\frac{Q^2}{Q_0^2}\right)}, \quad (3.10)$$

which has the same form as Eqn. (3.9), and relates α_s at some Q^2 to its value, α_s at some reference $Q^2 = Q_0^2$. This reference Q_0^2 is normally defined to be

$$\Lambda_{\overline{MS}} = \exp\left(-\frac{6\pi}{(33 - 2N_f)\alpha_s}\right), \quad (3.11)$$

which allows Eqn. (3.10) to be rewritten in its usual form,

$$\alpha_s(Q^2) = \frac{12\pi}{(33 - 2N_f) \ln\left(\frac{Q^2}{\Lambda_{\overline{MS}}^2}\right)}. \quad (3.12)$$

The quantity, $\Lambda_{\overline{MS}}$, that appears in this expression has actually been introduced in a way that is related to the renormalization procedure. This phenomenon, where a dimensional parameter is introduced into a dimensionless theory by the renormalization, is known as dimensional transmutation [69]. $\Lambda_{\overline{MS}}$ is a totally free parameter, in the sense that the theory has nothing to say about its value, and can *only* be determined experimentally. Different renormalization schemes will, however, involve different Λ 's. In this work the so-called minimal subtraction scheme is used exclusively.

The crucial difference between QED and QCD is contained in the signs appearing in the denominators of Eqns. (3.9) and (3.10). The minus sign in Eqn. (3.9) determines that for QED the coupling increase with Q^2 , while the plus sign in Eqn. (3.10) determines that the opposite will be so for QCD, and that the theory will be asymptotically free. This result implies that in attempting to pull a quark from a hadron the force tending to keep the quark in the hadron will increase as

the quark becomes more distant from the quarks remaining in the hadron. We shall see later that this idea is one of the principal motivations for the models we employ when calculating the fragmentation process in $e^+e^- \rightarrow$ hadrons.

3.3.2 The Importance of Second Order Terms in The Determination of α_s

The expression in Eqn. (3.12) is modified by the inclusion of two-loop diagrams to the following [70]:

$$\alpha_s(Q^2) = \frac{2\pi}{\beta_0 \ln\left(\frac{Q^2}{\Lambda_{\overline{MS}}^2}\right) + \left(\frac{\beta_1}{\beta_0}\right) \ln \ln\left(\frac{Q^2}{\Lambda_{\overline{MS}}^2}\right)}, \quad (3.13)$$

where the constants, β_0 and β_1 are defined by:

$$\begin{aligned} \beta_0 &= \frac{11N_c - 2N_f}{6} = \frac{23}{6} \\ \beta_1 &= \frac{17N_c^2 - 5N_cN_f - 3C_F N_f}{6} = \frac{68}{6} \\ C_F &= \frac{N_c^2 - 1}{2N_c}, \end{aligned} \quad (3.14)$$

where N_C gives the number of colors in the theory and has been put equal to 3 for the numbers given. The extension to the two-loop level is important because it uniquely determines $\Lambda_{\overline{MS}}$. The $\Lambda_{\overline{MS}}$ that arises in Eqn. (3.12) is poorly defined to 1st order in α_s , while a $\Lambda_{\overline{MS}}$ defined through Eqn. (3.13) is uniquely defined to all orders in α_s . This means that when determining α_s or $\Lambda_{\overline{MS}}$ experimentally full second-order expressions must be used, otherwise second-order contributions can mistakenly be absorbed into 1st order terms.

3.3.3 Screening and Antiscreening in QED and QCD

The variation of the coupling constants with Q^2 can be understood on physical grounds by considering the polarization of the vacuum. A bare charge in the vacuum (let's say a bare electric charge) is actually going to be surrounded by a cloud of virtual electron-positron pairs continually hopping in and out of the vacuum. The effect of the presence of the bare charge is to polarize this charge cloud by attracting

the positrons towards itself while repelling the virtual electrons. The bare charge is thus ‘screened’ by the charge cloud. When the charge cloud is penetrated by a high momentum probe, the probe sees a larger amount of the bare charge than it sees when it is outside the screening cloud. The interaction between the probe and the bare charge thus gets larger as the Q^2 increases and the probe penetrates more of the cloud. In QCD the the vacuum contains a sea of virtual quark-antiquark pairs *and* gluons. A bare color charge in the QCD vacuum attracts the colored objects from the vacuum and forms a color-charge cloud about itself. When this colored cloud is penetrated by a probe, the probe is surrounded by color charges, and the effect of the cloud is to compensate for some of the attraction between the probe and the bare color charge. In this case, then, the force becomes smaller as the Q^2 of the probe is increased. In actual fact the quarks in the charge cloud surrounding a bare color charge tend to screen in the same way as the electrons and positrons in the QED case. It is the presence of the gluons that causes the overall effect of the charge cloud to be ‘antiscreening’. This can be seen from the signs in front of the numerical factors in the denominator of Eqn. (3.12). The factor 33 is picked up by summing over gluon loops in Figure 3.6, while the factor $2N_f$ comes from the fermion loops. If the number of fermions is below $33/2$, the net sign in the denominator of Eqn. (3.12) is such that the gluon antiscreening effect dominates and QCD remains asymptotically free. In a world with more than this number of fermions, however, QCD would be similar to QED and confinement effects would be absent, with catastrophic consequences for hadrons!

3.4 Perturbative QCD Predictions

3.4.1 The Total Cross Section for $e^+e^- \rightarrow$ Hadrons

The cross section prediction of the quark parton model for the total cross section $e^+e^- \rightarrow$ hadrons was given in Eqn. (A.3), and the effects of electroweak corrections

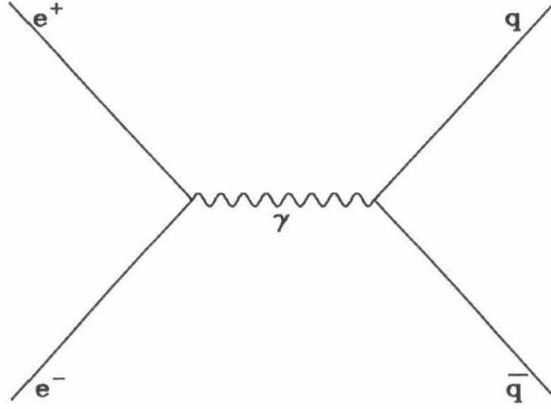


Figure 3.7 The zeroth order diagram for calculating the total hadronic cross section in $e^+e^- \rightarrow \text{hadrons}$

were included in Eqn. (3.1). Since the confinement mechanism guarantees that any parton final state will manifest itself as hadrons, the total cross section is calculated by computing the higher order corrections to the zeroth-order process shown in Figure 3.7, electroweak production of a quark-antiquark pair through e^+e^- annihilation. QCD modifies this cross section: bremsstrahlung of a hard gluon from one of the quarks produces a 1st order QCD correction. The diagrams involved are shown in Figure 3.8, where the emission of a real gluon from one of the quarks is shown; a process that gives rise to both infrared and collinear divergences. The explicit form of the cross section for the process shown in Figure 3.8 is [71]:

$$\frac{1}{\sigma} \frac{d^2\sigma}{dx_q dx_{\bar{q}}} = \frac{2\alpha_s}{3\pi} \frac{x_q^2 + x_{\bar{q}}^2}{(1-x_q)(1-x_{\bar{q}})}. \quad (3.15)$$

Here the cross section is expressed in terms of the energies of the partons scaled to the beam energy, Q . For the quark, antiquark and gluon these scaled energies are respectively, $x_q = 2E_q/Q$, $x_{\bar{q}} = 2E_{\bar{q}}/Q$, and $x_g = 2E_g/Q$. The appearance of only two of these x 's in Eqn. (3.15) is due to the presence of a further constraint from

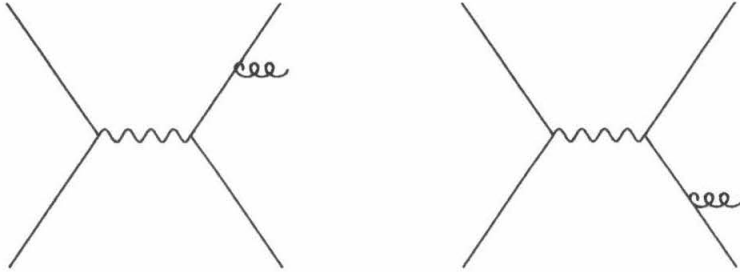


Figure 3.8 QCD diagrams that modify the quark parton model and electroweak predictions for the total cross section $e^+e^- \rightarrow \text{hadrons}$ to 1^{st} order in α_s

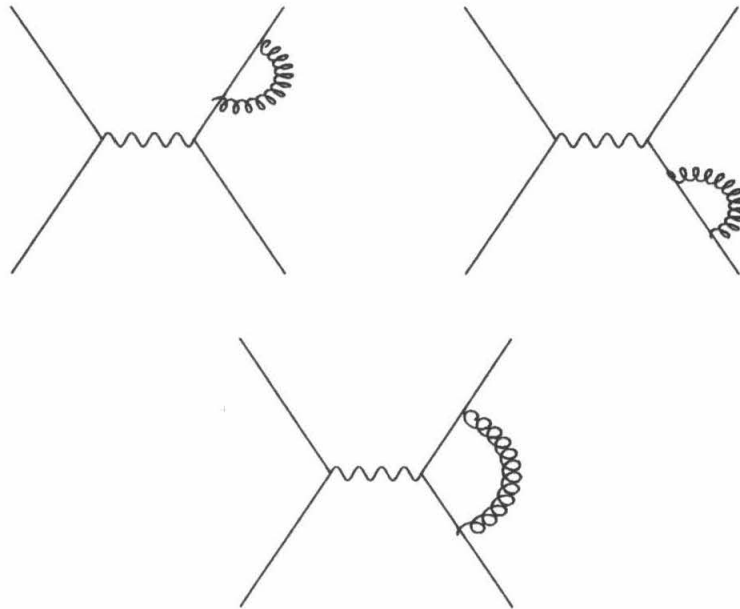


Figure 3.9 QCD loop diagrams that modify the quark parton model and electroweak predictions for the total cross section $e^+e^- \rightarrow \text{hadrons}$ to 1^{st} order in α_s

energy conservation,

$$x_q + x_{\bar{q}} + x_g = 2. \quad (3.16)$$

In order to evaluate the contribution of the gluon radiation to the total cross section, the expression in Eqn. (3.15) must be integrated over x_q and $x_{\bar{q}}$ on the interval $[0,1]$. It can be seen, that as x_q and/or $x_{\bar{q}}$ go to 1, the expression will diverge. These limits correspond to the gluon energy becoming very small, in which case, both factors in the denominator become infinite, and to the gluon becoming collinear with either the quark or antiquark, in which case, one of the factors becomes infinite. These are the ‘infrared’ and ‘collinear’ divergences respectively.

These divergences are canceled by the infrared divergences that arise in the one-loop diagrams shown in Figure 3.9; the resulting cross section is then finite. This is an example of a general theorem, due to Kinoshita, Lee and Nauenberg [72,73], which states that: divergences due to emission of real gauge bosons are cancelled by infrared divergences in loop diagrams involving virtual gauge bosons. This is related to the renormalization of the bare fermion masses as discussed above. When evaluated, these diagrams alter the total cross section as follows:

$$\sigma_{tot} = \sigma_{ew} \left(1 + \frac{\alpha_s}{\pi} \right), \quad (3.17)$$

where σ_{ew} is the electroweak cross section of Eqn. (3.1).

The calculation of the total cross section to full second-order in α_s has been performed, and the result is [74,75]:

$$\sigma_{tot} = \sigma_{ew} \left(1 + \frac{\alpha_s}{\pi} + K_{MS} \left(\frac{\alpha_s}{\pi} \right)^2 \right), \quad (3.18)$$

where

$$K_{MS} = C_F \left(0.538 N_c - \frac{3}{32} C_F - 0.08645 N_F \right) = 1.405 \quad (3.19)$$

Due to the complexity of the problem, this calculation has been performed by exploiting a relationship between the total cross section and the imaginary part of the

hadronic contribution to the vacuum polarization. The general idea behind such a calculation can be seen in the bottom diagram of Figure 3.4. If the internal loop in the propagator is cut in half, the final state of the left-hand diagram that results is essentially all possible hadronic final states. The contribution to the total amplitude of the un-cut diagram from this half-diagram is the imaginary part of the contribution from all internal loops containing quarks. A direct calculation of the total cross section through summing the partial two, three and four-parton cross sections has only been completed recently [76]. The direct calculation involves several terms that still have to be evaluated numerically. It is reassuring that the recent results are in agreement with the earlier results. At PETRA energies the QCD contribution to the total cross section is sufficiently small that it is at the limit of detectability by any single experiment, because of systematic errors in the measurement.

3.4.2 Jet Cross Sections in $e^+e^- \rightarrow$ Hadrons

At the center-of-mass energies at which PETRA operated, the dressing of the initial partons partially preserves the directions with which they were created. The hadrons are said to emerge as ‘jets’ into the detector where the directions of these jets reflects the underlying configuration of the partons. The experimental observation of jets is clear evidence supporting the idea of asymptotic freedom in QCD. Further, since three-jet events are considered to come from the bremsstrahlung of a hard gluon, the observation of three-jet events provides confirmation of QCD through the verification of the existence of the gauge bosons predicted by the theory. By studying the experimentally observed cross sections for $e^+e^- \rightarrow$ two, three or four-jets, it is possible to test the predictions of QCD in detail. In order to do this, however, the predictions of the theory for cross sections for producing two, three or four final state partons must be calculated. These predictions are then modified to take into account the dressing of the partons into jets so that the data may be

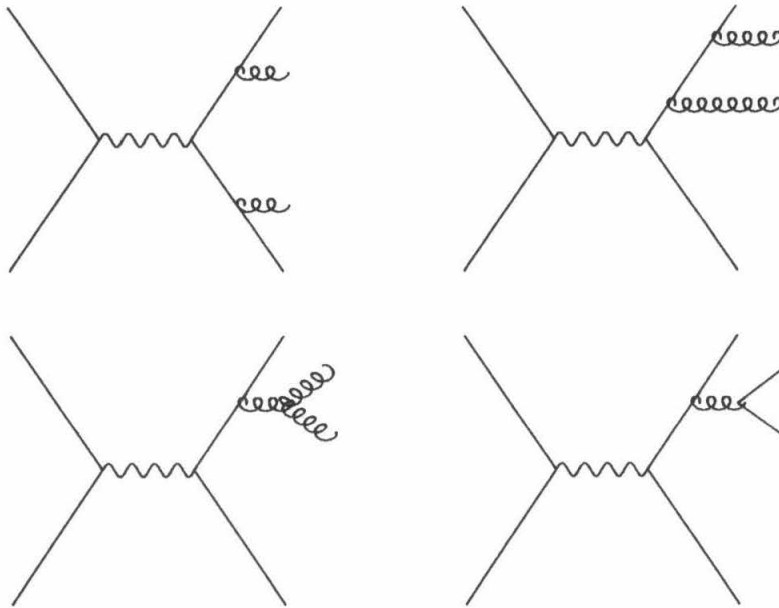


Figure 3.10 The 4-jet diagrams involved in calculating the cross section in $e^+e^- \rightarrow 3\text{-jets}$

compared to the theory.

Several calculations of the three-jet cross section have been made [50,49,48,77] and one (directly) of the two-jet cross section to full second-order [76]; the four-jet cross section has only been calculated to tree level [78]. Due to the complexity of the calculations, it is unlikely that third-order, or higher, calculations will be made in the near future, although substantial progress on the methods of evaluating higher order tree graphs have been made. The calculation of the three-jet cross section is of primary interest to experimenters, since this calculation is used in the measurement of α_s . The calculations involve the diagrams of Figures 3.10, 3.11, 3.9, and 3.8. Any of the diagrams in Figure 3.10 taken individually will contain both infrared and collinearly divergent pieces. The situation, however, is similar to that encountered above for the calculation of the total cross section, and the divergences are cancelled by divergences from the loop diagrams.

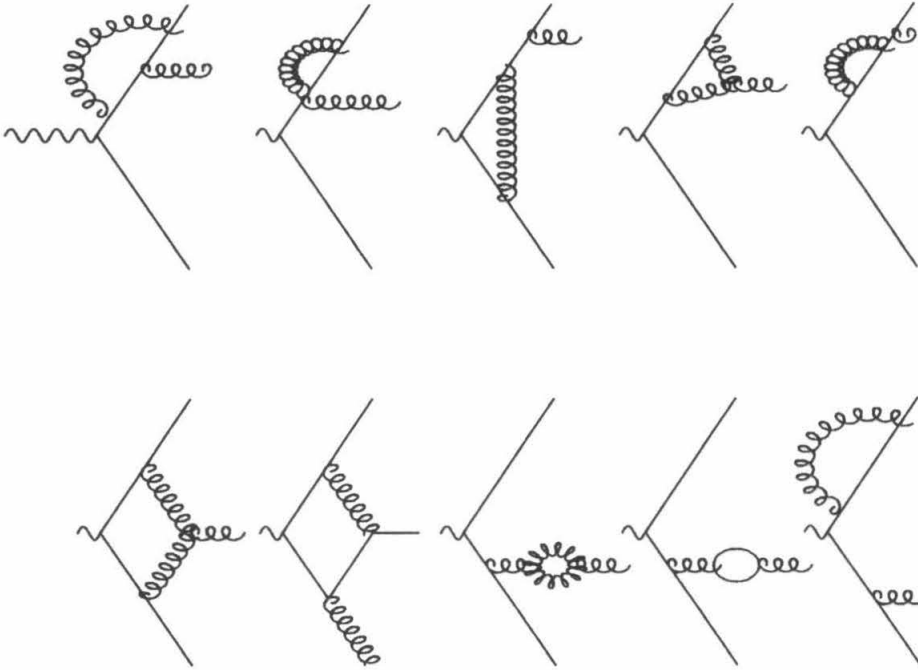


Figure 3.11 Loop diagrams for the complete 2^{nd} order calculation of the cross section $e^+e^- \rightarrow 3\text{-jets}$

The divergences are regulated by the introduction of a resolution criterion. Consider the top left diagram of Figure 3.10, with one of the gluons becoming collinear with the quark from which it originated. When this happens, the propagator for the quark between the γ - q vertex and the q - g vertex diverges. However, the gluon and the quark then become indistinguishable, and they are said to be irresolvable. When two partons are irresolvable, it doesn't make sense to talk about two partons anymore, and the pair are combined into a single parton. There is some free choice in the way the re-combination is performed and in the choice of which pair of partons to combine. However, the flavor signature of the partons must be preserved, so that a quark and a gluon are combined to form a quark, and two gluons are combined to form a gluon.

There are several different recombination algorithms that are in common use. In the 'momentum scheme', the 3-momenta of the partons are added, and the parton

energies are rescaled so that they sum to the total center-of-mass energy. In the ‘energy scheme’ the 4-momenta are added. In this work the momentum scheme is used exclusively¹, since this has the advantage of preserving the kinematics of the re-combined event. There are also several different ways of choosing the parton pair to be recombined. As pointed out above, the actual divergence arises in the intermediate propagator when its decay products become soft or collinear. In the ‘Partial Fractioned Dressing Scheme’ the decay products are recombined, and this recombination is performed only when the intermediate propagator diverges. In the ‘Direct Dressing Scheme’ recombination is performed whenever *any* pair of partons become indistinguishable, regardless of the presence of a divergent propagator. In general, the pair of partons that fail the cut are combined, although some calculations use different criteria. The prescription dependence of the calculations have been the subject of earlier work [27] and will be re-examined in Appendix B .

The distinction between resolvable and irresolvable pairs of partons is made on the basis of a cut in some jet-resolution variable. The original jet-resolution variable was introduced by Sterman and Weinberg [79], and has since become known as the (ϵ, δ) -cut. In this approach two partons are said to be irresolvable if one of them falls within a cone of half-opening angle less than $\cos^{-1}(\delta)$ positioned on the other, or if the energy of one of the partons is less than a fraction ϵ of the beam energy. A second resolvability criterion makes use of a scaled pseudo-invariant mass cut defined through the minimum invariant mass between any pair of partons. For every pair of partons the quantity

$$Y = 2 \frac{P_i P_j - \vec{P}_i \cdot \vec{P}_j}{(\sum_k P_k)^2} \quad (3.20)$$

is calculated and the minimum Y , Y_{min} , is required to be above some cut-off, Y_{cut} . To see how the matrix elements are used to calculate the partial cross section for

¹It has been shown that the results of experimental jet analyses are not affected by the choice of recombination scheme [27].

$e^+e^- \rightarrow \text{hadrons}$, we shall consider the full 2^{nd} order calculation of the cross section for e^+e^- into three jets.

The diagrams involved in the 2^{nd} order calculation of the 3-jet partial cross section are shown in Figures 3.8, 3.9, 3.10 and 3.11. Of the various calculations that have been performed only the ERT [50] calculation makes full use of the KLN theorem to cancel the divergences and return matrix elements that are independent of any jet-resolution variable. The remaining calculations achieve cancellation of the divergent diagrams through integration up to some Y_{min} that remains in the final expression for the cross section. Since, for experimental work one is interested in jet-resolution cuts at the parton level that are comparable to the post-fragmentation (finite) jet-resolution, the ERT calculation must be modified from its original form to include finite jet-resolutions. The calculations that retain a dependence on the jet-resolution variable all rely on approximations in order to evaluate the integrals arising in the calculations; as a result, they are found to be accurate only to the order of the resolution cut imposed. In the limit of vanishing jet-resolution cut, however, these calculations agree among themselves and with the precise results of ERT.

For this study a calculation by Zhu [27] is used. We shall refer to this calculation as the ERT/Ali/Zhu calculation, since it is product of several people's efforts. In this calculation the conversion of the ERT matrix elements into a form suitable for experimental applications is effected by a numerical integration of the divergent 4-jet contribution up to relevant values of the resolution cut. The 3-jet partial cross section can be written as

$$\sigma_3 = \sigma_3^B + \sigma_3^4 + \sigma_3^V. \quad (3.21)$$

Here the σ_3^B term is the 'Born' contribution from the 1^{st} order diagrams of Figure 3.8 for parton configurations that pass the jet-resolution cuts. The remaining two terms provide the 2^{nd} order correction to σ_3 . The term σ_3^4 comes from the 4-

parton diagrams of Figure 3.10 that fail the resolution cut once, (so-called ‘soft four jet’ part) and so contribute to the 3-parton rather than the two-parton cross section. The σ_3^V term (‘virtual corrections to the three jet cross section’), comes from the interference between the diagrams of Figure 3.11 with the 1st order diagrams of Figure 3.8 and provides the 2nd order virtual correction, which is divergent and cancels the divergent contribution from σ_3^4 . The actual calculation was performed with a sample of 10^7 Monte Carlo simulated events, originally generated with the ERT matrix elements and then reassigned as contributing to one of the terms in Eqn. (3.21), according to their survival of the jet-resolution cuts. The Direct Dressing, Y cut, minimum invariant mass momentum-recombination scheme was used, and the results were expressed in terms of a table of values for the complete 2nd order correction as a function of the variables x_q and $x_{\bar{q}}$ defined above.

In this work the Direct Dressing+ERT calculation of [27] has been repeated with lower statistics, using the matrix elements of [48]. A comparison of the results of a calculation based on the Direct Dressing scheme and results from Partial Fractioned Dressing has thus been possible. This is presented in Chapter 5.

3.5 Leading logarithmic QCD

The type of calculations described above, often referred to as fixed order matrix element calculations, are limited in so far as they have not been extended to cases where more than 4 partons appear in the final state. For higher multiplicity jet final states approximate QCD calculations are used. These calculations take into account only the leading logarithmic terms at each order in the perturbation expansion and so are called ‘leading log’ calculations [80]. While the calculations of the previous section are exact up to some order in the perturbation series, the leading log calculations discussed here are summations to all orders in the perturbation expansion over only the dominant logarithms.

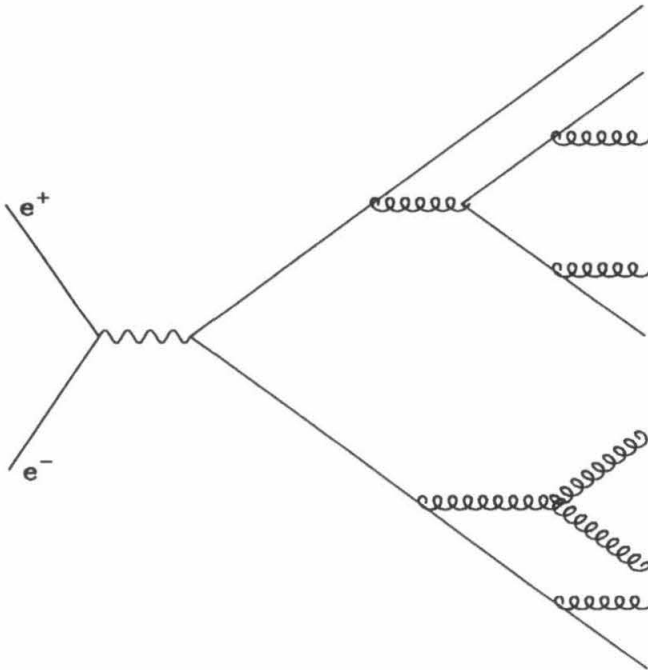


Figure 3.12 A leading logarithmic parton shower developing in the final state of $e^+e^- \rightarrow \text{hadrons}$

The inclusion of only leading log terms in the summation makes this approximation valid only for hadronic states such as that shown in Figure 3.12. Contrasting this diagram with that of Figure 3.1, the difference is seen to be the absence of loop sub-diagrams in Figure 3.12. This difference makes the Monte Carlo calculation of diagrams like Figure 3.12 possible and is the reason that the type of diagram in Figure 3.12 is calculable to all orders, while the diagram in Figure 3.1 is hopelessly non-calculable. The key is the factorization property of diagrams that lack loops which allows such diagrams to be taken apart branch by branch – something that cannot be done when branches are connected by loops.

The factorization property of diagrams of the type shown in Figure 3.12 also makes the calculation of such diagrams particularly amenable to the Monte Carlo approach. The diagram can be built-up from its sub-diagrams, of which there are only the three types shown in Figure 3.13.

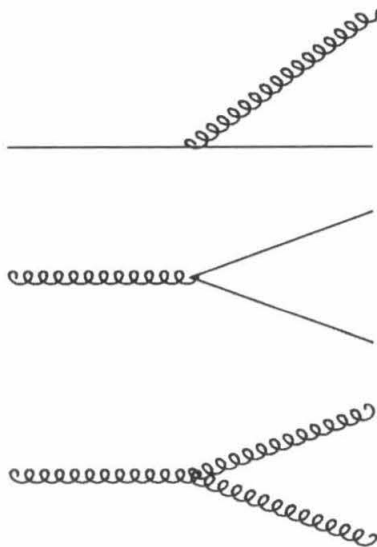


Figure 3.13 The basic elements from which any leading logarithmic parton shower can be constructed

Associated with the basic ingredients of Figure 3.13 are the Altarelli-Parisi splitting functions that give the probability of one of the basic splittings occurring as a function of the fraction of the available energy carried-off by the daughters at each splitting, z . These functions are:

$$P_{q \rightarrow qg}(z) = \frac{4}{3} \left[\frac{1+z^2}{1-z} \right], \quad (3.22)$$

$$P_{g \rightarrow gg}(z) = 6 \left[\frac{1-z+z^2}{z(1-z)} \right], \quad (3.23)$$

and

$$P_{g \rightarrow q\bar{q}}(z) = N_f \left[\frac{z^2 + (1-z)^2}{2} \right], \quad (3.24)$$

respectively for the splittings shown in Figure 3.13. With these splitting functions, the cross section for an arbitrarily populous parton final state can be built-up through the recursion relationship:

$$d\sigma_{N+1} = d\sigma_N \left[\frac{\alpha_s(t) dt}{2\pi t} P_{A \rightarrow BC}(z) dz \right], \quad (3.25)$$

which relates the cross section of an N parton final state to that for an $N+1$ parton final state formed by the addition of one of the building blocks of Figure 3.13 to the N parton diagram.

The practical implementation of the above ideas into a useful computer program requires that one eliminate the singularities that arise in the splitting kernels at $z=1$ or 0 . Rather than just generating splittings according to the recursion relation above, one generates splittings that give rise to daughter partons having an invariant mass above some cut. This invariant mass cut, called t_{cut} here, is similar to that discussed above as a jet-resolution cut for fixed order matrix elements. Unlike the jet-resolution cut of the previous section, however, this cut controls the soft parton distribution rather than the number of hard, well-defined 2, 3 or 4-parton configurations as is the case for the jet-resolution cuts. The production of many soft final state gluons at the end of the LLA² shower is an added bonus of the LLA method. It is possible to regard the vast numbers of soft gluons that arise at the end of a LLA parton shower as the first step in the perturbative generation of color screening.

3.5.1 Color Coherence in LLA Showers

The LLA shower approach is only as good as the approximations inherent within it. One such approximation is the omission of the next-to leading logarithmic terms. It can be shown that the neglect of these terms is equivalent to neglecting the interference between neighboring color emitters on the branches of the parton shower. This interference gives rise to destructive interference in the color field between the neighboring emitters and can be interpreted as a suppression in wide angle gluon radiation as the shower develops.

The incorporation of next-to leading order terms into the LLA formalism turns

²Throughout this work LLA is used to refer to the Leading Logarithmic Approximation.

out to be particularly simple. This is because it can be shown that the gluon coherence effect is equivalent to ordering the emission angles of subsequent radiation down the shower, so that, at any late time in the shower development, the emission angle is smaller than any previous emission angle from the same branch. The approximation that incorporates the leading and next-to leading logarithmic contributions only is referred to as the ‘double leading logarithmic approximation’ (DLA).

Chapter 4

Theoretical Outline: Fragmentation Models

4.1 Overview of The Fragmentation Process

The manner in which partons are transformed into hadrons is not at present understood. The final stages shown in Figure 3.1, therefore, must be modeled. Theoretical insight into the problem is taken from two sources, the first of which has already been mentioned: the asymptotic behaviour of the coupling constant. The second insight comes from the Schwinger Model, which is an exactly solvable gauge theory which gives rise to solutions that show all the properties of confinement [81, 82].

The Schwinger model is a 1+1 dimensional version of massless QED based on a Lagrangian of the form:

$$L = -\frac{1}{4}F_{\mu\nu}F^{\mu\nu} + i\bar{\phi}\gamma^\mu\partial_\mu\phi - g\bar{\phi}\gamma^\mu\phi A_\mu, \quad (4.1)$$

where g is the coupling constant between the (massless) fermion fields, ϕ , and the vector field A_μ . Under certain (not very special) circumstances the asymptotic solutions to this theory correspond to massive boson states of mass $\frac{g}{\sqrt{\pi}}$ [82]. The vacuum in this model is so polarizable that any free charge is immediately screened, and the massless ‘electrons’ of the Lagrangian vanish from the physical spectrum of the model. If the equations of motion of the model are solved for the special

case where the initial state consists of an electron-positron pair moving apart from each other, the asymptotically observed particles are massive dipole states. This behavior can be understood in terms of the vacuum polarization. In one dimension Coulomb's law is modified, and the electric field due to a charge is independent of the distance from the charge. As the initial electron-positron pair move apart, the vacuum polarization causes the pair production of new electron-positron pairs between them. These dipole pairs exactly cancel the electric field due to the charges initially present.

It is reasonable to suppose that a similar mechanism is responsible for the total screening of color that occurs in nature, and that the production of hadrons in the fragmentation process is similar to the production of the dipole states that arise in the Schwinger model [83]. This kind of argument has given rise to a series of fragmentation models known as string models. In these models a quark-antiquark pair is considered to be connected by a color flux tube, so that even though the gluons of QCD are massless, the vacuum polarization has modified the force law, from a Coulomb-like form into one that yields a linear potential. As the initially produced quark-antiquark pair in an e^+e^- collision move apart, a color flux tube is strung between them, and quark-antiquark pair production takes place in the tube. The production of a new quark-antiquark pair totally screens the color field, and as a result, two flux tubes now exist, each of which contains less energy than the original tube. The whole process repeats, with the break-up into more flux tubes, until all the energy is used up [84]. This is represented schematically in Figure 4.1, where the creation of quark-antiquark pairs leads to the creation of substrings, between which the color field is totally screened.

The QCD vacuum is vastly more complex than the simple vacuum of the Schwinger model, and so it is not possible to analyze the screening of the color field in the same way as is done for the 1+1 dimensional electric field. It is possible, however, to as-

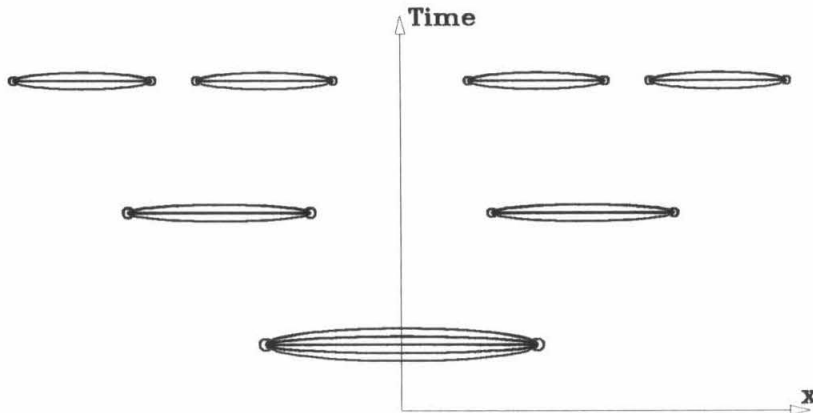


Figure 4.1 Illustrating the screening of the color field by the creation of quark-antiquark pairs in a color flux tube.

Model	Parton Generator	Fragmentation Model
Ali	ERT/Ali/Zhu	Field-Feynman
LundV4.3	ERT/Ali/Zhu	Lund-strings V4.3
LundV6.3	ERT/Ali/Zhu	Lund-strings V6.3
CIT2-FME	ERT/Ali/Zhu	Caltech-II
CIT2-LLA	LLA	Caltech-II
CIT2-DLLA	DLLA	Caltech-II

Table 4.1 The various model combinations used in this study

sume that the color flux tubes of the preceding discussion exist and to model their behavior. Further approximations are made, and the flux tubes are replaced with color strings that are elastic and one-dimensional. This gives rise to the string picture of hadronization which is employed, in various forms, in two of the fragmentation models used for this study.

A total of six different models for the process $e^+e^- \rightarrow \text{hadrons}$ have been investigated in this thesis. These six models are listed in Table 4.1, where they are shown decomposed into their parton generator and fragmentation model components. The various models in the table are all modifications of pre-packaged event generators

written for use in analyzing e^+e^- annihilation data. In all cases the initial state radiative corrections described above have been incorporated into the parton generator. There are two parton generators, ERT/Ali/Zhu, which is a generator for the processes: $e^+e^- \rightarrow q\bar{q}, q\bar{q}g, q\bar{q}gg, q\bar{q}q\bar{q}$, and LLA. The ERT/Ali/Zhu generator is an event generator based on the 2^{nd} order calculation described in the previous chapter, while the parton generator dubbed LLA is the LLA shower package from Gottschalk that is used in the Caltech-II fragmentation model[39,85]. The LLA generator provided with the Caltech-II fragmentation model includes an option for generating coherent parton showers. However, in this work the generator is used *exclusively* to generate non-coherent showers and next-to-leading logarithmic effects are incorporated as described below. The generator called DLLA is just the LLA generator, but with the additional feature that parton showers which do not possess the angle ordering property required for gluon coherence effects are rejected. The fragmentation models are labeled with the name of the fragmentation package from which they were taken, so that, for example, LundV6.3 has a fragmentation scheme taken from version 6.3 of the LUND Monte Carlo for e^+e^- annihilation.

In this chapter we describe the models used in the following work. We begin by describing the ‘Independent Jet’ fragmentation models based on the early work of Field and Feynman[30]. Next, the general methods common to both the string fragmentation models of Gottschalk *et al.*, Caltech-II, and the LUND group are described. We then continue with a description of the LUND fragmentation models, and the differences between the early version, Lund V4.3, and the most recent version, V6.3, are pointed out. We then describe the more recent model of Gottschalk *et al.* and point out where it differs from the LUND models. Finally, the detector simulation that is used to approximate the effects of the detector on the predictions of the various models is described.

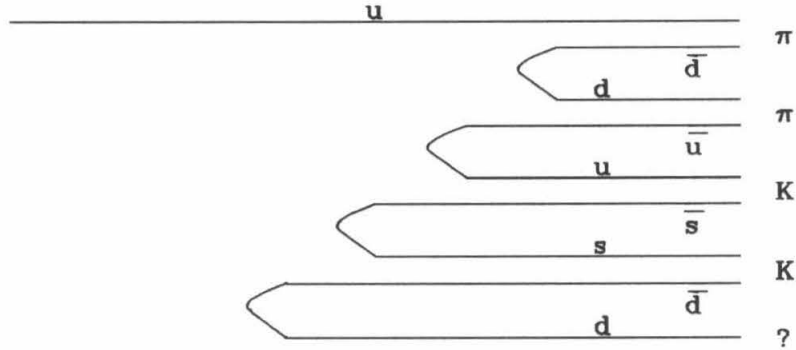


Figure 4.2 The independent fragmentation of quarks in the Field-Feynman model

4.2 Independent Jet Fragmentation

4.2.1 The Field-Feynman Model and its Variants

Although it is possible to think of the Field-Feynman model for hadronization as implementing color screening in the sense discussed above, it is more of a parametrization than a model [30]. Consequently, we use it with caution and do not attempt to make fundamental physics statements about hadronization from analyses of the data employing this model.

The idea behind this model is the fragmentation of an energetic quark by popping a series of quark-antiquark pairs out of the vacuum (so called ‘sea’ quarks and antiquarks), as illustrated in Figure 4.2. The basic process shown in the figure is:

$$q \rightarrow (q\bar{q}') + q', \quad (4.2)$$

where the $(q\bar{q}')$ form a meson, and the q' provides the quark for the next stage in the process. The flavors of the quarks that can be pulled from the vacuum are restricted to be u,d, or s, and the probabilities for producing a particular flavor are a free parameter of the model. For this study, typical probabilities for pulling a u,d or s quark out of the vacuum lie in the ratio 2:2:1 respectively, which is consistent with

data on inclusive kaon production[86]. This popping of quark-antiquark pairs from the vacuum may look like color screening in action, but there is no consideration of QCD in the model, and the quarks are not connected by a color string. For this reason, the quarks in a multiparton state (from one of the parton generators mentioned above) evolve totally independently of each other. The Field-Feynman model is, therefore, sometimes referred to as the *independent jet* model.

The process indicated in Figure 4.2 can be implemented in a computer program, provided a function that describes how the energy of q is to be shared between the meson and q' can be found. Such a function is called a fragmentation function, $f(z)$, and is defined in terms of the variable

$$z = \frac{(E + p_{\parallel})_M}{(E + p_{\parallel})_q}, \quad (4.3)$$

where the subscript M refers to meson quantities and q labels the original quark values. The form taken for $f(z)$ in the model is:

$$f(z) = 1 - a + 3a(1 - z)^2. \quad (4.4)$$

In principle there are many such fragmentation functions corresponding to the particular quarks and mesons participating in the process shown in Eqn. (4.2). In practice the fragmentation function given above is used for all cases, however, different values of the parameter a are used for different quarks. For this study, a is taken as 0.7 for u,d, and s quarks and 0.0 for c and b quarks. The harder fragmentation function for the heavy quarks reflects the fact that these quarks retain most of their energy during fragmentation[2]. Experimentally it is possible to tag hadron events containing charmed or bottom quarks by tagging D^* 's and high P_t leptons. It is found that the hardness of the c and b fragmentation does not significantly alter the overall appearance of the events[87,88]. The iteration of Eqn. (4.2) is terminated when the last quark pulled from the vacuum has an energy of $O(1 \text{ GeV})$, ie., its association with a hadron can be made directly.

The transverse structure of the jet is modeled by assigning a transverse momentum to the quarks pulled from the vacuum according to the Gaussian distribution:

$$\exp\left[-\frac{p_{\perp}^2}{2\sigma^2}\right]dp_{\perp}. \quad (4.5)$$

Clearly, the simple process illustrated in Figure 4.2 cannot permit the formation of baryons, and the fragmentation of gluons is also excluded. The model can be extended into a complete fragmentation scheme, and the expression ‘Field-Feynman’ will from now on refer to one such extension, due mostly to Ali¹ [31]. The most basic extensions from the Field-Feynman to the model used in this study involve the incorporation of gluons and baryons. Gluons are fragmented by first splitting them into a quark-antiquark pair according to Eqn. (3.23) and then fragmenting the quark and antiquark independently. Baryon production is permitted by introducing the possibility of pulling a diquark pair from the vacuum.

There are obvious problems with this simple model. One glance at Figure 4.2 shows that, for every initial parton fragmented, there will be a leftover quark or antiquark. These end-point quarks are arbitrarily thrown away and replaced by a pion, and as a result, the model doesn’t conserve flavor, charge or color. Worse, the model fails to conserve energy and momentum, in part because of the treatment of leftover quarks, but also inherently, due to the fact that massless partons are converted into massive jets. The imposition of energy-momentum conservation on the final hadrons is performed by a Lorenz boost of all the final hadrons along a vector $\vec{\beta}$ given by:

$$\vec{\beta} = \frac{-\Delta\vec{P}}{E_{tot}}, \quad (4.6)$$

where $\Delta\vec{P}$ is the momentum imbalance and E_{tot} the total energy in the event. Energy conservation is then imposed by rescaling all the particle momenta by a common factor. This procedure typically results in a three-jet event being boosted along an

¹The expressions ‘Independent Jet’, ‘Field-Feynman’ and ‘Ali’ model are used interchangeably in what follows.

axis antiparallel to the gluon direction, causing it to appear slightly more two-jetty. The overall effect of forcing energy and momentum conservation is the introduction of a mild global dependence of the final state configuration on the initial parton configuration, and the fragmentation ceases to be completely independent [25].

Apart from the objections above, the model is aesthetically unappealing for several additional reasons. The cut-off on the energy of the last quark, used to terminate the iterative procedure, is frame-dependent, and as a result, the model is not Lorentz invariant. The first hadrons produced in the cascade contain the original quark and antiquark, and as one goes down the cascade, the hadrons are produced from the ‘outside-in’. According to the ideas mentioned at the start of this chapter, one would expect that the hadrons are produced in the same order as that with which the quarks that they contain screened the color field. Hence, the slowest, and not the fastest, hadrons should be formed first, and the development of the jet should be ‘inside-out’.

QCD requires that a $q\bar{q}g$ configuration, in which the gluon is collinear with one of the quarks, is indistinguishable from a $q\bar{q}$ configuration. This is the basis for the validity of the jet-resolution cuts described in the previous chapter. The Ali model, however, is discontinuous in its predictions for parton pairs just passing or just failing the resolution cut. To see this, consider an event in which a quark and an antiquark pair, each carrying $1/2$ of the center-of-mass energy, are fragmented; the quark jet can contain hadrons having energies up to $1/2$ of the center-of-mass energy. Now consider the case where the quark is replaced by a quark and a gluon, each carrying $1/4$ of the center-of-mass energy. The particles produced by this system can only have energies up to $1/4$ the center-of-mass energy, and so the final state here is much softer than the earlier case, in which the parton pair fails the resolution cut and is recombined into a single quark. The system that just passes the resolution cut will also produce a final state having a particle multiplicity nearly

twice that of the same system that just fails the resolution cut.

Despite the objections given above, the Ali model provides a very good description of the observed data and provides a valuable tool when analyzing the data.

4.3 String Fragmentation Models

4.3.1 String Fragmentation: Ingredients

The basic idea behind string fragmentation models was introduced at the start of this chapter. A quark-antiquark pair, initially moving apart from each other, are connected by a string that has a constant tension. The equation of motion for such a system is then:

$$\frac{dp}{dt} = \begin{cases} \kappa & \text{if } p > 0 \\ -\kappa & \text{if } p < 0 \end{cases} . \quad (4.7)$$

The solutions of these equations, for a quark-antiquark pair initially moving apart, describe the well known yo-yo modes, shown in the string center-of-mass frame in Figure 4.3(a), and in a frame boosted along the x axis in Figure 4.3(b). The breaking of the string between the quark and antiquark by the creation of a quark-antiquark pair in the string, causes the color field to be totally screened between the two new string-ends. This is shown schematically in Figure 4.4, where the color field is shown as vanishing in the forward light-cone region of the string-break points, labeled 1, 2 and 3 in the figure.

The most severe problem with the independent jet models is their inability to deal with gluons in a reasonable fashion. The string formalism, however, can be naturally extended to incorporate gluons in a manner that has none of the problems mentioned above for the independent jet models. In the string model, since a gluon carries two color charges, it can be considered as a ‘hinge’ joining two sections of string. A gluon is then viewed as a kink in the string that carries energy and momentum, as illustrated in Figure 4.5. From this figure it can be seen that as the

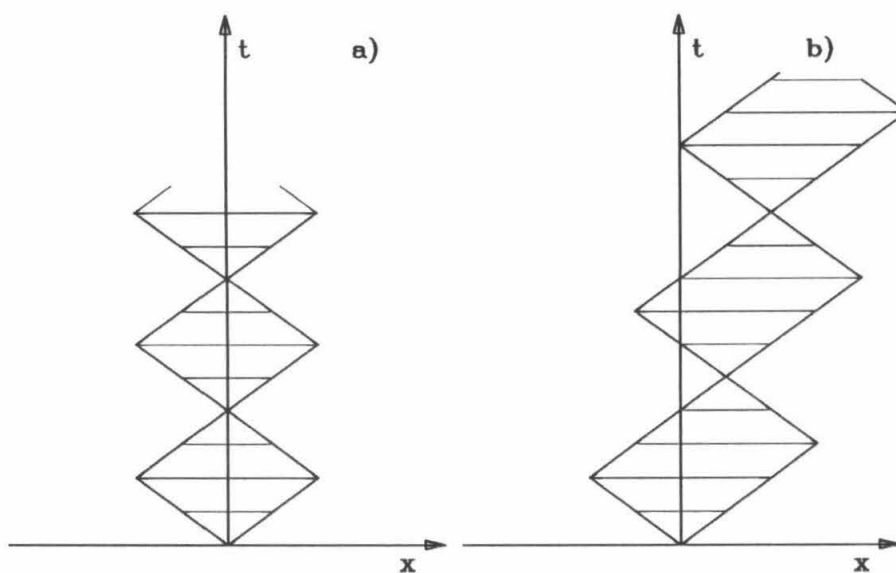


Figure 4.3 (a) The trajectories of a quark and antiquark pair connected by a string. (b) The trajectories as seen in a frame that has been boosted along the x axis

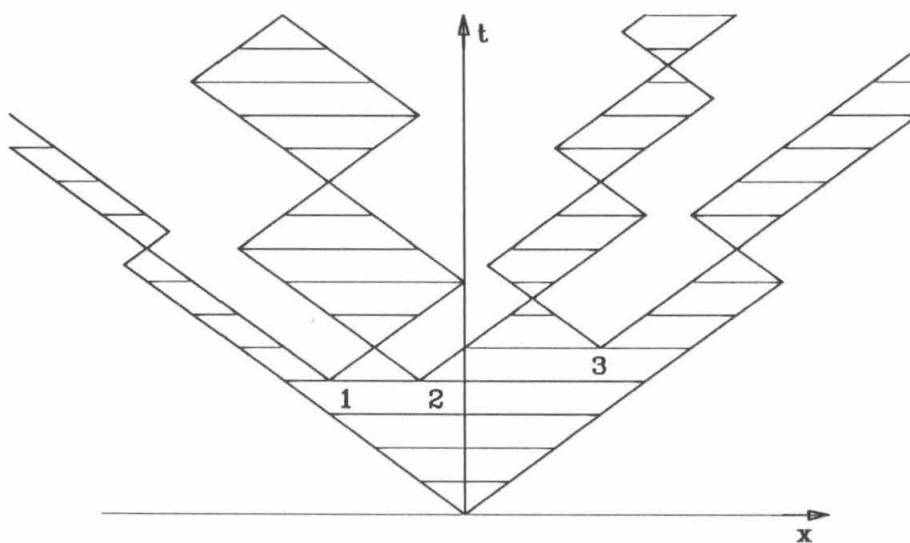


Figure 4.4 A schematic picture of the mechanism by which string breaking causes color screening

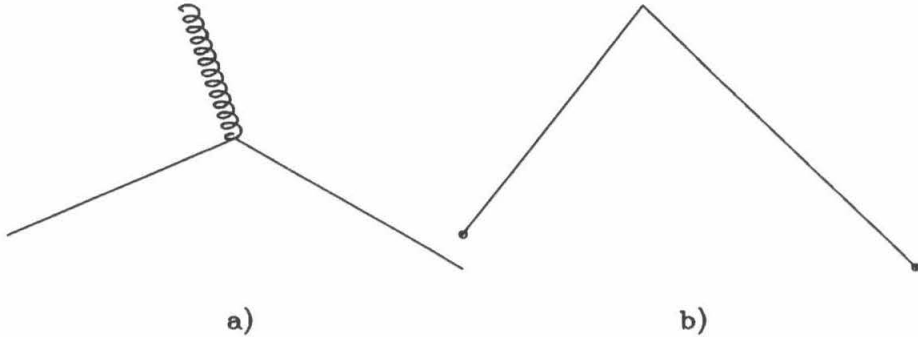


Figure 4.5 The inclusion of gluons in string fragmentation models as kinks on the string. a) The parton configuration. b) The string configuration.

gluon becomes collinear with the quark or antiquark the system goes over to a single string connecting the quark and antiquark in a smooth fashion.

Before the string idea can be incorporated into a fragmentation model, the method by which the partons are to be mapped onto the strings and the full equations of motion for the string dynamics, must be obtained. Since color is conserved, the mapping of partons onto colorless stringlike objects can be achieved by following the color flow away from the color production points. This is shown for a five parton final state in an e^+e^- annihilation event in Figure 4.6, where the parton state is one that might arise at the end of a LLA shower. Each of the colorless systems formed by this mapping are then evolved independently of one another.

The full equations of motion, for the string evolution, are derived from an action principle. Since a string is not a pointlike object, it is not possible to express its motion in terms of a proper time, however, there exists a two dimensional analogue. The area swept out by the string shown in Figure 4.3 is a function of κ , appearing in Eqn. (4.7), and the invariant mass, M , of the quark-antiquark pair. Since κ and

this idea to strings was made by Artu and Mennessier and replaces the proper time by the invariant area swept out by the string [89,90]. The probability of a string break occurring per unit area swept out by the string is then given by:

$$dP_b = P_0 dA, \quad (4.9)$$

the decay constant being replaced by a uniform string-breaking probability, P_b . Problems arise when this prescription yields a string-section having a mass below that of a pion. At this point the two string models described below adopt different methods.

4.4 The LUND Models

In the LUND models the basic process involved at a string-break point is:

$$string \rightarrow string + hadron, \quad (4.10)$$

where the point at which the string is to break is determined as discussed above. The hadrons that are broken off the strings are the final state hadrons of the model, so they are on-mass shell, and constraints must be placed on the possible spacetime distribution of the string-break points. Once a hadron has been broken off, the next string break is required to occur at a point on the remaining string that will, sometime in the future, still be a valid string-break point. The string-breaking points in the LUND model, therefore, have to be determined by the iteration of Eqn. (4.10) in conjunction with some fragmentation function, $f(z)$. This determines how energetic the hadron will be, and so, how much of the string will vanish at each break-point. With the basic branching given above, the model iterates until the remaining piece of string is of sufficiently small mass that it can be transformed into a single pair of hadrons.

The model, referred to here as LundV4.3, uses a fragmentation function of the

form:

$$f(z) = (1 + c)(1 - z)^c. \quad (4.11)$$

Clearly, the type of hadron that is removed from the string at the break-point depends on the flavor of the quark-antiquark pair responsible for the break. The simple Schwinger model mentioned earlier can be extended, by semi-classical arguments, to accommodate strings of finite thickness, such as QCD strings are expected to be [84]. This extension, carried over to QCD, requires that the quark-antiquark pair is viewed as tunneling out of the QCD vacuum and gives definite predictions for the quark production ratios. The function given in Eqn. (4.11) is also obtained from such tunneling arguments. It is worth noting that the tunneling arguments lead to huge suppressions in the charm and bottom quark production ratios, and that the assumption that only u, d, or s quarks screen (also made earlier for the Ali model) appears to be a good one.²

The actual dynamics of the string motion is based on infinitely thin strings, and as a result, there is no way to naturally introduce transverse momentum for the hadrons at the string-break point. The Gaussian prescription used for the Ali model is therefore applied, and the LUND models require a parameter σ_q from external sources. The introduction of transverse momentum into a string model is much more complicated than it is for an independent jet model; the additional energy associated with the transverse momentum must come from the string. If the string-break point, chosen by the above procedure, is close to the end of a string, then there may not be enough string left to form a hadron with the desired transverse momentum. In this case a new transverse momentum assignment must be made, and the process must be repeated until a physically possible transverse momentum is selected. The result of this is to severely deform the transverse momentum spectrum from the Gaussian of Eqn. (4.5). In fact, the Gaussian is severely truncated on each side.

²The production probabilities are in the ratio: u:d:s:c = 1:1:0.33:10⁻¹¹.

The fragmentation function of Eqn. (4.11) used in the early LUND model, LundV4.3, has the disadvantage of being asymmetrical. The physics results predicted by the model are dependent on which end of a string the iterative application of Eqn. (4.10) is started from. The principal difference between LundV6.3 and the early version is in the form of the fragmentation function [40]. In LundV6.3, the further requirement that the fragmentation function is symmetrical leads to a function of the form:

$$f_{ij}(z) = N_{ij} \frac{1}{z} z^{a_i} \left(\frac{1-z}{z}\right)^{a_j} \exp -(bm_{\perp}^2/z). \quad (4.12)$$

This function gives the probability for a quark of flavor i to combine with an anti-quark of flavor j , producing a meson having transverse mass m_{\perp} and energy fraction z . N_{ij} is a normalization constant. In principle the parameters are undetermined and different for different flavors; however, it turns out not to be necessary to use more than one value of a and b for all flavors.

The parameters discussed above are the principal ‘physics’ parameters in the LUND models. There are, however, many more parameters involved in the various decays of the hadrons produced, the details of the refinements made to accommodate heavy quarks, and the way subtle difficulties in the string dynamics (for breaks near the ends of the strings, for example) are overcome.

4.5 The Caltech-II Model

The Caltech model is an attempt to implement the idea of pre-confinement in a fashion that is in accordance with present day intuition about the way QCD would be if we could solve it [91,39]. The idea embodied in the Caltech model is that the final hadronization stage is a process which can be further factorized out of the fragmentation process, and that this final stage is no more than the decay of hadron-like, massive, colorless clusters. The early stages of the hadronization process are viewed as being the QCD motivated evolution of strings.

The principal differences between the version of the Caltech fragmentation scheme, taken from the Caltech-II model and used here, and the LUND models described above are :

- The basic iteration in the Caltech scheme is based on the splitting

$$string \rightarrow string + string. \quad (4.13)$$

- The Caltech scheme includes an elaborate low mass parametrization, based on low energy $e^+e^- \rightarrow$ hadrons data, to deal with the problem of strings having masses close to the hadron mass spectrum [36].
- Externally acquired transverse momentum for hadrons is excluded in the Caltech scheme.
- The reasons for the incorporation of a fragmentation function into the LUND models have been eliminated in the Caltech scheme by the adoption of the basic vertex $string \rightarrow string + string$. As a result there is no fragmentation function in the Caltech scheme.
- Although it is not of relevance to this study, we mention for completeness that the LLA parton shower generators that come with the LUND package are different to those supplied with the Caltech model. The LUND shower package requires that the shower evolution take place in a boosted reference frame so that angle ordering can be imposed.

With the removal of the mass-shell constraints of the LUND models and the consequent elimination of the need for a fragmentation function in the Caltech scheme, the string dynamics may now be governed by *only* the full 3+1 dimensional equations of motion, the initial parton state, and a single parameter related to the string tension and the string-breaking probability, ρ . The new prescription, however,

has made it possible for a string of arbitrary length to arise, and this is clearly unphysical for any string below the mass of a pion. This problem is related to the question of when to stop the string evolution and associate a string with a cluster, and its solution gives rise to the only other physically significant parameter of the scheme.

In this scheme the string evolution is terminated by a cut-off procedure, implemented as follows. A parameter W_{max} is introduced in the model, and for the particular string segment being considered, the two particle threshold W_{th} is determined. The quantity W_{cut} determined as :

$$W_{cut} = W_{max} + W_{th} \quad (4.14)$$

is evaluated. If the piece of string remaining after the break has a mass, W , below W_{cut} (i.e., less than W_{max} above threshold), then the string is passed to the cluster decay routines. If, on the other hand, the mass of the string segment is above W_{cut} , the string may be further evolved by the string evolution package with a probability P_{break} , or it may be passed to the cluster decay routines with a probability $1 - P_{break}$. The probability P_{break} is defined to be:

$$P_{break} = 1 - e^{\frac{1}{2}\rho(W - W_{th} - W_{max})^2/2}, \quad (4.15)$$

where ρ is given by:

$$\rho = P_0/\kappa^2. \quad (4.16)$$

The quantity ρ is a parameter that controls the string dynamics through the string tension and the uniform probability for the occurrence of string breaks. The quantities appearing in Eqn. (4.16) have been defined previously in connection with the discussion of Figure 4.3.

The remaining question to be answered by the Caltech scheme is: how should the string-break point be chosen? The only constraint put on the choice of a string-break point, in the Caltech scheme, is that it should leave a piece of string that is

above some hadron mass, otherwise the break can occur *anywhere* along the string. When the string-break point is chosen too close to the end of the string, the break point is shifted, so as to allow direct LUND-type breaks of the form:

$$string \rightarrow string + hadron. \quad (4.17)$$

4.6 Cluster Models

Although they will not be discussed in detail in this work, there exists another class of fragmentation models called cluster models, which we shall briefly mention for the sake of completeness. The original Caltech-I model [37] was of this type, and an investigation of that model provided the early basis of this study. In these models the color information from the perturbative QCD phase of the model is used to map the final state partons onto colorless clusters. These colorless clusters are then broken down into lower mass colorless clusters until they can be decayed into hadrons by a low-mass parametrization of the type that is included in the terminal phase of the Caltech-II scheme. The main drawback of these models is that the gluons are treated in the same way as they are in the independent jet models, i.e., they are split into a quark-antiquark pair and fragmented as a pair of quarks.

The Caltech-I model incorporated a LLA shower parton generator that was identical to that described in Section 3.4 for the Caltech-II model, with the exception that the $O(\alpha_s)$ matrix elements were not used for the first branch. The model was thus unable to reproduce the correct number of hard 3-jet events. A more serious problem with the model was that the physics predictions were sensitive to the value of the minimum invariant mass chosen for terminating the LLA shower. Worse, it was found that the value of Λ_{LLA} required by the model to fit the data was highly correlated to the value chosen for t_{cut} .

The deficiencies, mentioned above for Caltech-I, were corrected in the later ver-

sion, Caltech-II, by including a full string treatment of the gluons (see the discussion relating to Figure 4.5). There is only one cluster model that is still commonly used in the analyses of e^+e^- data; this is the BIGWIG (Branching Iterative Generator With Interfering Gluons) model from Webber [38]. BIGWIG incorporates a LLA shower generator which includes the gluon interference effects discussed earlier and a simple phase space cluster decay fragmentation scheme. The decision not to include BIGWIG in this study was made on the following grounds:-

- The termination of the LLA shower in the model is achieved through assigning large masses to the quarks and gluons. These masses play the role of the parameter t_{cut} , discussed in Section 3.4, and are arbitrary, non-physical parameters. The problem discussed above for the treatment of gluons arises in this model, and the physics results are, therefore, sensitive to the choice of the parton masses.
- At the end of the shower, the remaining partons are put on-mass shell and, as a result, the model does not implicitly conserve energy and momentum. If the energy of an event lies outside some window about the center-of-mass energy, then the event is rejected, while for events that lie within the window, the parton energies and momenta are rescaled in order that the energy and momentum of the event be conserved.
- The imposition of angle ordering on the partons from the LLA shower is performed by developing the shower in a reference frame where the initial quark-antiquark pair makes an angle of 90° with each other. Subsequently, the shower is boosted into the center-of-mass frame of the event. The imposition of angle ordering is manifestly non-Lorentz invariant, and as a result, the β for the boost should be regarded as a further non-physical parameter in the model. It is found that the physics predictions of the model are sensitive to the value

chosen for this boost.

- The degree to which the initial quark and antiquark are off-mass shell is determined from a flat distribution, which is most likely the wrong choice. The physics results are dependent on the initial choice of virtualness for the quark and antiquark, and it is not at all clear how this virtualness should be chosen.

4.7 Phenomenological Consequences of the Models

It is of interest to ask how the predictions of the various models described above might be expected to differ from each other. For the purposes of this study, there are two effects of interest, and both contribute to what has become known as the string effect. Consider the three-jet system shown in Figure 4.5(b). Within the context of the string fragmentation models, the gluon in this system is viewed as a kink in the string. The leading hadron in the gluon jet will be formed by string breaks on either side of the kink, leaving two string remnants as shown in Figure 4.7. The string remnants are then fragmented in their own rest frames, and later, boosted into the event center-of-mass frame. In the absence of any transverse momentum during the string breakup, and ignoring particle decays, the boost moves the final state particles onto a hyperbola in momentum space between the quark and gluon and between the antiquark and gluon directions. The particle flow for the event is then similar to that shown schematically in the figure. The effect is to pull particles (especially soft ones) out of the quark jets and put them in the region between the quark and gluon jets and to suppress the particle flow between the quark and antiquark jets. This effect has become known as the string effect.

While the string effect discussed above provides the most promising means for observing the consequences of strings in the experimental data, the situation is

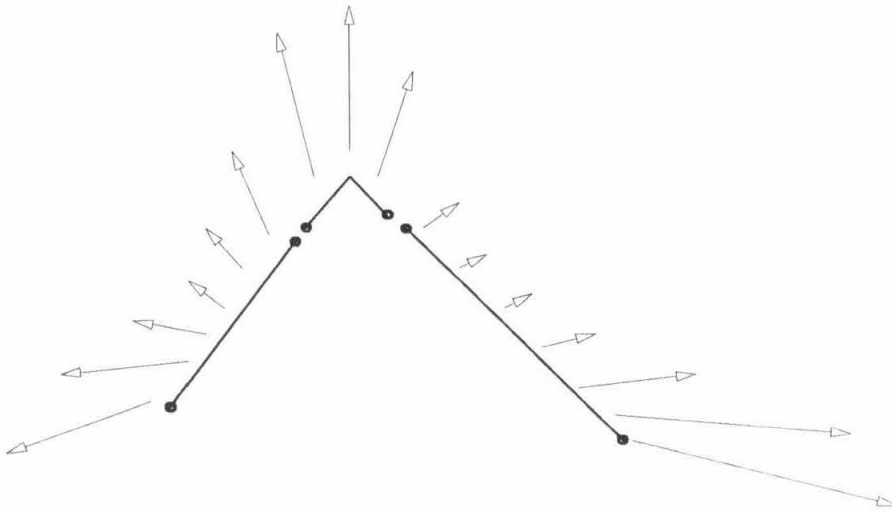


Figure 4.7 The breakup of strings in a three-jet system leading to the string effect.

further complicated by the consideration of soft gluons in LLA QCD. One way to think about the development of a LLA QCD shower is to regard the final state, containing N partons, as a color antenna. The evolution of this N parton final state into a $N+1$ parton final state involves the radiation of another gluon. Towards the end of the shower, the gluons being radiated are very soft, and consequently, have long wavelengths. These long wavelength, soft gluons are unable to see the detailed structure of the N parton final state of the shower and, rather, probe the shower as it was when it had $N-1$ partons in the final state. It can be shown that this effect leads to an enhancement in the soft gluon emission in the region between the gluon and quark jets, while decreasing the emission between the quark and antiquark jets. There has been considerable confusion in the literature as to whether the string effect is a result of QCD strings or a result of soft gluon interference effects at the perturbative QCD level. We shall address this problem in the next chapter.

Chapter 5

Model Comparisons at the Parton and Raw Track Level

5.1 Comparison of the ERT/Ali/Zhu Calculation with that of Gottschalk and Shatz

We have mentioned earlier that several calculations of the partial cross section for $e^+e^- \rightarrow$ hadrons have been made. Zhu has compared the ERT calculation to that of FKSS and found that the cross section from the FKSS calculation is between 10 and 30% lower than the corresponding ERT cross section, depending on the resolution cut used. Zhu traced the discrepancy between the two calculations to approximations made by the FKSS group [92].

In this study a comparison between the recent calculation of Gottschalk and Shatz [48] (henceforth called the GS calculation) and the ERT/Ali/Zhu calculation used by the MARK J group [27] has been made. This comparison is of interest for several reasons. First, it is a valuable check of the ERT/Ali/Zhu calculation. Second, the GS calculation is performed within the Partial Fractioned dressing formalism, while the ERT/Ali/Zhu calculation is based on the Direct Dressing scheme. A comparison of the two calculations, therefore, is of interest as a test of the consistency of the two dressing techniques. There has been much discussion concerning the bearing of the dressing scheme applied in these calculations on the values obtained

for the partial cross sections [28,29], and this comparison is of relevance to this discussion.

The comparison was made by imposing Direct Dressing resolution criteria on parton final states weighted by the GS matrix elements¹. The partons were generated with a Partial Fractioned Y_{cut} , $Y_{c,PFs} = 10^{-3}$, and subsequently, a Direct Dressing Y_{cut} , $Y_{c,DD}$, was applied. The contributions from the GS calculation can be labeled by the pole from which they originate, so that there are three contributions to the term σ_3^4 of Eqn. (3.21). These are labeled $(qg, 3)$, $(gg, 3)$ and $(qq, 3)$ indicating the pole of origin and the fact that they failed the resolution cut only once, and thus contribute to the three-jet partial cross section. In addition the contribution from those events generated as a three-parton configuration and passing the resolution cut, $(3, 3)$ – denoting 3 partons generated and 3 jets surviving –, is returned by the GS calculation of $\sigma_3^V + \sigma^B$. The total three-jet partial cross section can then be written as:

$$\sigma_3^{Tot} = \frac{\sigma_0}{N_{Gen}} \left[\frac{\alpha_s}{2\pi} \sum_n W_n(3, 3) + \left(\frac{\alpha_s}{2\pi}\right)^2 \left\{ \sum_n W_n(qg, 3) + \sum_n W_n(gg, 3) + \sum_n W_n(qq, 3) \right\} \right]. \quad (5.1)$$

The contribution to the four-jet partial cross section comes only from those events that were generated as four-parton configurations and that survived the resolution cuts. The four-jet cross section is then given by:

$$\sigma_4^{Tot} = \frac{\sigma_0}{N_{Gen}} \left(\frac{\alpha_s}{2\pi}\right)^2 \left[\sum_n W_n(qg, 4) + \sum_n W_n(gg, 4) + \sum_n W_n(qq, 4) \right], \quad (5.2)$$

where W_n refers to the weight of the n^{th} event and N_{Gen} the total number of events from each class generated. For the purposes of this calculation, equal numbers of events from the various poles were generated, so that the factor N_{Gen} is the

¹The notation of Section 3.4 is used in what follows.

Contribution	Number of final state post-cut partons		
	2	3	4
3-Jet	—	-0.2414 ± 0.0014	—
$q^* \rightarrow qG$	—	0.4614 ± 0.0024	0.0341 ± 0.0009
$g^* \rightarrow gg$	—	0.3492 ± 0.0013	0.0142 ± 0.0003
$g^* \rightarrow q\bar{q}$	—	0.0314 ± 0.0001	0.0023 ± 0.0001
Total GS :	0.3488 ± 0.0032	0.6006 ± 0.0031	0.0506 ± 0.0009
Ert/Ali/Zhu	0.3647 ± 0.0041	0.5838 ± 0.0041	0.0515 ± 0.0004

Table 5.1 Comparison of the partial cross sections from the ERT/Ali/Zhu calculation with those from the GS calculation, for $Y_{c,DD}=0.02$

Contribution	Number of final state post-cut partons		
	2	3	4
3-Jet	—	-0.2458 ± 0.0016	—
$q^* \rightarrow qG$	—	0.4142 ± 0.0023	0.0165 ± 0.0006
$g^* \rightarrow gg$	—	0.3016 ± 0.0012	0.0060 ± 0.0002
$g^* \rightarrow q\bar{q}$	—	0.0276 ± 0.0001	0.0011 ± 0.0001
Total GS :	0.4788 ± 0.0031	0.4976 ± 0.0030	0.0236 ± 0.0006
Ert/Ali/Zhu	0.5211 ± 0.0020	0.4553 ± 0.0020	0.0236 ± 0.0001

Table 5.2 Comparison of the partial cross sections from the ERT/Ali/Zhu calculation with those from the GS calculation, for $Y_{c,DD}=0.03$

same for each contribution. The two calculations were compared for $Y_{c,DD}$ (i.e., with Direct Dressing) of: 0.02, 0.03, 0.04 and 0.05. 10^5 events for each class were originally generated for the GS calculations, and 5×10^4 events were generated for the ERT/Ali/Zhu calculation. The matrix elements for this calculation had already been calculated with 10^7 events (on a larger computer at DESY) in the original work of Zhu. The results are presented in Tables 5.1, 5.2, 5.3 and 5.4, where the values have been normalized to correspond to a total cross section of 1.

The agreement between the two calculations is generally good. Certainly the four-jet partial cross sections agree, as they should, since these are just tree level

Contribution	Number of final state post-cut partons		
	2	3	4
3-Jet	—	-0.2325 ± 0.0017	—
$q^* \rightarrow qG$	—	0.3199 ± 0.0020	0.0080 ± 0.0004
$g^* \rightarrow gg$	—	0.2611 ± 0.0011	0.0028 ± 0.0001
$g^* \rightarrow q\bar{q}$	—	0.0241 ± 0.0001	0.00057 ± 0.00002
Total GS :	0.6162 ± 0.0028	0.3725 ± 0.0028	0.0113 ± 0.0004
Ert/Ali/Zhu	0.6273 ± 0.0019	0.3605 ± 0.0019	0.0118 ± 0.0003

Table 5.3 Comparison of the partial cross sections from the ERT/Ali/Zhu calculation with those from the GS calculation, for $Y_{c,DD}=0.04$

Contribution	Number of final state post-cut partons		
	2	3	4
3-Jet	—	-0.2134 ± 0.0017	—
$q^* \rightarrow qG$	—	0.2717 ± 0.0018	0.0043 ± 0.0003
$g^* \rightarrow gg$	—	0.2267 ± 0.0010	0.0014 ± 0.0001
$g^* \rightarrow q\bar{q}$	—	0.0210 ± 0.0001	0.00031 ± 0.00002
Total GS :	0.6879 ± 0.0027	0.3060 ± 0.0027	0.0061 ± 0.0004
Ert/Ali/Zhu	0.6974 ± 0.0012	0.2963 ± 0.0017	0.0062 ± 0.0002

Table 5.4 Comparison of the partial cross sections from the ERT/Ali/Zhu calculation with those from the GS calculation, for $Y_{c,DD}=0.05$

Contribution	Number of final state post-cut partons		
	2	3	4
3-Jet	—	-1.5758 ± 0.0055	—
$q^* \rightarrow qG$	—	1.0901 ± 0.0033	0.0351 ± 0.0012
$g^* \rightarrow gg$	—	1.0081 ± 0.0019	0.0144 ± 0.0004
$g^* \rightarrow q\bar{q}$	—	0.0658 ± 0.0001	0.0024 ± 0.0001
Total GS :	0.3601 ± 0.0069	0.5881 ± 0.0067	0.05181 ± 0.0018
Ert/Ali/Zhu	0.3647 ± 0.0041	0.5838 ± 0.0041	0.0515 ± 0.0004

Table 5.5 Comparison of the partial cross sections from the ERT/Ali/Zhu calculation with those from the GS calculation, for $Y_{c,DD}=0.02$ and $Y_{c,PFS}=10^{-5}$

calculations in each case. It can be seen that the agreement between the three-jet cross sections gets better as $Y_{c,DD}$ becomes larger; this is an indication that there is a dependence on the cuts implicit within the GS matrix elements. This problem can be overcome by choosing a smaller $Y_{c,PFS}$ than that taken here. In order to verify that this is the case, a calculation was made for a $Y_{c,PFS}$ of 10^{-4} , and $Y_{c,DD}$ equal to 0.02. Since the number of generated events that survive the cuts is lowered by the use of a small $Y_{c,PFS}$, this calculation was made with 5×10^5 events coming from each pole. The results are presented in Table 5.5, where it can be seen that the agreement between the two calculations is excellent.

The agreement, or lack of agreement, between the two calculations can be investigated in specific kinematic regions by comparing the predictions for the parton level Thrust. The Thrust of a parton configuration is defined through the expression

$$T = \max_{\vec{n}} \sum_i \frac{|\vec{p}_i \cdot \vec{n}|}{\sum_i |\vec{p}_i|} \quad (5.3)$$

and lies between $2/3$ and 1. For a two jet configuration the Thrust is 1, while for three and four jet configurations it lies on the interval $[2/3, 1 - Y_{c,DD}]$. A comparison of the total three-jet Thrust distributions from each of the two calculations is shown in Figure 5.1, where the specific contributions from the event classes in the GS

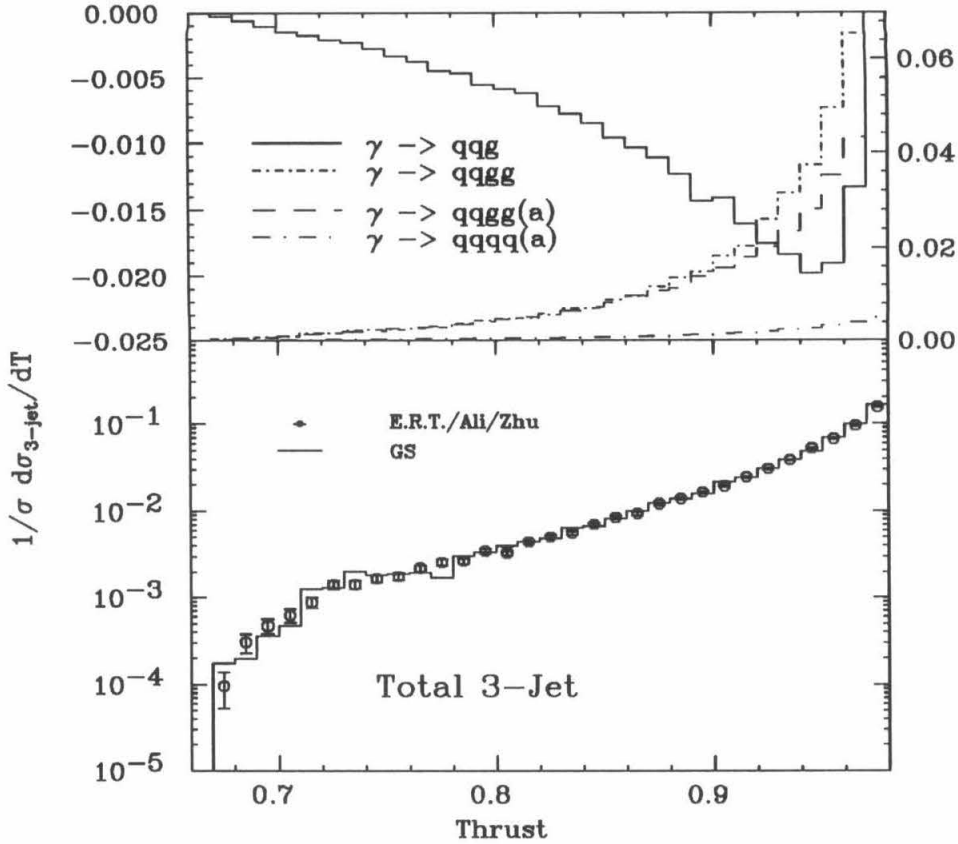


Figure 5.1 Comparison of the parton Thrust for three-jet events from the GS and ERT/Ali/Zhu calculations. The individual contributions from the poles for the GS calculation are shown in the top panel. The calculation shown is for $Y_{DD} = 0.02$

calculation are shown in the upper part of the figure. The curves in the upper panel labeled $qqg(a)$ and $qqqq(a)$ originate in the decay of an intermediate gluon as opposed to the curve labeled qqg , which originates in the decay of an intermediate quark. The solid line, qqg contribution, corresponds to the left-hand scale, while the remaining curves may be read-off on the right-hand scale.

5.2 Investigation into the Phenomenological Relevance of Gluon Coherence

Various groups have reported observation of the string effect discussed in Section 4.7, and there has been much discussion concerning its origin. Webber and the JADE

group have argued that the effect is a result of the soft gluon coherence effects in the development of LLA showers [41,42,43,38]. The effect has also been observed by the TPC group at PEP [44,45]. The JADE group base their contention on a comparison of the Caltech-I model and the Webber model, in which they find evidence for the effect in the Webber model (which includes gluon coherence) but not in the Caltech model (which omits gluon coherence).

In Figure 5.2 the soft gluon radiation patterns from a lowest-order LLA QCD calculation, which includes the effects of gluon coherence are shown [93]. The left-hand figure shows the emission probability for soft gluons, plotted in polar coordinates, from an otherwise perfect ‘Mercedes Benz’ event (the three hard partons have equal energies). It can be seen that the radiation is enhanced in the regions between the quark² and gluon jets and reduced in the region between the quark and antiquark jets. In Figure 5.2(b) the radiation pattern is shown integrated over all possible hard gluon directions lying between the quark and antiquark in three jet events. The soft gluon radiation pattern is decreased in the region between the quark and antiquark jets but enhanced in the region between the quark and gluon jets. It can be seen that the effect shown here is the same as that which is expected to arise in string fragmentation models for the fragmentation of qgg systems.

The theoretical calculation shown in Figure 5.2 cautions that the effect of the interference may not hold to all orders. The behaviour of the higher-order contributions is still under study, but for now we shall accept that there is such an effect. The question to be addressed then, is: to what extent are these soft gluon effects observable in the data?

The JADE study was based on a comparison of the Webber model with the Gottschalk model of [37], both of which are cluster-type models. The JADE study

²For the purposes of this discussion the term quark jet is used for both the quark jet and the antiquark jet.

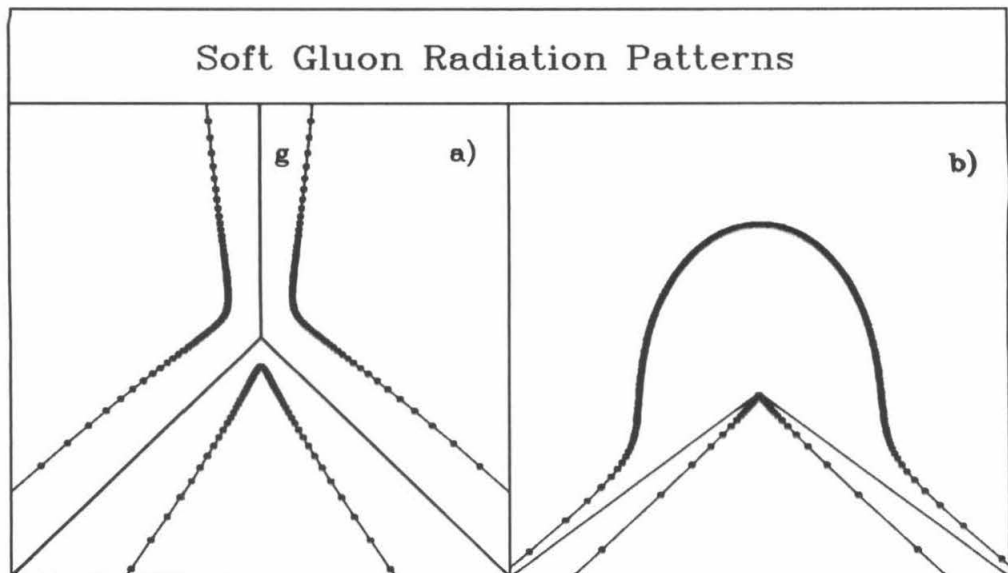


Figure 5.2 The results of a lowest-order analytic calculation of the soft gluon emission probabilities in a three-jet event. a) For a ‘Mercedes Benz’ event. b) Integrated over all possible gluon directions with the quark configuration shown.

assumed that the LLA showers incorporated into each model could be considered to differ only through the inclusion of angle ordering in the Webber model. Further, they ignored the differences in the fragmentation packages provided with the two models. For the purposes of this study, angle ordering was imposed as a switchable option on the parton final states from the Caltech-I LLA shower package, in order that the effects of angle ordering *alone* could be investigated. The reader is reminded that the Webber LLA shower evolution differs from that of Caltech-I in that it occurs in a boosted reference frame and fails to conserve energy and momentum.

The Caltech-I LLA shower package is used here in order that the results of this study be comparable to those of the JADE studies. It should be pointed out that the Caltech-I LLA shower differs from that used subsequently in this study through not including the $O(\alpha_s)$ matrix elements for the first branching in the shower.

The energy flow of the partons around the thrust axis, projected onto the event

plane, for events containing at least three partons is shown in Figure 5.3. The results shown in this figure include the effects of initial state radiative corrections and were obtained for a center-of-mass energy of 35 GeV. For all the data shown here the value of Λ_{LLA} was taken to be 600 MeV, otherwise the default quark masses of the Caltech-I package were taken. When an event contained an initial state radiated photon, this was included as one of the final state partons. It can be seen that the gluon interference effect, while small for both the values of t_{cut} shown in the figure, is more pronounced when the shower evolution is permitted to proceed to low Q^2 . Further, it can be seen that the effect of including angle ordering is *exactly* the same as the effect obtained by increasing the value of the shower termination parameter. This appears to be a general feature, at least at PETRA energies, of the coherence effect. The longitudinal momentum fraction for gluons coming out of the shower, and the parton multiplicities at the termination of the shower, both appear to display this effect. This is consistent with the result of a brief investigation into the coherence effect on the soft gluon distribution performed earlier by Odorico [94].

In Figure 5.4 the energy flow in the events that result when the partons of Figure 5.3(a) are fragmented with the Caltech-II string fragmentation model are shown. The enriched three-jet sample required for this plot was obtained by requiring that the events had broad-side Oblateness larger than 0.3. It is apparent that the difference between the pure LLA case and the LLA + angle ordering case, which is clearly visible at the parton level, is smeared by the raw track level. Since the effect of the detector will be to further smear the effect, we conclude that the effect indicated by Figure 5.2 is observationally irrelevant.

In the case of the Caltech-II fragmentation scheme, the mapping of the final state partons from the LLA shower onto strings circumvents the problem of cluster models discussed in Section 4.6. However, the Webber model maps partons onto

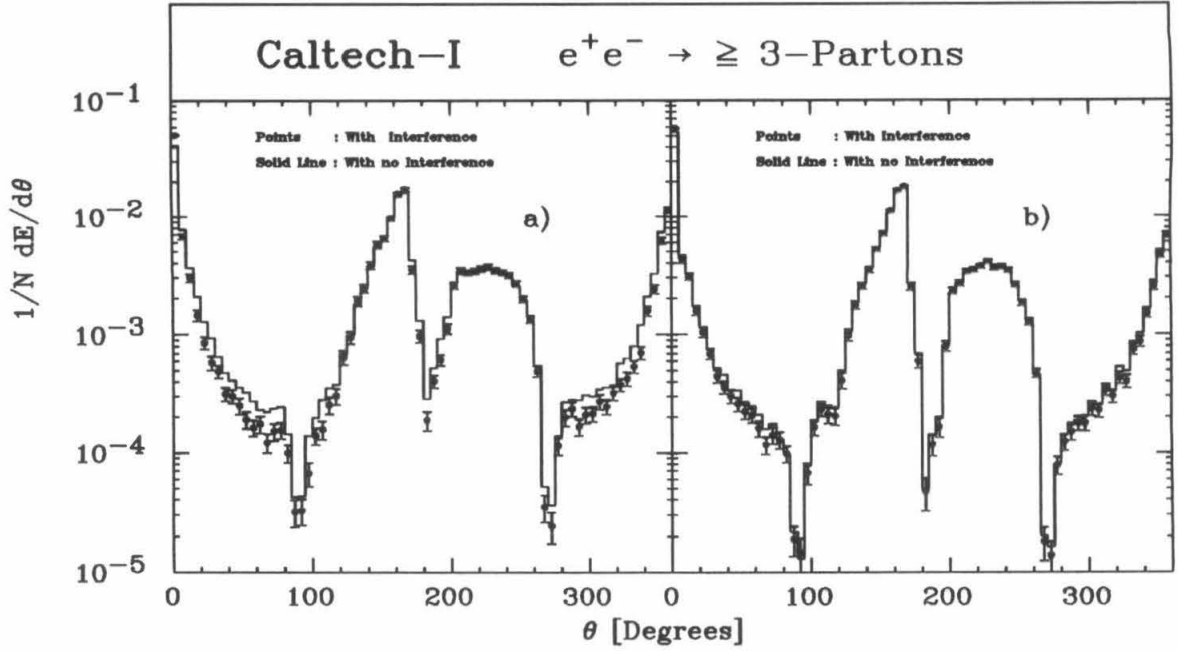


Figure 5.3 The energy flow around the thrust axis for partons generated with the Caltech-I LLA package. a) The results, with and without angle ordering, obtained for a shower cut-off of 4 GeV^2 . b) The results obtained for a shower cut-off of 15 GeV^2 .

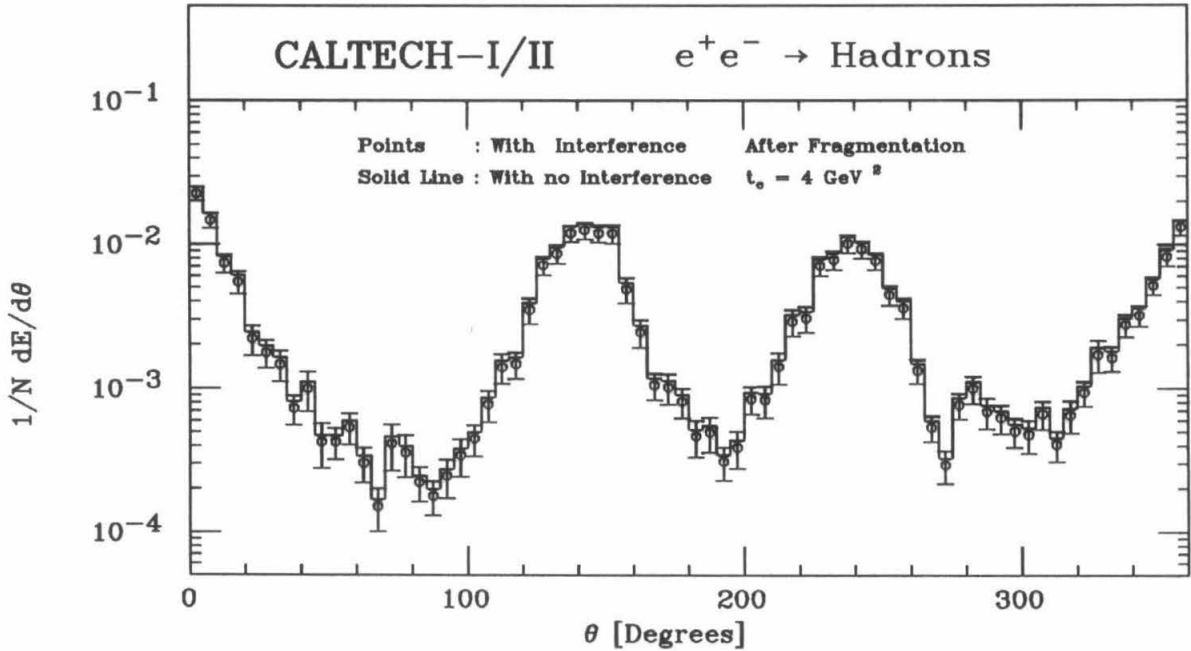


Figure 5.4 The energy flow around the thrust axis for hadrons generated with the Caltech-I LLA package and fragmented with the Caltech-II model. The non-observableness of gluon coherence effects is evident.

clusters, and as a result, the post-fragmentation results will be sensitive to variation in the shower termination parameter. The data shown in Figure 5.3 indicate that this may be of relevance to the form of the flower plot³ obtained from the model after fragmentation. That this is the case can be seen in Figure 5.5, where flower plots obtained with the Webber model for different gluon masses are shown. Due to the details of the method used in obtaining an angle ordered parton shower within the Webber model, it is not a simple matter to incorporate initial state radiative corrections with the model, and they are omitted from the results shown in the figure. Clearly, by a suitable choice of Q^2 for the shower termination, the Webber model can be made to fit any flower plot, and it is the freedom in the choice of this parameter, not the angle ordering, that determines the flower plots that result from this model. It might be expected that the flower plot would be sensitive to the magnitude of the boost used to define the angle ordering frame, however, we find that this is not the case. In what follows we adopt the CIT2-DLLA model, and, on the basis of the study presented here, assume that the differences between the combination CIT2-LLA and CIT2-DLLA are negligible.

5.3 Discussion

It has been found that the new $O(\alpha_s^2)$ calculation of the partial three-jet cross section, by Gottschalk and Shatz, is equivalent to the ERT/Ali/Zhu calculation. This equivalence is manifest when both calculations are used to calculate the same *dressed* partial cross section, and the GS calculation is used with sufficiently small Y_{PFS} that the small dependence displayed by the calculation, on Y_{PFS} , is unimportant.

Soft gluon coherence effects have been excluded as the source of the string effect

³The energy flow diagrams shown here are referred to as flower plots, since in a polar plot they resemble a flower with three petals.

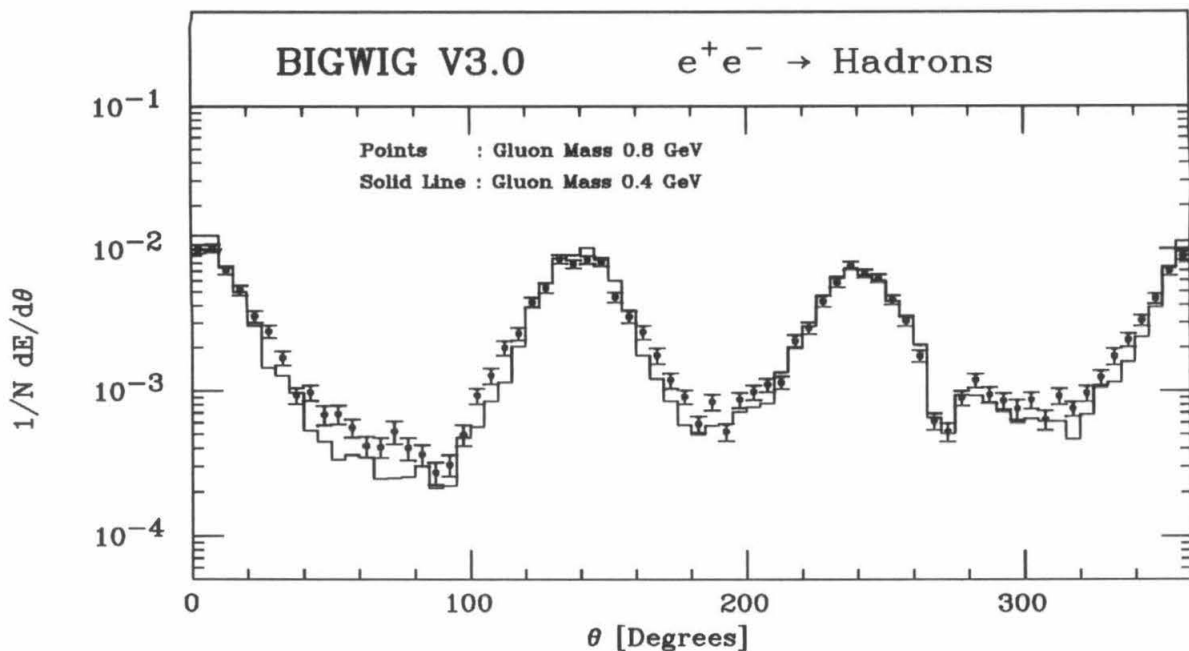


Figure 5.5 The energy flow around the thrust axis for hadrons generated with the BIGWIG V3.0 model with two different shower termination parameter values.

observed in the data (at least at PETRA/PEP energies). While soft gluon interference effects are visible in the density of energy flow at the parton level, and while the effect is consistent with the observed string effect, no such effect survives the fragmentation process. Further, it has been found that the density of energy flow in the regions between the jets, predicted by BIGWIG, is sensitive to the value of an arbitrary non-physical parameter, the shower termination scale. It is concluded that studies of the density of energy flow that have used the Webber model should be re-evaluated in the light of these findings.

Chapter 6

Tuning the Model Parameters

6.1 The Detector Simulation

The final connection between the QCD predictions, modified for fragmentation effects by one of the models described above, and the experimental data is made through the use of a Monte Carlo program that simulates the effects of the detector. The ‘raw tracks’ that are produced by the generators are fed to the detector simulation where they are traced through the various planes of the detector and their points of intersection with the detector planes are calculated. The particle identification information available from the generator is retained and each raw track is labeled as being electromagnetic or hadronic. If a track is to be treated as hadronic, it is considered to be a pion, while electromagnetic tracks are assumed to be electrons (except, of course, for tracking through the vertex detectors).

The program then calculates the angle of incidence of the track, with respect to the normal to the detector plane, and consults a series of look-up tables to find the required interaction with the detector plane. The look-up tables contain information from test-beam studies performed with electron and hadron beams and from detailed Monte Carlo studies [95]. For hadrons the energies: 0.5, 1.0, 1.5, 2.0, 3.0, 4.0, 5.0, 7.0 and 10.0 GeV were used for normally incident pions, while for non-normal particles the values at which test-beam data were taken are: 1.0, 2.0, 3.0, 5.0, 7.0 and 10.0.

Momenta [GeV]	Mean EM energy deposited			Mean Hadronic energy deposited		
	A-Ctrs	B-Ctrs	C-Ctrs	A-Ctrs	B-Ctrs	C-ctrs
0.10	0.915	0.079	0.007	—	—	—
0.30	0.856	0.122	0.021	—	—	—
0.50	0.816	0.157	0.027	—	—	—
0.70	0.773	0.191	0.035	—	—	—
1.00	0.706	0.250	0.044	0.197	0.172	0.321
1.50	—	—	—	—	—	—
2.00	0.683	0.241	0.075	0.163	0.150	0.351
3.00	—	—	—	0.131	0.126	0.362
4.00	0.617	0.275	0.108	—	—	—
5.00	—	—	—	0.101	0.101	0.356
6.00	0.560	0.310	0.130	—	—	—
7.00	—	—	—	0.088	0.085	0.351
10.00	0.477	0.364	0.159	0.073	0.081	0.336
15.00	0.478	0.331	0.191	—	—	—

Table 6.1 The look-up table used by the detector simulation for electrons incident on the A, B and C counters at 45° , and the same for hadrons incident at 50° to the normal.

For the electron case, 10 energy points were taken in the test-beam at: 0.1, 0.3, 0.5, 0.7, 1.0, 2.0, 4.0, 6.0, 10.0 and 15.0 GeV. For these energies, data is tabulated for tracks making angles with respect to the normal to the plane of $\cos \theta$ between 0.0 and 1.0 in steps of 0.1. The mean energy fraction deposited by the particle in the plane is found, as are the r.m.s. deviations of the energy deposited and the probabilities that the track will penetrate the plane.

The look-up tables for electrons and hadrons, incident at angles close to 45° used for the A, B and C counters, are shown in Table 6.1. For the case of incidence at 45° , the r.m.s. deviation of the energy deposited for hadrons is as given in Table 6.2. Information from the look-up tables for the energy fraction deposited by normally incident pions and electrons in the A, B and C counters is plotted in Figure 6.1.

The calculated hits are corrected for time of flight, attenuation in the scintillators, saturation in the phototubes and propagation times from the hit to the phototubes.

Momenta [GeV]	r.m.s. energy deposited			Hadron energy resolution
	A-Ctrs	B-Ctrs	C-Ctrs	σ_{had}
1.00	0.210	0.165	0.240	0.420
2.00	0.202	0.164	0.275	0.400
3.00	0.182	0.150	0.282	0.380
5.00	0.158	0.129	0.284	0.360
7.00	0.141	0.109	0.281	0.330
10.00	0.120	0.108	0.273	0.300

Table 6.2 The look-up table used by the detector simulation for hadrons incident on the A, B and C counters at 45° , giving the r.m.s. deviation on the mean energy deposited.

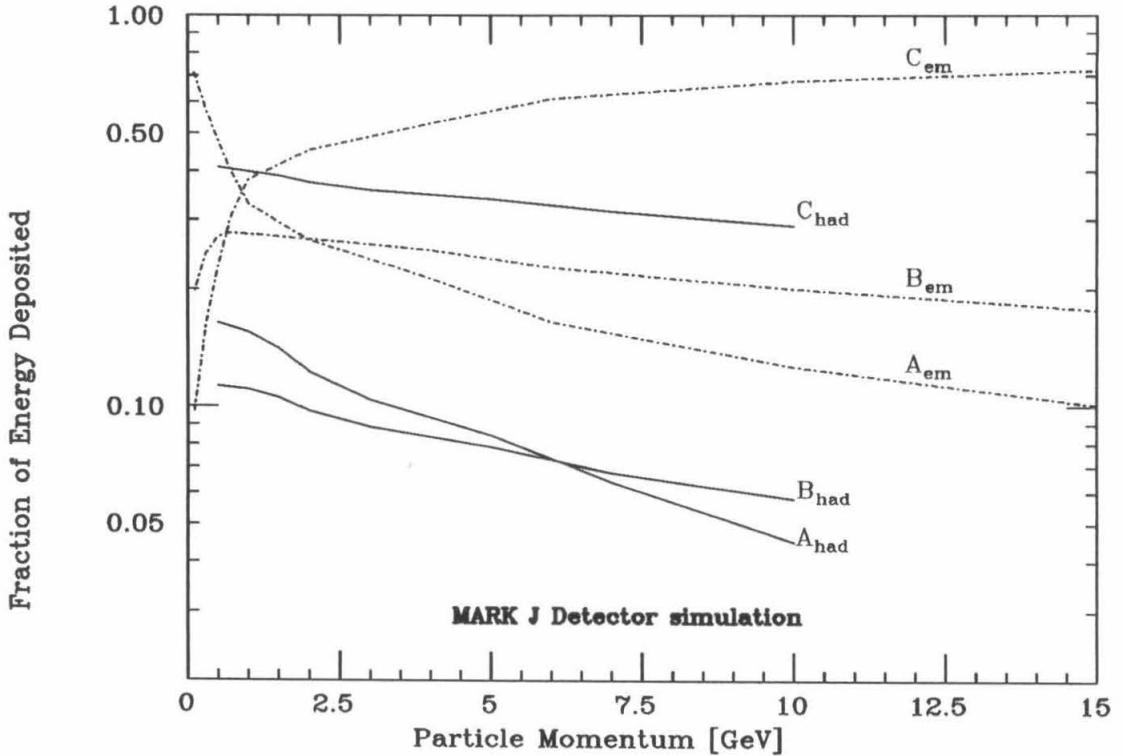


Figure 6.1 The fractional energy lost by hadrons and electrons on passing normally through the A, B and C counters.

In addition, corrections for time slewing and multiple hits are applied. Correlations between the calorimeter layers are introduced by summing the energy deposited in the various layers. These energies are then rescaled so that the mean value and fluctuations in the total deposited energy match experimental test beam data. Lateral spread of the energy, fluctuations, and the distribution of counter elements hit is simulated through detailed sub-models within the program. The calculated energy deposited by the track in each detector element hit is then digitized to provide an ADC and TDC value which is then written out in a format identical to the format used for the data actually obtained by the online system. These, Monte Carlo derived, data sets are then subjected to identical data reduction procedures as the 'real' data. The simulation program also simulates the drift chambers and takes into account the longitudinal and transverse beam spread of PETRA.

The performance of the whole detector simulation package can be judged by the data shown in Figures. 6.2 , 6.3, 6.4, where the actual and predicted energy dispositions in the detector for center-of-mass energies of 35 GeV and 44 GeV are shown. The effect of ignoring the contribution from two-photon and tau production is evident in Figure 6.3, where the data is seen to be above the pure QCD 'prediction' in the tails of the distribution shown.

One of the most important experimental uses of the detector simulation program is in the estimation of contamination in the hadron data set from tau and two-photon hadron production. Events are generated from these sources and passed through the detector simulation. Thereafter, these events can be mixed with pure one-photon exchange hadrons and subjected to the same analysis chain as the hadron data – a tedious and time consuming process that also involves visually scanning the events. The final Monte Carlo data set can then be studied to determine the rejection efficiency of the analysis chain and the hadron acceptance of the detector. In Figure 6.5 the results of such a study are shown. The data is compared to the

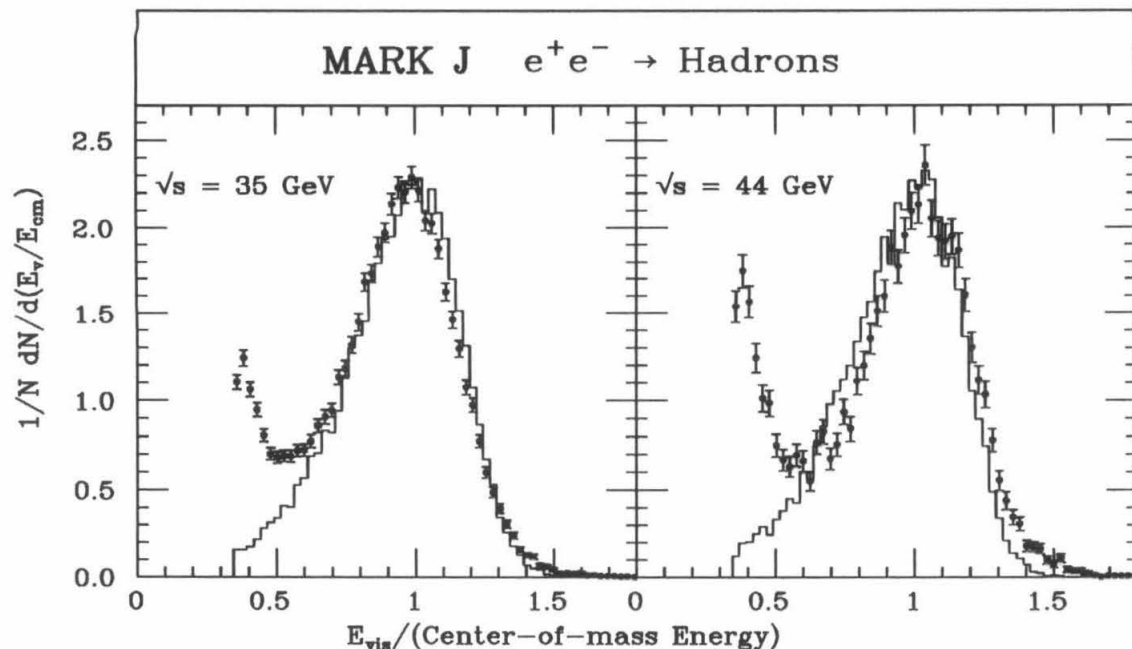


Figure 6.2 The energy fraction seen in the detector at 35 and 44 GeV. The solid histogram is the prediction for the LundV6.3 Monte Carlo and the full detector simulation.

Monte Carlo generated distributions for the processes of Figure 2.12. The rejection of two-photon contamination by the visible energy cut is evident. Tau rejection comes mainly from the cut on the number of reconstructed drift tube tracks in the vertex detector. The mean number of tracks for taus is 2.84 ± 0.96 (r.m.s.) for tau events and 8.70 ± 3.41 (r.m.s.) for hadron events at 35 GeV. The energy balance cut is effective in further removing events for which one of the taus decays leptonically, and the other appears in the detector as hadrons. This is illustrated in Figure 6.6, where the data in the left hand panel are pure hadron Monte Carlo events, while the right hand panel contains pure tau Monte Carlo events.

The acceptance of the detector at the three energies used most in this study is tabulated in Table 6.3. It can be seen that the acceptance determined for the models employing the Caltech-II fragmentation scheme is low. We shall see in later chapters that this fragmentation scheme produces jets that are too narrow, and that this is the reason for the low acceptance obtained with these models. The purity of

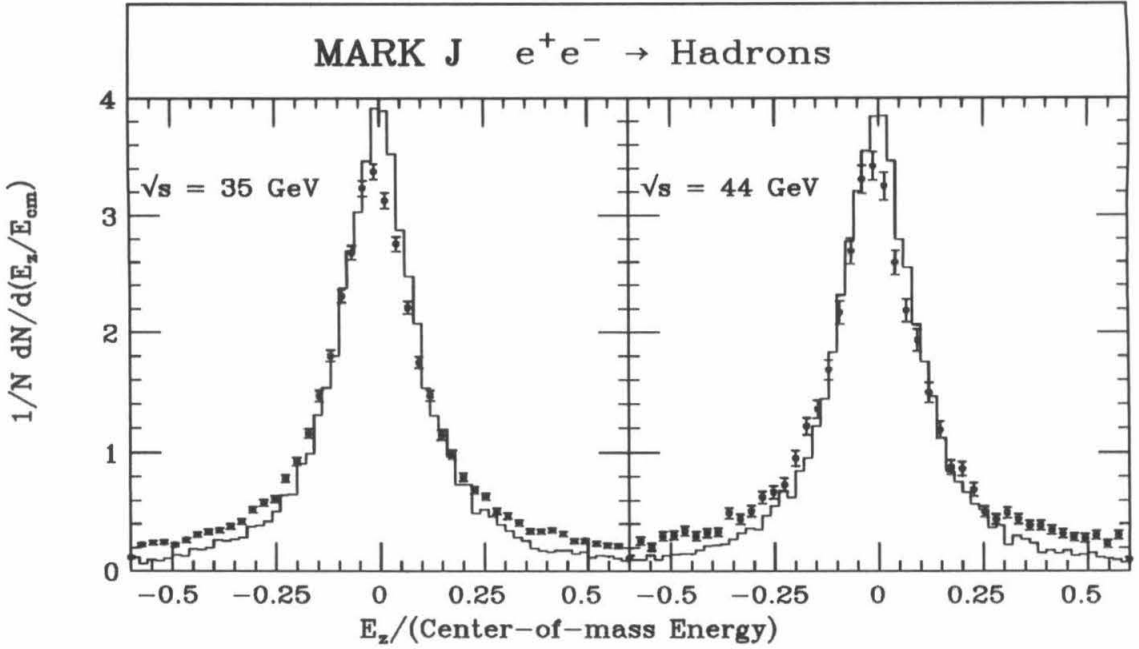


Figure 6.3 The missing z -direction energy fraction seen in the detector at 35 and 44 GeV. The solid histogram is the prediction for the LundV6.3 Monte Carlo and the full detector simulation.

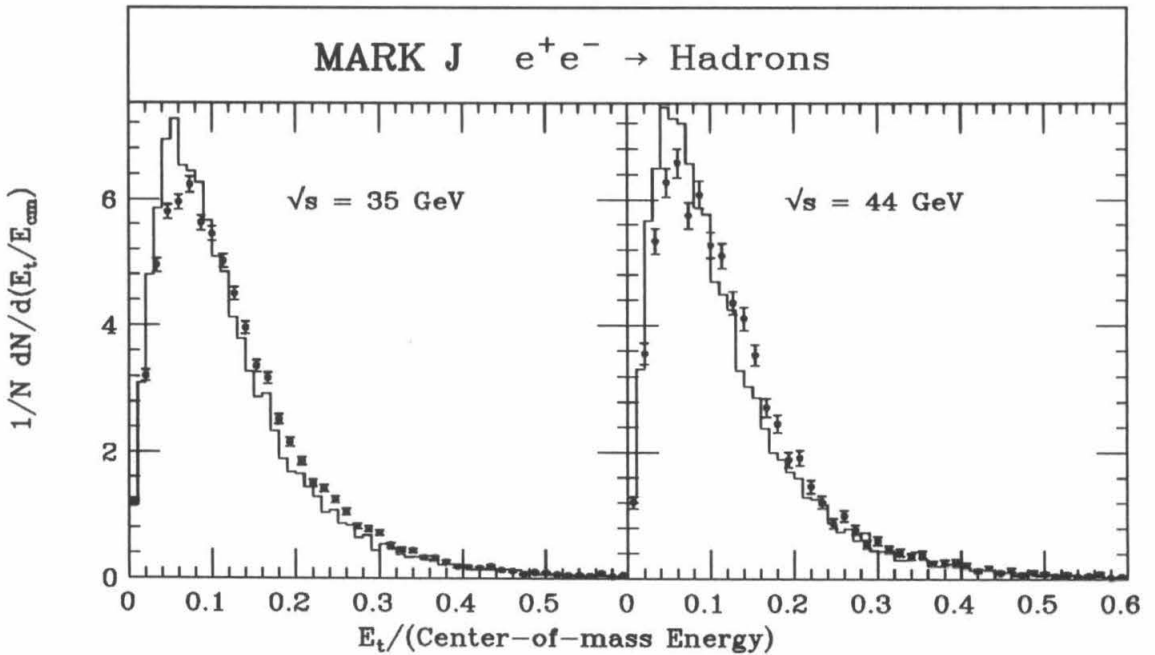


Figure 6.4 The missing transverse energy fraction seen in the detector at 35 and 44 GeV. The solid histogram is the prediction for the LundV6.3 Monte Carlo and the full detector simulation.

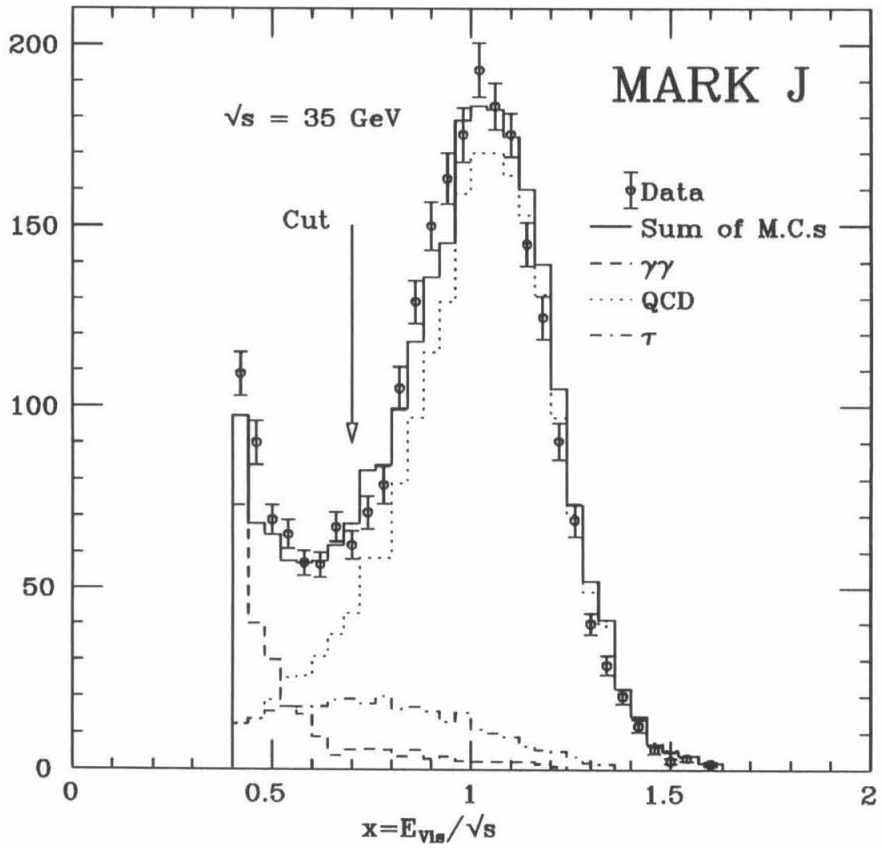


Figure 6.5 The energy fraction seen in the detector at 35 GeV. The solid histogram is the prediction for the Monte Carlo sum from the contributions shown.

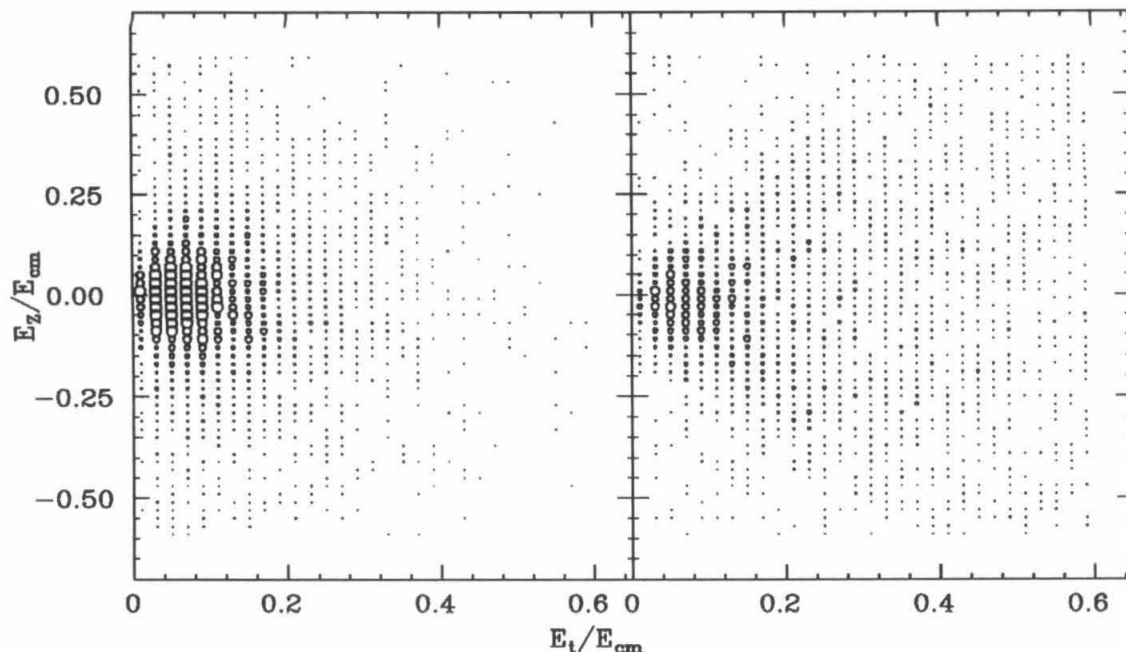


Figure 6.6 The energy imbalance in the detected energy for hadrons (left hand panel) and taus (right hand panel) as determined by Monte Carlo studies at 35 GeV.

the three jet sample used to obtain the flower plots shown in this study can also be estimated with the aid of the detector simulation. It is found that 17% of the total number of three-parton events generated eventually appear in the detector with a broad-side oblateness greater than 0.3, and that of these events, 70% were originally generated with three partons.

$\langle E \rangle$	22 [GeV]	35 [GeV]	44 [GeV]
Ali	73.5	77.4	77.5
LundV43	77.8	79.5	78.0
LundV63	73.3	75.3	75.0
CIT2-FME	63.3	71.4	72.4
CIT2-DLLA	62.6	71.0	72.6

Table 6.3 The detector acceptance (as a percentage) for hadron events determined with the models in this study. The errors on the above numbers are 1% statistical and 2% systematic for each model.

Model	σ_q	a	b	ρ	W_{max}	t_c	α_s	Λ_{LLA}
Ali	Y	—	—	—	—	—	Y	—
LundV4.3	Y	—	—	—	—	—	Y	—
LundV6.3	Y	Y	Y	—	—	—	Y	—
CIT2-FME	—	—	—	Y	Y	—	Y	—
CIT2-LLA	—	—	—	Y	Y	Y	—	Y
CIT2-DLLA	—	—	—	Y	Y	Y	—	Y

Table 6.4 Summary of the parameters in the various models that were tuned to the experimental data for this study. A Y indicates those parameters investigated in this model.

6.2 The Basic Model Parameters

The fragmentation models, described earlier, all involve certain parameters that cannot be predicted from the theory or determined through their relationship to experimentally measured quantities. These parameters must be fixed so that the model predictions agree as closely as possible with the data over the whole center-of-mass energy range available. In general these parameters exist to remedy some deficiency in the model, such as the absence of transverse momentum at the string-break points in the LUND models, or they serve to control the transition from one aspect of the factorization to the next; as such, they contain no physics. In all the models there is, however, a ‘physics’ parameter whose value is of interest. In the case of the models based on the ERT/Ali/Zhu parton generator, for example, the value taken by α_s is of *fundamental* interest. In the case of generators based on the LLA QCD parton showers, the value assigned to Λ_{LLA} is of some interest. It should be noted, however, that this Λ is *not* the $\Lambda_{\overline{MS}}$ which is fundamental in QCD.

The parameters considered as non-fixed in this study for each of the model combinations of Table 4.1 are listed in Table 6.4. Parameters not listed in the table are assumed to have been adequately determined by the model’s authors or by earlier experimental work.

The parameter, σ_q appearing in the Ali and LUND models, is the transverse momentum to be added at each iteration in the fragmentation chain according to Eqn. (4.5). This parameter is conspicuous in its absence from the Caltech fragmentation scheme, and this, together with the absence of a fragmentation function in the model, are considered the main attractions of the Caltech scheme. The fragmentation functions for the Ali and LundV4.3 models are taken to have been adequately determined by earlier work, and only the parameters a and b , occurring in the symmetric fragmentation function of LundV6.3, are considered here. There are two parameters in the Caltech fragmentation scheme that can be considered variable and not totally restricted by low energy data, ρ and W_{max} . ρ has been defined in Eqn. (4.16). It is related to both the string tension and the string-breaking probability, and it can be regarded as the central parameter in the model. The parameter W_{max} determines when the string evolution is terminated and the low-mass cluster decay mechanism starts and is essentially non-physical. The shower termination parameter t_c controls where the transition from the LLA perturbative QCD phase of the model to the start of the string fragmentation should occur.

6.3 Definition of the Shape Variables Used for Parameter Determination

One problem that is encountered when trying to fit model parameters to the MARK J data is that the momenta of individual particles are not measured, and further, neither are the particle multiplicities. As a result, it is necessary to find quantities that can be accurately measured with a calorimeter¹ and that are sensitive to the parameters in the models. For this study a selection of shape variables has

¹The energy deposited by two hits in the same calorimeter element cannot be distinguished from a single hit of the same total energy. Since the sum of two squares is not the same as the square of the sum, distributions of quantities containing energy deposits squared are ambiguous for the MARK J data.

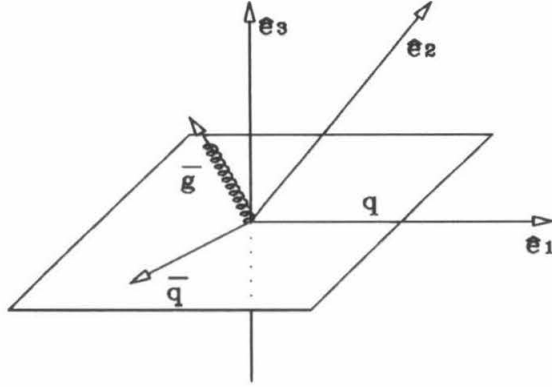


Figure 6.7 The coordinate system with respect to which the event is defined, and which defines the shape variables discussed in the text.

been chosen.

Thrust has been defined earlier in connection with the parton level comparisons of Chapter 5. It is possible to define two more quantities which are complementary to Thrust in describing the event: the Major and Minor [2]. It is also often convenient to describe the event in terms of three coordinate axes related to these variables. These are the Thrust, Major and Minor axes, \hat{e}_1 , \hat{e}_2 and \hat{e}_3 shown in Figure 6.7. The Thrust axis, \hat{e}_1 is first found by requiring that the quantity

$$\sum_i \frac{|\vec{E}_i \cdot \hat{e}_1|}{E_{vis}} \quad (6.1)$$

is maximized. The quantity in Eqn. (6.1), at its maximum, defines the Thrust (T) of the event, and it is the natural generalization of the Thrust described earlier. A vector \hat{e}_2 , perpendicular to the Thrust axis, is now defined, and the energy flow along this axis, which is given by:

$$\sum_i \frac{|\vec{E}_i \cdot \hat{e}_2|}{E_{vis}} \quad (6.2)$$

is maximized by varying the direction of \hat{e}_2 . This defines the Major axis, and, as for Thrust, the value of the expression in Eqn. (6.2) at its maximum defines the ‘Major’ (M) of the event. The Minor axis is then defined as that axis perpendicular to both of the above axes, and the ‘Minor’ (m) of the event is given by:

$$\sum_i \frac{|\vec{E}_i \cdot \hat{e}_3|}{E_{vis}}. \quad (6.3)$$

The Minor is the projected energy flow out of the event plane, where the event plane is defined by the Thrust axis together with the Major axis. The Major axis and Minor axis define a plane that divides the event into the ‘broad’ and ‘narrow’ hemispheres [2]. Once the three variables above have been calculated for an event, the Oblateness (O) can be found through the definition:

$$O = \text{Major} - \text{Minor}. \quad (6.4)$$

The Oblateness measures the flatness of the event, and roughly speaking, it is a measure of the transverse momentum in the event plane minus that out of the event plane:

$$O = \text{Major} - \text{Minor} \simeq (\langle P_T \rangle_{\text{In}} - \langle P_T \rangle_{\text{Out}}) / \langle P \rangle. \quad (6.5)$$

For a three-jet event the broad hemisphere of the event contains the gluon, while the narrow hemisphere contains only the quark, or antiquark. It is thus possible to construct variables that are sensitive to the fragmentation process and relatively insensitive to hard gluon bremsstrahlung effects by re-evaluating the quantities above for hits in the narrow hemisphere of the event only. Such quantities are: the narrow-side Thrust (T_N), Major (M_N) and Minor (m_N), and the narrow-side Oblateness (O_N). In a similar fashion, broad-side variables may be defined, and these are sensitive to the initial direction and energy of the gluon in the event. These variables are labeled with a ‘B’ subscript. In general, it is the perturbative QCD aspects of a given model that determine the prediction for broad-side event shapes, while narrow-

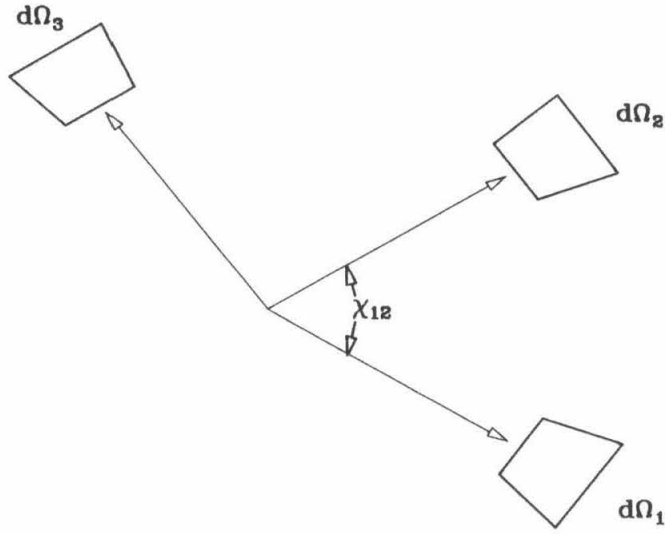


Figure 6.8 The Energy-Energy correlation function is formed by summing all products of energy deposits, into all pairs of calorimeter elements, subtending solid angle $d\Omega$, and separated by an angle χ .

side variables are found to be relatively insensitive to perturbative aspects of the calculation and depend, instead, mostly on fragmentation parameters.

A further variable, that we shall find very useful, is the Energy-Energy Correlation which is defined as follows:

$$\frac{1}{\sigma} \frac{d\Sigma}{d \cos \chi} = \frac{1}{N} \sum_{event} \sum_{i,j} \frac{E_i \cdot E_j}{E_{vis}^2} \delta(\cos \chi_{ij} - \cos \chi). \quad (6.6)$$

Referring to Figure 6.8, this variable can be viewed as the energy weighted sum over pairs of calorimeter hits whose relative angle lies in the range χ to $\chi + \Delta\chi$. The first summation in Eqn. (6.6) is over all the events in the data sample, while the second is over *all* pairs of calorimeter hits and includes the self-correlations. The Energy-Energy Correlation is histogrammed in bins of $\cos(\chi)$, so that a perfect two-jet event will give a contribution at +1 and -1, and the contributions near $\cos(\chi)=0$ come from events having a three-jet structure.

The Energy-Energy Correlation is sensitive to both the fragmentation and the

QCD sensitive aspects of the event topologies. On the other hand the *asymmetry* in the Energy-Energy Correlation,

$$\Sigma_A(\cos \chi) = \frac{1}{\sigma} \left[\frac{d\Sigma}{d \cos \chi}(\pi - \chi) - \frac{d\Sigma}{d \cos \chi}(\chi) \right], \quad (6.7)$$

is sensitive to the hard gluon bremsstrahlung, while being insensitive to the details of the fragmentation process, which are symmetric.

6.4 The Approach to the Fitting Problem

There are two possible strategies that can be followed when tuning Monte Carlo parameters. In one the data is corrected and the Monte Carlo is fitted to the corrected data, while in the other the Monte Carlo predictions are fed through the detector simulation, as described above, and the comparison is made directly with the data. The advantage of the first approach is that it is very fast. The weeks, or months, of computer time and many large disk and tape data sets that are typically required for a series of full detector simulation runs can be saved.

However, the savings in computer time that can be obtained by adopting the first approach, are achieved at a high cost. First, the correction factors to be applied to the data must be obtained from a Monte Carlo simulation program, and so, are dependent on the particular Monte Carlo used. Second, the corrections are, typically, applied on a bin-by-bin basis to the data, and so, do not take into account possible bin-to-bin correlations that may be large. Third, the correction factors themselves may be dependent on the parameters that one is interested in fitting.

It might be argued that correction factors could be found for each Monte Carlo to be tuned and that, provided these correction factors were not used for correcting data for comparison to another Monte Carlo, consistent results would emerge. While this may be the case for data based on information from tracking chambers, it is not the case for data originating in a calorimeter, and when there is an interest

in the soft particle characteristics, such an approach is inappropriate. Because of these problems, the second option above is used in this study, and the Monte Carlo predictions *after* the complete detector simulation are compared directly to the data. The cuts used in the data selection are that 70% of the available center-of-mass energy is visible in the detector and that the energy is balanced to within 50% of the visible energy. The Monte Carlo data and actual data were treated identically.

6.5 Tuning the Ali Model Parameters

For the purposes of this study, the only parameter considered not previously fixed in the Ali model is the transverse momentum parameter, σ_q . Unfortunately, the normal procedure for fitting σ_q , i.e., fitting to the squared transverse momentum in the events, cannot be used with the MARK J data because the MARK J is a calorimeter. The narrow-side shape variables defined above are, however, expected to be sensitive to the transverse momenta in the quark-jet and involve quantities linear in the energy deposits; they are, therefore, suitable for determining σ_q . The value of σ_q required to best fit the data is found to be strongly correlated to the value of α_s used at the perturbative QCD phase of the event generation, and it is, therefore, essential that both parameters be allowed to vary during the fitting.

At a center-of-mass energy of 35 GeV, between 5 and 20×10^3 Monte Carlo events were generated, with σ_q between 200 and 350 MeV, in 25 MeV intervals. The Monte Carlo predictions for the total, narrow-side and broad-side, Thrust, Oblateness, Major, Minor and Energy-Energy Correlation distributions were then calculated for ten α_s values, spaced evenly, between 0.10 and 0.20. For each of the distributions, the Monte Carlo prediction was compared to that obtained for the data, the χ^2 calculated and this χ^2 tabulated against σ_q and α_s . The χ^2 minima for each table, at constant σ_q , was then found by interpolating between the tabulated χ^2 values. The χ^2 minima contours thus obtained for six of the distributions are shown

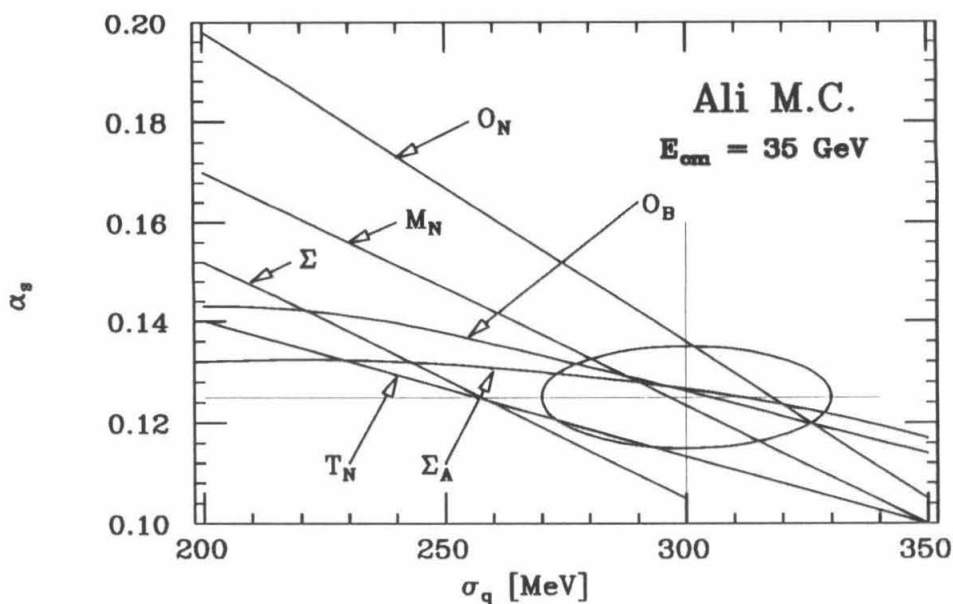


Figure 6.9 The results obtained by a simultaneous fit to the data in the strong coupling constant and σ_q for the Ali model. The ellipse indicates the limits on the preferred values for the parameters

in Figure 6.9. The distributions with the smallest χ^2 s were then visually compared to the data and limits on the parameter values determined; these are shown as an ellipse in the figure. The variables shown are: narrow-side Thrust T_N , narrow-side Oblateness O_N , narrow-side Major M_N , the broad-side Oblateness O_B , the Energy-Energy Correlation Σ , and its asymmetry Σ_A . The correlation between α_s and σ_q is apparent from the figure, and the correlation can be seen to be strongest for variables defined on the narrow-side of the events. The dependence of α_s on σ_q is least for Σ_A . As a check of this approach, visual comparisons of the model predictions against the data were made in the distributions.

The Monte Carlo predictions for the narrow-side Thrust and Oblateness, for $\alpha_s = 0.12$, are shown in Figure 6.10 for three values of the σ_q parameter, including the preferred value. The extreme tails of the distributions are not shown, since the statistical significance of the bin contents in these regions is minimal. It can be seen that a value for σ_q of 300 MeV is satisfactory for fitting both of the distributions

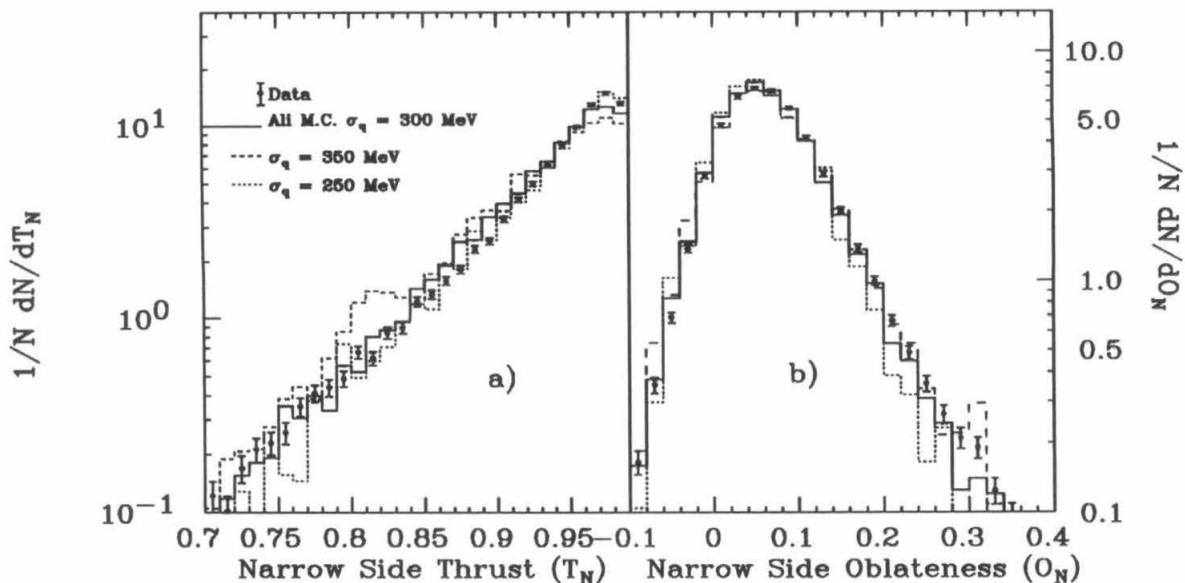


Figure 6.10 The Ali model prediction for, a) the narrow-side Thrust and, b) the narrow-side Oblateness, for the values of σ_q indicated in the left-hand panel.

shown.

6.6 Tuning the LUND Model Parameters

6.6.1 The Transverse Momentum Parameter in LundV4.3

The procedure followed above for the Ali model was repeated for the LundV4.3 model with a comparable number of events generated at σ_q values: 300, 400, 500, 600, 700, 800 and 900 MeV. The results are presented in Figure 6.11. By convention the transverse momentum parameter in the LUND models is equivalent to $\sqrt{2} \times \sigma_q^{actual}$, where σ_q^{actual} is the real width of the Gaussian used to generate the transverse momentum².

The preferred value of σ_q , shown in Figure 6.11, is 650 MeV, which corresponds to an actual σ_q of 460 MeV. The value previously used in the MARK J analysis was

²Readers attempting to compare the σ_q values here to those for the Ali model should recall the discussion of Chapter 4 concerning the truncation of the Gaussian P_t distribution in string models.

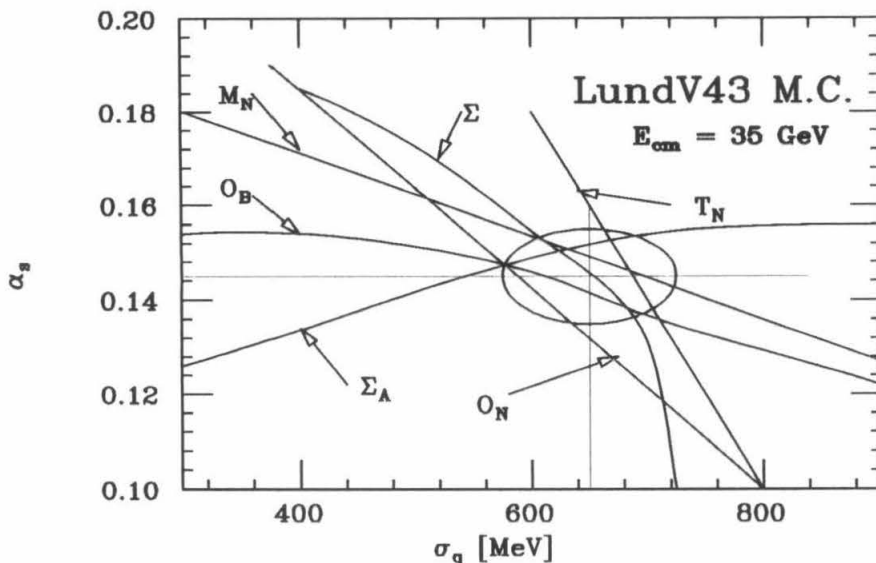


Figure 6.11 The results obtained by a simultaneous fit to the data in the strong coupling constant and σ_q for the LundV4.3 model. The ellipse indicates the limits on the preferred parameter values

700 MeV (corresponding to 495 MeV) and had been determined principally from the narrow-side Thrust data. The results of this study, while favoring a slightly lower value for σ_q , are consistent with the earlier determination. Since a very large number of Monte Carlo events had previously been generated at $\sigma_q = 700$ MeV, this is taken as the standard value.

The model predictions for two values of σ_q on either side of the standard value, together with the standard value, are compared to the data in Figure 6.12, for $\alpha_s = 0.15$.

From the figure it can be seen that the agreement between the model predictions and the data is generally good, and that σ_q is well determined to within ± 50 MeV.

6.6.2 Tuning the Parameters in LundV6.3

We have already mentioned that the LundV6.3 fragmentation scheme differs from the LundV4.3 scheme in having a symmetric fragmentation function of the

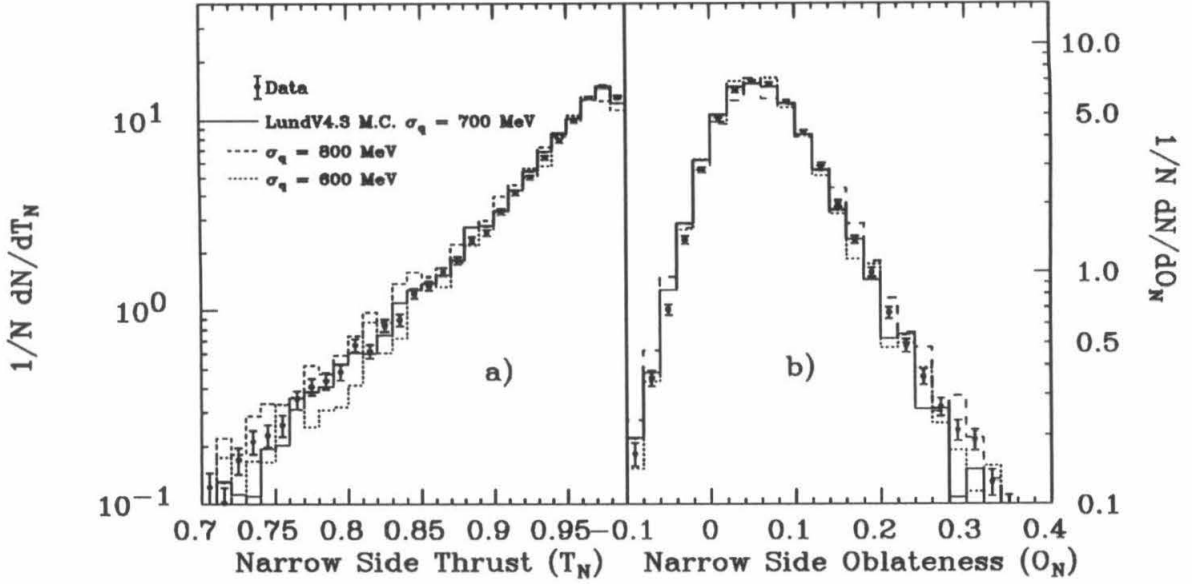


Figure 6.12 The LundV4.3 model prediction for, a) the narrow-side Thrust and, b) the narrow-side Oblateness, for the values of σ_q indicated in the left-hand panel.

form:

$$f(z) = \frac{1}{z}(1-z)^a \exp\left(\frac{-bM_T^2}{z}\right). \quad (6.8)$$

For very soft particles, when $z \rightarrow 0$, this function is regulated by the presence of the term $1/z \exp(-bM_T^2/z)$ and peaks at $z = bM_T^2$. For hard particles, when $z \rightarrow 1$, it is regulated by the factor $(1-z)^a$. The values of a and b which give a particular $f(z)$ are not unique; the fragmentation function with $a = 0.4$ and $b = 0.7$ used by the Mark II collaboration is very similar to that used by the TASSO collaboration where $a = 0.5$ and $b = 0.9$. To tune the fragmentation function it is adequate to choose a value for either a or b , and then vary the other parameter. The form of the function for a fixed value of $a = 1$ as b varies is shown in Figure 6.13 for a value of $M_T = 500$ MeV.

The optimum values for the fragmentation function parameters are also correlated with the value chosen for σ_q . Since a fit to three parameters is extremely time

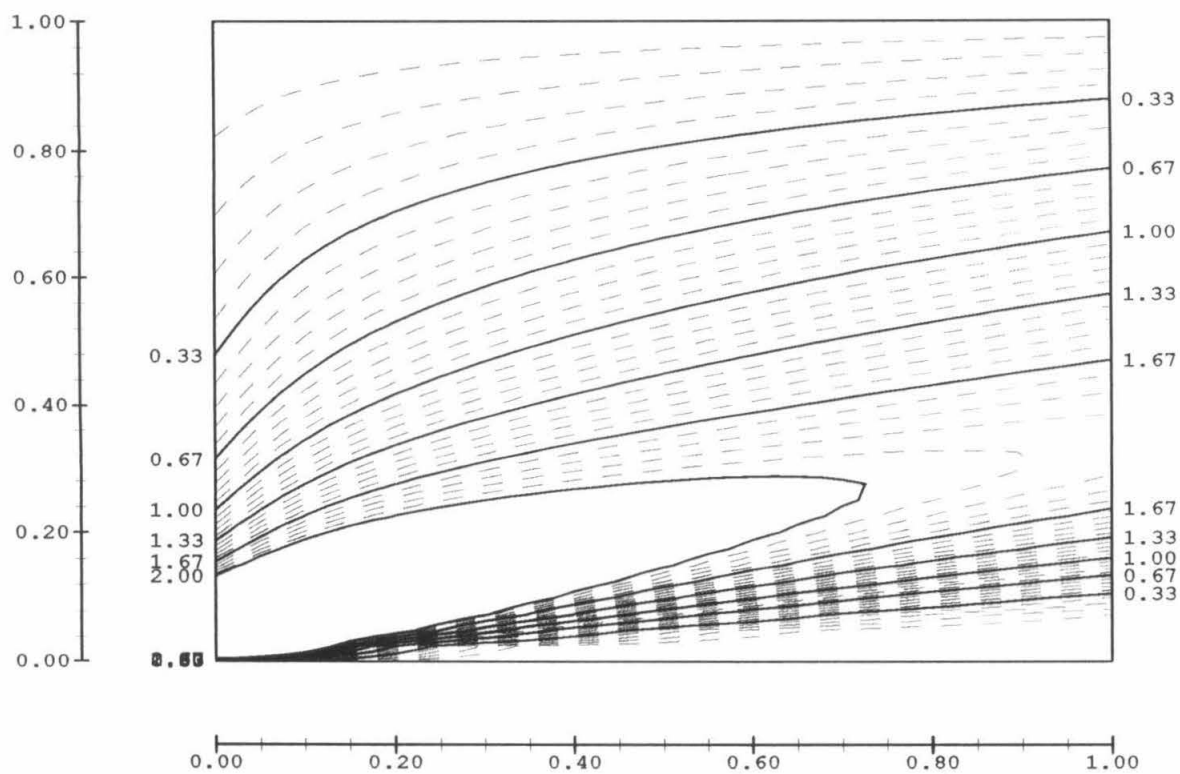


Figure 6.13 The variation in the form of the Lund symmetric fragmentation function as b varies with a held fixed and equal to 1.0. The contours indicate the points of constant magnitude for the fragmentation function. The vertical scale is the z scale, while b increases horizontally.

consuming, a preliminary fit at the raw-track level was first performed. Normally, the fragmentation function parameters are fitted by looking at the longitudinal momentum fractions of the particles; however, this is not possible when there is no distinction made between single particle hits and multi-particle hits.

It might be hoped that the Thrust distribution would be sensitive to the fragmentation function; however, this is not the case. As the fragmentation function becomes harder (peaks more in the high- z region), the number of particles having a large longitudinal momentum with respect to the Thrust axis increases, but this is at the cost of the contribution to the Thrust from a large number of soft particles. This will not be the case for a variable similar to Thrust, but in which the axis with respect to which the longitudinal momenta are referred to, is determined by maximizing the square of the longitudinal momenta. Such an axis is called the Sphericity axis and is defined as \hat{e} such that

$$\frac{\sum_i |\vec{p}_i \cdot \hat{e}|^2}{\sum_i |\vec{p}_i|^2} \quad (6.9)$$

is a maximum. As the fragmentation function changes the Thrust axis will move. For a hard fragmentation function the axis will be more aligned with the initial quark direction than for a soft fragmentation function, and this effect will be more pronounced for the Sphericity axis. The effect of the transverse momentum parameter, and of changes in the fragmentation function, can be investigated at the same time by looking at the transverse momenta with respect to the Sphericity and Thrust axes. In Figure 6.14 the mean momenta transverse to the Thrust and Sphericity axes are shown for various values of σ_q . The data shown in this plot are derived at the raw-track level, and the results for the Ali and LundV4.3 Monte Carlos are also shown. Figure 6.14 shows that, at the raw-track level, the LundV6.3 fragmentation scheme makes similar predictions to the Ali and LundV4.3 schemes when σ_q is near 500 MeV, $a = 0.9$ and $b = 0.5$.

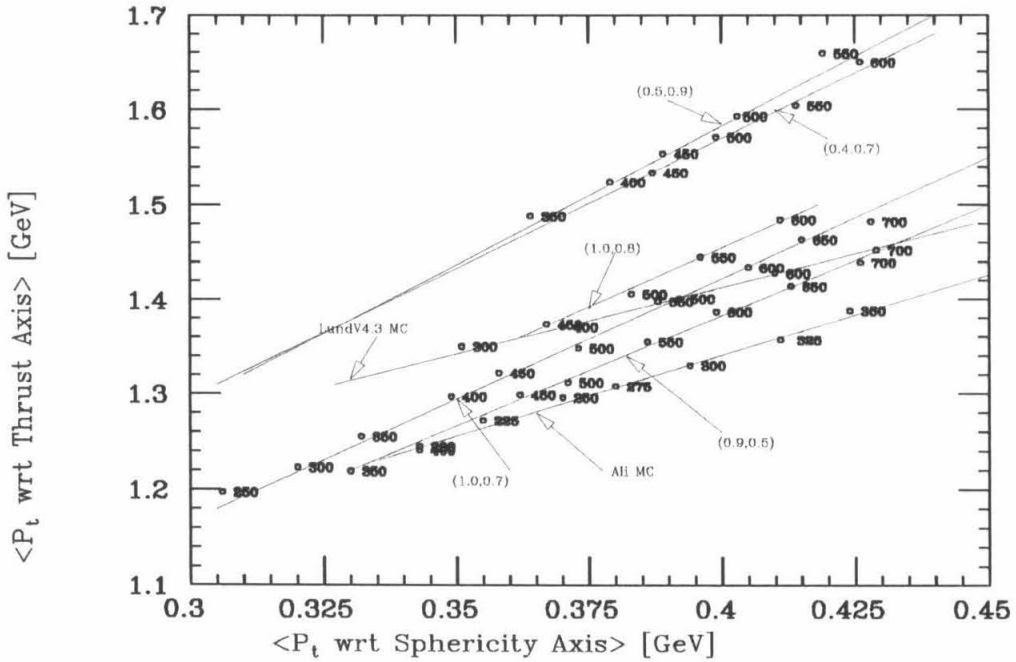


Figure 6.14 The mean values for the transverse momenta with respect to the Thrust and Sphericity axes for various fragmentation functions and σ_q values, obtained at the raw-track level with the LundV6.3 fragmentation scheme and ERT/Ali/zhu Partons. The numbers next to the data points indicate the σ_q with which the data was generated, and the LundV6.3 data are labeled with the notation (a,b) .

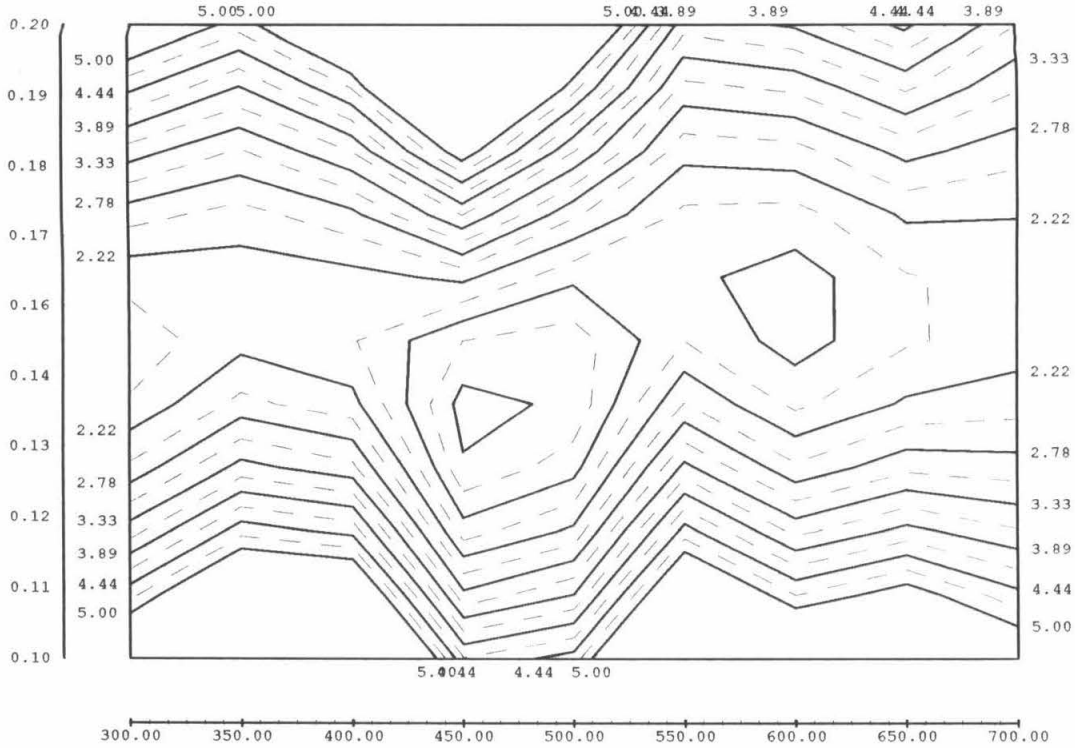


Figure 6.15 The χ^2 contours obtained by comparing the LundV6.3 model predictions for Σ_A to the data. The fragmentation function used to generate the model predictions used here was $a = 1.0$ $b = 0.7$. The left-hand scale is for α_s , while the horizontal scale is for σ_q .

Based on the results of the preliminary fit, events were generated with the fragmentation functions: $a = 0.9$ $b = 0.5$, $a = 1.0$ $b = 0.7$ and $a = 1.0$ $b = 0.8$, for several values of σ_q , and compared directly to the data after being processed through the detector simulation. The data sets with $a = 1.0$ and $b = 0.7$ were generated with σ_q values between 300 and 700 MeV at 100 MeV intervals. The χ^2 contours obtained by comparing the prediction for the Energy-Energy Correlation Asymmetry obtained with this fragmentation function against the data are shown in Figure 6.15. It can be seen that the χ^2 minima occurring at fixed values of σ_q follow lines similar to those obtained for the LundV4.3 and Ali models. When the minimum χ^2 lines, for several shape variables, are plotted, however, the intersection of the majority of the minima is at large σ_q , where the absolute values of the χ^2 s are large. Rather than follow the approach that was used for the Ali and LundV4.3 models then, we choose

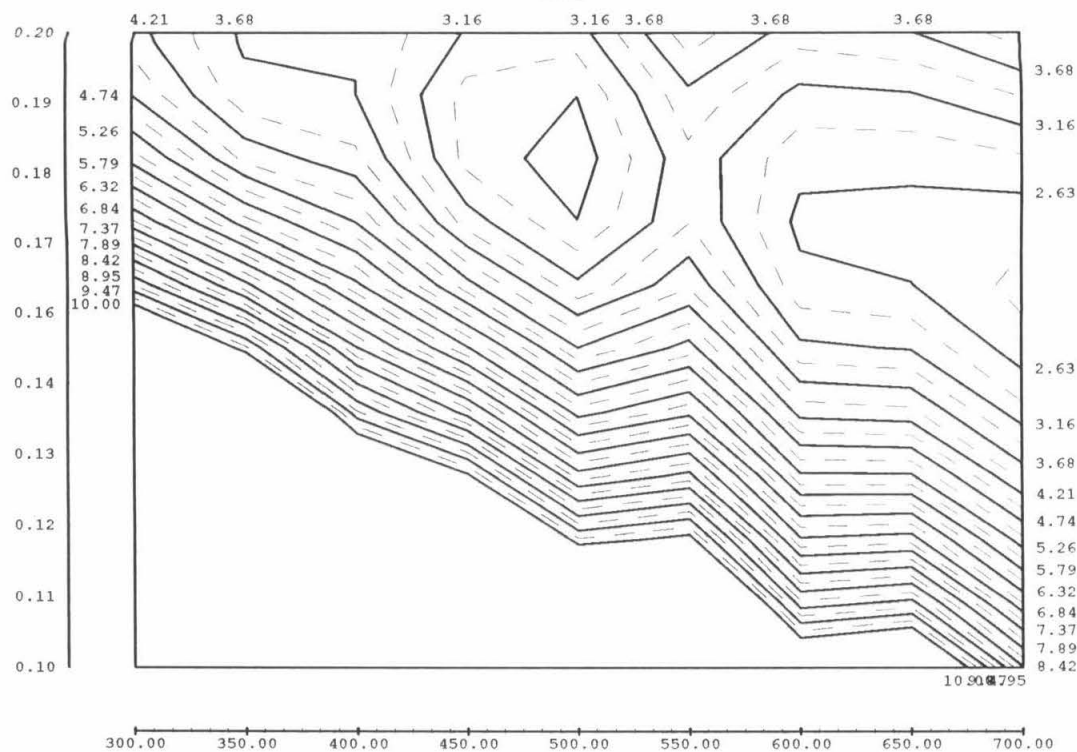


Figure 6.16 The χ^2 contours obtained by comparing the LundV6.3 model predictions for T_N to the data. The fragmentation function used to generate the model predictions used here was $a=1.0$ $b=0.7$. The left-hand scale is for α_s , while the horizontal scale is for σ_q .

to examine the contour plots, obtained as above for the Energy-Energy Correlation Asymmetry, for all the variables considered. This shows that the χ^2 minimum seen in Figure 6.15 at $\sigma_q=450$ MeV and $\alpha_s=0.135$ is a general feature for all the variables, and that the best, overall, value for σ_q is 500 MeV. The push to higher σ_q comes mostly from variables defined on the narrow side of the event, as an example, the χ^2 contours for the narrow-side Thrust are shown in Figure 6.16.

Having settled on a value of σ_q of 500 MeV for the fragmentation function with $a=1.0$ and $b=0.7$, data sets for the neighboring fragmentation functions (in the sense of neighboring in Figure 6.14) were generated. The σ_q values were: 450, 500, 550 and 600 MeV in the case of the function $a=1.0$ $b=0.8$, and: 500, 550, 600 and 650 MeV, for $a=0.9$ $b=0.5$. The optimum values for σ_q obtained with the new data sets were found to be slightly higher than for the data generated with $a=1.0$

and $b = 0.7$, namely 550 MeV for both. The χ^2 for each of the new data sets were, however, higher than for the original data set in the majority of the variables being considered. We conclude that the parameters for the fragmentation function arrived at in the preliminary fit are the optimum, and that the correct value of σ_q for the LundV6.3 model is 500 MeV, with $a = 1.0$ and $b = 0.7$ in the fragmentation function.

6.7 Tuning the Caltech Model Parameters

In this study the Caltech-II fragmentation scheme is used together with a LLA parton generator and also with the ERT/Ali/Zhu parton generator. The two combinations must, unfortunately, be regarded as separate models and the fragmentation parameters determined separately for each combination. The presence of many partons in the final state of the LLA shower dictates that there will be many small string fragments being passed to the fragmentation scheme when the LLA partons are used. In the case of the ERT/Ali/Zhu + Caltech-II combination, there are at most two strings at the start of the fragmentation, and it is unreasonable to hope that the same fragmentation parameters can equally serve both model combinations.

6.7.1 The Parameters of CIT2-FME

The Caltech fragmentation scheme has no artificial addition of transverse momentum. In this scheme *all* the transverse momentum comes from the decay of the low mass clusters, which tends to be isotropic in their rest frames. Consequently, the parameter that determines when the clusters should stop being evolved and decay and which controls the generation of transverse momentum in the model is W_{max} . The second parameter in the Caltech-II fragmentation scheme is ρ , which controls the dynamics of the string evolution. In actual fact, early raw-track studies showed that the generation of transverse momentum is more dependent on ρ than on W_{max} , and that the model predictions are relatively insensitive to the value of W_{max} .

To understand how this comes about, it must be realized that ρ acts as a decay constant for the invariant area swept out by the strings before they break. In fact, the probability of invariant area A being swept out by a string prior to a break is $e^{-\rho A}$, so that, the ‘area half-life’ is $\rho^{-1} \ln 2$. A small value for ρ implies that the string evolves for a long time and that, when it breaks, produces long daughter string pieces that correspond to massive clusters. Since these massive daughters decay isotropically, their decay introduces transverse momentum into their decay products that survives the boost of the products back into the lab frame. In the case of large ρ , the strings break at early stages in their evolution and the length of string available for breaking-off daughters is restricted, so that, low-mass high-velocity daughters result. The transverse momentum resulting from the decay of a low-mass high-velocity cluster does not survive the boost back into the lab frame, and so the transverse momentum for the large- ρ case is limited.

Since both W_{max} and ρ are expected to govern the generation of transverse momentum, and since both of these parameters are expected to be correlated to α_s , the simple techniques used in tuning the Ali and LundV4.3 models are not applicable here. Instead, the methods used for tuning the LundV6.3 model are adopted. First, at some fixed W_{max} , the ρ parameter is determined by allowing it to vary together with α_s . Next, W_{max} is allowed to vary while ρ is kept close to the optimized value found before.

The default value of ρ given by the model’s authors is 1.6 GeV. However, this is for the full Caltech-II model which uses LLA partons. An early raw-track sweep through ρ indicated that a much lower ρ value is required when partons from the Ert/Ali/Zhu parton generator are used. This point is discussed in detail in the next chapter.

Five thousand events were generated, with $W_{max}=2.2$ GeV, ρ values from 0.2 to 0.9 in steps of 0.1, and for α_s values ranging from 0.1 to 0.2 in steps of 0.01. These

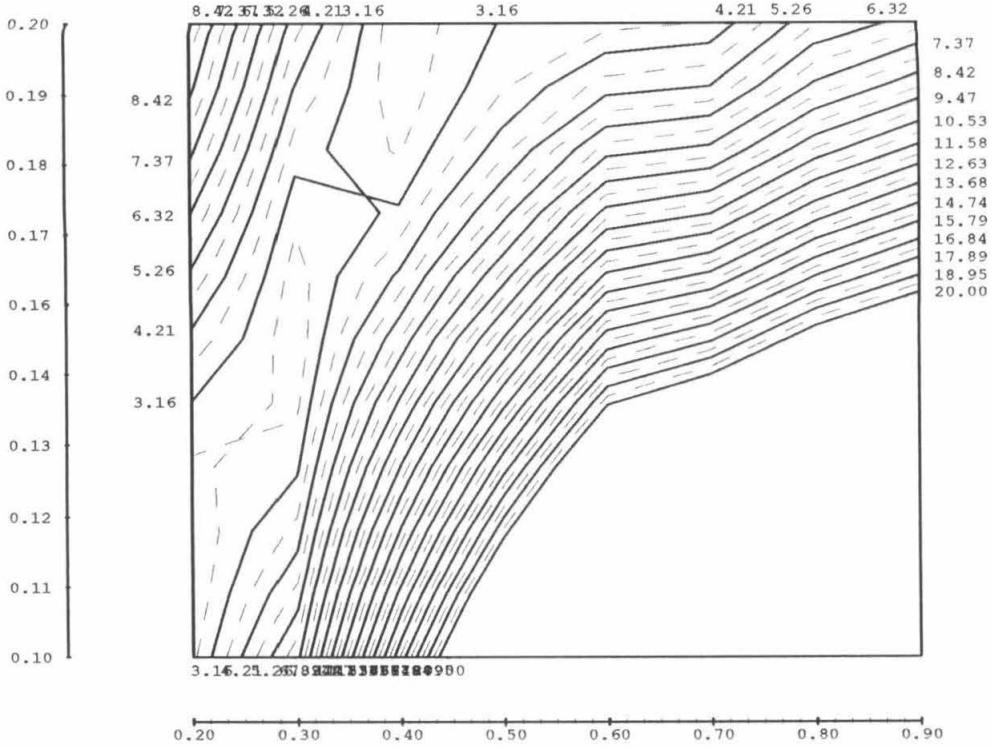


Figure 6.17 The χ^2 contours obtained by comparing the CIT2-FME model predictions for the narrow-side Thrust to the data. The value taken for W_{max} in calculating the model predictions used here was 2.2 GeV. The left-hand scale is for α_s , while the horizontal scale is for ρ .

data sets were then compared against the data, and χ^2 values were obtained. The χ^2 s obtained when comparing the model predictions to the data for the narrow-side Thrust are shown in Figure 6.17. From the figure it can be seen that the correlations existing between ρ and α_s are of the same form as those found between σ_q and α_s before, showing that ρ is closely related to the generation of transverse momentum in the model. The allowed values of ρ follow a band in the α_s - ρ plane, and this band is found to be similar for all the shape variables defined on the narrow side of the events. In Figure 6.18 the χ^2 contours obtained by comparing the model predictions for the broad-side Thrust against the data are shown. It can be seen that the contours for broad-side variables, taken together with those obtained for narrow-side variables, are sufficient to restrict ρ to a relatively small range around $\rho = 0.3$. This is consistent with the results of the raw-track study.

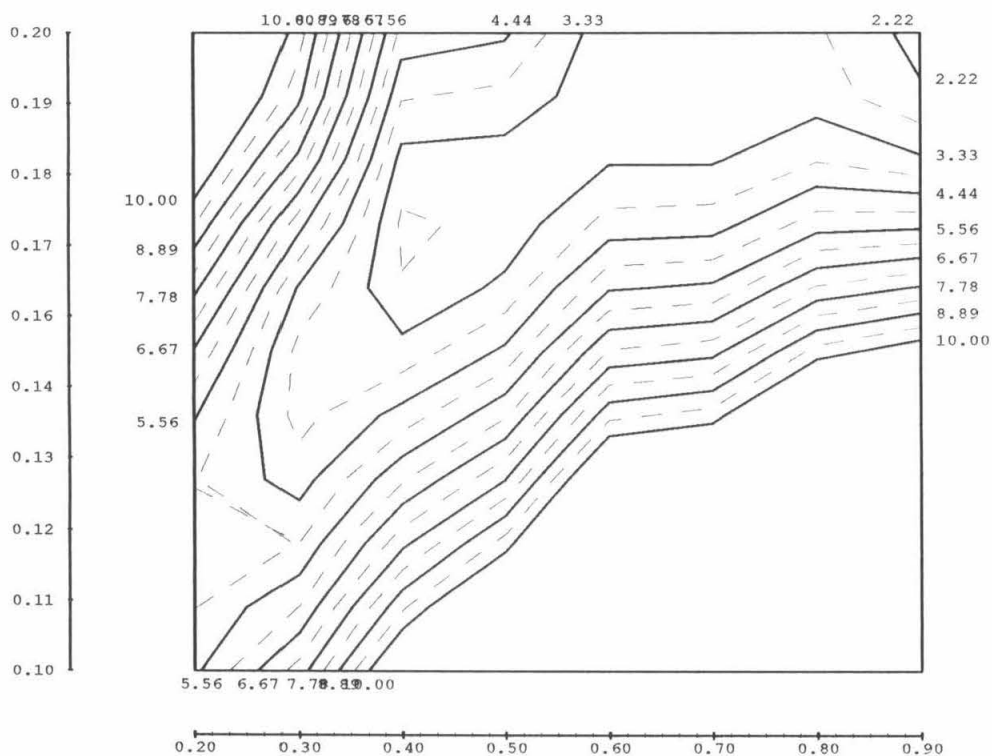


Figure 6.18 The χ^2 contours obtained by comparing the CIT2-FME model predictions for broad-side Thrust to the data. The W_{max} value used for calculating the model predictions used here was 2.2 GeV. The left-hand scale is for α_s , while the horizontal scale is for ρ .

Having fixed ρ at 0.3 for the case $W_{max}=2.2$ GeV, events were generated with $W_{max}=2.6, 2.8, 3.2$ and 3.6 GeV for ρ values between 0.2 and 0.5. Smaller values of W_{max} were excluded because a visual inspection of the distributions obtained with $W_{max}=2.2$ showed that the model predictions were lacking in transverse momentum. The changes in the model predictions, that resulted when W_{max} was increased, were mild, in agreement with what was encountered in the raw-track study, and it was not until W_{max} was above 3 GeV that the changes became clear. W_{max} was not increased beyond 3.6 GeV, since above this value it is not clear that the parameterization used for the low-mass cluster decays is reliable. While for some variables increasing W_{max} improved the agreement with the data, the overall agreement between the model predictions and the data became worse. In particular, it became difficult to find values for ρ that gave reasonable agreement for both broad-side and narrow-side variables. After a visual inspection of the various distributions, it was decided to adopt $W_{max}=2.2$ GeV and $\rho=0.3$ as the final optimized values to be used in this study.

6.7.2 The Parameters of CIT2-DLLA

The Fragmentation Parameters

The particular implementation of the ERT/Ali/Zhu calculation in the parton generator used for this study incorporates a mixing scheme, whereby data generated at fixed α_s can be mixed to provide a prediction for any desired α_s ³. This has the advantage that predictions for many values of α_s can be obtained without the need for a fresh run through the detector simulation program for each new α_s examined. Unfortunately, it is not possible to do the same for the various values of Λ_{LLA} that must be examined when investigating the correlations between Λ_{LLA} and ρ for the

³Partons belonging to each class, 2-parton, 3-parton, 4-parton soft, etc. are generated at a fixed value of α_s . The full second order weights for the events are later used to ‘mix’ the events as if they had been generated at any desired α_s .

ρ	T_B	T_N	Maj_B	Maj_N	Min_B	Min_N	O_B	O_N
0.2	0.862	0.927	0.320	0.212	0.173	0.133	0.154	0.079
0.3	0.871	0.933	0.310	0.201	0.167	0.127	0.149	0.074
0.4	0.877	0.938	0.301	0.195	0.160	0.122	0.148	0.073
0.5	0.881	0.942	0.296	0.187	0.154	0.117	0.151	0.070
0.6	0.885	0.941	0.286	0.191	0.151	0.117	0.143	0.074
0.7	0.884	0.944	0.290	0.187	0.148	0.115	0.150	0.071
0.8	0.887	0.945	0.287	0.182	0.149	0.113	0.147	0.070
1.0	0.887	0.945	0.287	0.182	0.149	0.113	0.147	0.070
Data	0.874	0.940	0.298	0.188	0.149	0.114	0.159	0.074

Table 6.5 Table of the means of several variables, as predicted by the CIT2-DLLA model combination. The errors on the values quoted for the data are $\pm 0.6\%$, while for the Monte Carlo data they are $\pm 1.8\%$.

model combination CIT2-DLLA. In order to limit the amount of computer time that would be required to tune this model combination, a raw-track study was performed first, and the CIT2-DLLA combination was compared to the various models already tuned. The value of the shower termination parameter was fixed at 1 GeV^2 at this stage; this value was low enough that the model predictions were insensitive to variations in t_c .

On the basis of the raw-track study, a nominal value for Λ_{LLA} of 600 MeV was taken, and a sweep through ρ was made. In Table 6.5 the predicted mean values of some of the distributions considered are given, together with values for the data. From the values listed in the table, it can be seen that the sensitivity of the means of the distributions to variation in the value of ρ is small, but that there is a (mild) tendency for Thrust type variables to favor smaller values of ρ than the remainder of the variables. In Figure 6.19 the variation in the χ^2 s for the variables is shown; here the difference between the Thrust and the remaining variables is very clear. The best compromise value for ρ can be read-off from Figure 6.19 as 0.6. Having obtained this value for ρ , W_{max} was varied to check the stability of the fit for ρ against variation in W_{max} . As before, it was found that the results are fairly stable

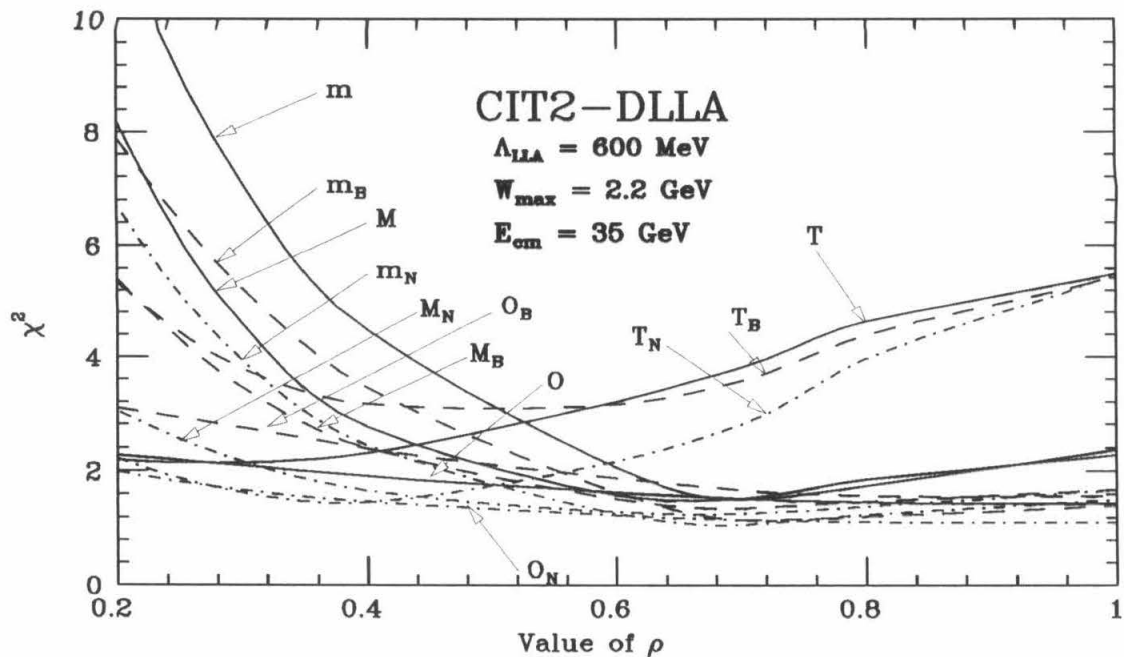


Figure 6.19 The χ^2 s obtained when comparing the predictions of CIT2-DLLA to the data. The parameters used are indicated on the Figure. The curves for narrow-side variables are shown with a dot-dash line, broad-side variables with a dashed line, and variables defined on the whole event are shown with a solid line

against variation in the value of W_{max} , and in particular, the prediction for Thrust cannot be made to agree with the data for any combination of ρ and W_{max} . We adopt the values $\rho = 0.6$ and $W_{max} = 2.2$ GeV as the defaults for the CIT2-DLLA model combination.

The Parameters Controlling the LLA Shower

The remaining free parameter in the CIT2-DLLA model combination to fix is the LLA strong coupling scale parameter, Λ_{LLA} . This variable determines the perturbative-QCD inspired behaviour of the parton final state from the LLA shower by determining the probability for gluon bremsstrahlung as the shower evolves. A large value of this parameter will enhance the amount of radiation at early, high Q^2 times and tend to increase the number of hard three-jet events that survive the fragmentation.

Λ_{LLA}	$\int_{-.72}^{0.0} \Sigma_A d \cos \chi$	$\int_{0.5}^{0.8} T dT$	$\int_{0.3}^{\infty} O_B dO_B$
0.4	0.0201 ± 0.0007	0.0984 ± 0.0052	0.1078 ± 0.0055
0.6	0.0214 ± 0.0008	0.1092 ± 0.0056	0.1095 ± 0.0056
0.8	0.0231 ± 0.0008	0.1230 ± 0.0065	0.1079 ± 0.0061
Data	0.0234 ± 0.0003	0.1238 ± 0.0023	0.1313 ± 0.0024

Table 6.6 The variation of the hard-QCD sensitive variables with Λ_{LLA} . ρ is kept at 0.6 and W_{max} at 2.2 GeV. The choice, $\Lambda_{LLA} = 0.8$, is indicated.

It has already been seen (but not remarked upon until now) that the Energy-Energy Correlation Asymmetry is relatively insensitive to the values of the fragmentation parameters, while sensitive to the hard-QCD based structure of the events. This can be seen in Figure 6.9 and 6.11, where Σ_A remains roughly constant as σ_q is varied. The mild fragmentation dependence in Σ_A can be almost completely eliminated by considering the integral of the distribution in this variable for regions where $\cos \chi$ is larger than -0.72, so that the two-jet, fragmentation sensitive region is excluded. It is also possible to identify the integrated Thrust distribution, below Thrust values of 0.8, and the integrated broad-side Oblateness, above Oblateness of 0.3, as being sensitive to hard-QCD processes and relatively insensitive to the fragmentation details.

Bearing in mind that there is a mild dependence in the above variables on the transverse momentum parameters of the Lund and Ali models, we first examine their sensitivity to variation in the value of ρ . The results of this investigation are shown in Figure 6.20. The figure indicates that for values of ρ above 0.6 the sensitivity of hard-QCD dependent quantities to variation in the fragmentation is minimal. However, the amount of hard bremsstrahlung from the early stages of the LLA shower is too low with this choice of Λ_{LLA} .

While holding ρ and W_{max} constant, Λ_{LLA} was varied. The effect of this variation on the variables being considered is shown in Table 6.6. These data show that the

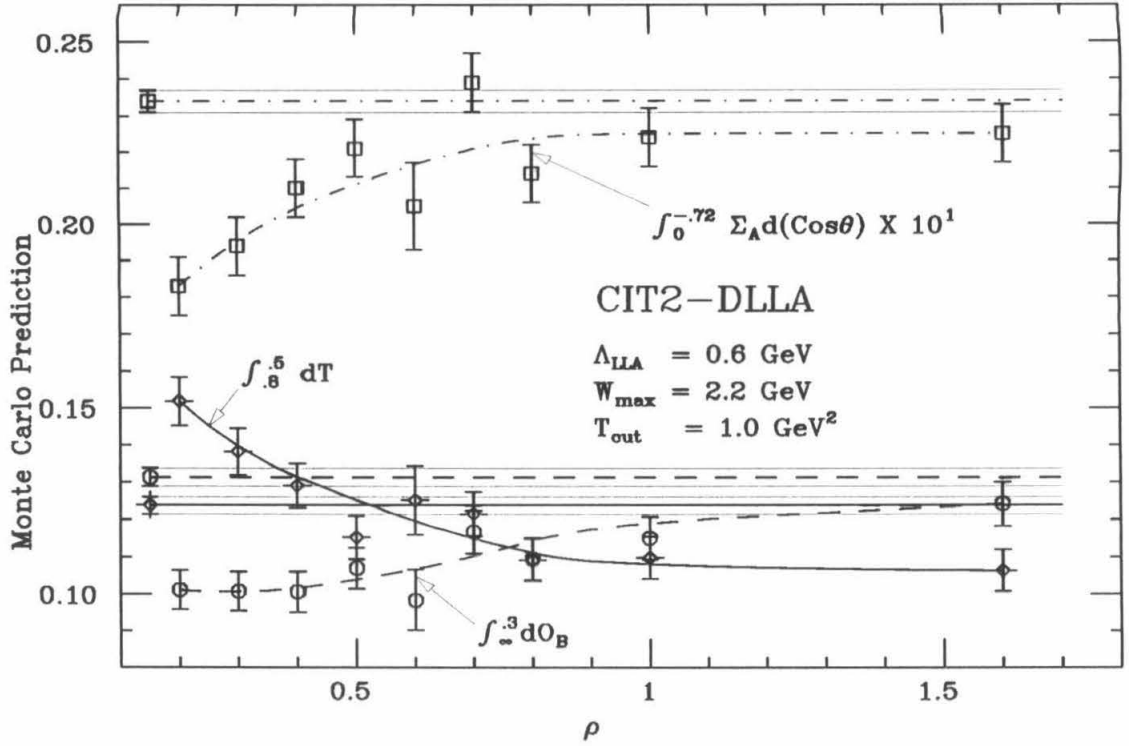


Figure 6.20 The dependence of the hard-QCD sensitive variables on the value of the ρ parameter. The values for the data are also shown.

Energy-Energy Correlation is sensitive to variation in Λ_{LLA} , while the Oblateness is not, and that the Oblateness cannot be fitted at the same time as Σ_A . The ability of the model to reproduce the correct value for the integrated asymmetry indicates that the LLA shower, together with $O(\alpha_s)$ matrix elements at the first branch, is an adequate treatment of the hard-QCD phenomena. However, the model is unable to correctly reproduce the Energy-Energy Correlation or the Thrust distributions for any choice of parameters. In Figure 6.21 the model predictions for Σ are compared with the data for two choices of Λ_{LLA} . Increasing Λ_{LLA} beyond 0.8 GeV causes the model to overshoot the asymmetry data and has to be excluded. A detailed comparison of the models with the data is presented in the next chapter, where the failings of the various models are also discussed.

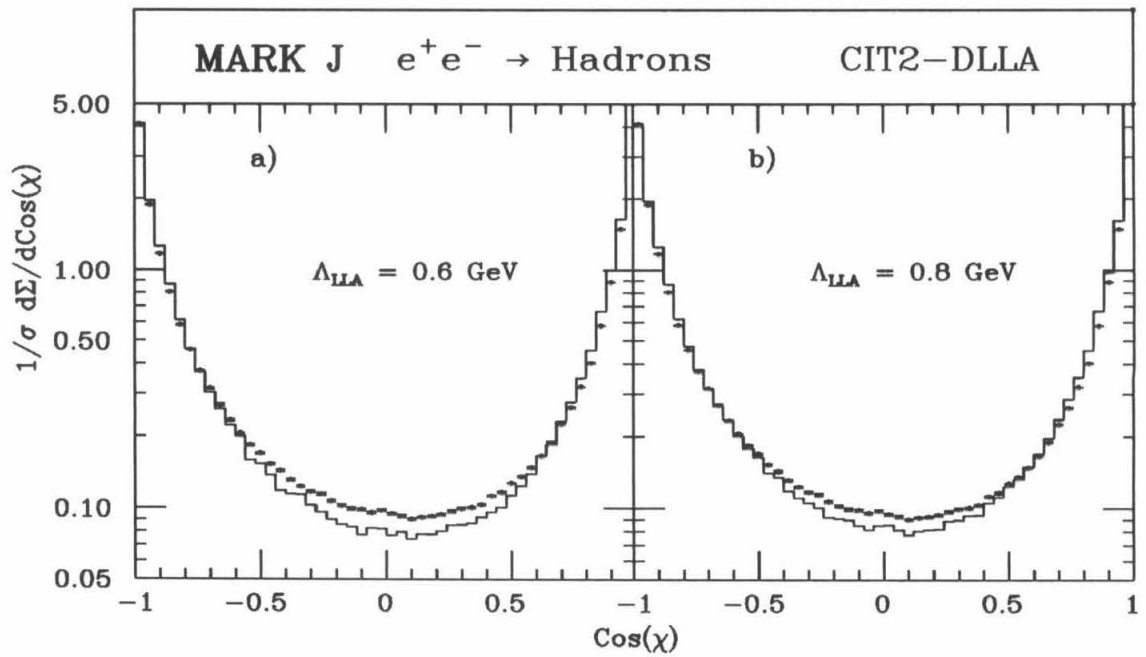


Figure 6.21 The CIT2-DLLA model prediction for Σ compared to the data for two values of Λ_{LLA} . The standard values for T_{cut} and W_{max} were used, and the data is at a center-of-mass energy of 35 GeV.

Chapter 7

Comparisons with Data

7.1 General Considerations

In this chapter the predictions of the various model combinations are compared with the MARK J data. The comparisons are made directly between model predictions, *after* being processed by the detector simulation, and the data. The 70/60/60 cuts are used throughout (see Section 2.5). Detailed comparisons between the Ali and LundV4.3 models with the data have been made previously [51], and while this study has also made such comparisons, we shall restrict most of our attention to the ‘new’ models. Further, the data taken at 44 GeV is new to this study. Therefore, initially we compare the models to the two large data sets at 35 GeV and 44 GeV and extend the comparison to the remaining data sets at the end of this chapter.

The string effect has not previously been investigated with the MARK J data, and the use of many different fragmentation models provides the opportunity for a study of this effect. We have already established, in Chapter 5, that the string effect must be due to the QCD strings used in fragmenting the partons rather than a consequence of soft gluon coherence effects occurring at the soft perturbative QCD stage of the event evolution. In this chapter we present comparisons of the various model predictions for the energy flow around the thrust axis of the events, and we further investigate the string effect.

The parameters used for the model predictions shown in this chapter are those obtained by the fitting procedure of the previous chapter.

7.2 Comparisons at 35 GeV and 44 GeV

In Appendix C comparisons between the model predictions and the data are shown for a multitude of shape variables. Since many of the variables shown have predictions that are sensitive to the value of α_s used, for the purposes of comparison all the plots for a particular model are shown for the same value of α_s . The values used are: 0.12 for the Ali model, 0.15 for the LundV4.3 model, 0.15 for the LundV6.3 model and 0.16 for the CIT2-FME model. For the CIT2-DLLA model a value of Λ_{LLA} of 800 MeV was used.

From these plots it can be seen that all the models do a reasonable job at describing the 35 GeV data, but that at 44 GeV the string models tend to underpredict the number of soft particles that are thrown well clear of the jets. This effect is most clearly seen in the narrow-side Major, where all the string models provide a good description of the data at 35 GeV. However, the comparisons at 44 GeV for the string models show a large depletion in the high-side tail of the model predictions for the narrow-side Major (as in Figure C.18, for example). In general, the plots in Appendix C show that the string model predictions are evolving faster with Q^2 than the data, while the Ali model predictions evolve at about the correct rate.

The tendency of a model to show large (larger than logarithmic) changes in its predictions with changing Q^2 is normally symptomatic of the presence of a fixed mass playing the role of a cut-off in the model. For the string models, this fixed mass arises as the mass scale at which the string evolution is terminated, i.e., at the hadron mass scale. In the string models that incorporate LLA shower packages an additional built-in fixed mass scale (t_{cut}) controls the termination of the shower development. Provided that t_{cut} is chosen sufficiently small, however, possible consequences of

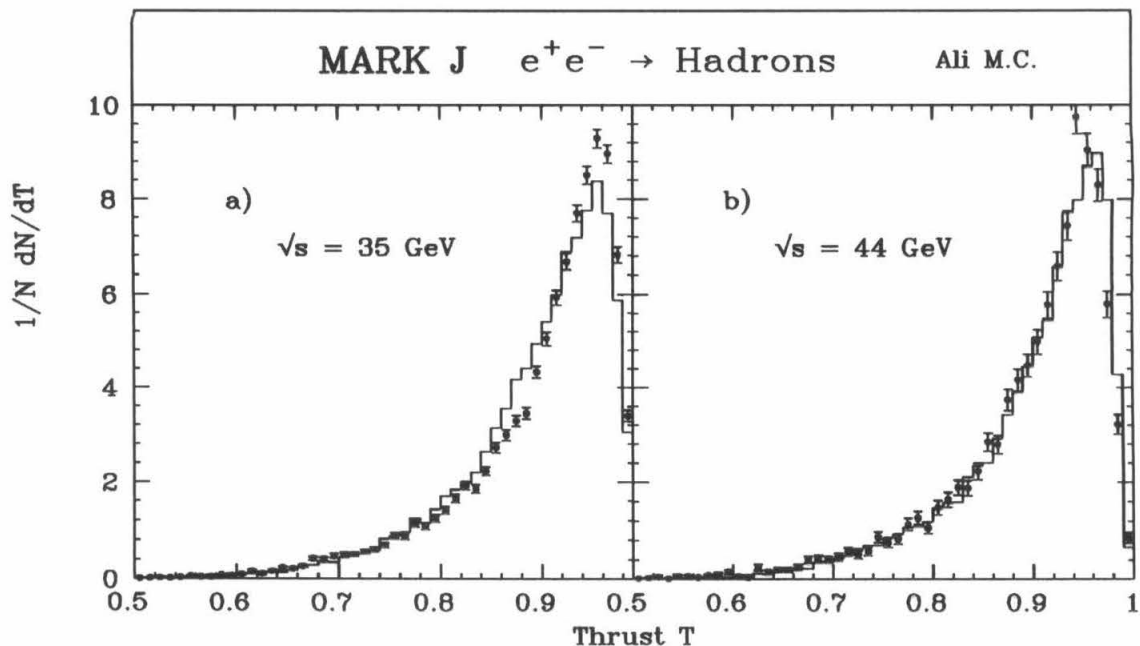


Figure 7.1 The Ali model predictions for the Thrust compared to the data at 35 GeV, a), and 44 GeV, b).

keeping this parameter fixed while varying Q^2 are irrelevant. For the Ali model, however, there are no such built-in mass scales that control the dynamics, and the model shows the logarithmic Q^2 dependence expected.

While the models fit the data well for most of the distributions shown in Appendix C, the model predictions for the Thrust variables are consistently low in the intermediate Thrust regions. In Figures 7.1 and 7.2 the predictions for the total Thrust from the Ali and LundV4.3 models are compared to the data. It can be seen that at 35 GeV both these models are capable of describing the low Thrust region, but that the high thrust region is less well described.

The LundV6.3, CIT2-FME, and CIT2-DLLA model predictions for Thrust are compared to the data in Figures 7.3, 7.4 and 7.5 respectively. It can be seen that the new models describe the data reasonably well in the low Thrust region, but that they also have problems in the high Thrust region. It is also clear that the tendency, seen in Appendix C, for the string models to predict more rapid Q^2 evolution for

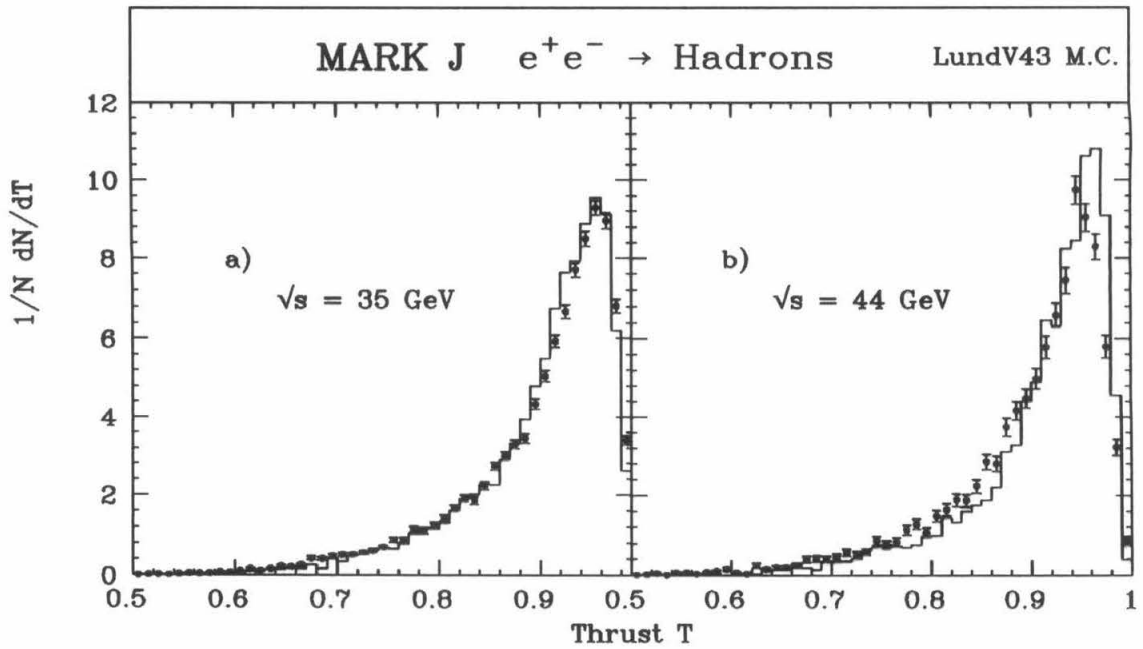


Figure 7.2 The LundV4.3 model predictions for the Thrust compared to the data at 35 GeV, a), and 44 GeV, b).

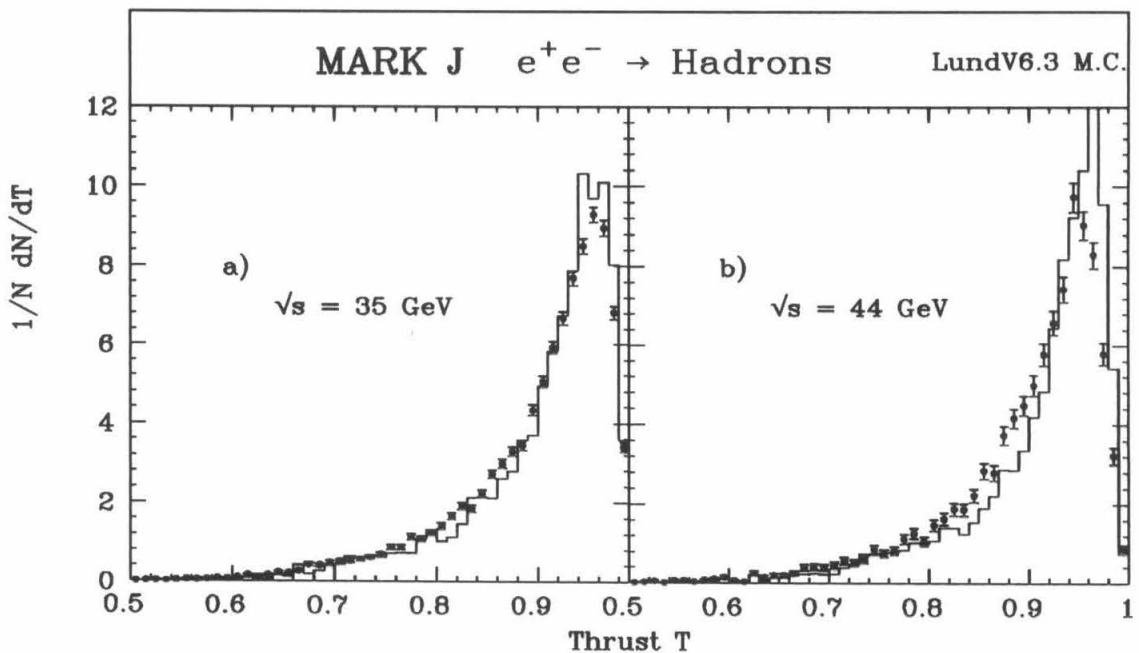


Figure 7.3 The LundV6.3 model predictions for the Thrust compared to the data at 35 GeV, a), and 44 GeV, b).

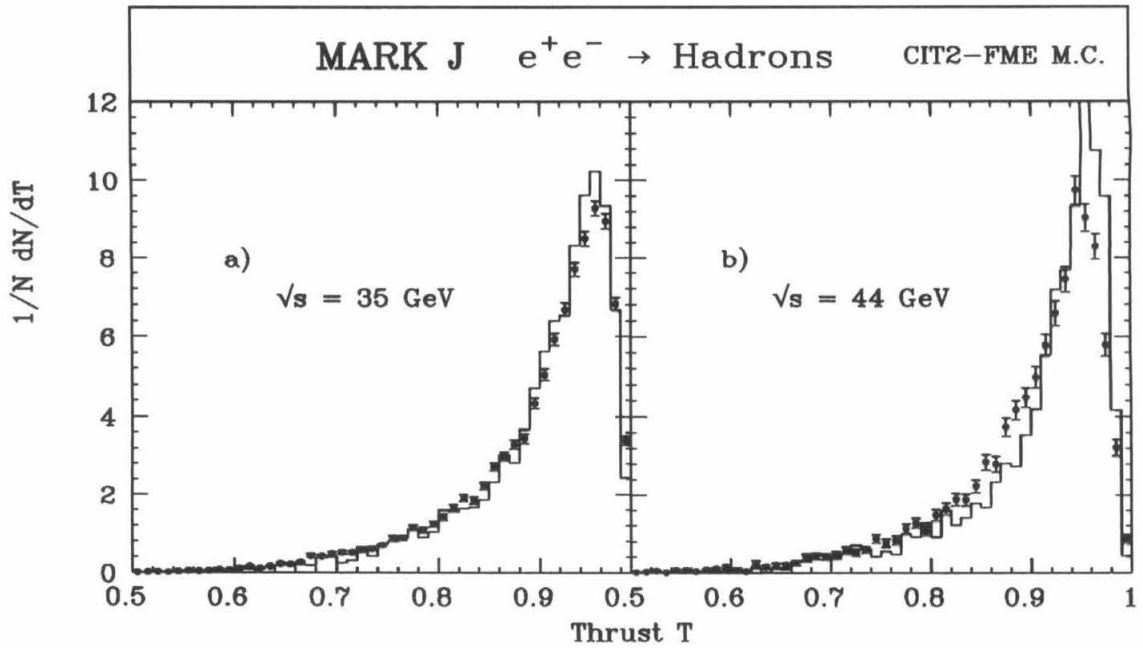


Figure 7.4 The CIT2-FME model predictions for the Thrust compared to the data at 35 GeV, a), and 44 GeV, b).

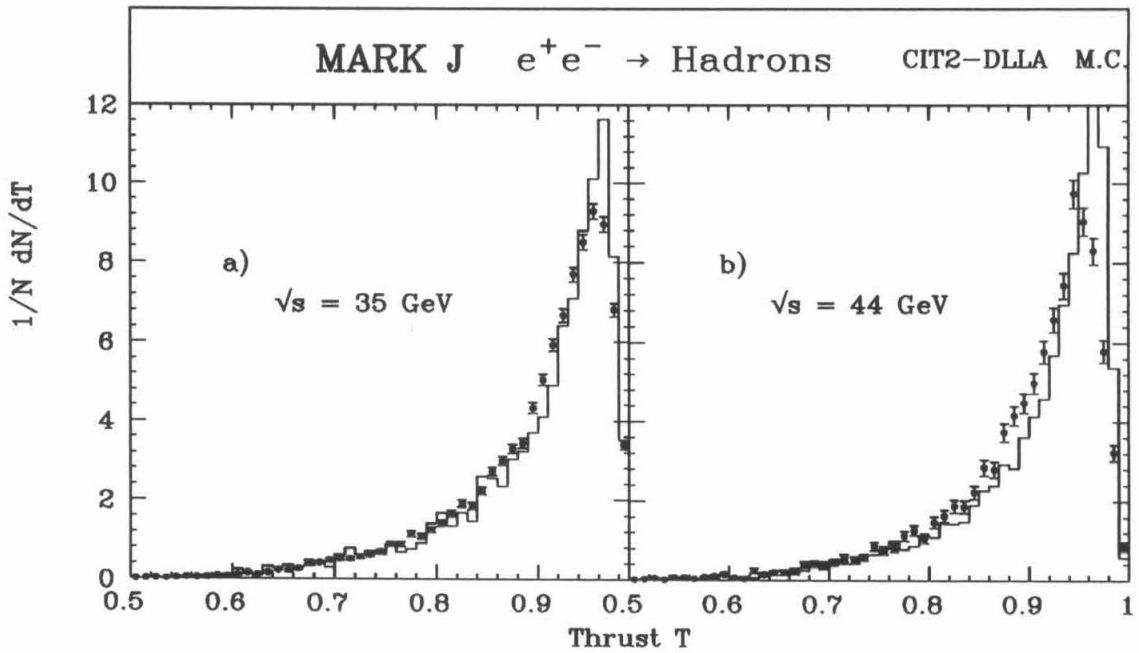


Figure 7.5 The CIT2-DLLA model predictions for the Thrust compared to the data at 35 GeV, a), and 44 GeV, b).

the event shapes is also displayed in the Thrust. It should be stressed that the high Thrust region is not sensitive to the hard-perturbative QCD structure of the events and that the failure of a particular model to fit the data in this region does not preclude its use in α_s measurements.

The high Thrust region is a particularly difficult region to model correctly. Higher order QCD effects are known to be large in this region, and it is expected to be highly dependent on the very soft structure in the underlying parton configurations¹. The magnitude of the higher order contributions to the Thrust can be judged from the data shown in Figure 5.1, where already the 2nd order correction in the range $0.7 < T < 0.95$ is about 20%. In the case of the model combinations incorporating fixed order matrix elements at the hard perturbative QCD level, the rapid change in the model predictions for the high Thrust region can be partially traced to the fixed Y -cut used. For a Y -cut of 0.02 (as used here), the minimum invariant mass of a resolvable parton pair is 5 GeV at $\sqrt{s} = 35$ GeV, while at $\sqrt{s} = 44$ GeV it is 6 GeV, already a change of 20%. The large spikes in the CIT2-DLLA model predictions for Thrust close to 1 are due to the omission of higher order terms in the LLA shower package used. These higher order corrections are known to be large and negative in this region.

The model predictions for the Energy-Energy Correlation function are compared with the data, at 35 and 44 GeV, in Figures. 7.6, 7.7, 7.8, 7.9 and 7.10. From these plots it can be seen that all the models are in reasonable agreement with the 35 GeV data. However, the Ali model is the only model that provides a good description of both the 35 GeV and 44 GeV data with the same parameter values. For all of the string models the trend is to underestimate the magnitude of the contribution to the central region of the Energy-Energy Correlation function (the region for which

¹At the parton level, for three-jet configurations, the Thrust is just $1 - Y_{min}$, where Y_{min} is the minimum invariant mass between any pair of partons in the event.

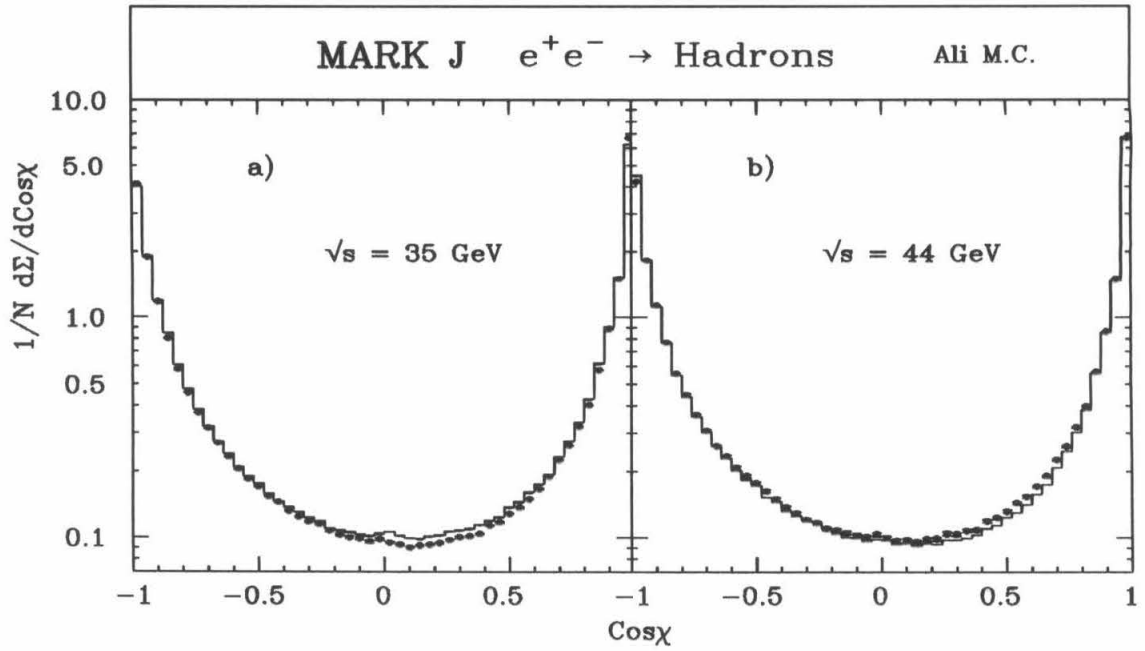


Figure 7.6 The Ali model predictions for Σ compared to the data at 35 GeV, a), and 44 GeV, b).

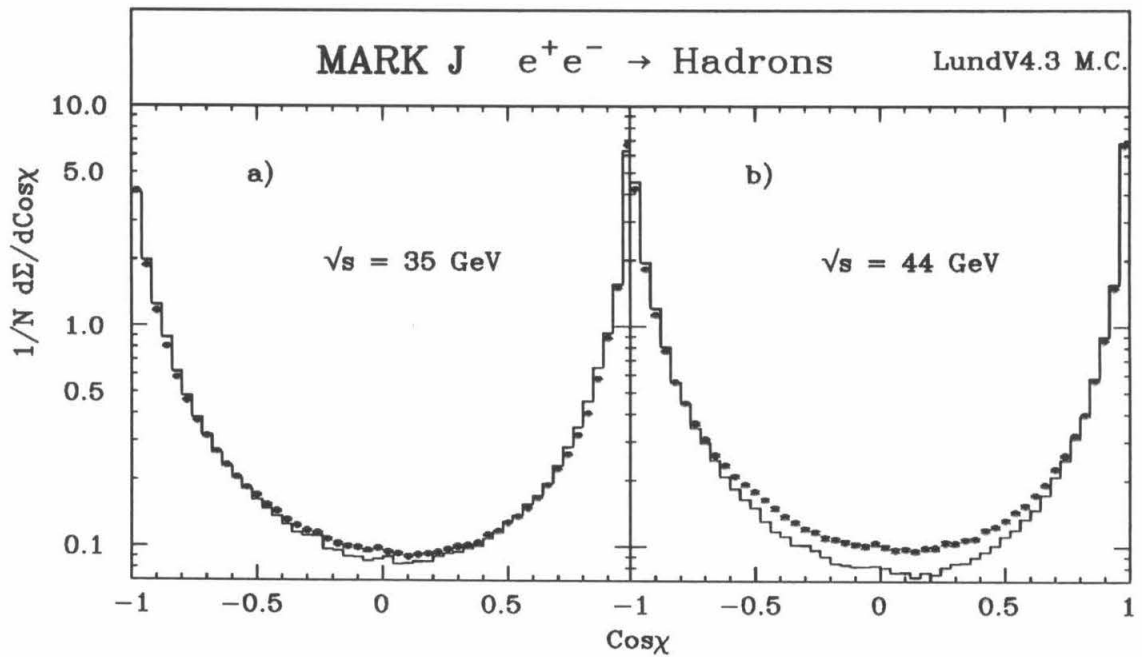


Figure 7.7 The LundV4.3 model predictions for Σ compared to the data at 35 GeV, a), and 44 GeV, b).

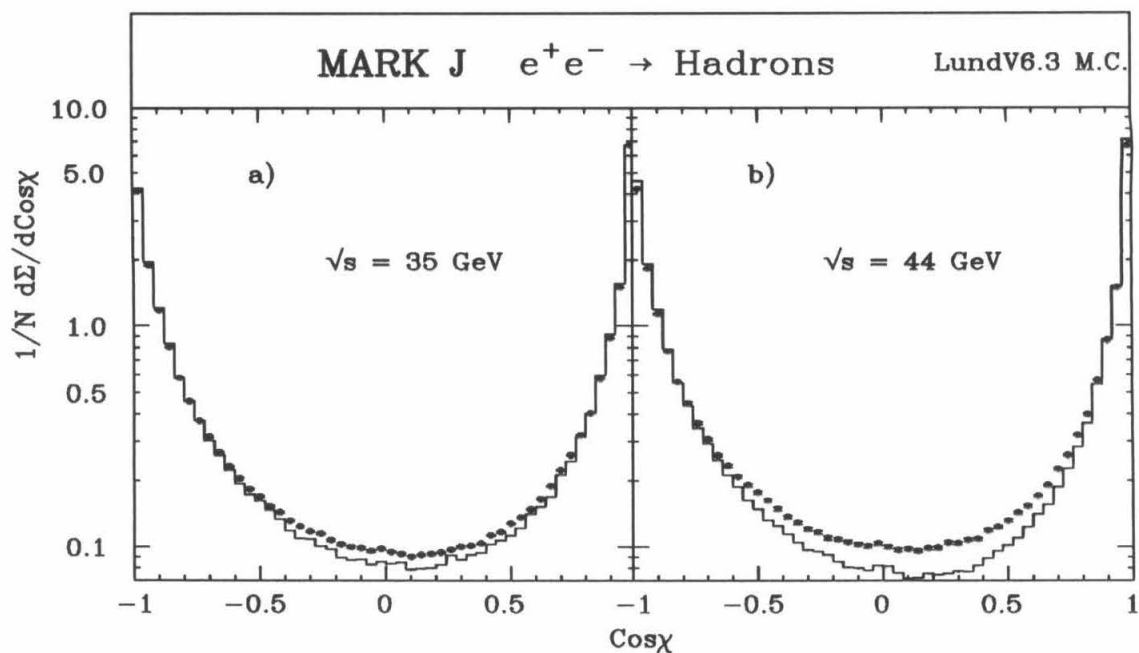


Figure 7.8 The LundV6.3 model predictions for Σ compared to the data at 35 GeV, a), and 44 GeV, b).

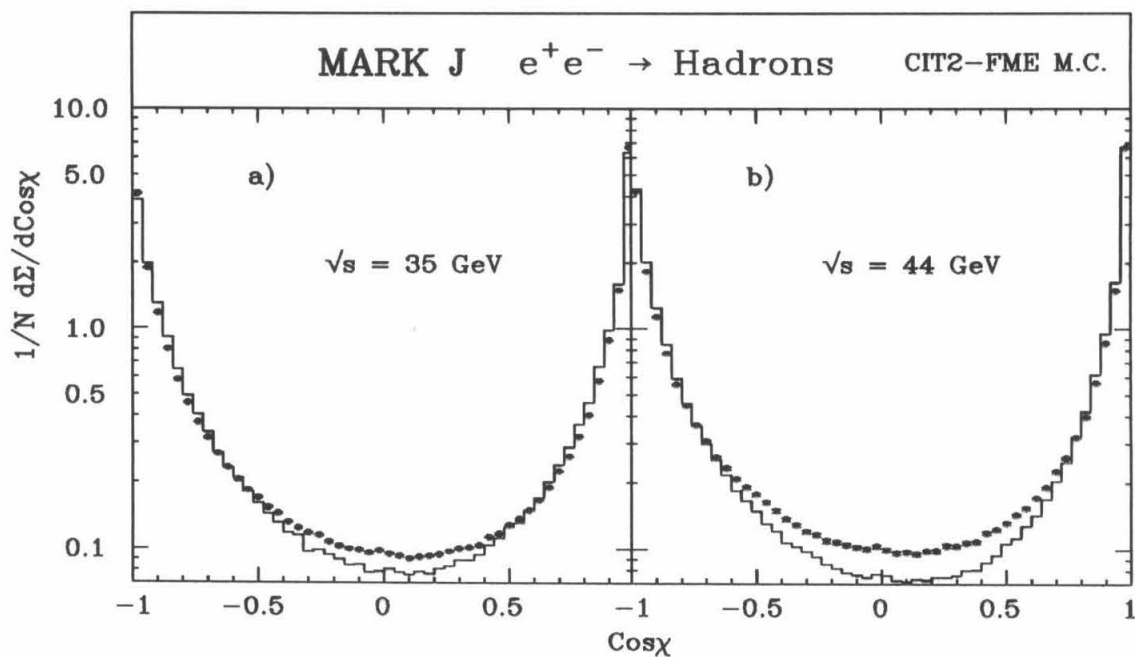


Figure 7.9 The CIT2-FME model predictions for Σ compared to the data at 35 GeV, a), and 44 GeV, b).

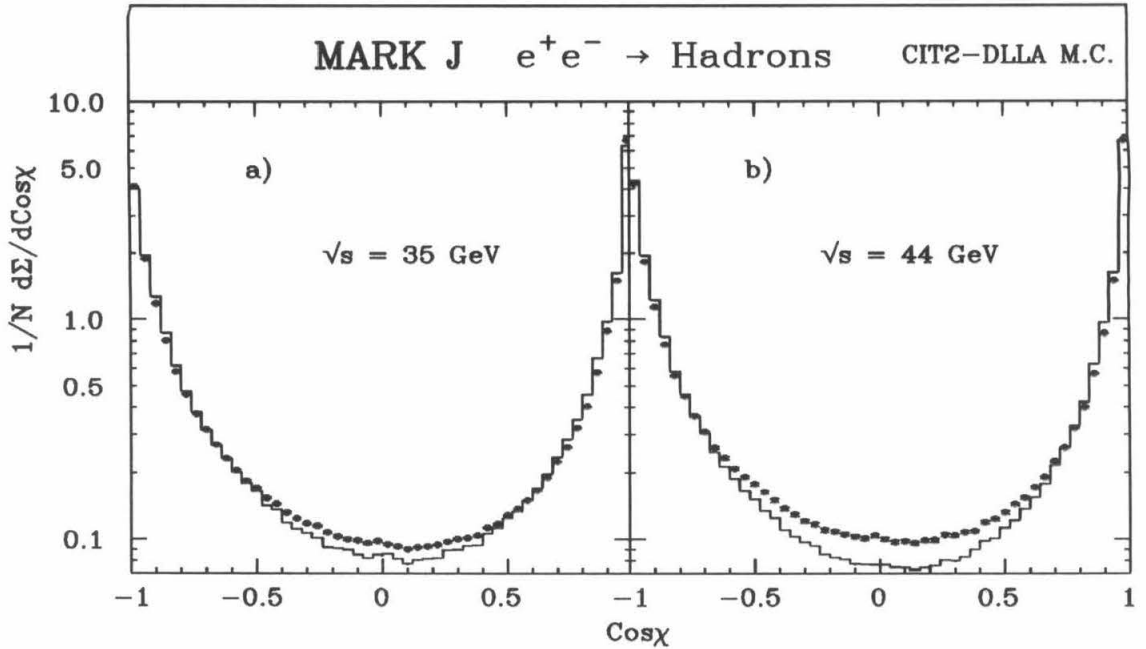


Figure 7.10 The CIT2-DLLA model predictions for Σ compared to the data at 35 GeV, a), and 44 GeV, b).

$|\cos \chi|$ is small). The effect can be seen to become worse at the higher energies, again reflecting the overly rapid evolution of the string model predictions with increasing Q^2 .

As indicated above, the failure of the models to provide a good description of the central region of the Energy Energy Correlation distribution does not preclude their use in α_s measurements. The hard QCD structure of the events is reflected in the *asymmetry* and not in the Energy Energy Correlation itself. The plots shown here, and those shown in the next chapter, indicate that the asymmetry is well described. The models, however, fail to symmetrically pull particles out of the two-jet region into the central region of the Energy-Energy Correlation. This reflects a failing in the fragmentation scheme, rather than a failure to correctly describe the hard gluon bremsstrahlung occurring in the initial development of the event.

The flower plots obtained from the model combinations are compared to the data in Figures 7.11 to 7.15. The purity of three-jet events for the data shown

in the flower plots is 70%, as discussed in Section 6.1. The tendency displayed by the string models in the Energy-Energy correlation plots, to not throw enough particles out of the two-jet region into the softer central parts of the plots, is also evident in the flower plots. It can be seen that the general trend is for the string models to underpredict the number of soft hits in the detector between the quark and antiquark jets. Further, the magnitude of this effect can be seen to become worse at the higher energy.

The flower plots provide information about the relative magnitudes of the hard and soft contributions to the central region of the Energy-Energy Correlation function. The hard contribution to the $\cos \chi = 0$ region comes from the hard bremsstrahlung of a gluon. The contributions to the flower plots from this source determine the form of the rightmost of the two central bumps in the flower plots; this is essentially a cut through the gluon jet. It can be seen that the gluon jet is well described by all the models at both energies shown. The soft contribution to the Energy-Energy Correlation near $\cos \chi = 0$ comes from the hits that contribute in the flower plots to the regions between the jets. The flower plots shown here indicate that (with the exception of the CIT2-DLLA model combination) it is in this region that the string fragmentation schemes tend to provide too small a prediction. This, of course, is the expected string effect. However, the plots show that the magnitude of the string effect is severely overestimated by the string models used here. In addition, the flower plots show that it is the prediction for the (soft) contribution to regions between the jets that is varying too rapidly with Q^2 for these models.

7.3 Comparisons at Low Energy

One of the main innovations in the Caltech-II fragmentation scheme is the inclusion of an elaborate parameterization of low energy cluster decays. This reflects the idea that low-mass cluster decays can be further factored out of the hadroniza-

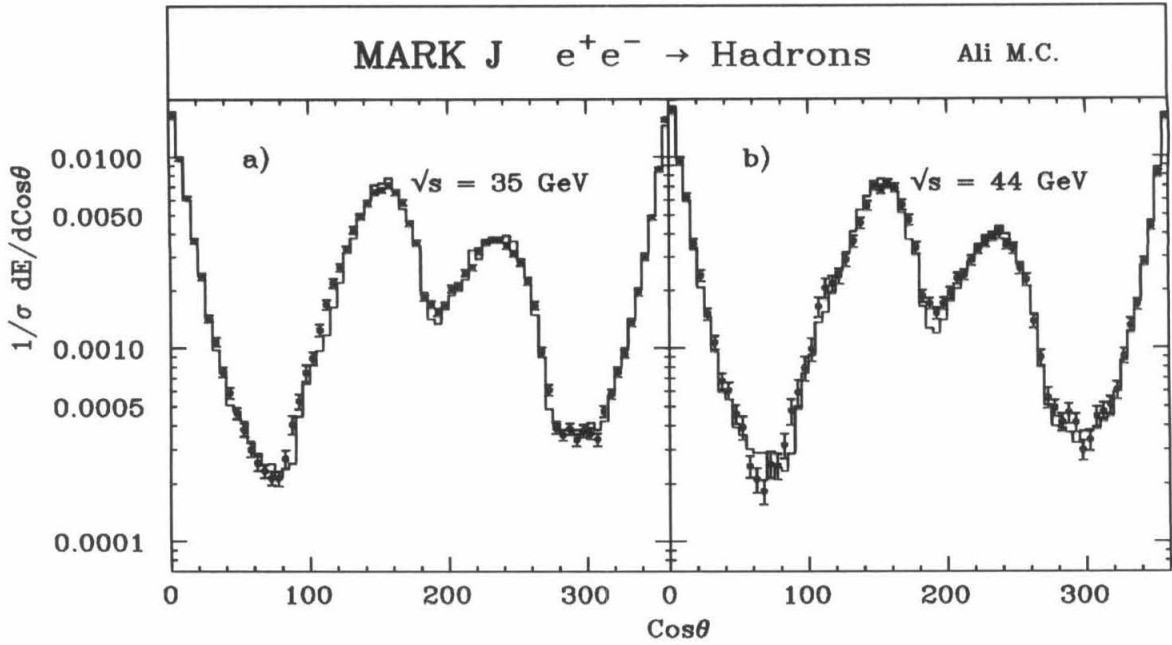


Figure 7.11 The Ali model predictions for the energy flow compared to the data at 35 GeV, a), and 44 GeV, b).

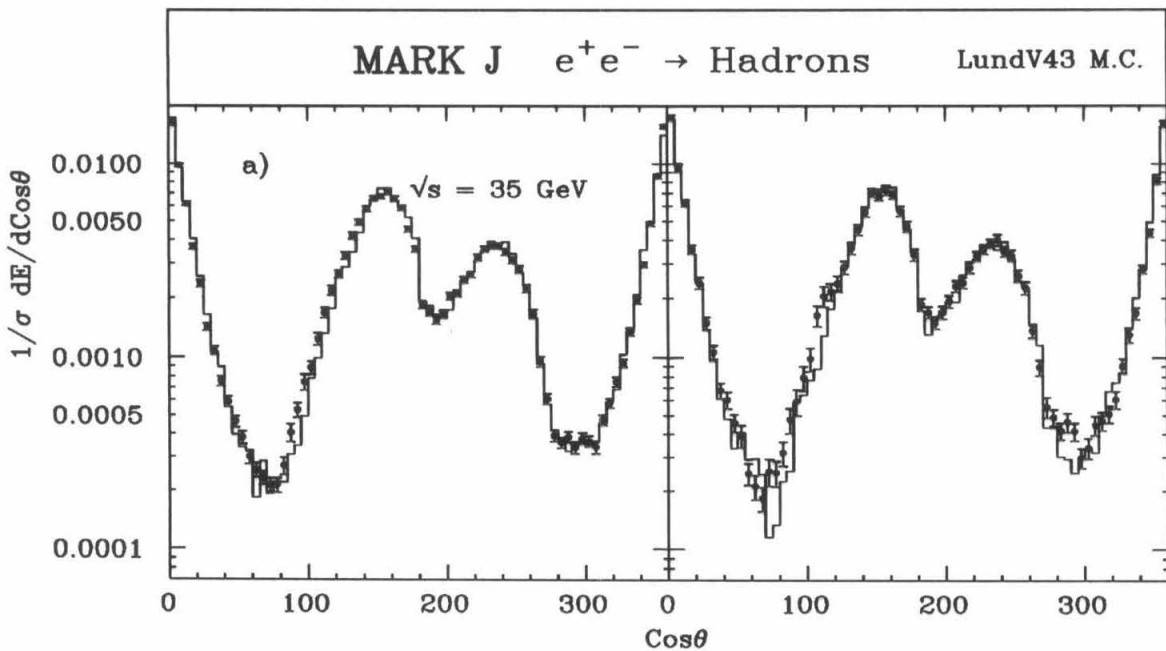


Figure 7.12 The LundV4.3 model predictions for the energy flow compared to the data at 35 GeV, a), and 44 GeV, b).

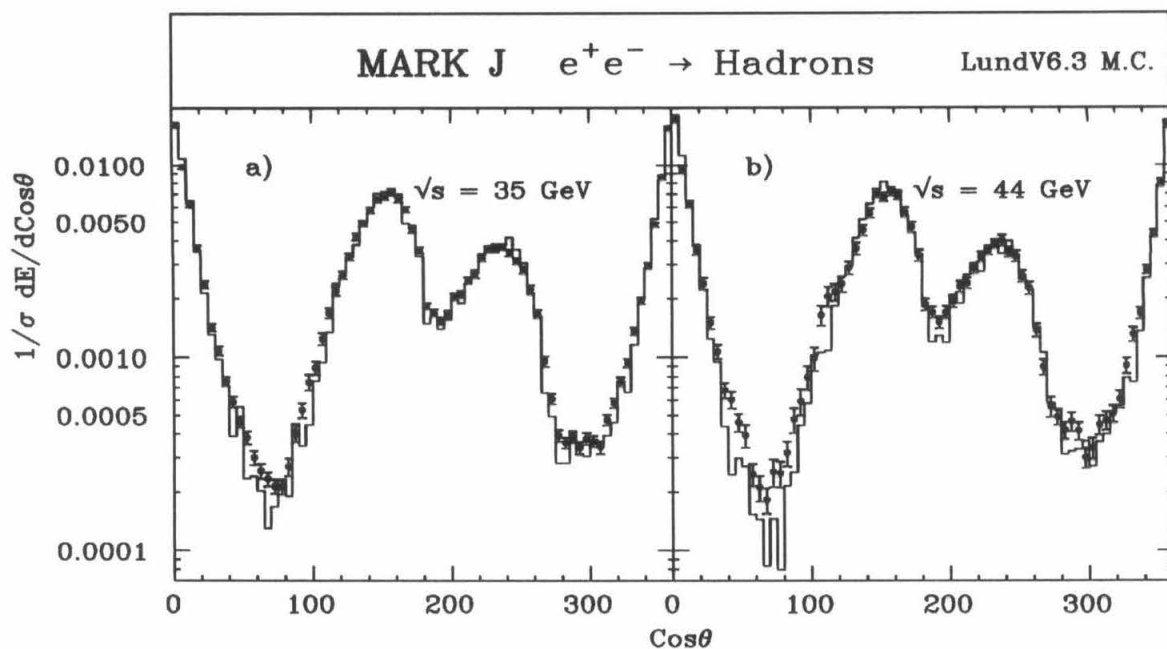


Figure 7.13 The LundV6.3 model predictions for the energy flow compared to the data at 35 GeV, a), and 44 GeV, b).

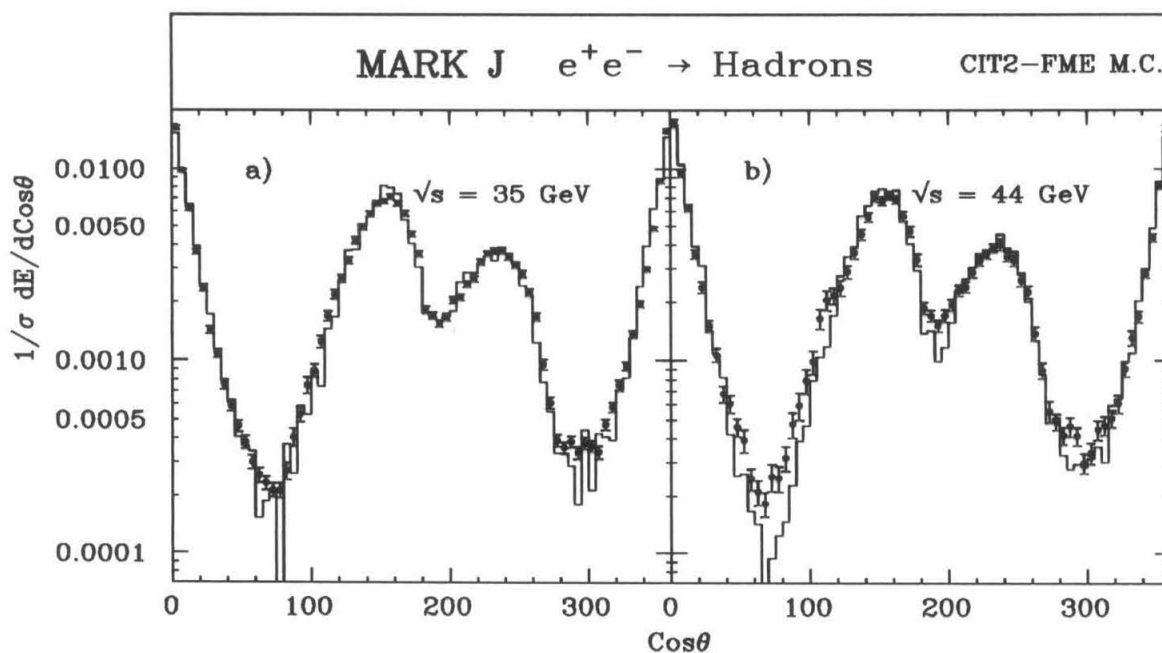


Figure 7.14 The CIT2-FME model predictions for the energy flow compared to the data at 35 GeV, a), and 44 GeV, b).

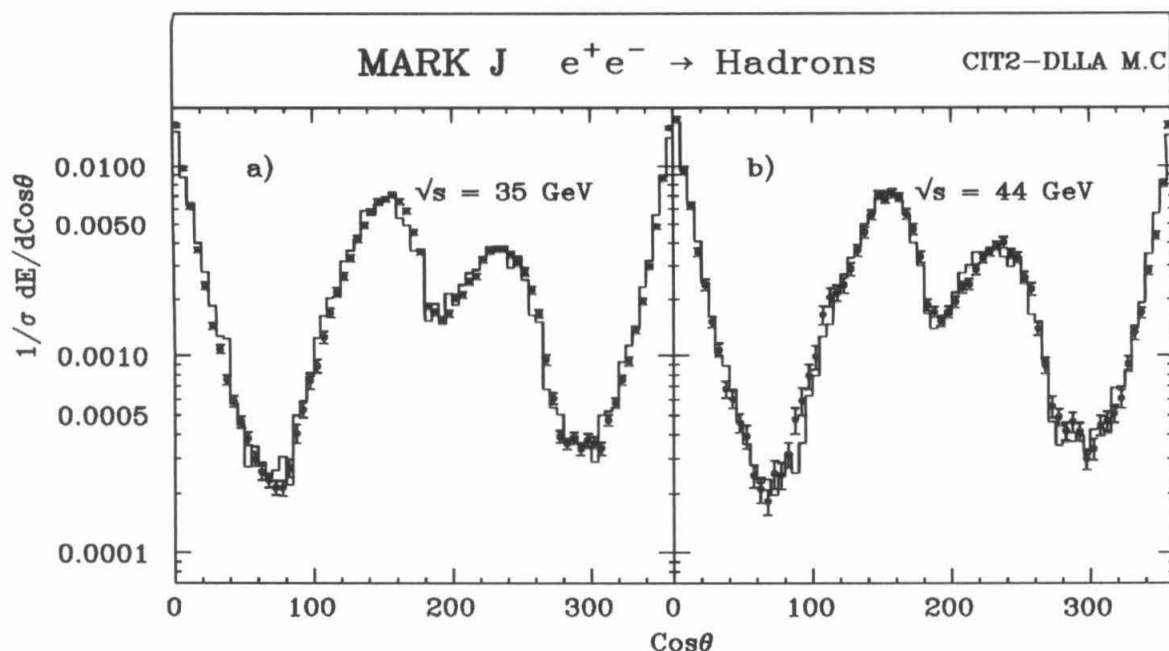


Figure 7.15 The CIT2-DLLA model predictions for the energy flow compared to the data at 35 GeV, a), and 44 GeV, b).

tion. By comparing the predictions of the model combinations incorporating this fragmentation scheme to the 14 GeV data, it is possible to test the performance of the parameterization. In Figure 7.16 the Thrust predictions from two model combinations that use the Caltech-II fragmentation scheme are compared to the 14 GeV data. The agreement with the data is good. Again, the lack of higher order corrections in the parton shower is evident in the high Thrust region of the predictions for the CIT2-DLLA model combination.

The model predictions at 22 GeV are compared to the data for the Thrust and Energy-Energy Correlation function in Figures 7.17 to 7.20. From these plots it can be seen that the model predictions agree roughly with the data, except for the tendency of LundV6.3 and the Caltech models to underestimate the number of soft particles away from the jet axes.

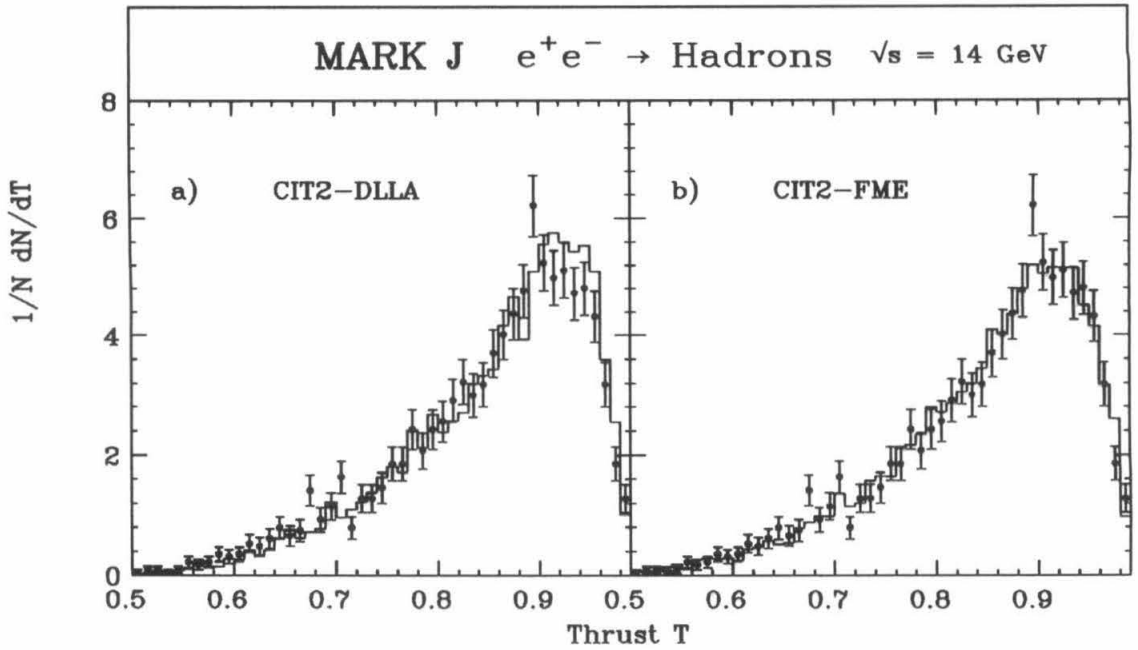


Figure 7.16 a). The CIT2-DLLA model predictions for Thrust compared to the data at 14 GeV, and b) The same for the CIT2-FME model combination.

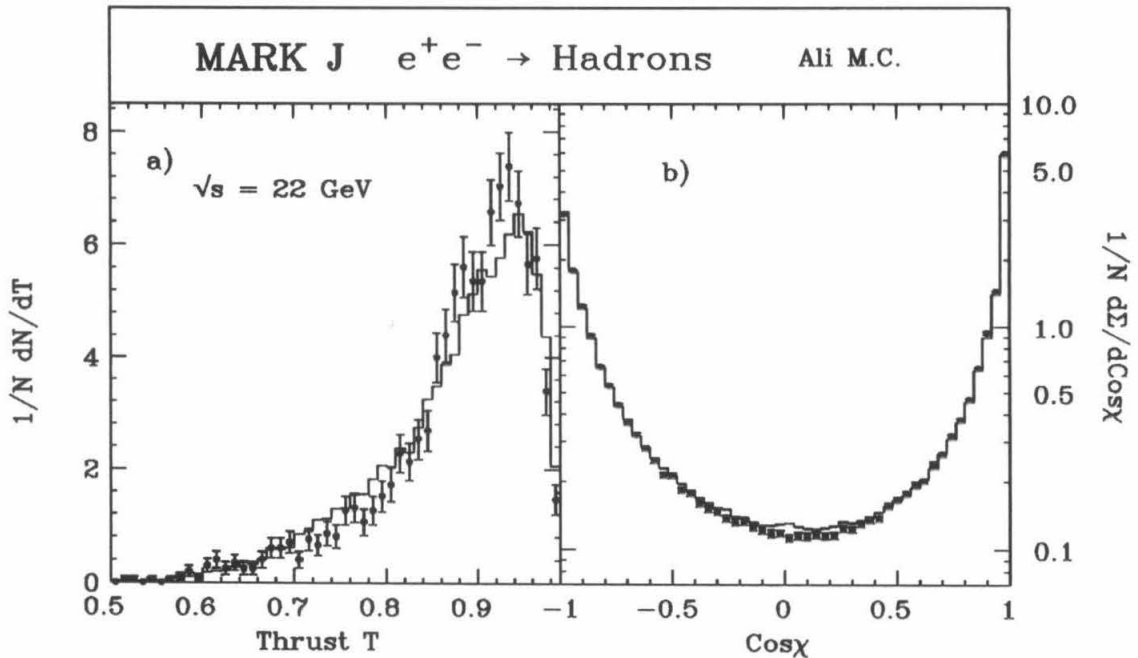


Figure 7.17 a). The Ali model predictions for Thrust compared to the data at 22 GeV, and b) The same for the Energy-Energy Correlation.

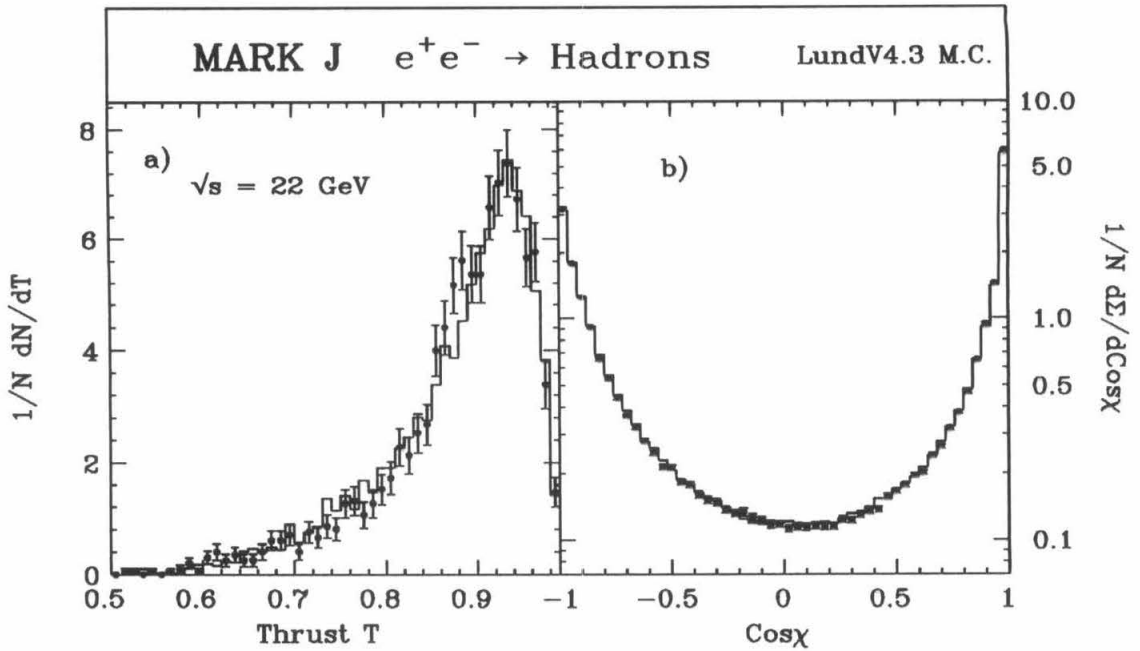


Figure 7.18 a). The LundV4.3 model predictions for Thrust compared to the data at 22 GeV, and b) The same for the Energy-Energy Correlation.

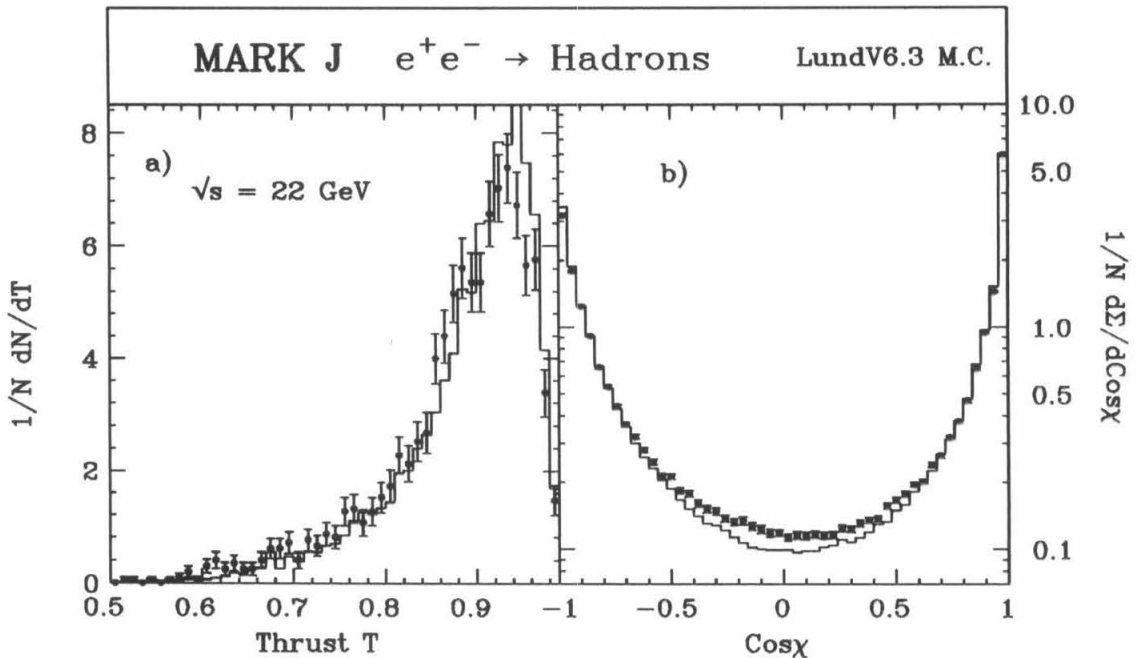


Figure 7.19 a). The LundV6.3 model predictions for Thrust compared to the data at 22 GeV, and b) The same for the Energy-Energy Correlation.

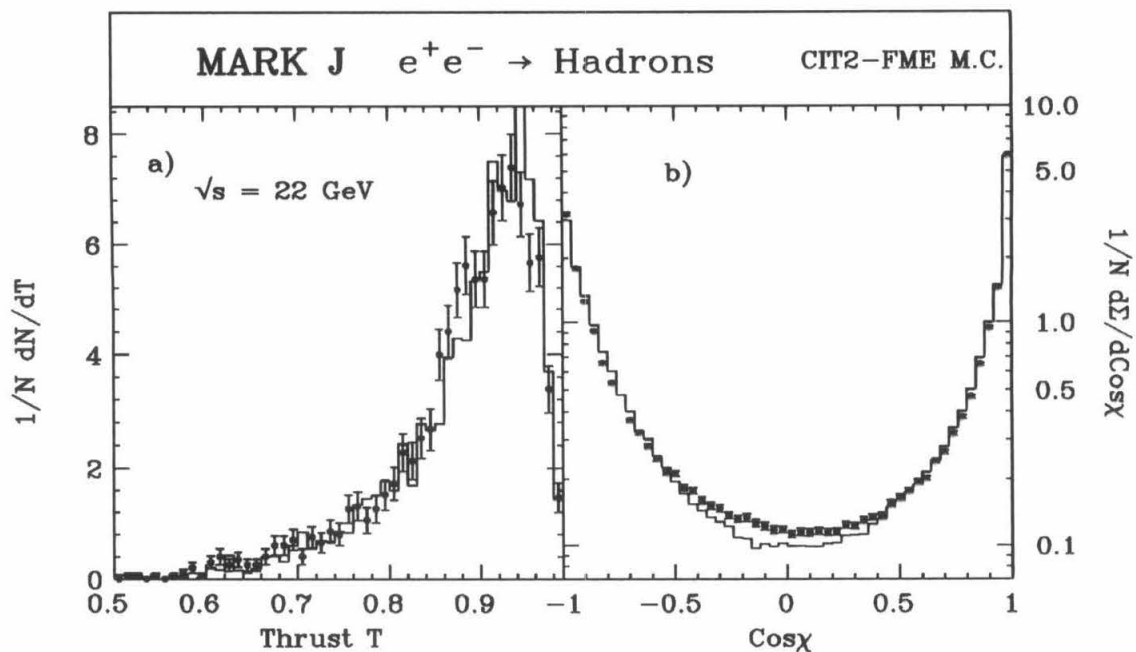


Figure 7.20 a). The CIT2-FME model predictions for Thrust compared to the data at 22 GeV, and b) The same for the Energy-Energy Correlation.

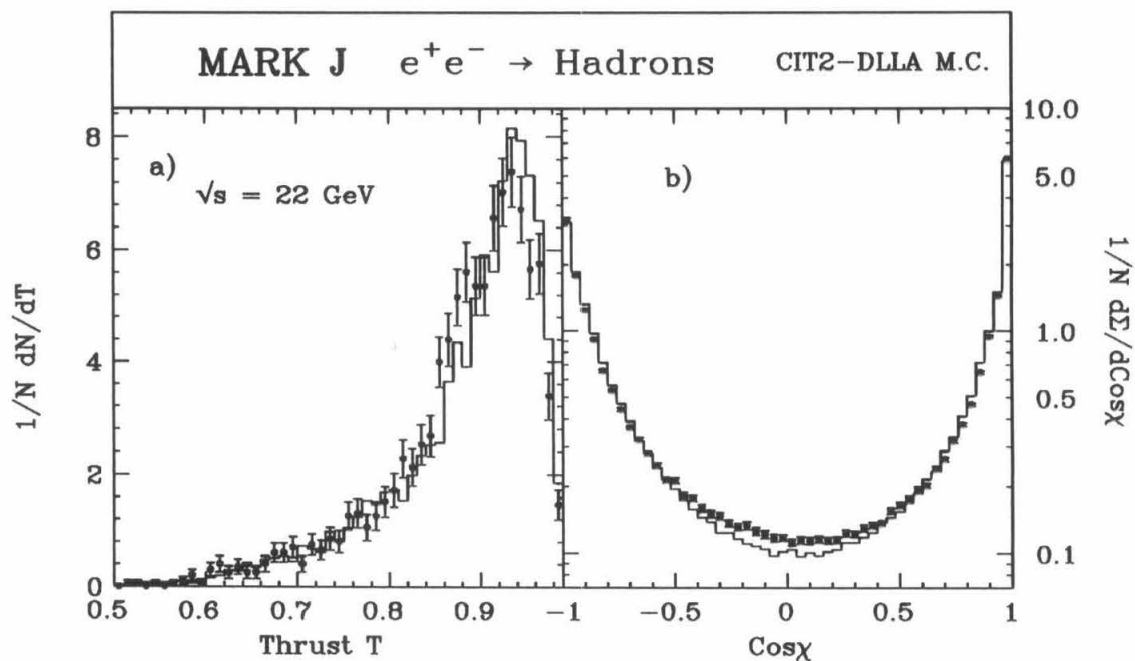


Figure 7.21 a). The CIT2-DLLA model predictions for Thrust compared to the data at 22 GeV, and b) The same for the Energy-Energy Correlation.

7.4 Discussion

The results presented in this chapter and Appendix C show that all the models investigated in this study can provide an approximate description of the data. Further, this is true even when a large energy range is considered. However, the Q^2 dependence of the string fragmentation model predictions is larger than that indicated by the data at the highest energies considered. This is most likely due to the presence of a fixed mass scale, in the form of the hadron mass spectrum, controlling the termination of the string evolution and the transition from strings to hadrons. The effect of this fixed cut-off can be reduced by incorporating LLA shower generators to model the soft QCD phase of the event development.

The CIT2-DLLA model combination is consistently better at describing both the 35 and 44 GeV data (an exception is in the Thrust). This indicates that some of the problems with the string models can be reduced by replacing the fixed order matrix element treatment of the parton generation with a LLA shower. While the FME approach can produce at most two string segments at the start of the string evolution, the LLA approach can lead to the presence of many smaller pieces of string at this point in the evolution of the event. Each of these smaller pieces of string must have a smaller fraction of the total center-of-mass energy than the strings appearing at the corresponding phase in the evolution of a FME system. They are, therefore, less sensitive to variation in the overall center-of-mass energy of the event.

This indicates that it is incorrect to regard the soft QCD aspects of the development of the events as being totally distinct from the string evolution occurring at the fragmentation stage. By determining the number of strings that are passed to the start of the fragmentation, the perturbative QCD aspects of LLA shower generators play a crucial role in the subsequent non-perturbative development of the event.

It has been found that it is not possible to obtain a good fit to both the Thrust and the Energy-Energy Correlation function that is maintained over a large range in Q^2 . This is partly due to the problems discussed above, but also a consequence of the much larger contributions from higher orders expected for the Thrust than for the Energy-Energy Correlation function.

7.4.1 The String Effect

The string effect is clearly visible in the Monte Carlo predictions for the energy flow. In the data, however, it is a much smaller effect than the models would lead one to believe. Close inspection of Figure 7.11(b) shows that the Ali does overestimate the energy flow between the quark and antiquark jets at the higher energies. However, the effect is statistically marginal. With the exception of the CIT2-DLLA model, the string models all underestimate the energy flow in this region. We find, however, that the Ali model provides a better description of the energy flow at all energies.

The existence of the string effect in the data is well established by Monte Carlo independent comparisons between $q\bar{q}g$ and $q\bar{q}\gamma$ events [96,97]. However, the connection between the string effect in the data and the string effect expected for string fragmentation models is less well established. It is not possible to measure the particle density between the jets with the MARK J detector, so the following remarks apply only to the energy flow in this region.

In Figure 7.22 the flower plots obtained with two different values of σ_q , on either side of the optimum value as determined in Chapter 6, are shown for the Ali model. As one would expect, the form of the flower plot is sensitive to the value of this parameter. Figure 7.23 shows the dependence of the prediction for the flower plot on σ_q for the LundV6.3 model and the dependence is seen to be large. Given this large dependence on the value of σ_q used in the models, and the fact that errors

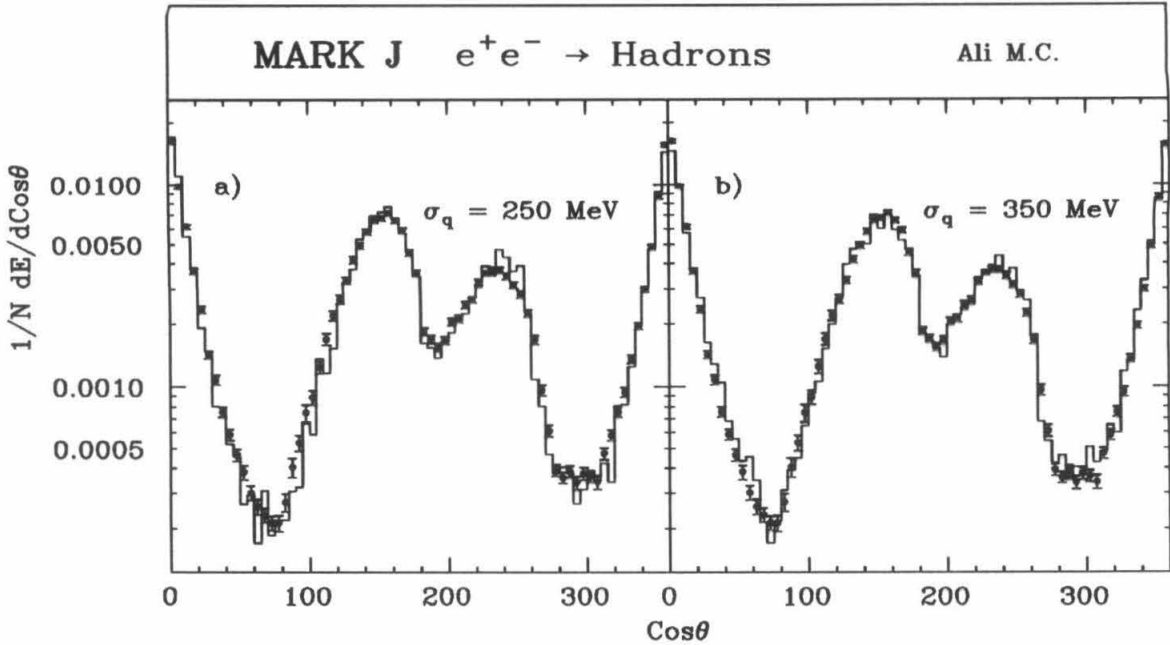


Figure 7.22 a). The Ali model predictions for the energy flow around the Thrust axis obtained with $\sigma_q = 250 \text{ MeV}$ compared to the data at 35 GeV, and b) The same for $\sigma_q = 350 \text{ MeV}$.

assigned to σ_q determinations are typically of the order of 50 MeV, these plots raise serious questions about prior claims to the observation of the string effect in the observed energy flows. Further, the sensitivity of the particle flow in three jet events is expected to be more sensitive than the energy flow to changes in the fragmentation parameters. It can be remarked that this study finds the form of the flower plots to be insensitive to the value of α_s used.

The results obtained here can be compared to the JADE results for the energy flow in three jet events. The early JADE studies compared the Hoyer and Lund model predictions for the energy flow to their data at 35 GeV [41,42]². For the JADE study, σ_q for quarks was taken as 300 MeV, while the gluons were fragmented with a σ_g of 500 MeV. This JADE study found that the Lund model was able to correctly describe the energy flow between the quark jets, but that the Hoyer model

²The Hoyer model is a variant of the Field-Feynman fragmentation scheme, in which gluons are assumed to fragment like quarks, but with a larger σ_g .

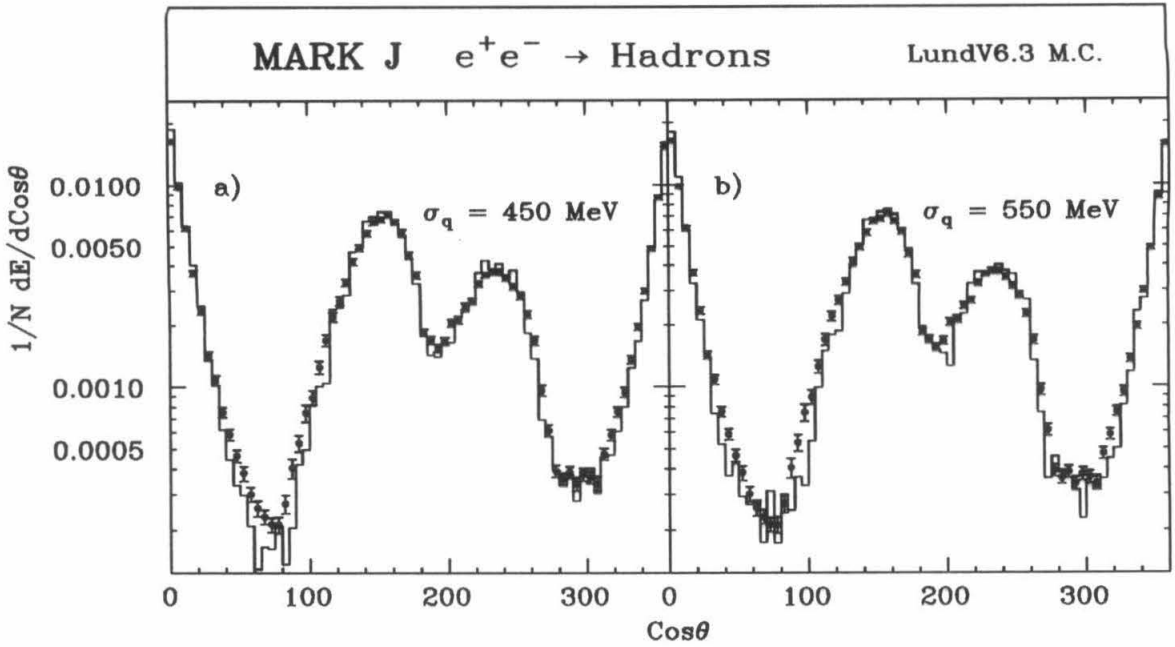


Figure 7.23 a). The LundV6.3 model predictions for the energy flow around the Thrust axis obtained with $\sigma_q = 450 \text{ MeV}$ compared to the data at 35 GeV, and b) The same for $\sigma_q = 550 \text{ MeV}$.

overestimated the energy flow in this region. The results shown here for the Ali and LundV4.3 models are in disagreement with these JADE results.

A later JADE study compared the Webber model to the Caltech-I model [43]. This study concluded that the Webber model described the energy flow correctly, while the Caltech-I model could not. On the basis of this study the JADE group claimed that at least some of the string effect was due to soft gluon coherence effects taking place in the LLA shower package provided with the Webber model. The discussion presented in Chapter 5 of this study indicates that this conclusion should be re-examined.

The TPC group has also studied the string effect by investigating the particle number densities between the jets [44,45]. The TPC study investigates the particle flows between the jets for particles whose momenta transverse to the event plane lie in various ranges. For the case that all particles in the event are considered, the TPC results are consistent with those found in this study. However, for particles

having a large momentum component perpendicular to the event plane, and for heavy particles, the TPC study finds that the data favors the string models.

The results of this study are also, at least partially, consistent with the results obtained by the TASSO collaboration [98]. They found that for particles carrying a longitudinal momentum fraction > 0.04 (the longitudinal momentum fraction is $P_{particle}/E_{beam}$) the Ali model was able to correctly describe the energy flow, while the Lund model was not. For softer particles, however, the data favored the Lund model over the Ali model.

7.4.2 Comparison with Other Studies

The MARK II collaboration has compared the full Caltech-II model, the LundV6.3, with parton shower and fixed order matrix element parton generation, and the Webber models to their *corrected* data at 29 GeV [99]. For the LundV6.3 model, the MARK II study used a σ_q value of 265 MeV, in contrast to the value of 500 MeV used here. For the CIT2-DLLA model, the MARK II study used the default parameters determined for the model in Ref. [39], while this study uses a ρ value of 0.3 as opposed to 1.6 GeV⁻², and a value of Λ_{LLA} of 0.8, as opposed to 0.6 GeV.

The results shown here are largely consistent with the MARK II findings. However, the MARK II study found that the CIT2-DLLA model is unable to describe the Minor, and the Thrust, while this study finds that the CIT2 models can adequately describe these distributions (see the plots for these variables in Appendix C and above), at least for the 35 GeV data. A possible source for this discrepancy is the procedure used in the MARK II study to correct the data. The correction factors used were obtained by taking the weighted average of the correction factors obtained from all the models. The weighting was determined by the quality of the fits of the models to the data. Since the Caltech-II model shows the worst fit to the Thrust of all the models considered, this method of correcting the data exaggerates

the discrepancies between the Caltech-II prediction for Thrust and the data, while de-emphasizing those for the other models. The MARK II study also finds that the LundV6.3 model underestimates the number of events having high Minor values, a result consistent with that found here. It has been pointed out by Gottschalk that the parameter values used in the MARK II study for the LundV6.3 model do not provide a good fit to the Energy-Energy Correlation (unfortunately, the MARK II study omitted the Energy-Energy Correlation in their paper). This is in agreement with the results found here [91].

7.5 The Role of Transverse Momentum in String Models

It has been remarked in Chapter 4 that the addition of transverse momentum to the string model formalism cannot be performed in a totally consistent fashion. If the string break occurs close to the end of a string segment, then there may not be enough string available to generate the desired transverse momentum for the hadron. This causes the transverse momentum spectrum for hadrons produced by string models to be truncated.

Of the fragmentation schemes investigated in this study, the Caltech-II scheme is unique in its omission of arbitrarily generated transverse momentum. In this model *all* the transverse momentum is generated by the cluster decays occurring after the string evolution. From the failure of this model to fit the intermediate Thrust and central Energy-Energy Correlation function regions it is apparent that this general method of imparting transverse momenta to the final state hadrons in these models is flawed. For the string fragmentation schemes the central region of the Energy-Energy Correlation function is underpopulated by soft particles. The truncation of the P_t distribution that arises in the string formalism, but is absent in the independent fragmentation framework, explains the failure of the string models

to fit the Energy-Energy Correlation function.

The incorporation of transverse momentum into the framework of string fragmentation is going to be a difficult task, and it is clear that such a goal cannot be accomplished as part of this study. However, the effect of adding uncorrelated (with respect to the string orientation) transverse momentum to the hadrons produced by string fragmentation can be investigated, and we now proceed to discuss the effects of doing this.

Since the absence of transverse momentum is most apparent in the CIT2-FME model combination, it was decided to add transverse momentum to this model combination. The procedure was as follows. Each hadron in the final event was associated with a parton, where the assignment depended on which parton had its initial direction most closely aligned with the final hadron direction. A Gaussian-distributed random P_t was then chosen, with a standard deviation of σ_q , and this was vectorially added to the hadron momentum vector in a direction perpendicular to the quark direction associated with each hadron. The resulting hadron momentum vector was then rescaled so that the total energy associated with the hadron was the same as it was before the transverse momentum was added. This way of adding transverse momentum clearly avoids the problems encountered when adding transverse momentum within the string framework, however, this kind of P_t is correlated to the parton directions, and not to the string directions. Within the string framework, the transverse momentum would have to be added at the string break points and should reflect the orientation of the piece of string that breaks as the P_t is generated. With these deficiencies in mind, we now present the results of this introductory study.

The addition of transverse momentum had the expected effect on the Thrust distribution, of moving events out of the region near $T=1$, towards lower Thrust values. The mean values of the Thrust and narrow-side Thrust distributions are

	Data	100 [MeV]	150 [MeV]	200 [MeV]	250 [MeV]	300 [MeV]
$\langle T \rangle$	0.9002	0.9063	0.0944	0.9022	0.8981	0.8937
$\langle T_N \rangle$	0.9395	0.9447	0.9429	0.9400	0.9372	0.9345

Table 7.1 The mean Thrust and narrow-side Thrust for the data and CIT2-FME model with various amounts of additional transverse momentum

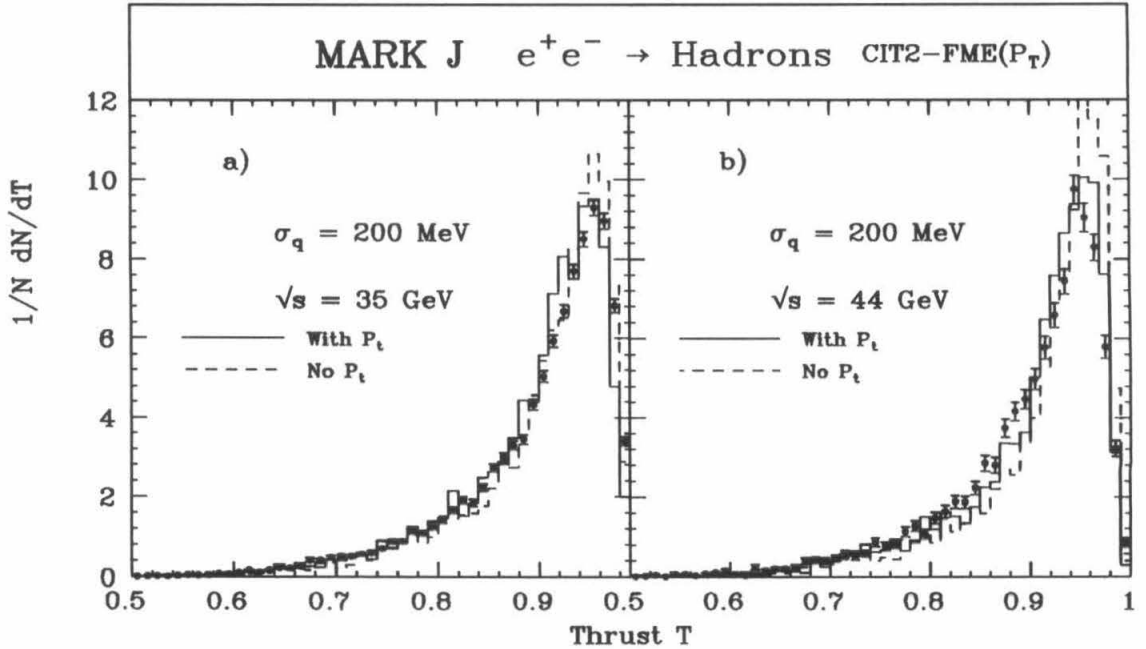


Figure 7.24 The modified CIT2-FME model predictions for the Thrust compared to the data at 35 GeV, a), and 44 GeV, b). The dashed line shows the prediction for the unmodified model.

given as a function of σ_q , for a fixed value of α_s of 0.15, in Table 7.1. The Thrust distribution obtained with $\sigma_q=200$ MeV and $\alpha_s=0.15$ is compared to the data at both 35 and 44 GeV in Figure 7.24. From Figure 7.24 it can be seen that the width of the jets has increased and the spike at high Thrust values has been removed. The quality of the agreement has improved in the intermediate low Thrust region, but in the intermediate high Thrust region, the model now overpredicts the number of events. It should be remarked at this point that the addition of transverse momentum has brought the acceptance obtained with this model into line with those obtained with

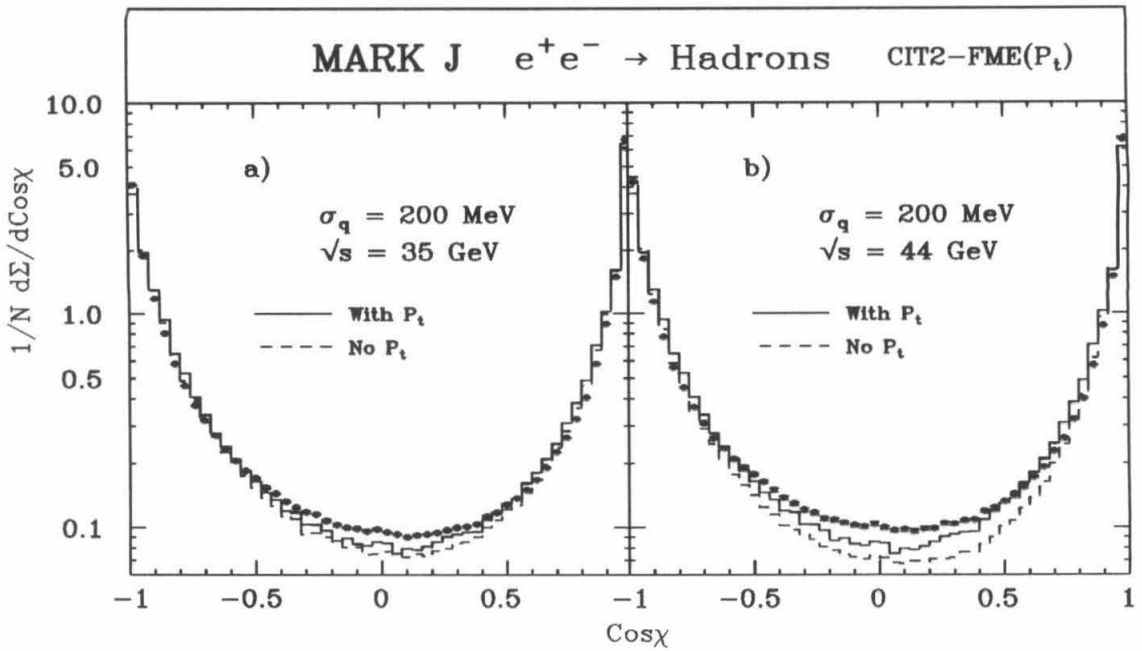


Figure 7.25 The modified CIT2-FME model predictions for the Energy-Energy Correlation function compared to the data at 35 GeV, a), and 44 GeV, b). The dashed line shows the prediction for the unmodified model.

the Ali and Lund models.

The effect of adding transverse momentum to this model combination on the prediction for the Energy-Energy Correlation function is shown in Figure 7.25. Again, it can be seen that the addition of transverse momentum is a step in the right direction. However, adding additional transverse momentum to try and obtain agreement in the central region of the plot destroys the agreement in the region near $\cos\chi=1$. The equivalent plot for the energy flow with respect to the thrust axis for three jet events is shown in Figure 7.26. In the regions between the gluon and quark jets, the addition of transverse momentum has improved the agreement. In the region between the quark and antiquark jet, however, the change is minimal.

From Figures 7.24-7.26 it is apparent that adding a simple Gaussian P_t around the parton directions affects those event characteristics that are intermediate between the hard and soft components of the events. The flower plot indicates that

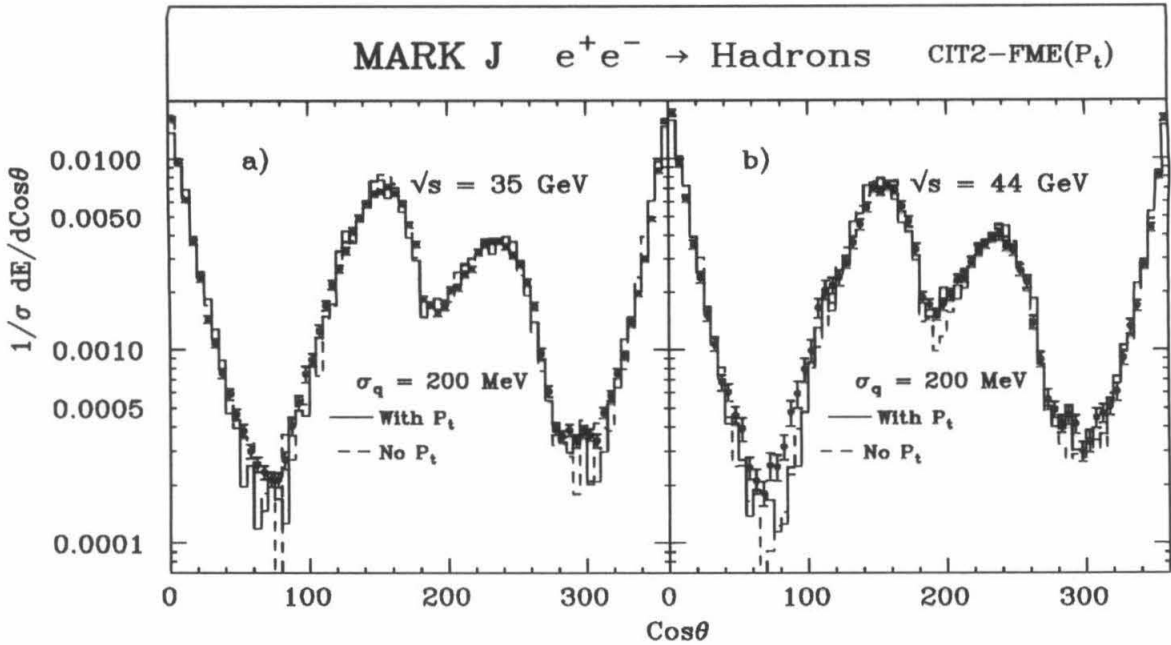


Figure 7.26 The modified CIT2-FME model predictions for the energy flow compared to the data at 35 GeV, a), and 44 GeV, b). The dashed line shows the prediction for the unmodified model.

there is still a deficiency in the number of soft particles being thrown into the region between the quark and antiquark jets.

A preliminary study showed that the agreement between the model predictions and the data could be improved if transverse momentum was added only to the soft hits in the events. In this context soft hits were defined to have $x = E_{particle}/E_{beam} < x_0$, where x_0 is a cut-off nominally chosen to be 0.07. Adding transverse momentum in this manner involves the introduction of two new parameters, σ_q and x_0 , so that tuning the modified model becomes a time consuming job. However, since the color charge carried by gluons is larger than that carried by quarks, QCD provides a definite prediction for the mean transverse momentum of gluon jets in terms of the mean transverse momentum of quark jets. The QCD prediction is that, at least asymptotically, the mean transverse momentum of the gluon jets is $\frac{9}{4}$ that of the quark jets. QCD also predicts that the particles in the gluon jet should have a softer fragmentation function than those in the quark jets. Therefore, by adding

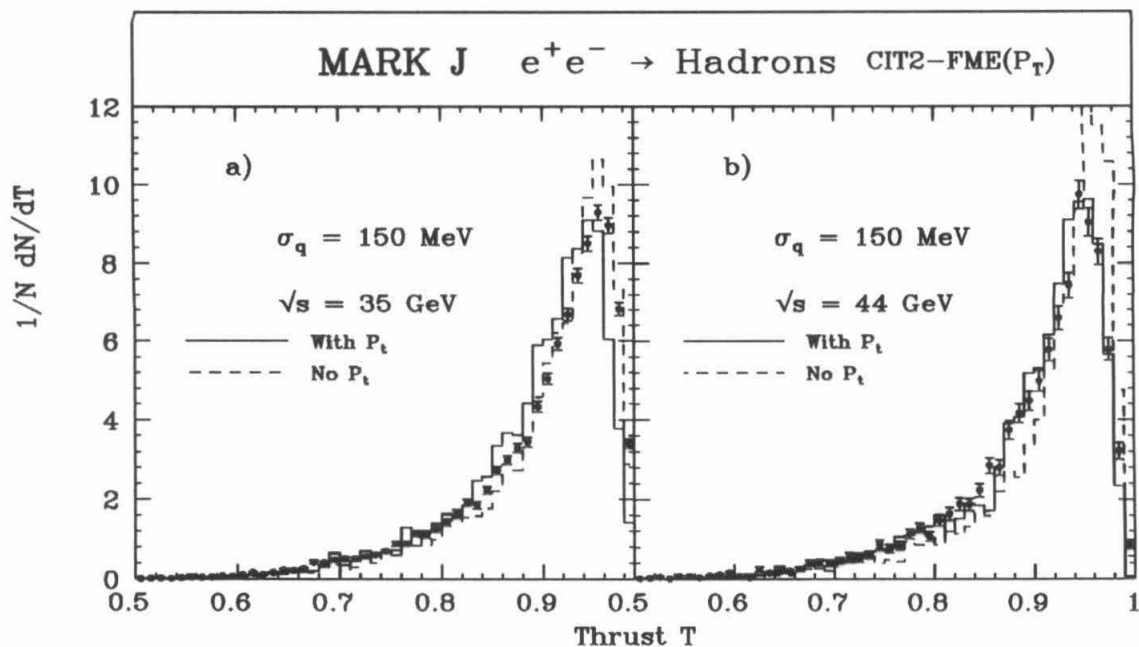


Figure 7.27 The second modified CIT2-FME model predictions for the Thrust compared to the data at 35 GeV, a), and 44 GeV, b). The dashed line shows the prediction for the unmodified model.

different transverse momenta to particles in the quark and gluon jets it is possible to preferentially impart transverse momentum to the soft components of the event.

The scheme outlined above was modified so that hadrons associated with a gluon were given a transverse momentum chosen from a Gaussian having a width $\sigma_g = \frac{9}{4}\sigma_q$. The results obtained from this scheme with $\sigma_q = 150$ MeV are shown in Figures 7.27 to 7.29. It can be seen that the results obtained with this modification are better than those obtained by adding transverse momentum uniformly to the event. From the flower plot it is evident that the addition of transverse momentum in this way has correctly populated the region between the gluon and quark jets, but that the modified model still underestimates the energy flow between the quark and antiquark jets. A more complete study would consider the factor $\frac{9}{4}$ as an adjustable parameter and simultaneously fit this ratio and σ_q .

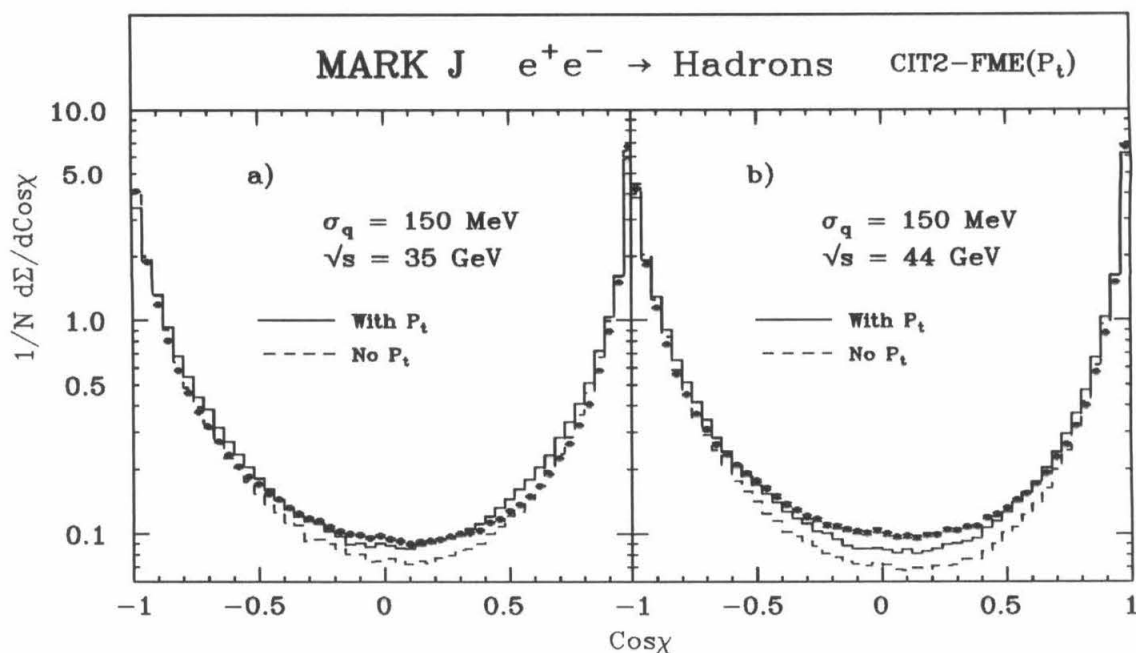


Figure 7.28 The second modified CIT2-FME model predictions for the Energy-Energy Correlation function compared to the data at 35 GeV, a), and 44 GeV, b). The dashed line shows the prediction for the unmodified model.

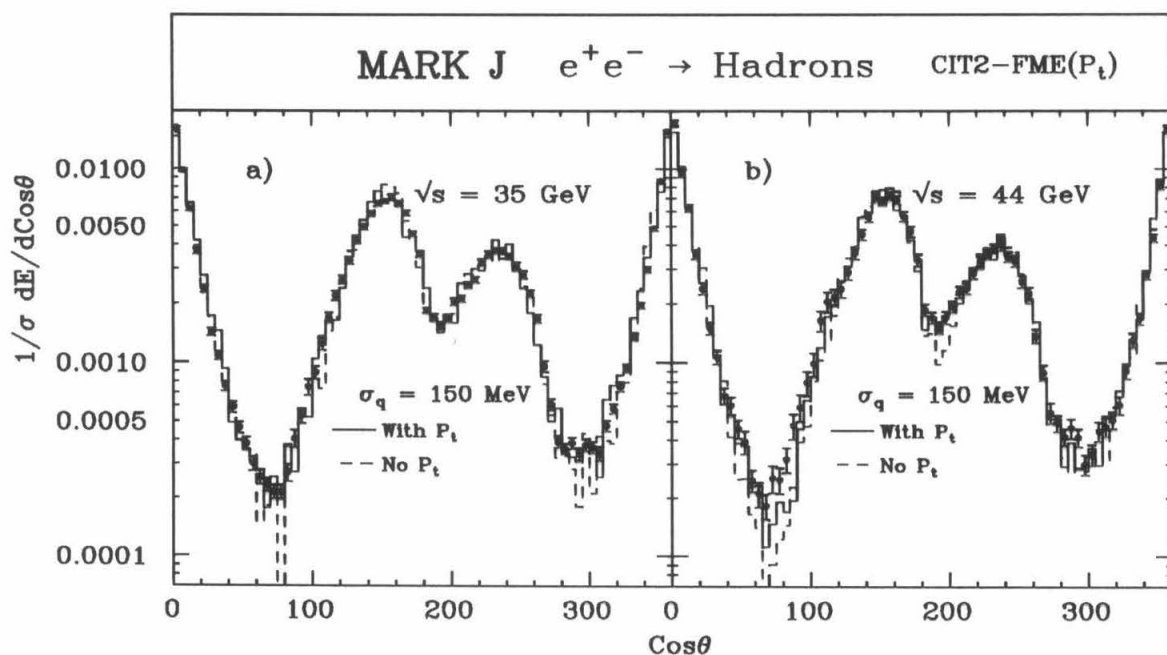


Figure 7.29 The second modified CIT2-FME model predictions for the energy flow compared to the data at 35 GeV, a), and 44 GeV, b). The dashed line shows the prediction for the unmodified model.

7.5.1 Conclusions

There are four main conclusions from this study:

- The string effect has not been observed in the MARK J data. However, the effect is observed in the Monte Carlo generated data, where its magnitude is seen to be dependent on the choice of fragmentation parameters used. This study concludes that the effect cannot be attributed to the effects of soft gluon coherence phenomena taking place at the perturbative QCD stage of the event evolution.
- The problem of incorporating transverse momentum into string fragmentation models needs to be resolved. It appears that the addition of transverse momentum correlated to the *parton* directions can significantly improve the agreement between the models and the data. This indicates that transverse momentum arises in e^+e^- annihilation through *both* fragmentation effects and effects occurring at the hard stages of the event evolution, when the participants still retain knowledge of the parton orientations. This conclusion is further reinforced by the observation that the CIT2-DLLA model correctly describes the transverse momentum structure of the events. It appears, therefore, that smearing the parton directions prior to fragmenting the partons is equivalent to fragmenting the partons, and then adding some transverse momentum correlated to the parton directions.
- Present day string models are incapable of simultaneously describing the Thrust and Energy-Energy Correlation. This appears to be partly due to the absence of a proper treatment of the way the particles acquire transverse momentum, and partly due to the lack of understanding of higher order corrections.

- The presence of a fixed mass cut-off in the string fragmentation models, in the form of the hadron mass scale that determines the termination of string evolution, causes faster than logarithmic evolution of the predictions for these models. They are unable to correctly describe the data at all energies.

Specific suggestions for improvements to be made to future fragmentation schemes are:

- The Caltech-II prescription for breaking colorless clusters off of strings is preferable to the Lund scheme, in which hadrons are peeled off of the strings directly. By scaling the W_{max} parameter in the Caltech-II scheme with Q^2 it seems likely that the faster than logarithmic evolution of the model predictions can be controlled.
- At present there seems to be no consistent way of incorporating transverse momentum into the string formalism at the string-break points. The problems associated with adding transverse momentum are more exaggerated for LLA-string fragmentation combinations due to the presence of many kinks on the strings. It seems likely that an approach similar to that briefly investigated here will have to be adopted. The Caltech-II scheme of imparting transverse momentum to the hadrons through the isotropic decays of colorless clusters appears adequate for hadrons originating in massive clusters. However, for hadrons originating in the decay of smaller clusters some additional transverse momentum is required.
- The possibility of simultaneously fitting the Energy-Energy Correlation function and the Thrust appears remote as long as higher order corrections are omitted from the models.

Chapter 8

Comment on Systematic Errors Assigned to α_s Measurements

8.1 General Considerations

The problem of extracting a value for α_s from the hadronic data obtained in e^+e^- annihilation has in the past caused much debate within the physics community. Most of the debate has centred on the following three topics: the validity of the perturbative QCD calculation used, the magnitude of the systematic uncertainty due to fragmentation effects, and the correct choice of a kinematic variable with which to make the measurement. The third point is, by now, well settled, with the result that the Energy-Energy Correlation Asymmetry is accepted as the variable of choice. The properties required of a variable from which α_s is to be extracted, aside from the obvious fact that it must be sensitive to the rate of hard gluon bremsstrahlung, are that:

- It must be possible to measure it experimentally with good resolution;
- The magnitude of contributions from higher order terms in the perturbation expansion must be small;
- It should be insensitive to the jet resolution cuts applied at the level of the perturbative calculation to determine the number of partons in the event;

- It should be relatively insensitive to fragmentation effects.

Since higher than $O(\alpha_s^2)$ calculations are not available, the higher order contributions to any variable must be estimated. This is achieved in two ways: the relative magnitudes of the first and second order contributions and the dependence on the parton-level jet-resolution cut are studied. If the second order contribution is small compared to the first order contribution, then it is assumed that the higher order corrections will be small as well. If the variable is stable under variation of the jet-resolution cut, the implication is that the higher order corrections are, at least, stable, since at the parton level the expansion representing these variables in powers of the resolution cut resembles the corresponding perturbation series. It has been shown that the 2^{nd} order contributions to the Energy-Energy Correlation function are small, and that its asymmetry is insensitive to variation in the jet resolution cuts [27,100,101,102,103].

The relative insensitivity of the Energy-Energy Correlation Asymmetry to the details of the fragmentation process has already been seen in Figure 6.9 where the χ^2 's obtained by comparing Σ_A to the data are seen to vary only slowly with changing σ_q . Other variables that have been used by PETRA and PEP experiments to extract α_s values have been: the integrated Thrust up to $T = 0.8$, the integrated broad-side Oblateness beyond $O_B = 0.3$, the three-jet rate as reconstructed with a jet-finding algorithm, and the transverse momenta of the events, both in and out of the event plane. None of these variables is as 'good' as Σ_A for extracting α_s , according to the criteria given above, although the rate of events having $O_B > 0.3$ comes close. Recent analysis by the MARK J on the 'Planar Triple Energy-Energy Correlation' gives consistent results, of similar quality to those obtained with Σ_A . The P.T.C also satisfies the 'good' variable criteria presented above [104].

The question of the validity of some of the earlier 2^{nd} order calculations used has also been resolved, and the discrepancies have been shown to come from the neglect

of terms of higher order in the jet resolution variables arising in the FKSS calculation [77]. The discussion of Chapter. 4, which shows that the GS calculation agrees with the ERT/Ali/Zhu calculation, confirms that these calculations are correct.

The question of the model dependence apparent in the α_s determinations has, however, persisted. Most groups report slightly higher values for α_s when string fragmentation schemes are used compared to the values obtained with independent jet models. The magnitude of these discrepancies has been steadily decreasing as the problems have become better understood. The original LundV4.3 Monte Carlo program, for example, incorporated the FKSS matrix elements, and so was apt to yield higher values for α_s . It was also found that the value of α_s obtained with independent jet models was sensitive to the method used to impose energy and momentum conservation at the end of the fragmentation [25].

Several detailed analyses aimed at extracting the value of α_s from the MARK J data have been performed previously, and it is not intended to duplicate that work here [27,18,105,51]. However, the availability of additional fragmentation models to this study makes it possible to reassess the uncertainties due to fragmentation effects in the α_s values obtained previously. The MARK J determinations (1983-1986) of α_s have used the asymmetry in the Energy-Energy Correlation, and recently the PTC. In these earlier determinations the Energy-Energy Correlation Asymmetry, $\Sigma_A(\cos \chi)$, was fitted to the data in the region $-0.72 \leq \cos \chi \leq 0.0$, and the bin-to-bin correlations in the distributions obtained for Σ were taken into account in the chi-squared determination.

Capell has thoroughly investigated the systematic uncertainties that arise in the MARK J α_s measurements from experimental sources, such as the acceptance criteria for hadronic events and the response of calorimeter elements [51]. The stability of the Energy-Energy Correlation against changes in the acceptance criteria is illustrated in Figure 8.1. In this figure the 44 GeV data used in this study (selected with

the 70/60/60 cuts and shown as the data points) is compared with data selected with various different selection criteria (shown as the histograms). It can be seen that the only major discrepancy occurs when no additional selection criteria are applied to the data, apart from the 35/50/50 cut that the event must pass to be written to the 'dst'. As discussed in Chapters 2 and 6, these distributions contain varying amounts of two-photon and tau-pair background. Further, the Energy-Energy Correlation function is insensitive to possible effects arising from miscalibration of the detector. In Figure 8.2 the 44 GeV data used in this study is compared to the same data but with the Z-position of the counter hits smeared with a Gaussian of full-width 20 cm. The smeared data is shown as the histogram, and the data points are the un-smeared data. It is clear that the two-jet events become slightly fatter, but the central region of the Energy-Energy Correlation is unchanged, as is the perturbative region of Σ_A .

In this chapter the new models investigated for the bulk of this study are used to further investigate the fragmentation model dependence of the α_s values extracted from the data. Since it has already been shown that the variation in the α_s values obtained are far more sensitive to the fragmentation models used than they are to the experimental details of the method used, in what follows, systematic errors due to the detector response are assumed small (previous MARK J studies show that detector effects lead to uncertainties in α_s of $\simeq 0.01$).

8.2 The Determination of α_s

For the purposes of estimating the magnitude of the variations in the values of α_s obtained with different fragmentation schemes, the elaborate methods required for the detailed studies mentioned above are not necessary. In this study the value of α_s has been extracted by fitting the prediction for Σ_A to the data over the $\cos \chi$ region -0.72 to 0, and from the broad-side Oblateness integrated beyond 0.3. A

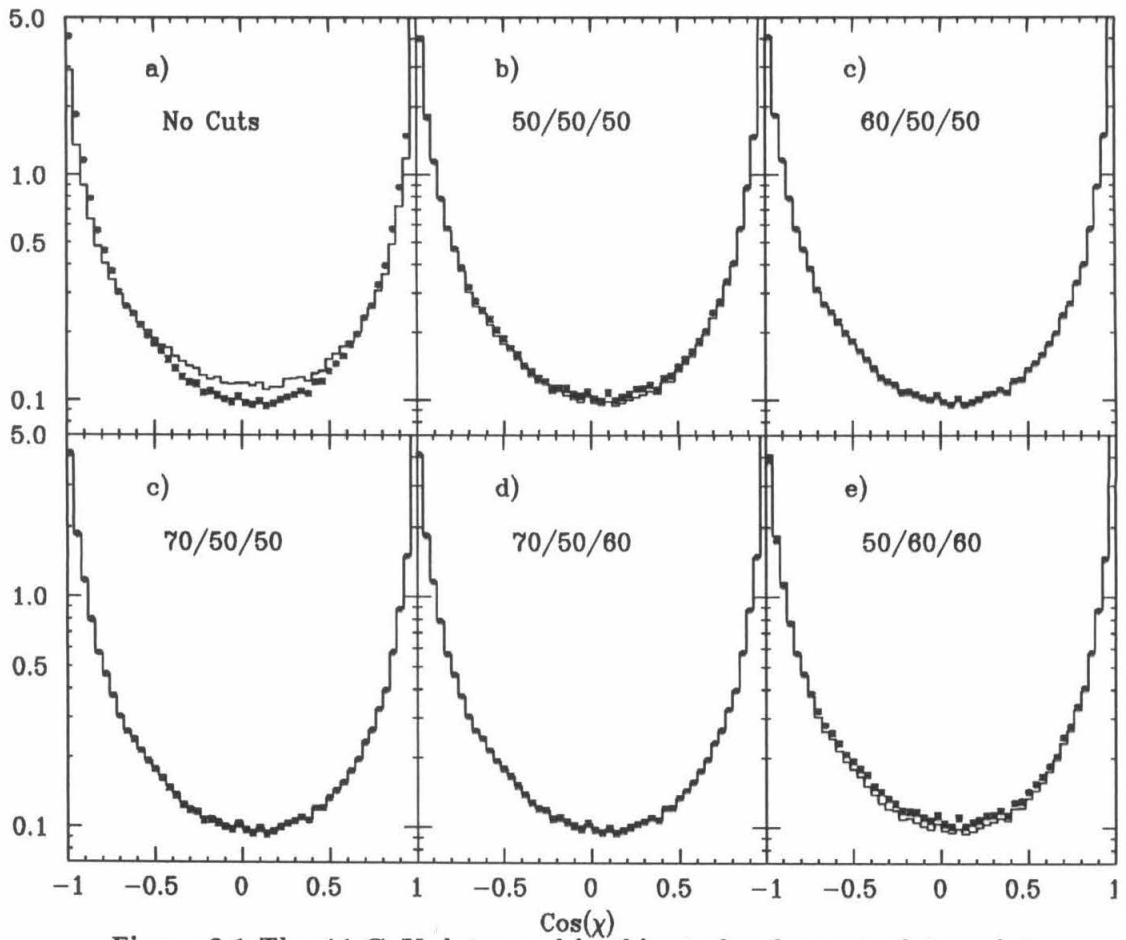


Figure 8.1 The 44 GeV data used in this study, shown as data points, compared to 44 GeV data selected with the selection criteria indicated in the individual panels.

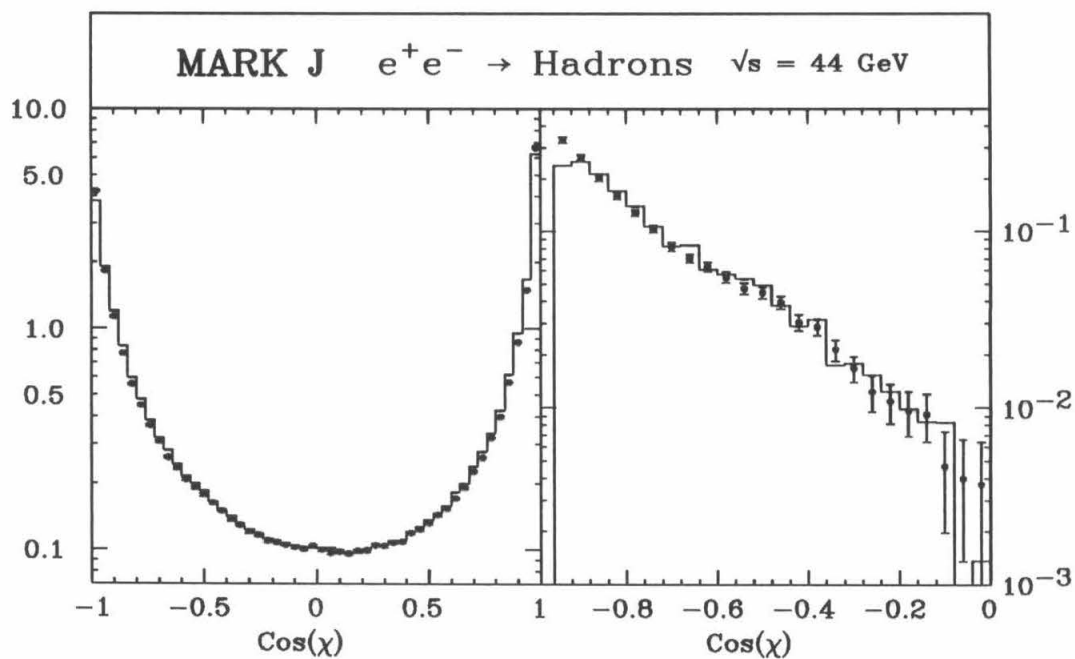


Figure 8.2 The 44 GeV data used in this study, shown as data points, is compared to the same data having had the Z-positions of the reconstructed hits smeared by a Gaussian of width 20 cm for the Energy-Energy Correlation function (left) and its asymmetry (right).

σ_q [MeV]	Σ_A	$\int_{0.3}^{\infty} O_B dO_B$	$\int_{0.5}^{0.8} T dT$
225	0.119 ± 0.009	0.122 ± 0.012	0.132 ± 0.010
250	0.124 ± 0.009	0.125 ± 0.013	0.125 ± 0.011
275	0.121 ± 0.009	0.138 ± 0.012	0.130 ± 0.012
300	0.121 ± 0.005	0.125 ± 0.014	0.112 ± 0.010
325	0.101 ± 0.010	0.116 ± 0.012	0.112 ± 0.010
350	0.091 ± 0.010	0.143 ± 0.012	0.092 ± 0.013

Table 8.1 The values of α_s obtained from the Ali model for the tabulated values of σ_q

σ_q [MeV]	Σ_A	$\int_{0.3}^{\infty} O_B dO_B$	$\int_{0.5}^{0.8} T dT$
300	0.146 ± 0.010	0.127 ± 0.007	0.195 ± 0.010
400	0.142 ± 0.010	0.135 ± 0.007	0.192 ± 0.010
500	0.142 ± 0.011	0.145 ± 0.012	0.177 ± 0.010
600	0.148 ± 0.015	0.146 ± 0.013	0.176 ± 0.010
700	0.146 ± 0.010	0.150 ± 0.010	0.148 ± 0.013
800	0.135 ± 0.015	0.150 ± 0.010	0.150 ± 0.013

Table 8.2 The values of α_s obtained from the LundV4.3 model for the tabulated values of σ_q

‘poor’ variable, the Thrust integrated up to 0.8, has also been used to determine α_s , for comparison.

The values of α_s obtained with the above three variables from the Ali model, for various values of σ_q , are shown in Table 8.1, for a center-of-mass energy of 35 GeV. The corresponding values for α_s extracted from the LundV4.3 model are given in Table 8.2. The values shown in Tables 8.1 and 8.2 are consistent, within errors, with results obtained previously [18]. The ability of the Ali and LundV4.3 models to describe the perturbative regions of Σ_A and O_B is illustrated in Figures 8.3 and 8.4. The plots shown in the right-hand panels are shown on a linear scale in Figure C.51 and Figure C.52.

In Table 8.3 the values obtained for α_s with the LundV6.3 model, at center-of-mass energy 35 GeV, are shown. The quality of the LundV6.3 fit to the data in

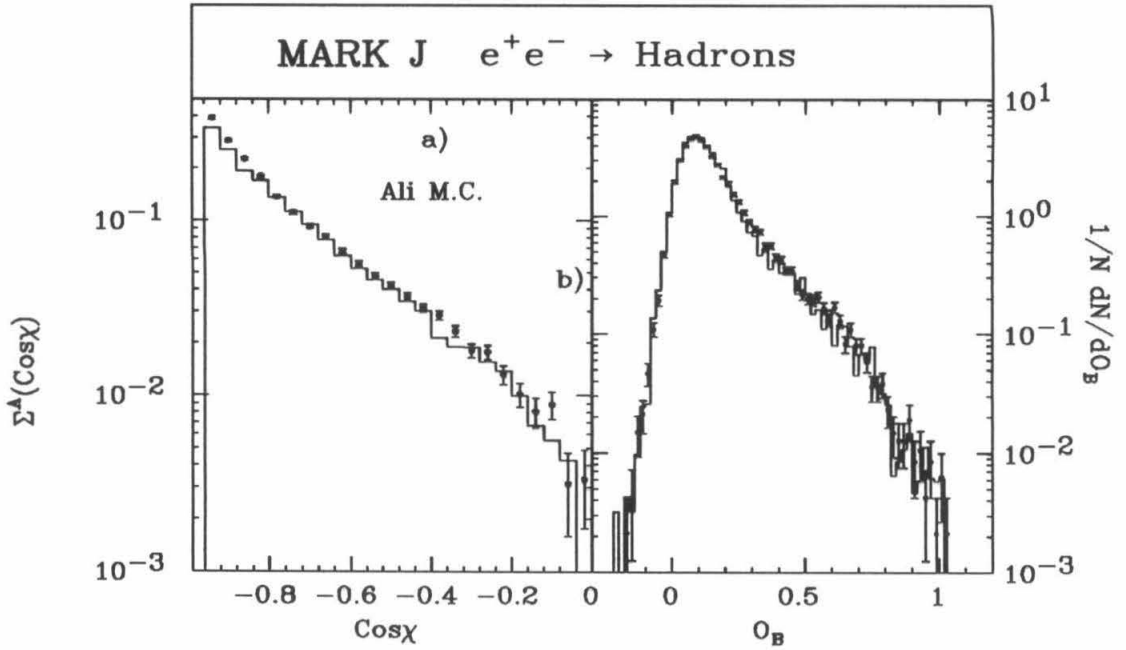


Figure 8.3 The predictions of the Ali model for Σ_A and O_B at 35 GeV, with $\alpha_s = 0.11$ and $\sigma_q = 300$ MeV

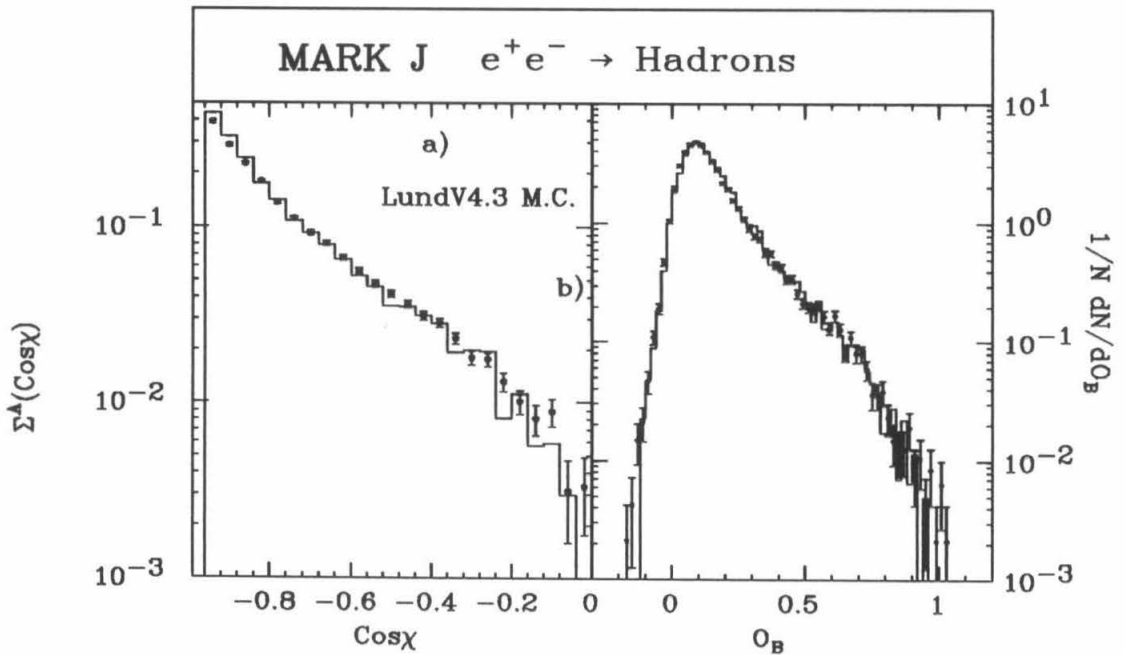


Figure 8.4 The predictions of the LundV4.3 model for Σ_A and O_B at 35 GeV, with $\alpha_s = 0.15$ and $\sigma_q = 700$ MeV

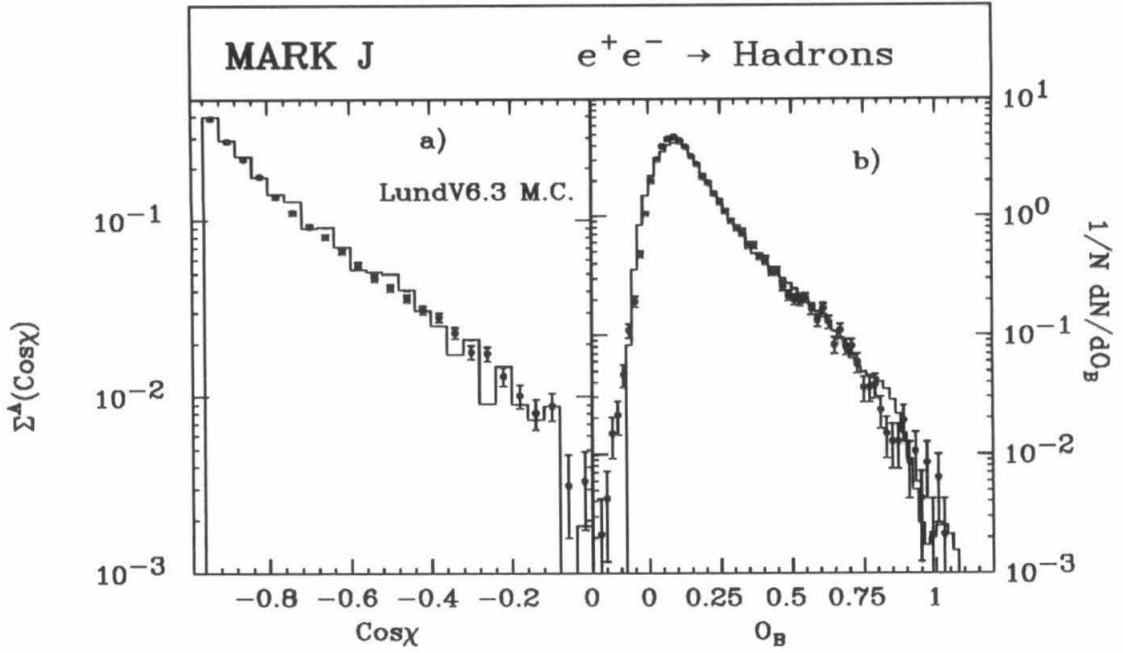


Figure 8.5 The predictions of the LundV6.3 model for Σ_A and O_B at 35 GeV, with $\alpha_s = 0.15$ and $\sigma_q = 500$ MeV

σ_q [MeV]	Σ_A	$\int_{0.3}^{\infty} O_B dO_B$	$\int_{0.5}^{0.8} T dT$
300	0.159 ± 0.011	0.139 ± 0.012	0.195 ± 0.014
350	0.159 ± 0.011	0.136 ± 0.012	0.192 ± 0.015
400	0.163 ± 0.011	0.145 ± 0.013	0.193 ± 0.014
450	0.141 ± 0.009	0.145 ± 0.013	0.175 ± 0.013
500	0.148 ± 0.010	0.152 ± 0.014	0.172 ± 0.013
550	0.157 ± 0.011	0.151 ± 0.014	0.170 ± 0.012
600	0.149 ± 0.010	0.145 ± 0.013	0.165 ± 0.012
650	0.152 ± 0.011	0.148 ± 0.013	0.175 ± 0.013
700	0.153 ± 0.012	0.144 ± 0.013	0.164 ± 0.012

Table 8.3 The values of α_s obtained from the LundV6.3 model for the tabulated values of σ_q

ρ/W_{max}	Σ_A	$\int_{0.3}^{\infty} O_B dO_B$	$\int_{0.5}^{0.8} T dT$
0.3/2.2	0.163 ± 0.013	0.165 ± 0.008	0.184 ± 0.012
0.4/2.2	0.147 ± 0.011	0.170 ± 0.008	0.192 ± 0.013
0.6/2.2	0.162 ± 0.012	0.155 ± 0.010	> 0.20
0.8/2.2	0.155 ± 0.011	0.150 ± 0.013	> 0.20
0.8/2.8	0.147 ± 0.009	0.135 ± 0.010	0.200 ± 0.013

Table 8.4 The values of α_s obtained from the CIT2-FME model for the tabulated values of ρ and W_{max}

the perturbative regions of the broad-side Oblateness and Σ_A can be judged from Figure 8.5, where the model predictions for $\alpha_s = 0.15$ with σ_q taken as 500 MeV are shown compared to the data. The broad-side Oblateness data shown here is presented on a linear scale in Figure C.53. The numbers shown in Table 8.3 are in agreement with preliminary numbers obtained by the members of the MARK J group. Their number, obtained by a fit to the Asymmetry distribution that includes the full covariance matrix, is 0.1543 ± 0.0051 .

The values obtained with the CIT2-FME model combination are given in Table 8.4. The ability of the CIT2-FME combination to fit the perturbative regions in Σ_A and O_B is shown in Figure 8.6 (also see Figure C.54).

From these tables it can also be seen that of the three jet measures investigated, the integrated Thrust shows by far the largest dependence on the fragmentation details, while fitting the Asymmetry shows the least, and the integrated broad-side Oblateness is intermediate between the two. The tables also show that the tendency for the string models to yield higher values of α_s than the independent jet models, that was reported for the earlier string models, is also seen in the two new string models investigated here.

It can also be seen, from the tables presented here, that the integrated Thrust is not, as had been previously believed, a suitable variable for making α_s measurements. The variation in the α_s values obtained with this variable as the frag-

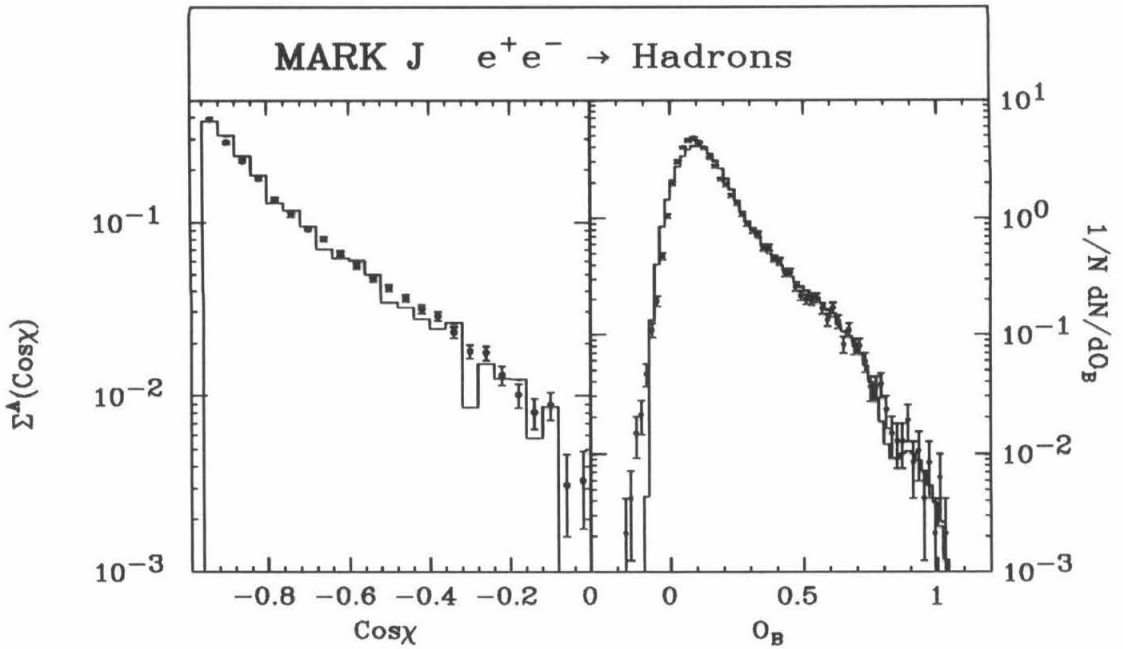


Figure 8.6 The predictions of the CIT2-FME model for Σ_A and O_B at 35 GeV, with $\alpha_s = 0.16$ and $\rho = 0.3$

mentation parameters are varied is large. This behavior is related to the apparent sensitivity of the Thrust on higher order corrections (as discussed in the previous chapter). Already, as can be seen from Figure 5.1, the magnitude of the second order corrections to the Thrust are large.

The systematic error on each individual α_s value is estimated from the variation between the α_s values given in the above tables. The variation in the α_s values obtained from the asymmetry and the Oblateness is of order 0.004, while the variation from changing the fragmentation parameters is of order 0.008. Accordingly, the systematic error on the individual α_s values is estimated to be ± 0.009 .

8.3 Discussion

The results presented in this chapter indicate that the present systematic errors assigned to α_s measurements on the basis of the fragmentation model dependence, of about 20%, are unchanged by the inclusion of two new fragmentation models. The

two models previously considered were regarded as extreme views of the fragmentation process; the true fragmentation effects are then assumed to be intermediate between the two. The two new models introduced in this study are closer in spirit to the LundV4.3 model than they are to the Ali model, and this is reflected in the values of α_s obtained here.

The values of α_s previously obtained in e^+e^- experiments are summarized in Table 8.5 and Figure 8.7. Only those measurements that employed the ERT calculation for the three-jet partial cross-section are shown. The corresponding results for the measurements using the FKSS calculation are given in Appendix D¹. The values obtained in this study are consistent with these previous measurements.

In particular, when α_s values obtained with the two Lund models are combined this study finds $\alpha_s = 0.147 \pm 0.014$. When the values obtained with *all* the string models are combined the average is $\alpha_s = 0.155 \pm 0.019$. Since the Caltech-II fragmentation scheme does not include a fragmentation function, or impart externally determined transverse momentum to the hadrons, we regard it as separate from the other string models investigated. We then find, for the ratio $\alpha_s^{String}/\alpha_s^{i.j.}$:

$$\alpha_s^{String}/\alpha_s^{i.j.} = 1.280 \pm 0.023, \quad (8.1)$$

where the average value of α_s from the two Lund models has been used. If we take the α_s obtained with the CIT2-FME model into account we obtain $\alpha_s^{String'}/\alpha_s^{i.j.} = 1.280 \pm 0.023$.

The Caltech-II fragmentation scheme can be regarded as a pure string model, since there is no arbitrary addition of transverse momentum. The remaining string models considered here, however, do add ‘arbitrary’ transverse momentum to the hadrons. In a sense the Caltech model should be considered as one extreme view of

¹The FKSS results are given only for completeness, since they appear in the literature. It must be emphasized, however, that these α_s values are systematically high, for the reasons discussed in Chapter 3 and Appendix 2 .

fragmentation, the Ali model the other extreme, and the Lund models as intermediate. From the discussion of the previous chapter it can be seen that the Caltech-II fragmentation scheme fails to fit the data in regions where transverse momentum plays a crucial role. The second of the two modified Caltech-II schemes that were introduced in the previous chapter, and that included transverse momentum added differently to the gluon and quark jets, is intermediate between the two extremes mentioned above. For this modified Caltech-II model the α_s value obtained is 0.133 ± 0.014 at 35 GeV when $\sigma_q = 150$ MeV ($\sigma_g = 337$ MeV). The value of α_s to be expected from a fully modified version of the Caltech-II scheme would be of this order.

Group	QCD	Frag.	α_s	$\alpha_s^{Str.}/\alpha_s^{i.j.}$	Ref.	Year	
MARK J	ERT	Lund	0.14 ± 0.010	1.272 ± 0.008	[18]	83	
		Ali	0.12 ± 0.010				
MARK J	ERT	Lund	0.134 ± 0.005	1.175 ± 0.007	[105]	85	
		Ali	0.114 ± 0.005				
TASSO	ERT	Lund	0.160 ± 0.012	1.280 ± 0.013	[21]	84	
		Ali	0.12-0.13				
PLUTO	ERT	Lund	0.145 ± 0.006	1.074 ± 0.008	[19]	85	
		Ali	0.135 ± 0.006				
TASSO	ERT	Lund	0.150 ± 0.018	1.190 ± 0.024	[106]	87	
		I.J. ^a	0.134 ± 0.016				
CELLO	ERT	Lund	0.161 ± 0.018		[106]	87	
		GS	Lund				0.159 ± 0.009
MARK II	GS	Lund	0.158 ± 0.011	1.264 ± 0.019	[107]	87	
		I.J. ^b	0.11-0.14				
MARK J This Work	ERT	Lund ^c	0.147 ± 0.014	1.215 ± 0.019		87	
		CIT2	0.163 ± 0.013				
		String ^d	0.155 ± 0.019				1.280 ± 0.023
		Ali	0.121 ± 0.013				

^aAverage over different independent jet models

^bAverage over different independent jet models

^cAverage value obtained with LundV4.3 and LundV6.3

^dAverage value obtained from all string models investigated

Table 8.5 Summary of α_s values obtained in e^+e^- annihilation near center-of-mass energies of 35 GeV. The errors shown on the values obtained in this study are statistical only, systematic errors are discussed in the text.

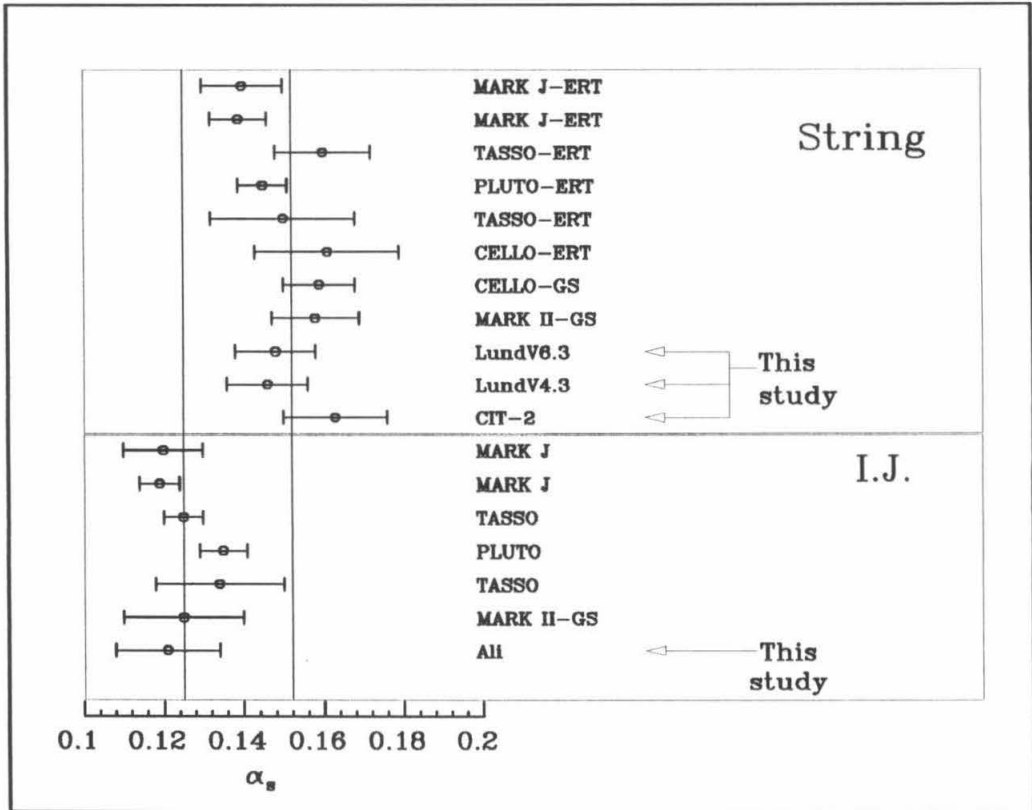


Figure 8.7 Comparison of α_s values obtained in e^+e^- annihilations. These values were all obtained from the asymmetry in the Energy-Energy Correlation function. The notation GS indicates a value extracted through the use of the Gottschalk-Shatz calculation.

Chapter 9

The Highest Energy Data from PETRA

9.1 Introduction

In August 1984 PETRA reached its highest operating energy of 46.78 GeV. At this time the the MARK J observed an unusual increase in the number of hadronic events produced with an accompanying muon, where the muons were well isolated from the hadronic energy in the events [108,52,53]. This is a clear signal for the production of a new quark flavor. At first the MARK J was the only PETRA experiment that reported this observation. Two years later, however, the JADE collaboration later reported identical findings using data taken at the same time as the MARK J in 1984 [53]. The MARK J signal consisted of 8 events having an accompanying muon and Thrust less than 0.8, where only 1.9 were expected. The JADE signal consisted of 5 events of this type where only 0.5 were expected. The luminosity available to the JADE experiment was 1.7 pb^{-1} , while the MARK J accumulated 2.8 pb^{-1} . The other PETRA experiments, CELLO and TASSO, accumulated luminosities of 2.2 pb^{-1} and 1.1 pb^{-1} respectively. Neither TASSO or CELLO report seeing anything unusual in this data, although it should be remarked that their acceptance for inclusive muons is significantly less than MARK J or JADE.

The numbers reported for these events are too small for them to be consistent

with the production of a new charge $2/3$ quark (top). The reported numbers are, however, consistent with the production of a new charge $1/3$ quark (b'). Generally the muon momentum is low, and both JADE and MARK J each have one event containing two muons.

In this chapter the results of a search for anomalous behavior in the extreme high-energy hadronic data are reported.

9.2 A Comparison Between the High-Energy Data and a Control Data Set at 44 GeV

The standard MARK J procedures for identifying the onset of top quark production in the hadronic data sample are: a measurement of the total cross section and the study of the event Thrust. On passing the top threshold the total cross section is expected to jump, and the event topologies are expected to change (the jump in R expected is shown in the next chapter).

If the virtual photon produces a quark antiquark pair each with mass near the beam energy, the quark and antiquark are produced nearly at rest, and their fragmentation into hadrons is nearly isotropic – such events have low Thrust values. On the other hand, for a quark antiquark pair produced well above threshold, the Lorentz transformation of the resulting fragmentation products into the lab frame results in well collimated jets of hadrons, and the events have high Thrust. If a new heavy flavor production threshold is crossed, the number of low Thrust events is expected to increase.

In Figure 9.1 the Monte Carlo prediction for Thrust is compared to the high energy data for the case when top production is permitted, and for the case when only 5 flavors can be produced. The left hand panel of the figure shows the data obtained at E_{cm} between 44 GeV and 46 GeV, while the high energy data is shown in the right hand panel. The 6-quark predictions shown in this figure are obtained

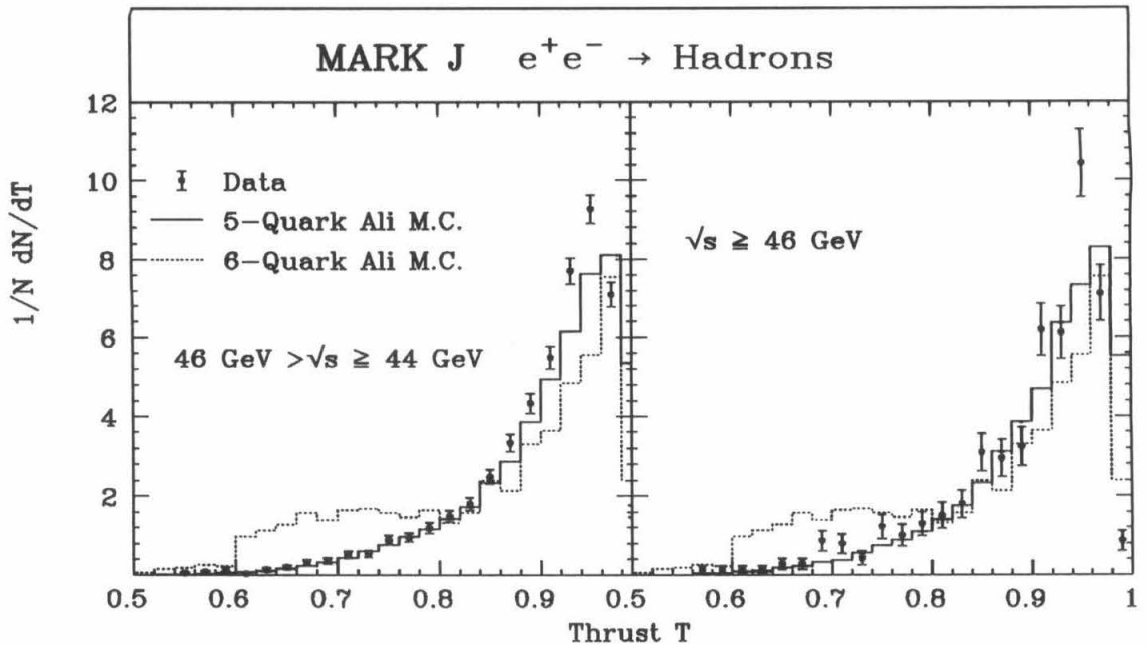


Figure 9.1 The Monte Carlo predictions for Thrust in the 5-quark and 6-quark cases. The high energy data is shown on the right, and the data taken between 44 and 46 GeV is shown on the left.

with a top quark mass of 20 GeV, and the Ali fragmentation scheme was used. While it is clear that the data shown in the right hand panel is in disagreement with the 6-quark prediction, it is also clear that the agreement with the 5-quark model is worse for the high energy data than for the lower energy data.

While the data shown in Figure 9.1 are suggestive, it is evident that the Monte Carlo predictions are insufficient for the purposes of investigating the high energy data for the presence of new physics. Therefore, rather than compare the data to the Monte Carlos, we choose to compare the high energy data to a control data set taken at center-of-mass energies between 44 and 46 GeV. The main interest in this comparison is the identification of a discrepancy in the hadron data that reflects similar tendencies to those found in the inclusive muon data. Since the inclusive muon data is suggestive of a new quark flavor, we search for an excess of events consistent with the onset of a new flavor threshold. The main advantage of comparing two data sets, rather than comparing the data to a Monte Carlo prediction,

is the elimination of Monte Carlo uncertainties. Further, by comparing data with data the problem of having only calorimetric data available is also removed, and we need no longer restrict ourselves to infrared safe variables alone. Indeed, we may use non-infrared safe variables as tools for searching for changes in the soft structure of the event topologies.

A preliminary study was made with the aim of identifying variables that were sensitive to the onset of new flavor production. Apart from Thrust, the following variables were found to display sensitivity to new flavor production: Sphericity, Aplanarity, and the first four Fox-Wolfram event moments [109,110]. Of these variables Sphericity is non-infrared safe, while the remainder are safe. The Fox-Wolfram moments are a generalization of the Energy-Energy Correlation function defined previously. They are defined in terms of the energy deposits in calorimeter elements and the Legendre polynomials as follows:

$$H_l = \frac{1}{\sqrt{E_{vis}}} \sum_{i,j} (\vec{E}_i \cdot \vec{E}_j) P_l(\cos \theta_{ij}). \quad (9.1)$$

The odd Fox-Wolfram moments tend to be sensitive to two-jet structure in the events, while the even moments are sensitive to spherical event topologies. For the odd moments two-jet events contribute to the distributions near 0, and for the even moments they contribute near 1. For spherical events the even moments are small and the odd moments are close to 0.5. It can be shown that the even moments are closely related to the Thrust. However, we find that these variables have differing sensitivity to top production and so we continue to use them. For both the high energy data and the low energy control data, the distributions in these variables were determined and a detailed comparison between the two data sets made. After applying 70/60/60 cuts, there were 663 events in the high energy sample and 3442 events in the control sample¹. The results of the comparison are shown in Figures 9.2(a) and (b), 9.3(a) and (b) and 9.4(a) and (b). From the

¹This analysis was performed before the 1986 data at 44 GeV had been analyzed.

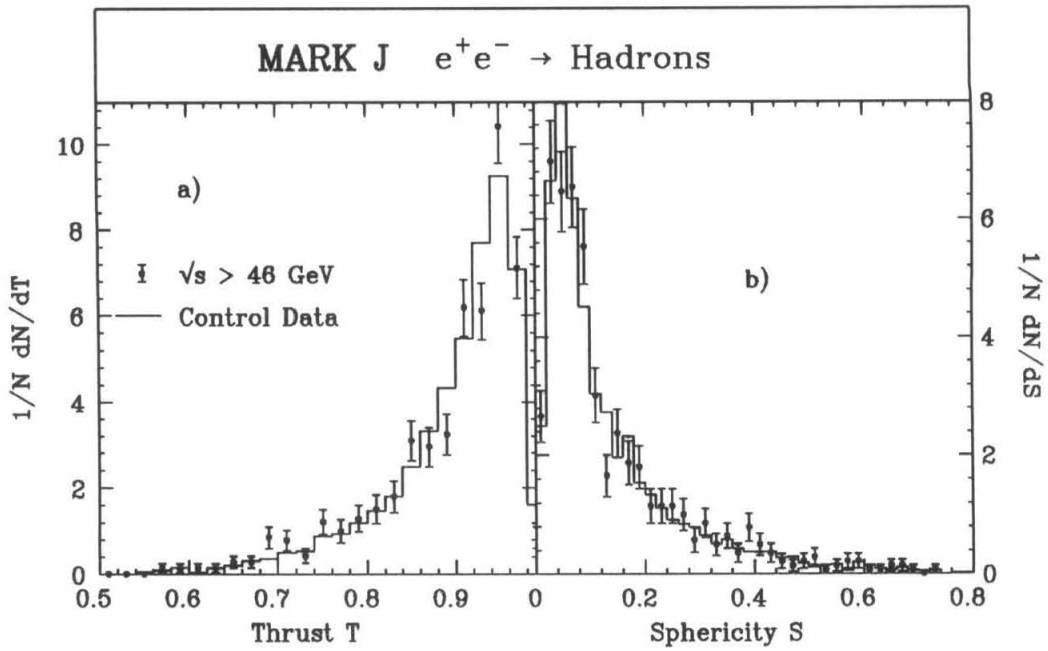


Figure 9.2 a) The Thrust distribution for the high energy data compared to the low energy control data. b) As a), but for Sphericity. The high energy data is shown as the data points, while the control data is presented as the histogram.

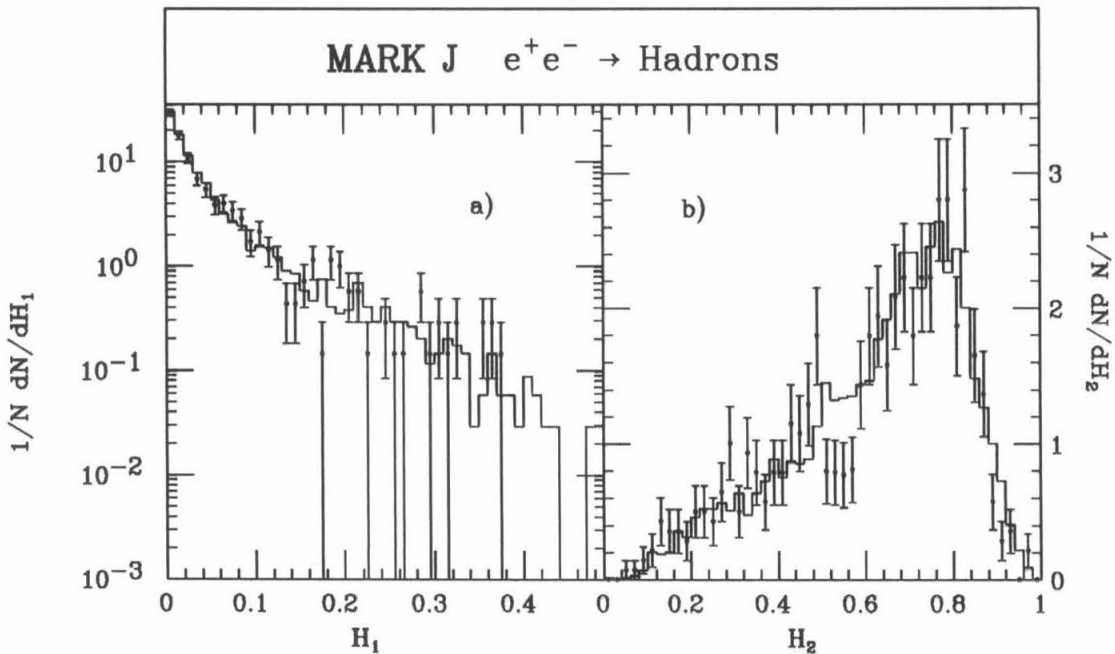


Figure 9.3 a) The distribution in H_1 for the high energy data compared to the low energy control data. b) As a), but for H_2 . The high energy data is shown as the data points, while the control data is presented as the histogram.

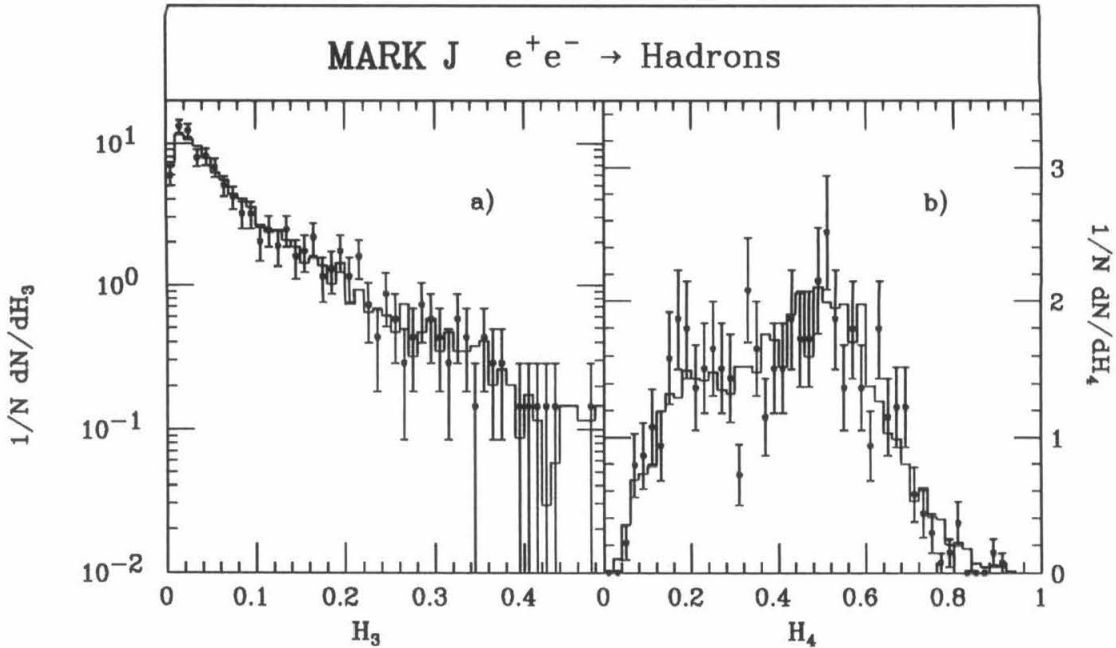


Figure 9.4 a) The distribution in H_3 for the high energy data compared to the low energy control data. b) As a), but for H_4 . The high energy data is shown as the data points, while the control data is presented as the histogram.

figures it can be seen that the differences exhibited between the two data sets are small, but that where there are differences, they are consistent with a small excess of spherical events in the high energy data sample.

In order to further investigate the statistical significance of the deviations visible in the plots, cuts were applied to the distributions. On the basis of the Monte Carlo study, these cuts were chosen such that the events contributing above, or below, the cut are predominately from top production. The cuts selected are given in Table 9.1, where the means of the distributions for the high energy and control data sets are also shown. The control data set was used to predict the number of events expected in the high energy data above, or below, the appropriate cut for each distribution. The results of this are presented in Table 9.2. The numbers show that the high energy data is consistent with the control data, apart from a minor discrepancy in the number of high Sphericity and low Thrust events.

Variable	Cut	\langle Control \rangle	\langle H.E. Data \rangle
H_1	≥ 0.10	0.0469(8)	0.0482(18)
H_2	≤ 0.54	0.6279(11)	0.6140(105)
H_3	≥ 0.10	0.0862(15)	0.0861(33)
H_4	≤ 0.28	0.4141(70)	0.4054(154)
Thr	≤ 0.75	0.8988(153)	0.8927(338)
Apl	≥ 0.20	0.0714(12)	0.0754(285)
Sph	≥ 0.14	0.1347(23)	0.1386(53)

Table 9.1 The cut-regions selected to search for top in the high energy data, and the means of the distributions shown above, for the control data and the high energy data. Numbers in parenthesis are statistical errors.

Variable	Expected Events	Observed Events	Deviation [σ 's]
H_1	92.00 ± 4.3	96 ± 9.1	0.30
H_2	238.6 ± 7.2	238 ± 12.5	0.00
H_3	203.8 ± 6.4	211 ± 12.1	0.38
H_4	208.5 ± 6.5	231 ± 12.4	1.19
Thr	45.90 ± 3.0	62 ± 7.5	1.52
Apl	33.77 ± 2.6	40 ± 6.1	0.72
Sph	198.8 ± 6.3	239 ± 12.5	2.14

Table 9.2 The number of events in the cut region expected from the control data compared to the actual number observed in the high energy data. The right hand column gives the discrepancy in standard deviations.

Variable	χ^2	N d.o.f.	Significance [%]
H_1	37.18	34	40
H_2	56.71	46	17
H_3	25.81	44	100
H_4	49.07	41	17
Thr	36.08	42	75
Apl	22.21	36	90
Sph	46.40	42	35

Table 9.3 The results of a χ^2 comparison between the control data and the high energy data. The right hand column gives the probability that the two data sets were sampled from a common source.

Variable	$ D_{mn} \times 10^{-2}$	Significance [%]
H_1	3.0	>30
H_2	5.7	5
H_3	2.1	>30
H_4	3.2	27
Thr	3.9	19
ApI	4.1	17
Sph	2.1	>30

Table 9.4 The results of applying a Kolmogorov-Smirnov test of the comparison between the control data and the high energy data. The right hand column gives the probability for D_{mn} to take a value as large as the tabulated value.

Region	Expected Events	Observed Events	Deviation [σ 's]
$T_N < 0.8$	18.5±2.5	27±5.2	1.1
$T < 0.8$ and $O > 0.3$	15.4±2.4	22±4.7	0.9
$T < 0.8$ and $O_B > 0.3$	21.4±3.0	30±5.5	1.0
$T < 0.8$ and $m_B > 0.3$	15.8±2.4	14±3.7	-0.3
$T < 0.8$ and $M_B > 0.7$	16.2±2.4	18±4.2	0.3
$T_N > 0.9$ and $O_B < 0.2$	402.5±31.4	386±19.6	-0.3
$T_N > 0.9$ and $O_B > 0.3$	36.7±4.4	31±5.6	-0.1
$T_N < 0.9$ and $m_B > 0.3$	7.4±1.4	6±2.4	-0.4
$T_N > 0.9$ and $M_B < 0.3$	296.3±24.0	291±17.1	-0.1
$T_B < 0.8$ and $O > 0.2$	49.5±5.5	60±7.7	0.8
$T_B < 0.8$ and $O_B > 0.3$	45.8±5.2	60±7.7	1.1
$T_B > 0.8$ and $m_B < 0.3$	424.9±32.9	395±19.9	-0.6
$T_B < 0.8$ and $M_B > 0.7$	18.2±2.7	22±4.7	0.5

Table 9.5 The number of events in various cut regions expected from the control data compared to the actual number observed in the high energy data. The right hand column gives the discrepancy in standard deviations.

Returning to Figures. 9.2 to 9.4, it can be seen that simply counting events above, or below, the cut is not necessarily the best way to compare the two data sets: the differences are often in the form of a bump or a dip. In order to compare the two data sets in a more reasonable manner then, a χ^2 test is made to the hypothesis: that both the high energy data and the control data were sampled from a common data set. The test statistic used is:

$$\chi^2 = \sum_i^N \frac{(n_{pi} - n_{oi})^2}{n_{pi}}, \quad (9.2)$$

where n_{pi} is the predicted contents of the i^{th} bin obtained by extrapolating from the control data, n_{oi} is the observed contents in the i^{th} bin of the corresponding distribution for the high energy data, and N the number of non-trivially empty bins in the histograms. The results of the χ^2 comparison are shown in Table 9.3

As a further comparison a Kolmogorov-Smirnov test was performed. In this test, rather than compare the distributions directly, the cumulative distributions are compared. The maximum difference between the two cumulative distributions is then found, and the magnitude of this difference is used to determine the probability that the two data sets were sampled from a common source. The test statistic in this case is:

$$D_{mn} = \max |S_m(x) - S_n(x)|, \quad (9.3)$$

where S_m and S_n are the cumulative distribution functions of the two data sets containing m and n events respectively. The results obtained with this test are shown in Table 9.4

It is also possible to compare the two data sets by comparing their population of certain regions in scatter plots. Since the results above hint at a slight excess of spherical events, the regions of the scatter plots investigated were chosen to be those populated by spherical events. The possibility that narrow jets were missing from the high energy data set was also investigated by studying the narrow-side

Thrust distribution. The scatter plot regions investigated were selected on the basis of a Monte Carlo study to be sensitive to new flavor production mechanisms. The regions, their expected contents on the basis of the control data set, and their observed contents are given in Table 9.5.

9.3 Comparisons with the Multidimensional Discriminant Function

As a final test of the high energy data, the methods of multidimensional discriminant analysis were applied. The idea here is to combine the information from several distributions into a single distribution. Consider the situation illustrated in Figure 9.5, where two hypothetical data sets are plotted in the two variables: A and B. If the two data sets had been plotted as a histogram in either one of the two variables, it would be impossible to separate the data into two classes. On the other hand, when information from both variables is used at the same time, by making a scatter plot, the separation of the data into two distinct classes becomes clear. Multidimensional discriminant analysis generalizes this idea from a scatter plot in two dimensions to one in an arbitrary number of dimensions. The method relies on finding a line, such as that shown in the figure, in the higher dimensional space formed by the variables being considered, onto which the data can be projected. This line must be found by Monte Carlo studies and is obtained by fitting so that the maximum separation between the two event classes is achieved.

For this study the variables used above were combined to give a line having the form:

$$0 = \frac{a_1A + a_2T + a_3S + a_4O + a_5H_2 + a_6H_3 + a_7H_4}{N}, \quad (9.4)$$

where,

$$N = 1/\sqrt{\left(\sum_{i=1}^7 a_i^2\right)}. \quad (9.5)$$

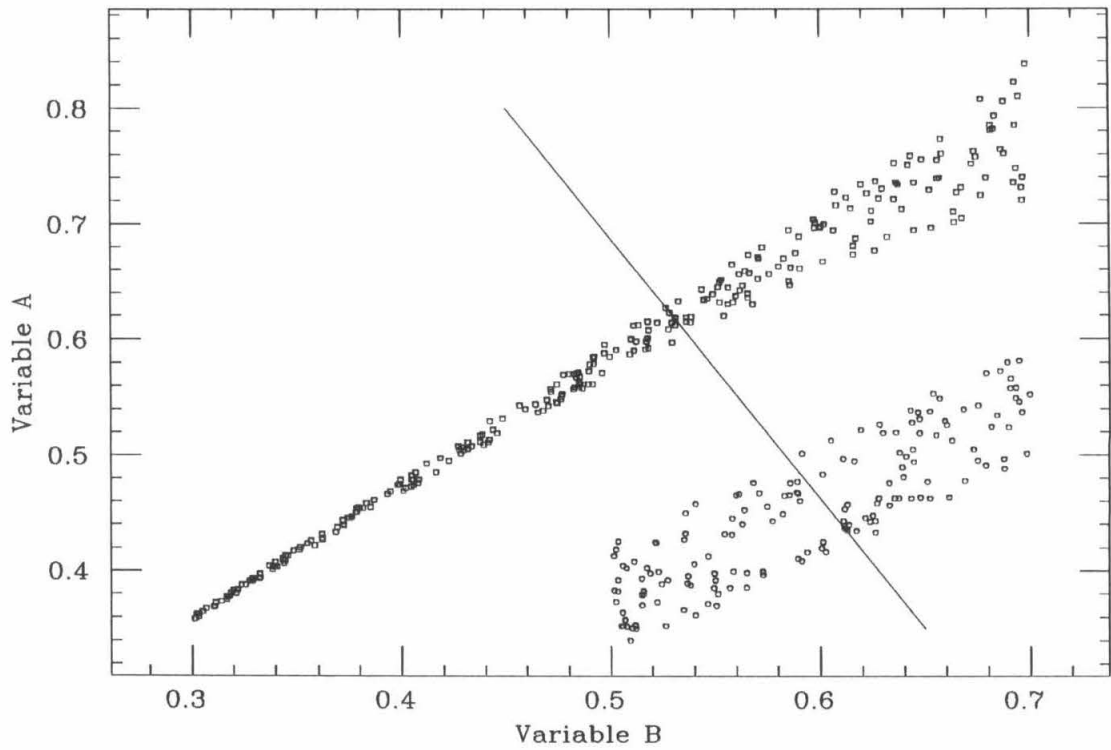


Figure 9.5 Hypothetical example of two data sets plotted in the plane formed by two variables. While the two data sets are not distinguishable in either variable, the combined variable, shown as a line, provides 100% separation.

a_1/A	a_2/A	a_3/A	a_4/A	a_5/A	a_6/A	a_7/A
-0.0036	-0.0037	-0.0042	0.6547	-0.6415	0.3842	-0.1102

Table 9.6 The values of the coefficients defining a line that optimizes the separation of a top enriched hadron data sample from the background

The coefficients, a_i , were determined by a least squares fit that maximized the quantity:

$$\chi^2 = \frac{M_b - M_t}{\sigma_b^2 + \sigma_t^2}. \quad (9.6)$$

M_t and M_b are the means of the distribution obtained by projecting events generated at 35 GeV, with a 20 GeV top quark, and at 35 GeV with u,d,s,c, and b quarks only, onto the line, respectively. σ_a^2 and σ_b^2 are the corresponding variances of the two distributions.

The coefficients for the equation given in Eqn. (9.4) obtained by the least squares fit are given in Table 9.6. The results of projecting the Monte Carlo generated events onto the line defined by these coefficients are shown in Figure 9.6. In Figure 9.6, the contribution from the top containing events is shown with the dash-dotted line, that from the u,d,s,c and b event background with a dashed line, and the total distribution is shown by the solid histogram. It is clear that the discriminant function provides much better separation than the Thrust shown in Figure 9.1. The result of applying this discriminant function to the data is shown in Figure 9.7. It can be seen that the high energy data and the control data are similar. Both the χ^2 and the Kolomogorov-Smirnov test exclude the presence of new phenomena at the 30% confidence level.

9.4 Discussion

The analysis presented here has shown that no claim can be made, on a firm statistical basis, for the observation of new phenomena in the highest energy hadronic

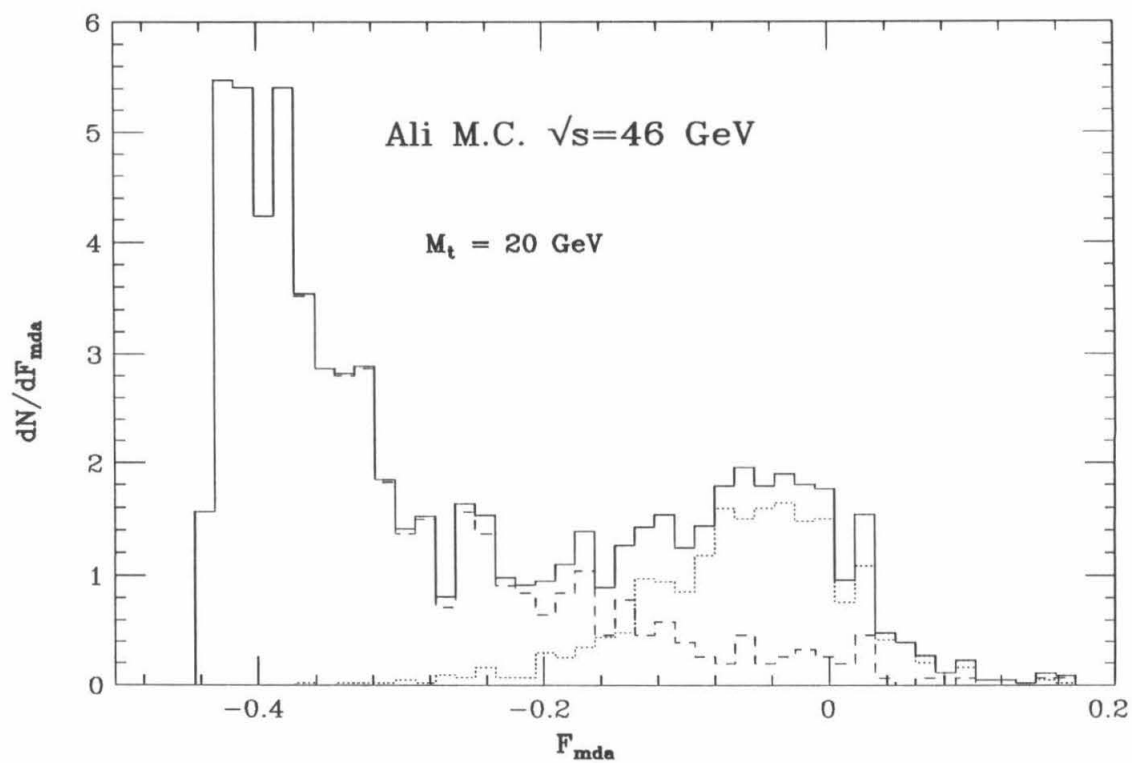


Figure 9.6 The separation achieved with the multidimensional discriminant function of the text for events containing a 20 GeV top quark from the background events.

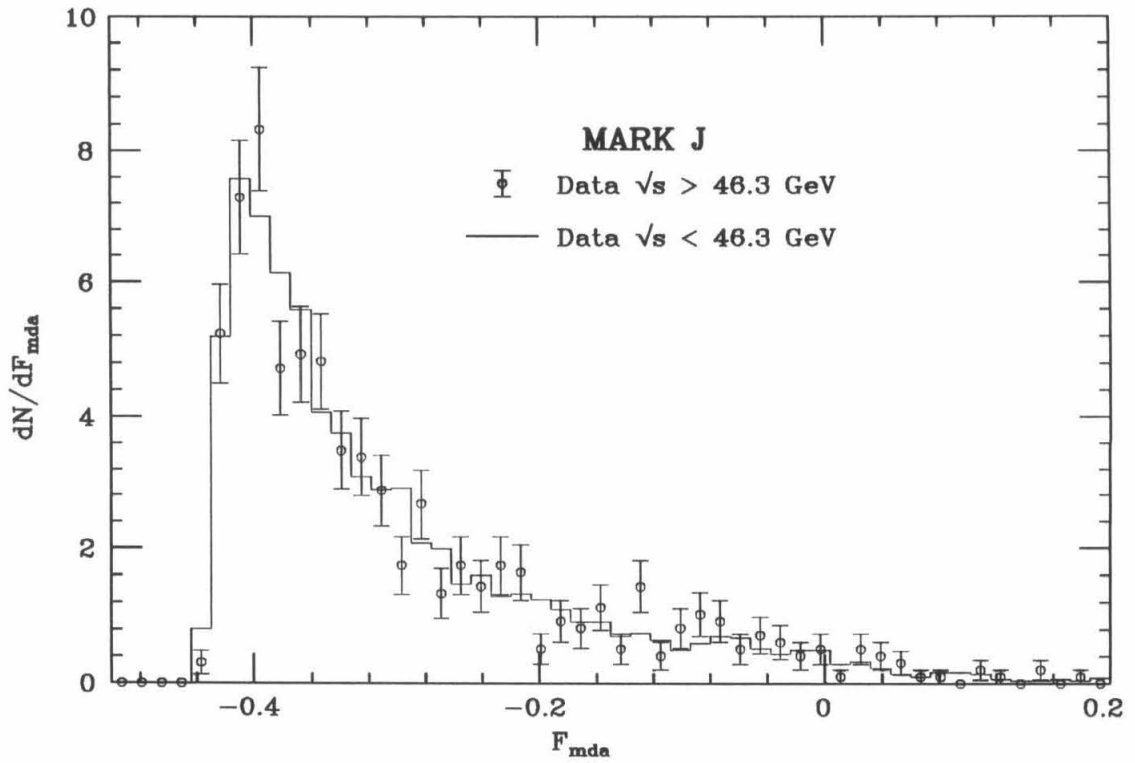


Figure 9.7 The distributions obtained with the multidimensional discriminant function of the text, for the high energy data and the low energy control data set.

data taken at *PETRA*. The inclusive muon signal still remains, however, and the resolution of the mystery will have to wait for results from *TRISTAN*, *SLC* and *LEP*. The detailed analysis of the inclusive muon signal shows that the events are planar, which seems incompatible with the idea that these events have their origin in a newly produced quark. Further, the *JADE* experiment sees no signal in their electron channel, which is also inconsistent with the production of a new quark. In fact, the observation of a signal in the muon, but not in the electron, channel is inconsistent with $\mu - e$ universality and presents one of the biggest mysteries related to these events.

Chapter 10

Top Production in e^+e^- Annihilation at LEP Energies

10.1 Introduction

One exciting possibility for the future (ca. 1990-1992) is the discovery of the Top quark at LEP, (which will explore the center-of-mass energy range up to 200 GeV). Until 1987, PETRA experiments only ruled out Top quark masses below 23 GeV [111]¹. Apart from providing a missing piece to the Standard Model, the discovery of the Toponium resonance will most likely provide the opportunity to perform spectroscopy-type experiments and, so further investigate the quark-antiquark potential. If it turns out that the mass of the Top is less than 1/2 that of the Z^0 , Top containing final states would be expected to be copiously produced at LEP-I (which will cover the energy range up to 110 GeV).

When a Top quark is produced in $e^+e^- \rightarrow Z^0 \rightarrow X$ there are expected to be several possible signatures:-

- The total hadronic cross section is expected to jump abruptly as one passes over the Toponium production threshold.

¹At the Hamburg conference in 1987 the UA1 collaboration presented data that apparently rules out a Top quark mass below 45 GeV. This study, however, was performed prior to this conference and so used the earlier estimates for the quark mass. The general conclusions are still valid for the heavier quark.

- Since the Top quark has a sizable branching ratio for semi-leptonic decays, the inclusive lepton rate is expected to jump on crossing the production threshold.
- For the same reason that one expects to see a rise in the total inclusive lepton rate on crossing the Top threshold, one would also expect to see an increase in the inclusive multi-lepton rate.
- The event shapes of Top events are expected to be different from the ‘background’ events. In particular for events in which the Top decays hadronically, the events are expected to be more spherical, and less ‘two-jetty’. This is partly due to the fact that the Top quark is far more massive than the background quarks and so is produced with low velocity, and partly due to the 3-jet decays $t\bar{t} \rightarrow ggg(\gamma)$, which produce planar spherical events and are expected to be present in Toponium resonance decays.
- For events in which the Top quark decays semi-leptonically into hadrons and a muon, the event topology is also expected to differ from background processes. The muon in such events is expected to be well-isolated from the rest of the energy in the event. The muon is thus expected to make a large angle with respect to the event Thrust axis, i.e., the muon gains a large transverse momentum with respect to the decaying quark.

In this chapter the results of a brief Monte Carlo investigation into the above effects are reported. This study used the Lund V6.3 simulation program, with the fixed order matrix element option for parton generation. The results are organized as follows.

First, the effects on the total cross section due to production of Top quarks of various masses are investigated. Then, the expected changes in the inclusive muon rates are presented, and the event topologies of inclusive muon events containing a Top quark are compared to background inclusive muon events. Finally, the event

shapes of hadron events originating from Top production are contrasted with those of non-Top containing events, and a method for extracting Top containing events is described.

10.2 The Effect of Top on the Hadronic Cross Section

There are several different possibilities that must be considered when investigating the effects of Top production at LEP. First, the Toponium mass could be below the Z^0 pole. Second, the Toponium resonance could be on the pole but below the peak. Third, the resonance could be on the pole and close to the peak. The fourth possibility, that the Top quark mass is more than $1/2$ the Z^0 mass, is of relevance to phase 2 of LEP only. For the purposes of the following calculations, the Z^0 mass is taken as 94.0 GeV and $\sin^2 \theta_W$ is taken as 0.23, unless otherwise stated.

In Figure 10.1 the Monte Carlo expectation for the quantity R is shown as a function of \sqrt{s} and for several Top quark masses. The solid line gives the expectation for a six-quark model, where the Top quark mass is 47 GeV, i.e., $M_{Z^0}/2$, and does not include the effects of radiative corrections or Toponium- Z^0 mixing. At the upper end of the Z^0 peak, a dot-short-dash line can be seen to emerge below the solid line; this is the five-quark prediction (again without radiative corrections). The effect of the radiative corrections is illustrated by the dot-long-dash line, which is the prediction for a 47 GeV Top quark with the radiative corrections included (note that interference between initial and final state diagrams has been omitted here). The effects of the radiative corrections near the pole are easily understood. Above the pole initial state bremsstrahlung lowers the hadronic center-of-mass energy so that the event is again on the pole; this accounts for the long radiative tail on the high-energy side of the pole. For events just below the pole, radiation of a hard photon from the initial state moves the event further from the pole, towards the

low energy side. Since the cross section varies rapidly in this region, the total cross section is lower than the case where radiative corrections are excluded. Well below the pole, the electroweak effects are minimal and pure QED radiative corrections dominate. This has the effect of increasing the cross section by roughly 30% [112,54]. The dashed line in the figure shows the prediction for a Top quark mass of 20 GeV, and this can be compared directly to the data points shown. The data are from the MARK J experiment and have been corrected for the effects of initial state radiation. Clearly a Top quark of mass 20 GeV is excluded by the data [52]. It is apparent from this figure that the line-shape of the Z^0 pole is dominated by the radiative corrections, and that, before attempting to find Top by total cross section measurements, the radiative corrections must be fully understood. The shape of the cross section near the Z^0 pole is shown in Figure 10.2, where the pole region of Figure 10.1 is drawn on an expanded scale. The shift in the apparent Z^0 peak position due to radiative corrections is approximately 200 MeV.

The case where $M_t = M_{Z^0}/2$ is particularly interesting. In this case there exists the possibility of direct interference between Toponium states in the Z^0 propagator and the propagator itself. This causes the total cross section to undergo rapid fluctuations near the pole. Observation of such behaviour would provide extremely strong support to any claims relating to the discovery of Top. However, apart from the fact that the Toponium resonance must coincide with the Z^0 pole to within less than 3 GeV for such effects to be seen, the effect is most likely washed out by the LEP machine width [113]. The interference effect has been ignored in the above calculations. It is interesting to note that the enhancement on the high-energy tail of the pole is larger for a light Top quark than for a Top quark of mass close to $1/2 M_{Z^0}$. This is a result of the β dependence of the branching ratio for $Z \rightarrow t\bar{t}$ where β is the Top quark velocity, $\beta = (1 - 4m_t^2/Q^2)^{1/2}$ [114]. With this expression for β , the partial width for $Z^0 \rightarrow t\bar{t}$ can be written in terms of the Top quark neutral

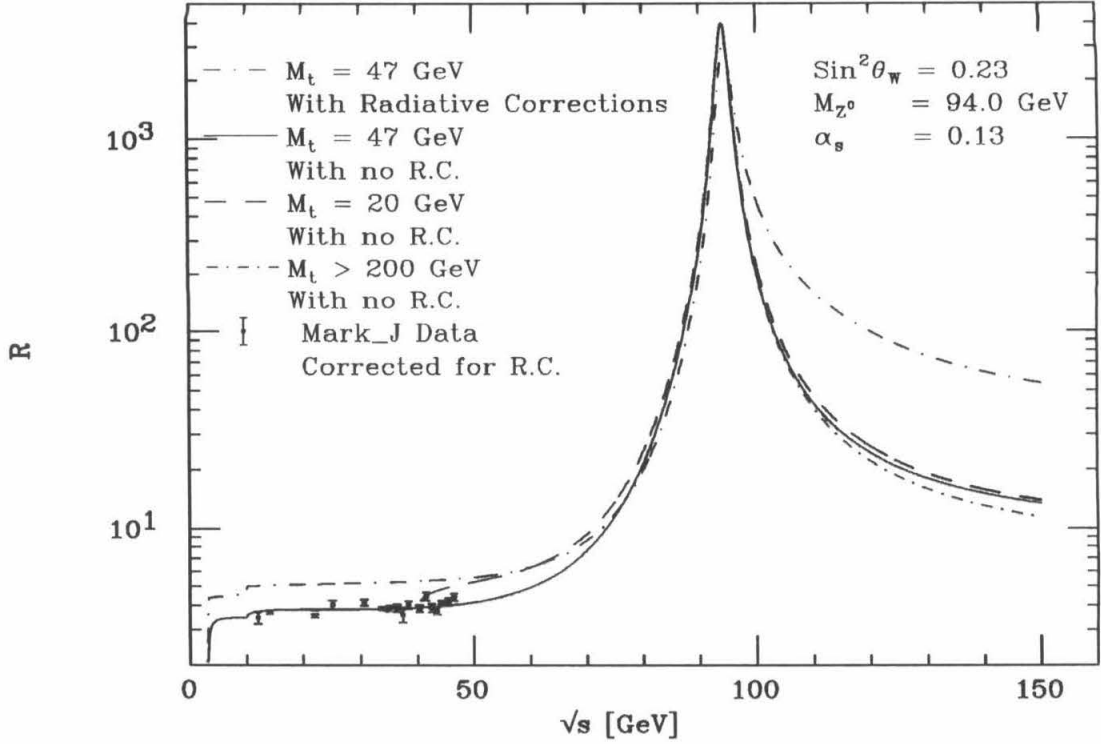


Figure 10.1 R as a function of E_{cm} for various Top quark masses, and illustrating the effect of radiative corrections

current coupling constant, $v_t = 1 - \frac{8}{3} \sin^2 \theta_W$, $a_t = 1$:

$$\Gamma(Z \rightarrow t\bar{t}) = \frac{1}{8\pi} \frac{G_F m_Z^2}{\sqrt{2}} \beta \left[v_t^2 \frac{3 - \beta^2}{2} + a_t^2 \beta^2 \right]. \quad (10.1)$$

This expression is altered by QCD radiative corrections as follows:

$$\frac{3 - \beta^2}{2} \rightarrow \frac{3 - \beta^2}{2} \left\{ 1 + \frac{4}{3} \alpha_s \left[\frac{\pi}{2\beta} - \frac{3 + \beta}{4} \left(\frac{\pi}{2} - \frac{3}{4\pi} \right) \right] \right\} \quad (10.2)$$

$$\beta^2 \rightarrow \beta^2 \left\{ 1 + \frac{4}{3} \alpha_s \left[\frac{\pi}{2\beta} - \left(\frac{19}{10} - \frac{22\beta}{5} + \frac{7\beta^2}{2} \right) \left(\frac{\pi}{2} - \frac{3}{4\pi} \right) \right] \right\}. \quad (10.3)$$

An appropriate choice for α_s here is :

$$\alpha_s = \frac{12\pi}{25 \log 4p_t^2 / \Lambda_{MS}^2}, \quad (10.4)$$

where $p_t = \beta m_z / 2$.

The values of the cross section and the R value at various center-of-mass energies are shown for several Top quark masses in Tables 10.1, 10.2 and 10.3. In the tables

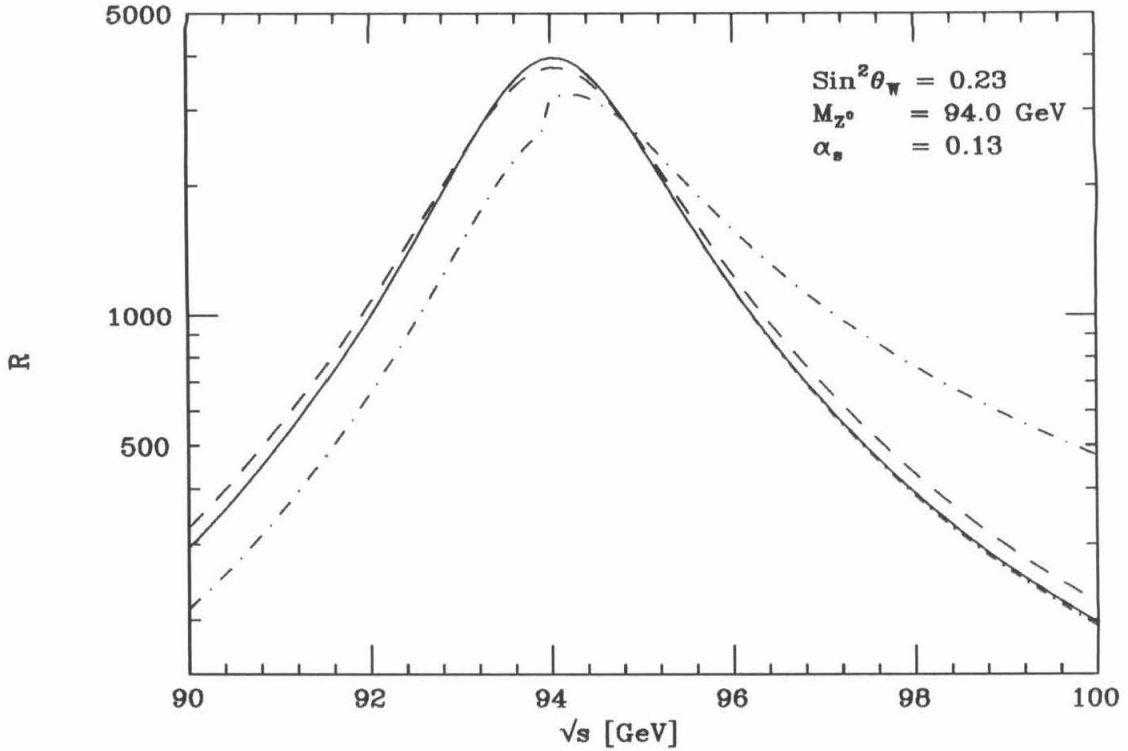


Figure 10.2 R as a function of E_{cm} for several choices of the Top quark mass, and illustrating the effects of radiative corrections at the pole

the first column gives the center-of-mass energy, and the second column gives the total cross-section including the contribution from a Top quark. The next two columns give the corresponding cross section and R value for the Topless case, and the last column gives the ratio between the total cross section for the case with Top present and the Topless case. Tables 10.1, 10.2, 10.3 correspond to Top quark masses of 30.0 GeV, 47.0 GeV, and 47.0 GeV (including radiative corrections).

The relative contributions of the various quark flavors to the total cross section as a function of the center-of-mass energy are illustrated in Figure 10.3, where the quark composition of the events is shown. The β dependence near threshold is apparent at both the bottom and Top thresholds. The large variation in the fraction of charge $2/3$ quarks produced that was indicated in Figure 3.3 at PETRA energies, is seen to have been washed out by the inclusion of initial state radiative corrections. For more massive Top quarks the contribution to the cross section at the pole is

Table 10.1 The prediction for the total hadronic cross section and R value for $e^+e^- \rightarrow Z^0 \rightarrow q\bar{q}$, with Top mass $M_t = 30.0$ GeV and no radiative corrections.

E_{cm}	$\sigma_0(6)$ [nb]	R(6)	$\sigma_0(5)$ [nb]	R(5)	$\frac{\sigma_0(6)}{\sigma_0(5)}$
60.00	0.119	4.920	0.119	4.920	1.000
65.00	0.136	6.620	0.120	5.835	1.135
70.00	0.154	8.713	0.135	7.627	1.142
75.00	0.200	12.933	0.177	11.495	1.125
80.00	0.318	23.482	0.289	21.291	1.103
85.00	0.716	59.585	0.658	54.775	1.088
90.00	3.372	314.635	3.110	290.207	1.084
91.00	5.628	536.910	5.188	494.958	1.085
92.00	10.696	1043.026	9.852	960.657	1.086
93.00	23.023	2294.091	21.178	2110.237	1.087
94.00	37.585	3826.063	34.519	3513.928	1.089
95.00	23.927	2487.789	21.939	2281.151	1.091
96.00	11.420	1212.502	10.452	1109.742	1.093
97.00	6.160	667.736	5.626	609.872	1.095
98.00	3.782	418.448	3.446	381.321	1.097
99.00	2.551	287.998	2.319	261.813	1.100
100.00	1.840	211.958	1.668	192.202	1.103
105.00	0.625	79.397	0.559	71.029	1.118
110.00	0.331	46.120	0.292	40.697	1.133
115.00	0.214	32.567	0.186	28.372	1.148
120.00	0.154	25.588	0.133	22.036	1.161
125.00	0.119	21.458	0.102	18.293	1.173
130.00	0.096	18.779	0.081	15.867	1.183
135.00	0.081	16.924	0.068	14.190	1.193
140.00	0.069	15.576	0.057	12.973	1.201
145.00	0.060	14.559	0.050	12.055	1.208
150.00	0.053	13.769	0.044	11.343	1.214

Table 10.2 The prediction for the total hadronic cross section and **R** for $e^+e^- \rightarrow Z^0 \rightarrow q\bar{q}$, with Top mass $M_t = 47.0$ GeV and radiative corrections included.

E_{cm}	$\sigma_0(6)$ [nb]	R(6)	$\sigma_0(5)$ [nb]	R(5)	$\frac{\sigma_0(6)}{\sigma_0(5)}$
90.00	2.269	211.764	2.269	211.764	1.000
91.00	3.669	350.016	3.669	350.016	1.000
92.00	6.768	659.927	6.768	659.927	1.000
93.00	14.560	1450.765	14.560	1450.765	1.000
94.00	31.289	3185.155	26.723	2720.295	1.171
95.00	24.877	2586.578	21.244	2208.808	1.171
96.00	14.882	1580.059	12.705	1348.977	1.171
97.00	9.647	1045.749	8.234	892.504	1.172
98.00	6.851	757.991	5.844	646.661	1.172
99.00	5.193	586.412	4.429	500.075	1.173
100.00	4.123	474.949	3.514	404.848	1.173
105.00	1.881	238.862	1.599	203.152	1.176
110.00	1.146	159.794	0.973	135.603	1.178
115.00	0.797	121.382	0.675	102.787	1.181
120.00	0.597	99.069	0.505	83.725	1.183
125.00	0.470	84.669	0.397	71.423	1.185
130.00	0.384	74.708	0.323	62.913	1.187
135.00	0.321	67.470	0.270	56.728	1.189
140.00	0.275	62.011	0.231	52.064	1.191
145.00	0.239	57.774	0.200	48.444	1.193
150.00	0.210	54.410	0.176	45.569	1.194

Table 10.3 The prediction for the total hadronic cross section and R value for $e^+e^- \rightarrow Z^0 \rightarrow q\bar{q}$, with Top mass $M_t = 47.0$ GeV and no radiative corrections.

E_{cm}	$\sigma_0(6)$ [nb]	R(6)	$\sigma_0(5)$ [nb]	R(5)	$\frac{\sigma_0(6)}{\sigma_0(5)}$
90.00	3.142	293.165	3.142	293.165	1.000
91.00	5.278	503.505	5.278	503.505	1.000
92.00	10.181	992.792	10.181	992.792	1.000
93.00	22.762	2268.117	22.762	2268.117	1.000
94.00	38.921	3962.068	38.921	3962.068	1.000
95.00	23.652	2459.208	23.525	2446.010	1.005
96.00	10.875	1154.655	10.785	1145.114	1.008
97.00	5.782	626.753	5.718	619.797	1.011
98.00	3.529	390.430	3.479	384.955	1.014
99.00	2.373	267.998	2.333	263.421	1.017
100.00	1.710	197.007	1.675	193.016	1.021
105.00	0.582	73.896	0.560	71.110	1.039
110.00	0.309	43.135	0.292	40.716	1.059
115.00	0.201	30.635	0.186	28.378	1.080
120.00	0.146	24.209	0.133	22.039	1.098
125.00	0.113	20.413	0.102	18.294	1.116
130.00	0.092	17.953	0.082	15.868	1.131
135.00	0.077	16.251	0.068	14.191	1.145
140.00	0.066	15.016	0.057	12.973	1.157
145.00	0.058	14.084	0.050	12.056	1.168
150.00	0.052	13.360	0.044	11.343	1.178

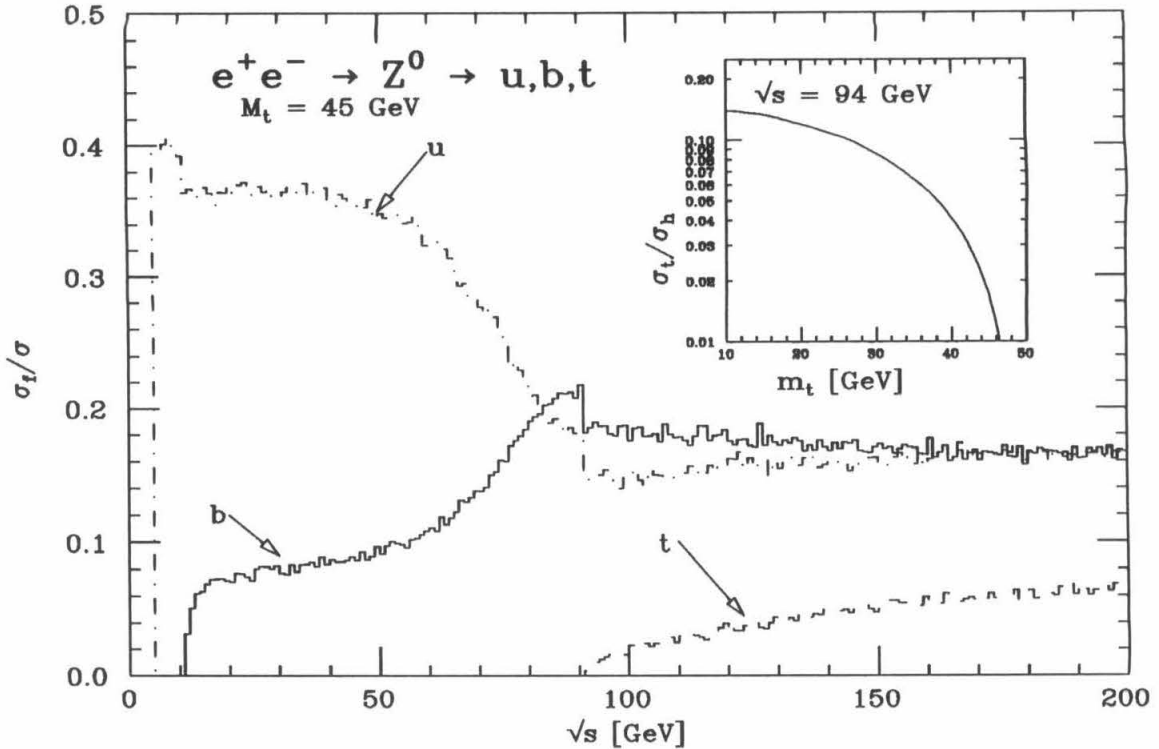


Figure 10.3 The energy dependence of the event flavor composition, including the effects of full radiative corrections.

diminished. It is important to note that the ‘copious production’ of Top on the pole is due to the large cross section, not to any enhancement in Top production. The insert in Figure 10.3 shows the branching ratio for $Z^0 \rightarrow t\bar{t}$ decays as a function of the Top quark mass, in the form of the ratio of hadronic events originating in Top production.

10.3 The Effect of Top on the Inclusive Lepton Rate

The inclusive lepton rate at various center-of-mass energies obtained from a Monte Carlo calculation are presented in Table 10.4. The values given assume a Top quark mass of 30 GeV and are expressed as the mean number of muons, or electrons, per event. The data shown here are illustrative only, since the effects of detector efficiencies for low momentum muons are excluded. The jump in the

E_{cm}	$\langle\mu\rangle$	$\langle e\rangle$	$\langle\gamma\rangle$	$\langle N\rangle$	$\langle N_{Ch}\rangle$
40.0	0.103	0.282	15.3	31.4	14.5
50.0	0.100	0.279	16.6	34.2	15.8
55.0	0.101	0.293	17.2	35.4	16.4
65.0	0.168	0.387	19.2	39.9	18.4
70.0	0.192	0.415	20.2	41.8	19.3
80.0	0.176	0.416	21.4	44.5	20.6
90.0	0.180	0.463	22.4	46.9	21.9
94.0	0.178	0.445	22.8	47.8	22.4

Table 10.4 Monte Carlo predictions for the inclusive lepton rates as a function of \sqrt{s} . Also given are the predictions for the number of photons per event and the total, and charged, multiplicities.

inclusive muon rate is illustrated in Figure 10.4 where the inclusive muon data from Table 10.4 is plotted. The jump in the rate on crossing the Toponium threshold is clearly visible, and represents an increase in the inclusive muon rate of 78%. It can be seen that the rate is roughly independent of \sqrt{s} on either side of the threshold and equal to 0.101 muons per event below and 0.178 above the production threshold.

10.4 The Effect of Top on the Event Topologies: All Events

As mentioned before, events containing a Top quark are expected to have different topologies from background events. In general, the events are expected to be more spherical than events originating in u,d,s,c or b quarks, and it is possible to search for Top by looking for an excess of such events. Since Top containing events have a higher probability of containing a muon in the final state, the expected excess of spherical events is likely to be more apparent in the inclusive muon data.

In Figure 10.5 the Thrust distribution for events generated at a center-of-mass energy of 94 GeV is shown together with the corresponding inclusive muon data.

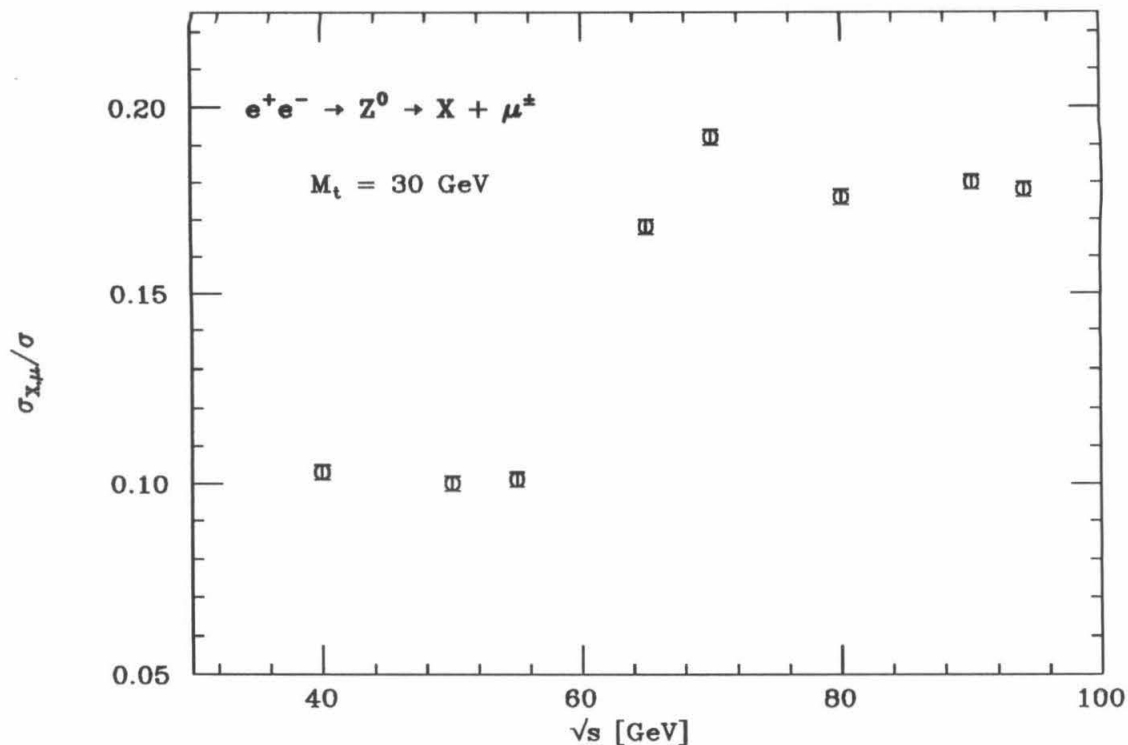


Figure 10.4 The μ -inclusive event rate versus \sqrt{s} for a Top quark of mass 30 GeV

For these plots the muon momentum was required to be larger than 1.2 GeV. This is close to lowest momentum muons expected to be detectable in the L3 detector to be installed at LEP. In the figures that follow, the solid line gives the prediction for 5 flavors, the dashed line the prediction including Top, and the dotted line the predicted contribution for Top alone. The data shown in Figure 10.5 was generated with a Top mass of 45 GeV, and the effects of initial state radiative corrections are included. The data shown in the figure are the normalized to give a prediction for an integrated luminosity of 300 pb^{-1} corresponding to 9.2×10^6 events for the case with Top present, or 8.0×10^6 events for the 5 quark case². The predictions for inclusive muon events are also shown in the plot. The corresponding distributions for Sphericity, Oblateness and the fourth Fox-Wolfram moment are shown in Figures. 10.6, 10.7, 10.8. It is clear that the enhancement in the region of spherical

²This corresponds to roughly 18 months of running at LEP, if the design luminosity is achieved.

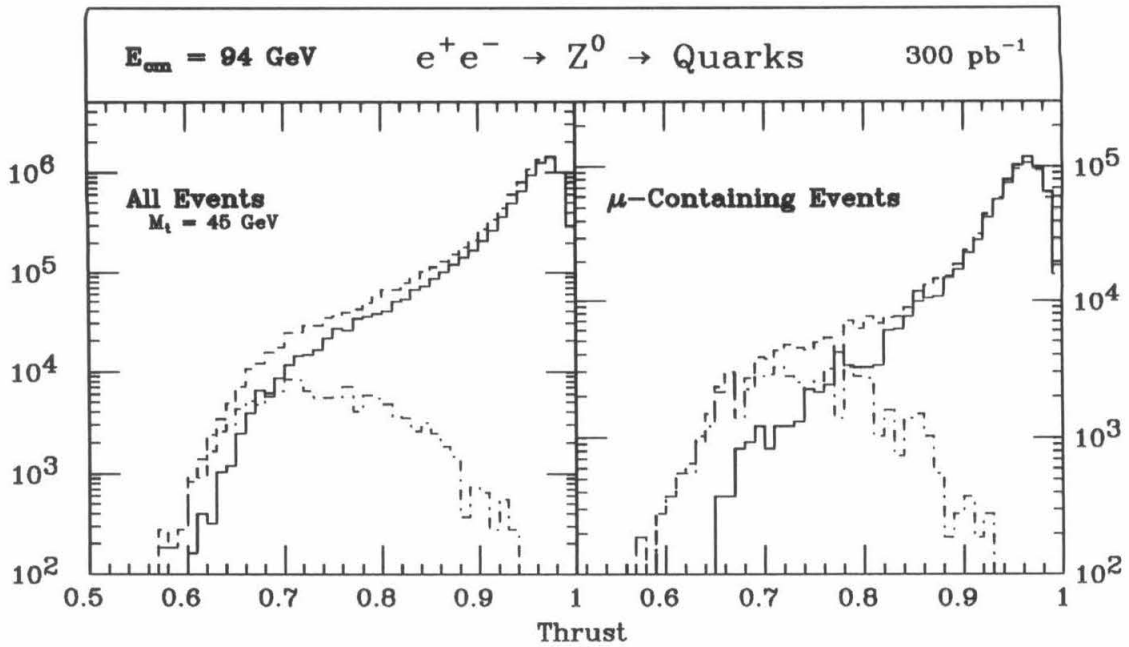


Figure 10.5 The prediction for the event Thrust on the Z^0 pole with, and without, Top production. The right-hand plot shows the prediction for the inclusive muon data

events is larger in the inclusive muon data, however, this gain is achieved at a cost in the number of events of a factor of ten.

On the Toponium resonance, the decays $t\bar{t} \rightarrow ggg$ and $t\bar{t} \rightarrow gg\gamma$ are expected to become important. Since these events are expected to have high Oblateness, the event shapes on the resonance should differ significantly from continuum events. The dominant decays on the resonance are still the single quark decay events that we have discussed in the off-resonance case above. This is illustrated in Figure 10.9 where the results of a Monte Carlo calculation are shown. The figure shows the event Sphericity and Oblateness for 5000 events of the form $Z^0 \rightarrow t\bar{t}$ (SQD events), and the prediction for 5000 Toponium decays into ggg and $gg\gamma$ final states. It can be seen that the two types of event populate different regions in the scatter plot.

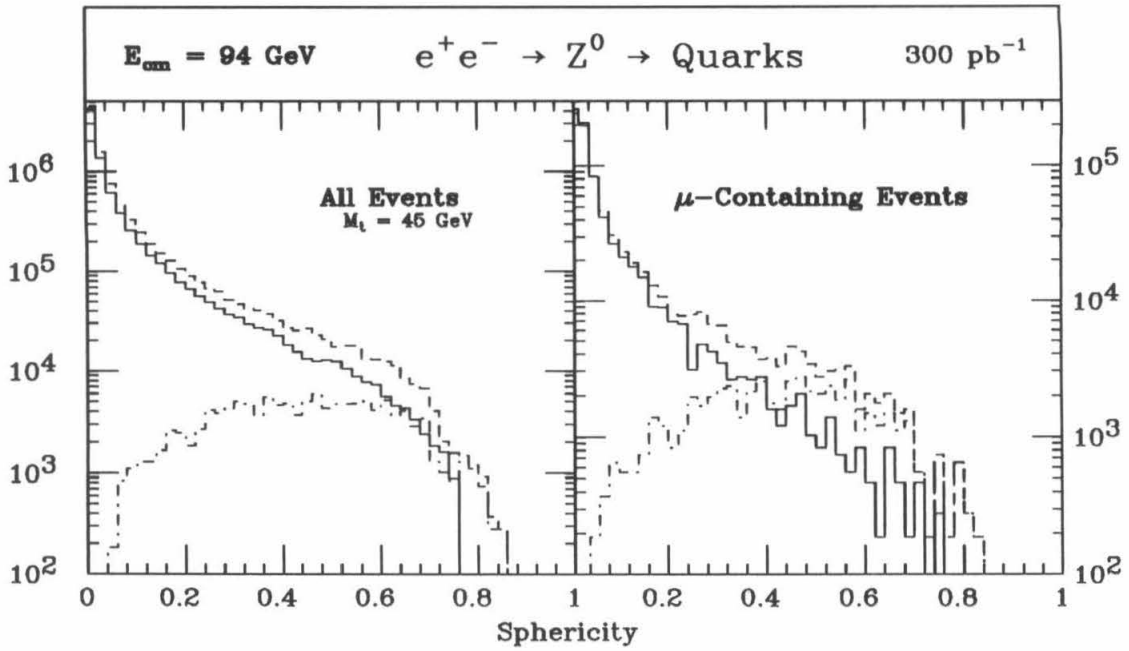


Figure 10.6 As Figure 10.5, but showing the prediction for Sphericity

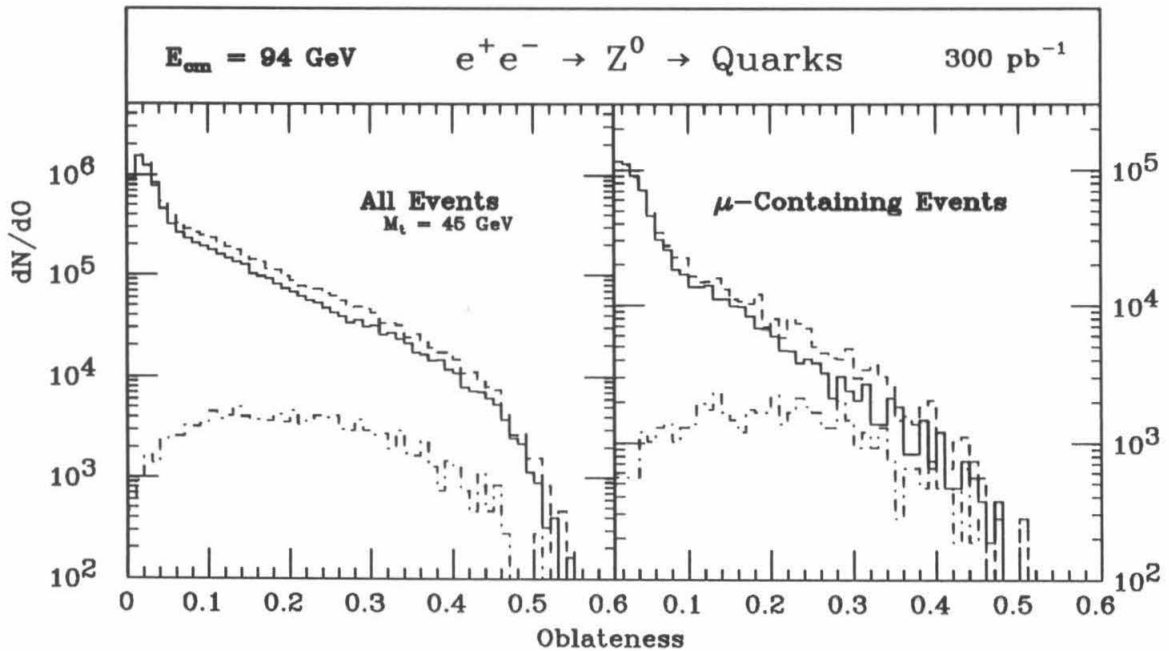


Figure 10.7 As Figure 10.5, but showing the prediction for Oblateness

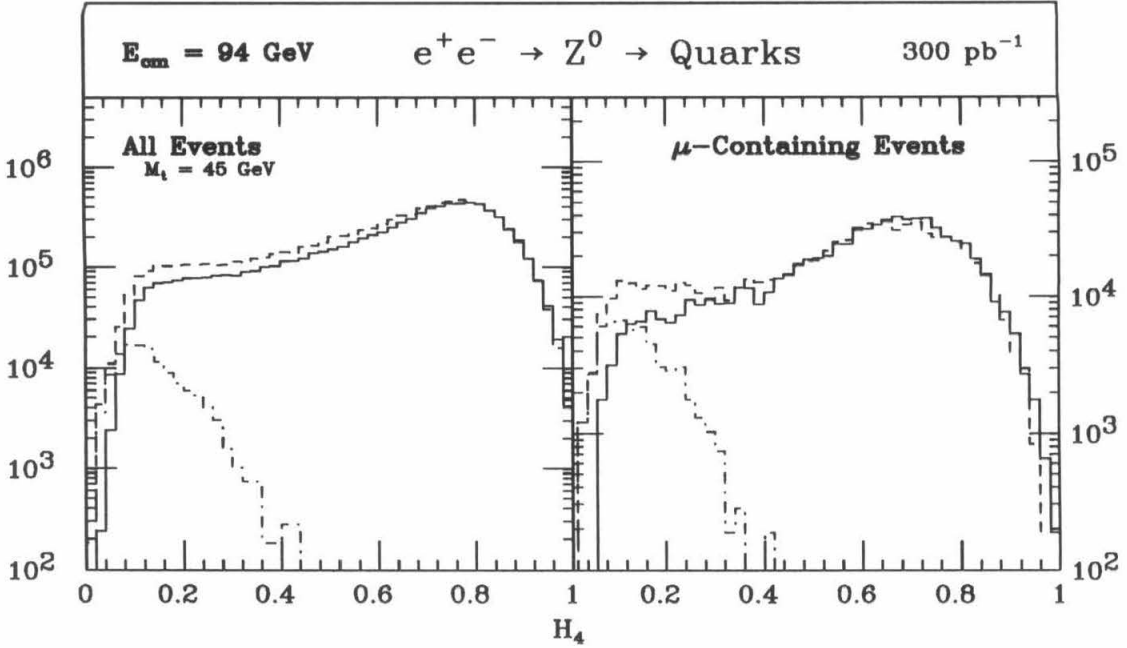


Figure 10.8 As Figure 10.5, but showing the prediction for H_4

The branching ratios for Toponium decays to these two configurations are given by³:

$$\Gamma_{ggg} = \Gamma_0 \frac{10(\pi^2 - 9)}{81\pi} \frac{\alpha_s^3}{e_t^2 \alpha^2}, \quad (10.5)$$

and,

$$\Gamma_{gg\gamma} = \Gamma_0 \frac{8(\pi^2 - 9)}{9\pi} \frac{\alpha_s^2}{\alpha}, \quad (10.6)$$

where Γ_0 is the hypothetical decay rate of Toponium to e^+e^- ignoring the effects of the Z^0 .

It can be seen that where $t\bar{t}$ -SQD events do have spherical topology they tend not to be very planar, these are the events in the lower right-hand part of the plot. The events due to Toponium $-ggg$ and $-gg\gamma$ decays, however, tend to be concentrated into two bands along the diagonal from the lower left-hand to the upper-right hand corner of the plot, and a band above the diagonal. The upper band can be identified with Toponium $\rightarrow gg\gamma$ events and the lower with Toponium $\rightarrow ggg$ events. Decays

³In the absence of decays into charged Higgs particles which are predicted by some non-standard electroweak theories.

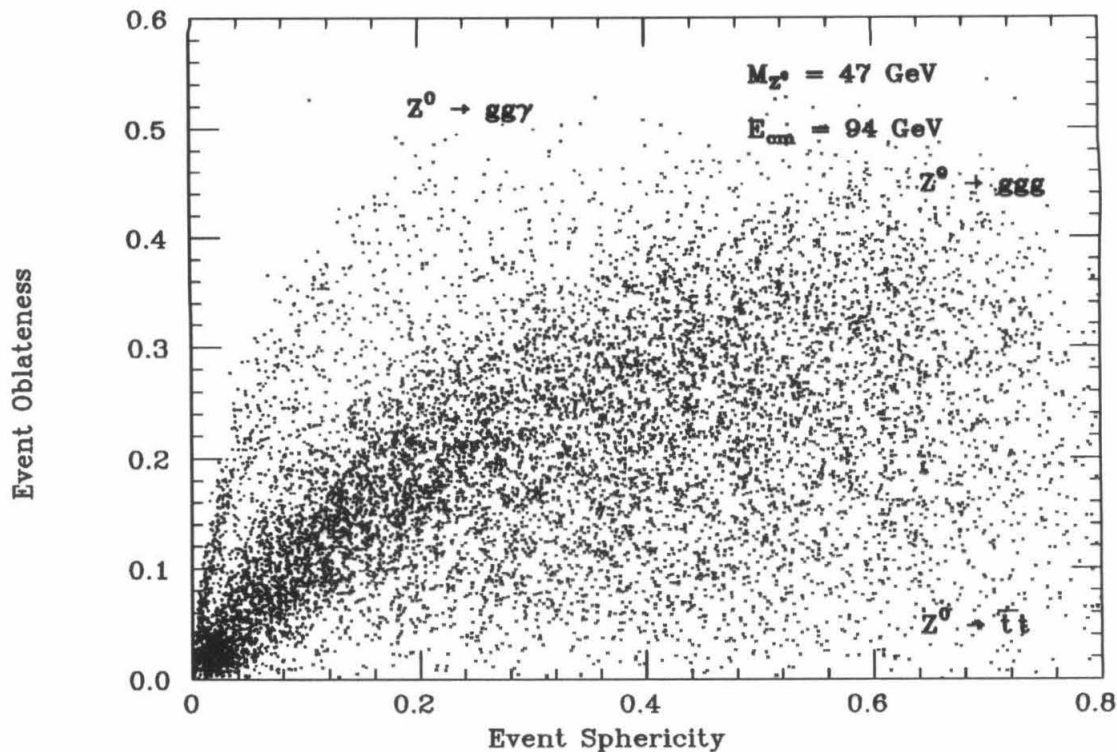


Figure 10.9 Monte Carlo prediction for the Oblateness, and Sphericity of events from $t\bar{t} \rightarrow V^0 \rightarrow ggg(\gamma)$ and $t\bar{t} \rightarrow Z^0 \rightarrow t\bar{t}$ at 94 GeV

in which one of the gluons is soft, or in which one of the γ 's is soft, appear 'two-jetty' and are concentrated in the region of low Sphericity and low Oblateness.

10.5 Event Topologies: Inclusive Muon Events

As remarked earlier, events containing a semi-leptonically decaying Top quark are expected to be different to events originating in the semi-leptonic decay of a bottom or charmed quark, in that the muon is well isolated from the hadronic energy in the event. This difference is well illustrated by examining the amount of energy that is contained in the event within a cone of $1/2$ -opening angle $\delta_{1/2}$ around the muon direction. In Figure 10.10 the amount of energy in the event contained within a cone of $1/2$ -opening angle $\delta_{1/2}$ is histogrammed against $\cos(\delta_{1/2})$. It can be seen that for small opening angles ($\cos(\delta_{1/2})$ near one) the amount of energy within

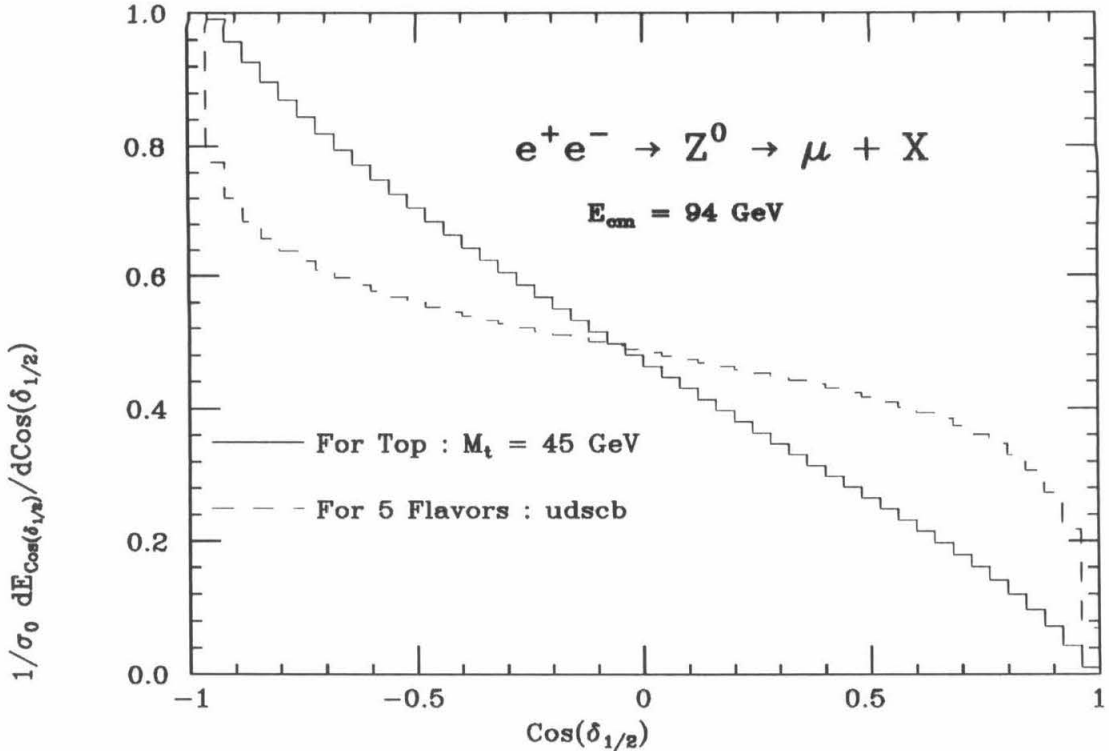


Figure 10.10 Illustrating that events originating in Top-quark decays contain muons that are isolated from the hadronic energy in the event

the cone for Top-events is significantly lower than for 'conventional' events. When $\cos(\delta_{1/2})$ is near 0., i.e., the cone divides the event into two hemispheres, nearly half the energy has been contained in the cone, so that the events are fairly well balanced. The near-linearity of the line for the Top events indicates that the events are very spherical.

From Figure 10.10 it can be seen that Top and non-Top containing events might be separated by a cut on the energy contained within a cone of half-opening angle $\delta_{1/2} = \cos^{-1} 0.70$. In Figure 10.11 this is illustrated for events generated at 94 GeV. The difference between Top-containing and u,d,s,c and b events is clear. In this figure the distributions shown have been normalized so that there are the same number of $t\bar{t}$ events as there are u,d,s,c and b events. It can be seen that significant Top enrichment can be obtained by cutting on these variables, but that the amount of background contamination is still high. It should be remarked that the trend

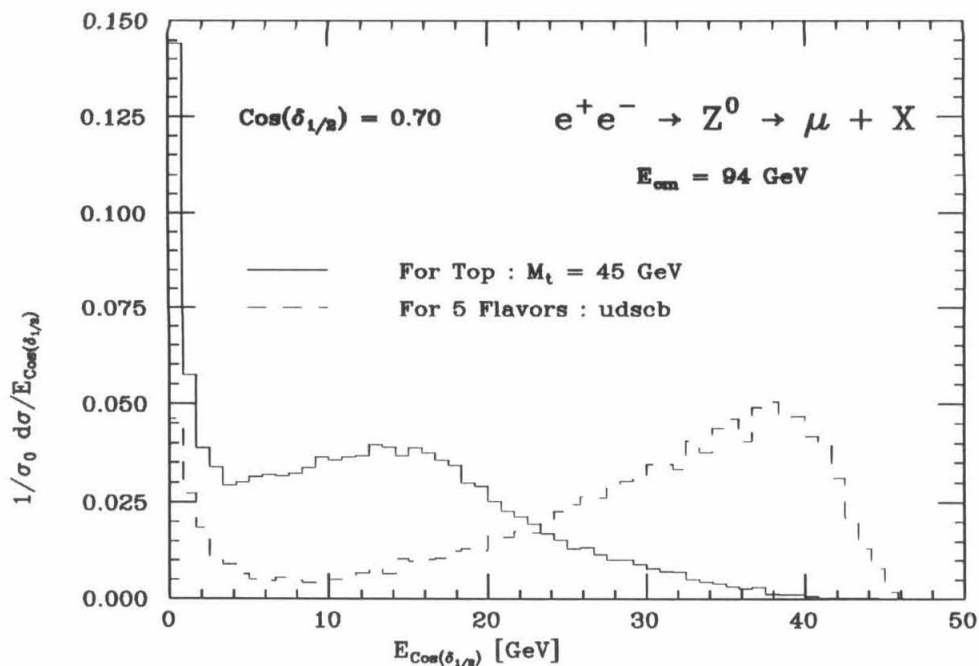


Figure 10.11 The amount of energy within a cone of 1/2-opening angle $\cos(\delta_{1/2})=0.70$ around the muon direction

shown in the plots is the same for lighter Top quarks.

As a final illustration of the isolation of the muon originating in Top decays, in Figure 10.12, the energy-weighted $\cos(\theta)$ of the angle between the tracks and the muon is shown.

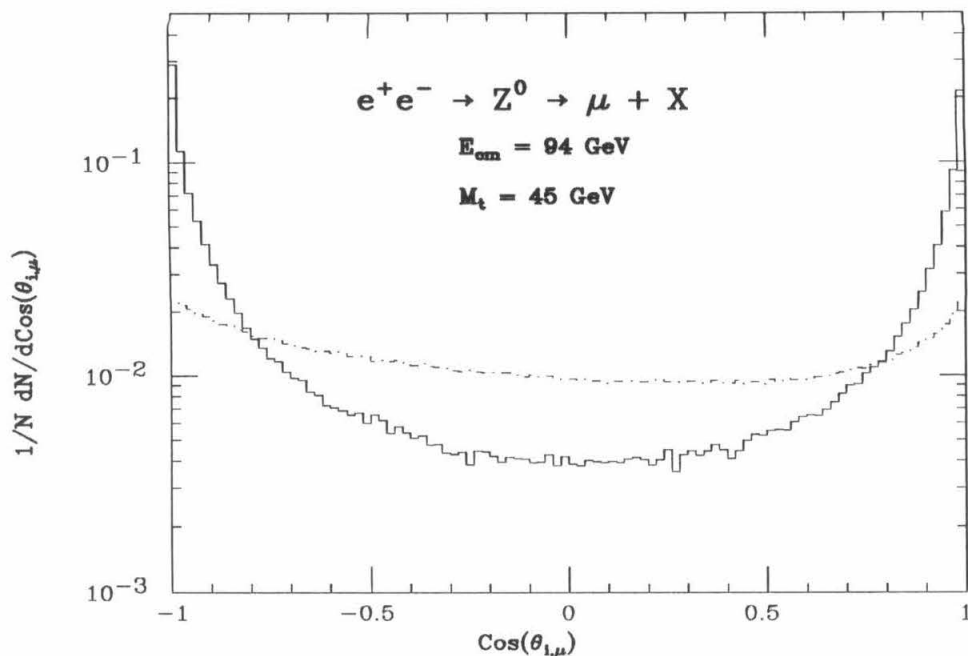


Figure 10.12 The energy-weighted $\cos(\theta)$ distribution for Top containing and conventional events for a 45 GeV Top quark at 94 GeV. $\cos(\theta)$ is the angle between the track and the muon direction. The solid line is for conventional quarks, while the dot-dashed line is obtained with Top-containing events.

a_1/A	a_2/A	a_3/A	a_4/A	a_5/A	a_6/A
0.1898	0.1388	0.1814	0.5962	0.7013	0.2541

Table 10.5 The values of the coefficients defining a line that optimizes the separation of a Top enriched hadron data sample from the background

10.6 Isolating a Top-enriched Hadron Sample

From the plots presented above, it is clear that the identification of events originating in Top quark production is far from trivial. In all cases there is significant confusion between conventional events and the Top containing events. Even when the inclusive muon data is used, at the cost of statistics, the confusion still remains.

The problem is compounded when the Toponium production threshold is close to the Z^0 pole, when the branching ratio for $Z^0 \rightarrow t\bar{t}$ is small. This is illustrated in Figure 10.3, where it can be seen that for a Top quark of mass 45 GeV the

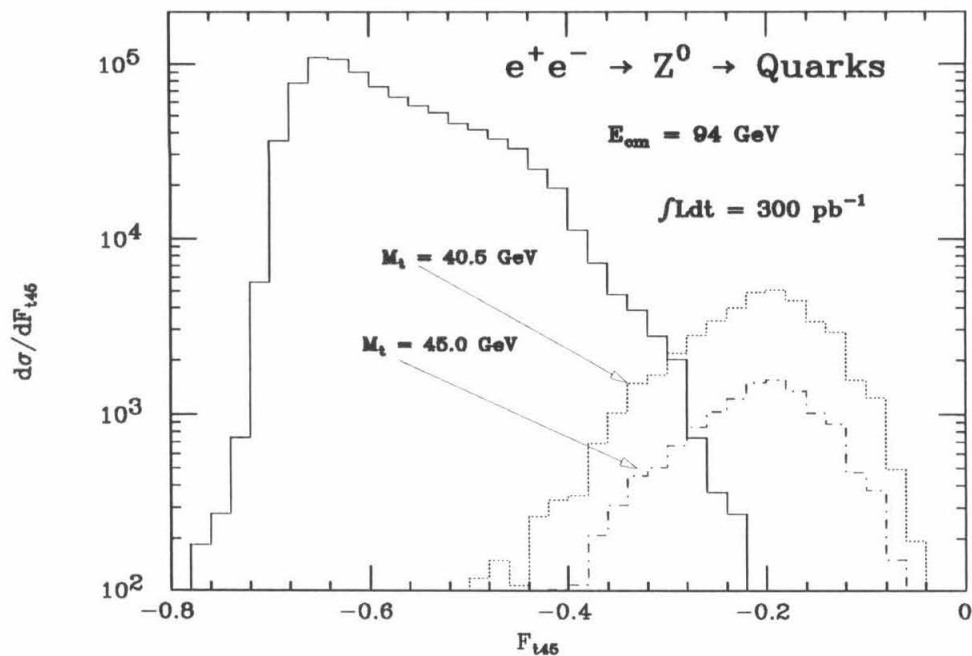


Figure 10.13 The results of applying a multidimensional discriminant function to the predictions for Top and background events at 94 GeV for a Top quarks of masses 45 and 40.5 GeV

Cut	uds [%]	c [%]	b [%]	t [%]	Bgnd [%]
0.4	32.9	12.2	27.5	27.3	72.6
0.3	11.1	6.4	15.8	66.7	33.2

Table 10.6 The quark composition of two data sets selected by cutting on the discriminant function described in the text

branching ratio for the Z^0 to decay into Top is only 1.21%. The fraction of hadronic events from Z^0 decays originating in Top quarks as a function of the Top quark mass is shown in the insert to Figure 10.3. In this chapter the problem of isolating a Top enriched sample from the hadronic data for a Top quark of mass 45 GeV is investigated. Since the branching ratio for $Z^0 \rightarrow t\bar{t}$ is small for a Top quark of this mass this presents a non-trivial problem.

For isolating Top-containing events a multidimensional discriminant analysis similar to that discussed in the previous chapter in relation to the MARK J data, has been made [115]. Two thousand Monte Carlo events were generated, and events originating in conventional quark production, and events originating in Top production, were separately projected onto a line of the form:

$$0 = \frac{a_1 T + a_2 S + a_3 O + a_4 H_2 + a_5 H_3 + a_6 H_4}{A}, \quad (10.7)$$

where,

$$A = 1/\sqrt{\left(\sum_{i=1}^6 a_i^2\right)}. \quad (10.8)$$

Here T is the event Thrust, S the Sphericity, O the Oblateness and the remaining terms involve the second, third and fourth Fox-Wolfram event moments of the event. The coefficients a_i are determined by a least squares fit that maximizes the quantity:

$$\chi^2 = \frac{M_b - M_t}{\sigma_b^2 + \sigma_t^2}. \quad (10.9)$$

Here M_t and M_b are the means of the distributions for signal-events ($t\bar{t}$ events) and the background (u,d,s,c and b) events respectively, *after* the events have been projected onto the line defined by Eqn. 10.7. The σ 's are the corresponding variances for the two distributions. The idea is to maximize the separation between the two distributions while reducing the leakage into each distribution from the tail of the other. The result of a least squares fit to optimize the discrimination between events containing a 45 GeV Top quark from normal hadron events yields the 'multidimensional discriminant function' having the a_i 's given in Table 10.5.

The efficiency of the method is illustrated in Figure 10.13, where the distribution obtained by projecting Top containing events onto the above line is shown, together with the distribution obtained for background events. The plot shows the results for two Top quark masses, 45 GeV (dot-dash line) and 40.5 GeV (dotted line). The background events are shown as a solid line. The relative normalizations of the distributions correspond to the true production ratios at a center-of-mass energy of 94 GeV, the branching ratio for $Z^0 \rightarrow t\bar{t}$ when the Top quark mass is 40.5 GeV is 4%. For the data shown in the figure corresponding to a Top quark mass of 45 GeV, a cut on the discriminant function at 0.4 is 96.7% efficient in selecting Top events and 97.6% efficient at rejecting the background. The event quark compositions for data sets selected by cutting on the discriminant function at 0.3 and 0.4 are given in Table 10.6, where it can be seen that the method is capable of isolating a Top sample of 67% purity from an original sample containing only 1.21% Top events.

It should be pointed out that the variables used in the construction of this discriminant function are correlated with each other, and that a simpler function could probably be obtained from fewer variables. In addition, this function was constructed from variables that don't require information about the leptons, so it is useful for selecting a pure hadron data sample. If, however, one desired a pure Top quark sample, the inclusive muon data could be used, and a measure of the isolation of the muon included in the definition of the discriminant function. Clearly, the method is highly dependent on the Monte Carlo program, and as a result, is most suited to problems such a Top identification where reliable Monte Carlo predictions can be made.

The results presented in this chapter are obviously just a start, and the application of the Monte Carlos investigated in this study to the problem of predicting event topologies at LEP still has to be addressed. This problem will be the subject of a later study. For now, however, it is clear that the multidimensional discriminant

analysis techniques investigated here are promising, and there is hope that they can be extended to make a useful tool for LEP physics.

Chapter 11

Conclusions

11.1 Summary

In this thesis three new parton level generator/fragmentation scheme combinations for use in e^+e^- annihilation have been tuned to and compared to the MARK J hadronic data. The parton generators investigated were the leading log parton shower generator supplied with the Caltech-II e^+e^- annihilation model and the 'in house' MARK J parton generator incorporating the full 2^{nd} order corrections referred to as the ERT/Ali/Zhu calculation. The two new fragmentation schemes were taken from the JETSET V6.3 Monte Carlo package, produced by the LUND group, and from the Caltech-II model, produced by Gottschalk and Morris. The Caltech-II fragmentation scheme has been incorporated with the ERT/Ali/Zhu parton generator to form a full model for e^+e^- annihilation into hadrons, and this model has been dubbed the CIT2-FME model. The Caltech-II fragmentation scheme has also been added to the LLA shower generator supplied with the Caltech-II scheme, and angle ordering imposed on the parton shower to form another e^+e^- annihilation model called the CIT2-DLLA model. This should be identical to the original full Caltech-II model. The JETSET V6.3 fragmentation scheme has been added to the ERT/Ali/Zhu parton generator to produce a model that has been called LundV6.3. Including the two models already available to the MARK J collabora-

tion, the LundV4.3 and Ali models, a total of five models have been compared to the data.

11.1.1 Results

It has been found that the Monte Carlos describe the data reasonably well over a large energy range. However, the presence of a fixed mass-scale in the string fragmentation schemes (in the form of the hadron mass scale arising at the end of the string evolution) leads to non-logarithmic jet evolution for these models. This causes discrepancies between the model predictions and the high energy data. Further, it has been found that the transverse momentum structure predicted for the jets by string models is unrealistic for soft particles. Specific suggestions for improvements to be included in the next generation of fragmentation schemes have been made. In particular:

- The Caltech-II approach, of breaking clusters off of the strings, appears to be preferable to the Lund approach, where hadrons are peeled directly off of the strings. Although the Caltech-II scheme involves the introduction of an additional parameter (W_{max}), it appears that some external control over the termination of the string evolution is required and that the point at which the string evolution terminates should scale with the Q^2 of the event.
- A method for adding transverse momentum to hadrons originating in color strings is required. The Caltech-II method of obtaining a limited transverse momentum from the isotropic decay of colorless clusters appears to be adequate for describing the gross features of the events. It is not clear that the remaining transverse momentum required should be correlated to the string orientations at the time of breaking. A component of transverse momentum correlated to the parton directions appears to be adequate.

- The string formalism is suited for use with LLA parton generators, and such parton generators appear to provide the best way of overcoming the problem of soft gluon generation. Future models for electron-positron annihilation should incorporate a mixture of 2nd order QCD matrix elements and LLA QCD at the parton generation phase. This will make the transition from the hard perturbative stage of the event evolution to the softer pre-confinement stages more continuous.
- The incorporation of higher order terms into the parton generation is required. Since a third order calculation is not likely in the near future, this will have to be accomplished by the correct merging of fixed order matrix elements with LLA QCD.

The recent discussion concerning the relationship between soft gluon coherence effects in leading log QCD parton generators and the string effect has been shown to be irrelevant at PEP/PETRA energies. This study finds no evidence for the presence of the string effect in the MARK J data. However, the effect is observed in the Monte Carlo predictions, where it is found to depend critically on the model predictions for soft particles.

The magnitudes of the systematic errors assigned to previous measurements of the strong coupling constant, α_s , are found to be consistent with the estimate of the uncertainties obtained in this study, which includes the new Monte Carlo models. Further, a comparison has been made between the existing ERT/Ali/Zhu 2nd order calculation for the dressed three-jet cross section and a dressed version of the more recent calculation of Gottschalk and Shatz, and the two found to be in perfect agreement with respect to their use for α_s determinations. The contribution to the systematic error that must be assigned to α_s determinations due to theoretical uncertainties has, therefore, been found to be zero.

The highest energy hadronic data obtained by the MARK J has been thoroughly examined in the light of the observation of an excess number of low thrust events in the corresponding inclusive muon data. No statistically significant evidence for new physics in the highest energy MARK J hadronic data has been found.

The general features of events originating in top quark production have been investigated, and certain aspects of inclusive muon events originating in top production have been contrasted against events produced by the lighter five quark flavors. The use of multidimensional discriminant analysis methods for isolating a top enriched data sample at LEP has been investigated, a discriminant function has been identified, and the method has been found to be promising.

11.2 Looking to the Future

PETRA has now been incorporated into the injection system for HERA, and the possibility of more data being accumulated at the energies discussed in this work is excluded. The next generation of machines are, however, coming online: TRISTAN (May '87), SLC (late '87 or early '88) and LEP ('89).

At the higher energies afforded by the new machines, the fragmentation smearing of the underlying QCD will be much less than at PETRA energies. This will make possible more precise studies of the partial cross sections into 2 and 3-jet events. The accuracy of α_s determinations, therefore, will be improved.

There are two new aspects to performing QCD studies at the new machines. First, the process $e^+e^- \rightarrow Z^0 \rightarrow$ jets will make it possible to kinematically reconstruct multi-jet events at the Z^0 pole. Second, if the toponium resonance is below the Z^0 pole, kinematic reconstruction of multi-jet events from toponium decays will be possible, especially at LEP (a study of QCD at energies above the Z^0 will be possible only at LEP-II). The kinematic reconstruction of multi-jet events will make it possible to study the triple-gluon vertex. This is important, since it is in the

production of 4-jet events that the first tree-level indications of the full non-abelian structure of QCD are revealed.

As this study has indicated, much work needs to be done before the present day fragmentation models can be used with confidence at higher energies. Another problem that will have to be resolved is the magnitude of higher than 2^{nd} order terms in the QCD calculations for $e^+e^- \rightarrow N$ -jets. These effects will be clearer at the future machines than at PETRA, where 4-jet events are already visible. (At PETRA the rate of 4-jet events is underestimated by the Monte Carlos when the 3-jet rate is fixed to agree with the data). The possibility of obtaining a 3^{rd} order calculation soon for the partial cross sections is remote, and the only solution will be to resort to the use of leading log-type calculations to supplement the fixed order perturbative results. Early studies with the pure LLA generator supplied with the Caltech-I model showed that pure leading log QCD underestimates the number of hard 3-jet events observed in the data. The DLLA generator used in this study incorporated 1^{st} order QCD matrix elements for the generation of the first gluon branch. It is likely¹ that DLLA generators incorporating 2^{nd} order matrix elements will be available in the near future. Such generators, however, will be combinations of fixed order QCD and leading log QCD. The relationship between the 2^{nd} order α_s used for the fixed order matrix elements and the value of Λ_{QCD} used in the leading log event evolution will have to be clarified.

Given that LLA QCD will play a pivotal role in future studies of QCD, it is clear that future work will focus on the extent to which perturbative QCD and fragmentation can be factored. The availability of data over a very wide range of Q^2 , up to 200 GeV at LEP-II, will help elucidate this problem.

¹Private communication with T.D. Gottschalk.

Appendix A

Static Quarks and Flavor

The idea that nucleons might be composite objects was originated by Gell-Mann [116], Zweig [117] and Ne'eman [118] in 1961. Around this time it was observed that the nucleons, and the new particles being produced in particle accelerators, could be classified as members of representations of the gauge group $SU(3)$. This observation gave rise to the idea that hadrons are composed of more elementary entities, called quarks, that were members of an $SU(3)$ triplet [119]. The quarks would have to have fractional charge, spin $1/2$ and baryon number $1/3$, and would have to be three different 'flavors': 'up', 'down' and 'strange'. With this scheme the mesons could be constructed from quark-antiquark pairs, while the baryons were thought to contain three quarks. This idea successfully predicted the existence of a new particle, the Ω^- , which was discovered in 1964 [120]. Despite the successful prediction of the existence of the Ω^- , quarks were still thought of as little more than mathematical artifacts. It remained until the late 1960's for quarks to be taken seriously as possible real, physical particles.

Much as the α -particle scattering experiments performed by Rutherford revealed the existence of a nucleus in the atom, so 'Deep Inelastic Scattering' experiments, in which leptons are scattered off nucleons, performed at SLAC, revealed that nucleons contained pointlike constituents [121,122,123]. The experiments performed at SLAC in the second half of 1967 showed that for inelastic scattering of electrons from

protons the measured cross-section remained large at high momentum transfer [124]. This situation was unexpectedly similar to the situation that arose in elastic electron-electron scattering but deviated sharply from the situation that was observed in elastic electron-proton scattering. The results were interpreted in terms of the higher energy electron beams being used in the inelastic scattering experiments ‘probing’ substructure within the proton. The lower energy electron probes of the elastic scattering experiments, however, just saw the bulk of the proton and the electrons here scattered from the proton as a whole. These ideas led Feynman to propose that at high enough momentum transfer the electron probes being employed in the inelastic scattering experiments were seeing ‘partons’ within the proton. Further, these partons had to be point-like for the momentum transfer dependence of the cross-section to look like the electron-electron data [125]. These ideas were consistent with a more theoretical approach that had been taken by Bjorken *et al.*, which indicated that in the limit of high momentum transfer so called structure functions would exhibit ‘scaling’ [126]. This was shown to be related to the ideas of Feynman, and Bjorken’s approach was seen to be supportive of the quark-parton model.

These pointlike partons were subsequently shown to possess all the properties of quarks. Miller *et al.* showed that the partons must have spin $1/2$ rather than be spin zero objects [127]. Experiments were also performed in which the proton structure was probed by neutrinos. The definitive such experiments were performed at CERN with the aid of a large bubble chamber, called Gargamelle, that was constructed in a neutrino beam. By looking at scattering of neutrinos from protons, data that depended only on the weakly (the word ‘weakly’ here pertains to the weak interaction) charged constituents could be obtained. This data showed that only $1/2$ of the proton’s momentum was carried by the partons, that the phenomenon of scaling carried over to neutrino scattering, that the charges of the partons were indeed $1/3$ and $2/3$, and finally that there were three valence quarks in the proton [128,129].

Since these early measurements, more experiments have further reinforced the idea that hadrons are composite objects made from point-like constituents and that these constituents are the quarks of Gell-Mann *et al.* [130,131]. The main results of these experiments can be summarized as follows :

- Hadrons are composed of more elementary objects, quarks, that have spin $1/2$, charge $1/3$ or $2/3$, and baryon number $1/3$. Mesons are composed of a quark-antiquark combination, and baryons contain three quarks.
- Within a hadron the quarks behave as quasi-freely moving particles. This phenomenon, that at short distances or high energies, quarks behave as quasi-free particles, has come to be known as asymptotic freedom.
- Free quarks cannot be observed; rather, when a quark is struck from a nucleon, it ‘dresses’ itself with other quarks and is manifest as a hadron.
- The quarks appear to carry only about $1/2$ of the total energy carried by the hadron, the remainder appears to be carried by non-weakly interacting, electrically neutral ‘gluons’.

Although the quark-parton model gained support mostly from the deep inelastic scattering experiments outlined above, there was additional experimental support from several other sources. We shall not enter into a complete discussion of the motivation for the quark model, but rather, in the remainder of this section, we briefly mention some important experimental observations.

The Drell-Yan production of muon pairs in hadron-hadron scattering was shown to be in qualitative agreement with the predictions of the quark model. In particular, the cross-section was found to follow the correct power dependence as the mu-pair invariant mass increased [132,133].

Experiments performed at the ISR (a proton-proton colliding beam facility at CERN) showed that the inclusive high transverse momentum hadronic cross section did not fall off as fast as expected [134]. This discrepancy can be accounted for if one attributes the excess high P_t hadrons as arising from hard scattering between constituent quarks in the protons being scattered, and so provides evidence for quarks within the protons.

Some of the most compelling evidence to date that quarks exist as the physical particles from which hadrons are constructed comes from studies of the J/ψ system. The J/ψ system consists of a series of heavy particles that were discovered in 1974 [135,136,137] and that could not be incorporated into the existing quark model with three flavors. The J/ψ system can, however, be understood within an extended quark model with four flavors where the fourth flavor is called ‘charm’. In this model the J/ψ is made from a charmed quark and an anticharmed quark bound together to form the ground state of a quasi-atomic, $J = 1$, system that can be excited into states of various angular momenta (having higher total energy). The particles that are observed correspond to different excitations of the system, and transitions between the various excited states take place through the emission of γ -rays [138]. In the same way that a study of the atomic spectroscopy of the hydrogen atom shows that the atom consists of two constituents (the electron and the proton), a study of the J/ψ system shows it to be made from two point-like constituents. However, unlike the hydrogen atom case, where the interaction between the constituents is well understood, the interaction between the quarks in the J/ψ is only partly understood. However, a precise understanding of the level structure has been obtained in terms of a binding potential, $V(r)$ as given in Eq. A.1, which is derived from quark-parton and quantum chromodynamics (QCD) arguments [139,140,141]:

$$V(r) = \frac{8\pi}{33 - 2n_f} \Lambda \left(\Lambda r - \frac{f(\Lambda r)}{\Lambda r} \right), \quad (\text{A.1})$$

where

$$f(t) = \frac{4}{\pi} \int_0^\infty dq \frac{\sin(qt)}{q} \left[\frac{1}{\ln(1+q^2)} - \frac{1}{q^2} \right].$$

On the basis of Eq. A.1, it is possible to predict the γ -transitions of the J/ψ system under the assumption that it is a quark-antiquark system, and, where the transitions have been observed, the agreement with the theory is good [142,143,138,144]. In 1977, a further quark was discovered, the bottom quark [145]. As in the charm-anticharm system, a series of new particles is observed near the quark production threshold, so too in this system, a series of new particles is observed. This system, known as the Upsilon system, can be studied in the same way as the charmonium system and, again, the experimental data is consistent with the idea that the system is made from a quark-antiquark pair [139]. There is theoretical motivation for the existence of another quark, the top quark, but to date (and ignoring false alarms) no evidence for this particle has been found.

Above the production thresholds for the charm-anticharm and bottom-antibottom systems, electron-positron annihilation provides another confirmation of the existence of quarks. When an electron and positron annihilate, they produce a massive virtual photon that can couple to a final state consisting of a pair of quarks. The angular distribution of these quarks reflects the spin that they carry, and the observed distribution is consistent with them being the original spin 1/2 constituents of the hadrons [4]. High energy electron-positron annihilation is the main theme of this thesis and so a full discussion of the phenomenon is given in Chapter 3.

A fuller discussion of the motivation for the quark model can be found in Refs. [146] and [147]. A very complete and readable account of the conceptual history underlying the acceptance of the quark-parton model can be found in the book,

"Constructing Quarks", by Andrew Pickering [148].

A.1 Static Quarks and Color

Despite the success of the static quark-parton model in predicting the existence of the Ω^- particle and correctly describing the results of deep inelastic scattering, problems still remained. According to the quark model, the Ω^- was to be interpreted as a ground state baryon of spin 3/2 constructed from three spin 1/2 quarks in a totally symmetric configuration. These three spin 1/2 quarks all had to carry the same flavor (the Ω^- is the ground state combination of three s-type quarks). If the quarks in the Ω^- were identical, the system would violate the Pauli principle because they must all be in the same (ground) state. This problem was overcome by Greenberg [149] who introduced an additional quantum number to be carried by the quarks, called color [150]. The quarks in the Ω^- can now be in an antisymmetric state with respect to color interchange, and the Pauli principle is no longer violated.

In order to always be able to obey the Pauli principle (in a system composed of three quarks), there must be at least three colors. That there are exactly three colors is deduced from measurements of the π^0 lifetime and R , the ratio of the total hadronic cross section to the pointlike QED (quantum electrodynamics) cross section in e^+e^- annihilation. The theoretical prediction for R involves taking the sum over the number of non-identical quarks that can be produced, and hence provides a direct measurement of the number of colors [68]. The theoretical prediction for R is given by the following expression :-

$$R = \frac{\sigma(e^+e^- \rightarrow q + \bar{q})}{\sigma(e^+e^- \rightarrow \mu^+ + \mu^-)} = N_c \sum_{i=1}^{N_f} Q_i^2 \frac{\beta_i(3 - \beta_i^2)}{2}. \quad (\text{A.3})$$

In this expression the sum over the squares of the electric charge is taken over the different quarks and so runs from 1 to the number of flavors, N_f . The factor N_c takes into account the number of different colors each quark have, and the factor involving

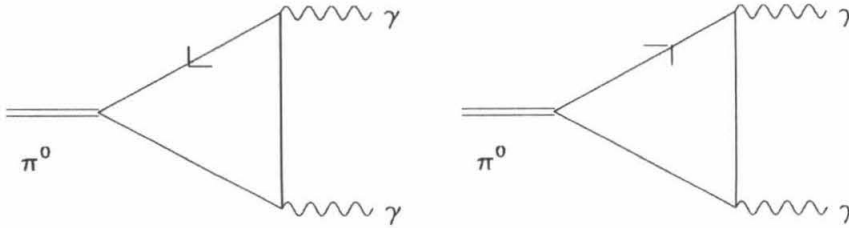


Figure A.1 The diagrams that contribute to the theoretical prediction for the rate $\pi^0 \rightarrow 2\gamma$

the β_i 's is a threshold factor, which is equal to 1 far from threshold. The number of colors can then be found by measuring R at an e^+e^- center-of-mass energy far from any quark production thresholds, at which the number of allowed flavors is known [151].

The theoretical calculation of the decay rate for $\pi^0 \rightarrow 2\gamma$ involves the calculation of a Feynman diagram that includes an internal triangle, the axial anomaly, as shown in Figure A.1. In evaluating this diagram, a sum over the number of different quarks that can carry momenta around the triangle must be performed – a number that will depend on the number of colors a quark can carry. It is found that exactly three colors are required in order that the theoretical prediction for the π^0 lifetime agree with the experimentally measured value [152].

A.2 Dynamic Quarks and QCD

So far we have described quarks as building blocks for hadrons, but we have said nothing about how quarks might interact with each other. The modern picture of the interactions between particles is that the fundamental interactions arise through the exchange of gauge bosons. The gauge bosons appear when local gauge symmetry is imposed on some field in a theory. Hadrons interact through the strong interaction and, in an effort to construct a theory of this interaction, the ideas outlined above

were combined with the ideas of (QED). QED is the theory of the electromagnetic interaction, which was arrived at by quantizing the electromagnetic field. QED's immense range of successes in predicting experimental results have made it the paradigm for the construction of gauge theories for other fundamental interactions. As an illustration of the predictive powers of QED, we give the example of the QED prediction for the value of the anomalous magnetic moment of the muon. QED predicts this quantity to be $a_{th} = (1165920.6 \pm 12.9) \times 10^{-9}$ [153], while experiments carried out in a muon storage ring at CERN yielded the experimental result $a_{exp} = (1165924 \pm 8.5) \times 10^{-9}$ [154]. The agreement between QED and experiment is clearly impressive.

The result of merging QED and the ideas of the quark model is the present candidate for a theory of the strong interaction, quantum chromodynamics (QCD) [68, 155]. In QCD, quarks are the carriers of a 'color charge' that acts as the source of a 'color field'. It is this color field that mediates the strong force. In direct analogy to QED, the color field is locally gauged, but in contrast to QED, a non-Abelian $SU(3)$ group symmetry is imposed. In QED, the imposition of a local $U(1)$ gauge symmetry on the field gives rise to a single gauge boson, the photon. In QCD, the gauging of the color field gives rise to eight gauge bosons called gluons.

Unlike the gauge bosons of QED that carry no electric charge, the gluons of QCD carry one unit of color 'charge' and one unit of anticolor 'charge' (the color charge is different than the anticolor charge). This is connected with the gauge group being non-Abelian, and it is responsible for most of the peculiarities of QCD [156]. Since the gluons in QCD carry charge, they can interact with each other as well with the quarks. This gives rise to a phenomenon known as asymptotic freedom, which is the property of QCD to become a strong coupling theory at *large* distances [68]. The large distance behavior of QCD is essentially not yet formulated. All we really know about this sector of QCD is obtained from experiment and can be summed-up as

follows: only color singlet combinations of quarks and gluons can exist as isolated particles. Another way of saying this is that you can never observe an object that is carrying a non-zero color charge. This is commonly called ‘confinement’. The concepts introduced in this Appendix are described in more detail in Chapter 3.

Appendix B

The Recombination Dependence of the Three-jet Cross Section

Having applied some jet resolution test to a parton configuration, the question of how to recombine partons that fail the resolution criterion has to be addressed. The choice of which parton pairs the resolution criteria are to be applied to is determined by the dressing scheme employed, and as discussed in Chapter 3, the Direct Dressing scheme applies the resolution criteria to *all* parton pairs, while the Partial Fractioned Scheme applies the resolution criteria to *only* parton pairs joined by a divergent propagator.

The jet resolution criteria employed to date are of two types. One is the Sterman Weinberg (SW) criteria defined by the (ϵ, δ) cut. Here, a pair of partons is defined to be irresolvable if one of them lies within a cone of half-angle δ centered on the other, or if either of the partons has energy less than ϵ of the beam energy. The second resolution criteria is based on calculating the invariant mass between the parton pair, and the pair is said to be irresolvable if this invariant mass is below some cut, Y_{cut} .

There are many possible schemes for deciding what should be done for partons failing the resolvability criteria. In the original SW prescription, if the pair failed the δ cut, then they were combined with either the energy scheme or the momentum

scheme described in Chapter 3. If, however, the pair passed the δ cut but failed the ϵ cut, then the soft parton was discarded and the momenta rescaled such that the event energy was conserved. This approach was later found to be wrong [27]. Simple physics considerations would suggest that discarding partons from the event is an incorrect procedure, since it is final state hadrons that are observed and not the partons present in the initial event configuration. Nevertheless, the question of what to do within the SW scheme with partons that fail the ϵ cut has remained - for the δ cut it is clear that the pair failing the cut are in some sense adjacent and should be combined. This question does not arise in the Y -cut scheme, since the pair that fail the cut are also in some sense adjacent, so that it makes sense to combine this pair.

The earlier work of Zhu [27] has established the following:

- There is *no* dependence of the three-jet partial cross section on the recombination scheme used to combine parton pairs failing the resolution criterion with respect to the use of the energy recombination scheme or the momentum recombination scheme.
- Discarding partons that fail the ϵ -cut in the case that SW resolution criteria are employed, leads to a 6% reduction in the three-jet partial cross section.
- Keeping the partons that fail the ϵ -cut in the case that the SW resolution criteria are used, and combining the minimum invariant mass pair, leads to the same result as for the case where the Y -cut resolution criteria are used and the pair failing this cut are combined.

Recently, Gutbrod *et al.* have re-opened the discussion on the question of the recombination dependence of the partial three-jet cross section [157]. Gutbrod *et al.* investigate the Thrust distribution that results for the cut/recombination schemes listed in Table B.1. The various schemes summarized in the table are as follows.

Scheme	Type of cut	Recombination scheme
SW	ϵ, δ	Pair failing cut(δ), discard(ϵ)
SW'	ϵ, δ	Pair failing cut(δ), Random(ϵ)
MM	ϵ, δ	Pair failing cut(δ), Minimum Y -pair(ϵ)
MM'	ϵ, δ	Pair failing cut(δ), Minimum Y -pair(ϵ) then ϵ, δ on 3-parton configuration

Table B.1 The various recombination schemes investigated by Gutbrod *et al.*

The SW scheme is the original ϵ, δ scheme in which the partons failing the ϵ cut are discarded. The SW' scheme is a modified scheme in which the parton failing the δ -cut, rather than being discarded, is recombined with another parton in the event *at random*. In both these schemes the parton pair failing the δ cut is recombined. In the MM scheme the ϵ, δ cut is applied and if a pair of partons fails the cut the minimum invariant mass pair in the event is found and this pair are combined. The MM' scheme further applies the ϵ, δ test to the three-parton configurations obtained after the MM scheme has been applied.

Gutbrod *et al.* conclude that: since the different recombination schemes they investigated lead to different three-jet partial cross sections, and since there is no clear theoretical preference for adopting one scheme over the other, the $O(\alpha_s^2)$ predictions for the three-jet cross section are not unique. As a consequence of this, they argue that the systematic uncertainties in the α_s measurements have been underestimated by the neglect of theoretical uncertainties.

In this Appendix it is argued that there is so far only one viable recombination scheme applicable to the calculation of the three-jet partial cross section, and that this must be the minimum invariant mass recombination scheme. The problem is clearly divisible into two separate parts, one is the choice of the resolution criteria, and the second is the choice of recombination scheme. Here the resolution criteria chosen is the minimum invariant mass cut. Having decided whether a parton pair

are resolvable, rather than do the natural thing and recombine the pair adjacent in ‘invariant mass space’, we combine one of the partons within the pair failing the cut to a parton chosen at random, and show that this leads to inconsistent results.

The results of applying direct dressing to parton configurations obtained with the GS matrix elements using this random-parton recombination scheme are given in Tables B.2, B.3, B.4 and B.5.

Comparing these results with those of Chapter 5 obtained with the minimum invariant mass recombination scheme, it can be seen that the three-jet cross section varies dramatically between the two schemes. The four-parton partial cross sections are the same for either scheme, which is to be expected. However, the three-jet cross section changes considerably due to the increased occurrence of the process four \rightarrow three \rightarrow two-partons occurring with the random-parton recombination scheme. This behaviour can be understood as follows. Consider the parton configuration shown in Figure B.1(a), and assume that partons 1 and 4 fail the invariant mass cut. Now, when these partons are combined, because they are the minimum invariant mass pair, the configuration that results is that shown in Figure B.1(b), and this configuration passes the next round of resolution cuts. Now consider the same configuration in which parton 4 was combined with, say, parton 2 under the random-partner recombination scheme at the first application of the cuts. The resulting configuration will be as shown in Figure B.1(c). When the second pass is made with the invariant mass cut, the configuration of Figure B.1(c) will fail the cut, partons 1 and 2 being combined to yield the two-jet configuration shown in Figure B.1(d). As a result many more of the four-parton configurations that previously contributed to the three-parton cross section now contribute to the two-parton cross section, and the three-jet cross section is reduced.

The above discussion shows that no credence can be given to *any* recombination scheme that changes the ‘hard’ topology of the parton configuration. Clearly in

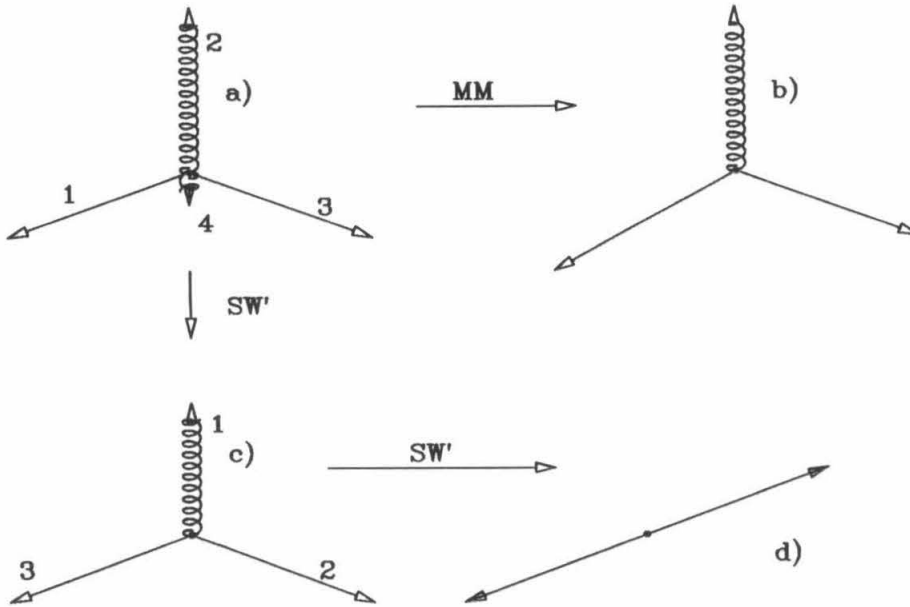


Figure B.1 The origin of the difference in the three-parton cross sections between the calculation in which minimum invariant mass pairs are combined, and that in which partons are combined at random

an event with many soft partons, it would be possible to envisage recombination schemes in which all the soft partons are recombined with only the hard partons in the event - an absurd occurrence since the event topology is now determined by the soft low Q^2 structure of the event. It is hoped that the discussion presented here has pointed out the absurdity of random parton recombination schemes, and that the unique validity of the minimum invariant mass recombination scheme is apparent. When this is accepted, the calculation presented in Chapter 5 can be interpreted as determining the systematic error on α_s due to theoretical uncertainties as being 0.

Contribution	Number of final state post-cut partons		
	2	3	4
3-Jet	—	-0.2414 ± 0.0014	—
$q^* \rightarrow qG$	—	0.4084 ± 0.0023	0.0341 ± 0.0009
$g^* \rightarrow gg$	—	0.2764 ± 0.0012	0.0142 ± 0.0003
$g^* \rightarrow q\bar{q}$	—	0.0276 ± 0.0001	0.0023 ± 0.0001
Total GS_R :	0.4784 ± 0.0050	0.4710 ± 0.0050	0.0506 ± 0.0009
Ert/Ali/Zhu	0.3647 ± 0.0041	0.5838 ± 0.0041	0.0515 ± 0.0004

Table B.2 Comparison of the partial cross sections from the ERT/Ali/Zhu calculation with those from the GS calculation, for $Y_{c,DD}=0.02$, and with random-parton recombination

Contribution	Number of final state post-cut partons		
	2	3	4
3-Jet	—	-0.2458 ± 0.0016	—
$q^* \rightarrow qG$	—	0.3392 ± 0.0021	0.0165 ± 0.0006
$g^* \rightarrow gg$	—	0.2300 ± 0.0010	0.0060 ± 0.0002
$g^* \rightarrow q\bar{q}$	—	0.0233 ± 0.0001	0.0011 ± 0.00001
Total GS_R :	0.6298 ± 0.0048	0.3466 ± 0.0048	0.0236 ± 0.0006
Ert/Ali/Zhu	0.5211 ± 0.0020	0.4553 ± 0.0020	0.0236 ± 0.0001

Table B.3 Comparison of the partial cross sections from the ERT/Ali/Zhu calculation with those from the GS calculation, for $Y_{c,DD}=0.03$, and with random-parton recombination

Contribution	Number of final state post-cut partons		
	2	3	4
3-Jet	—	-0.2325 ± 0.0017	—
$q^* \rightarrow qG$	—	0.2832 ± 0.0019	0.0080 ± 0.0004
$g^* \rightarrow gg$	—	0.1951 ± 0.0009	0.0028 ± 0.0001
$g^* \rightarrow q\bar{q}$	—	0.0199 ± 0.0001	0.00057 ± 0.00002
Total GS_R :	0.7230 ± 0.0033	0.2657 ± 0.0046	0.0113 ± 0.0004
Ert/Ali/Zhu	0.6273 ± 0.0019	0.3605 ± 0.0019	0.0118 ± 0.0003

Table B.4 Comparison of the partial cross sections from the ERT/Ali/Zhu calculation with those from the GS calculation, for $Y_{c,DD}=0.04$, and with random-parton recombination

Contribution	Number of final state post-cut partons		
	2	3	4
3-Jet	—	-0.2134 ± 0.0017	—
$q^* \rightarrow qG$	—	0.2450 ± 0.0018	0.0043 ± 0.0003
$g^* \rightarrow gg$	—	0.1653 ± 0.0008	0.0014 ± 0.0001
$g^* \rightarrow q\bar{q}$	—	0.0169 ± 0.0001	0.00031 ± 0.00002
Total GS_R :	0.7802 ± 0.0034	0.2137 ± 0.0044	0.0061 ± 0.0004
Ert/Ali/Zhu	0.6974 ± 0.0012	0.2963 ± 0.0017	0.0062 ± 0.0002

Table B.5 Comparison of the partial cross sections from the **ERT/Ali/Zhu** calculation with those from the **GS** calculation, for $Y_{c,DD}=0.05$, and with random-parton recombination

Appendix C

Model Comparisons: Plots

In order to avoid cluttering the main bulk of the text with plots, many of the comparisons of the model predictions with the data are presented in this appendix.

For all the comparisons shown here, the 70/60/60 event selection cuts were used, and the model predictions are shown after having been processed by the detector simulation. The comparisons for Thrust, the Energy-Energy Correlation function and the flower-plots have been given in Chapter 7; the comparison for the Energy-Energy Correlation Asymmetry has been presented in Chapter 8. The α_s values used for the following plots are the same as those used in Chapter 7.

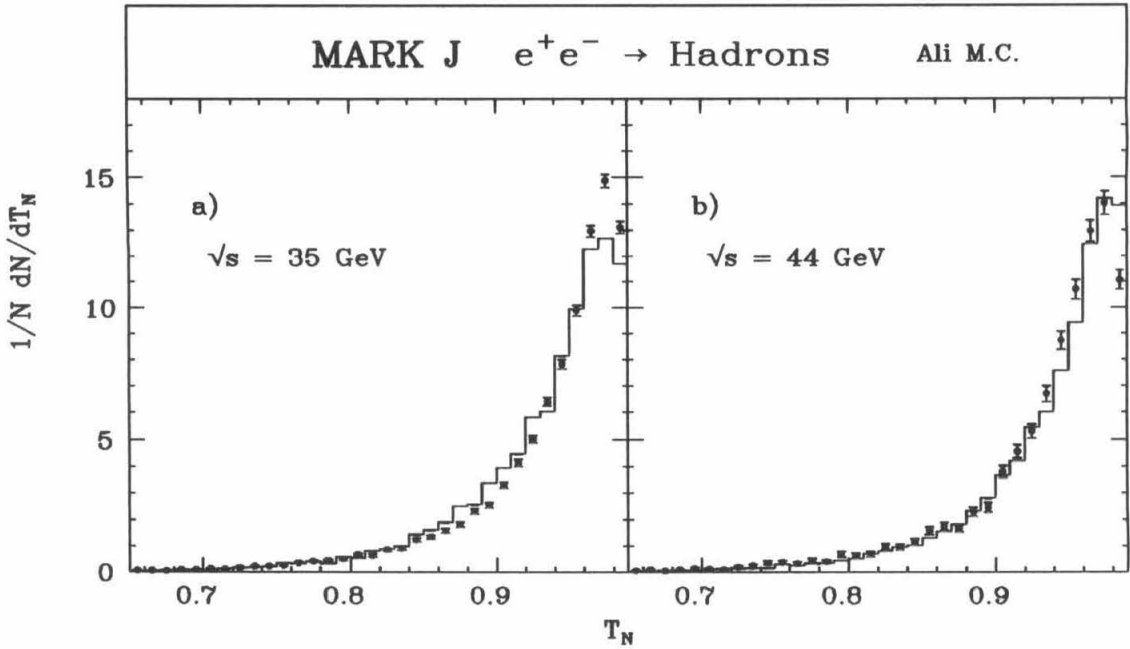


Figure C.1 The Ali model predictions for T_N compared to the data at 35 GeV, a), and 44 GeV, b).

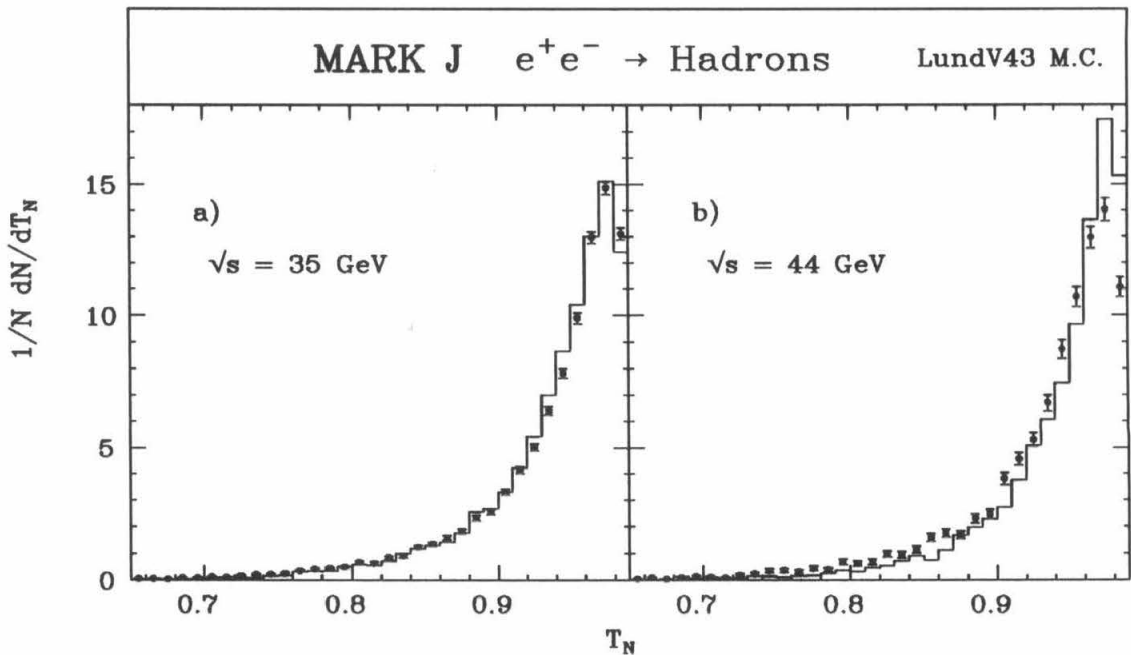


Figure C.2 The LundV4.3 model predictions for T_N compared to the data at 35 GeV, a), and 44 GeV, b).

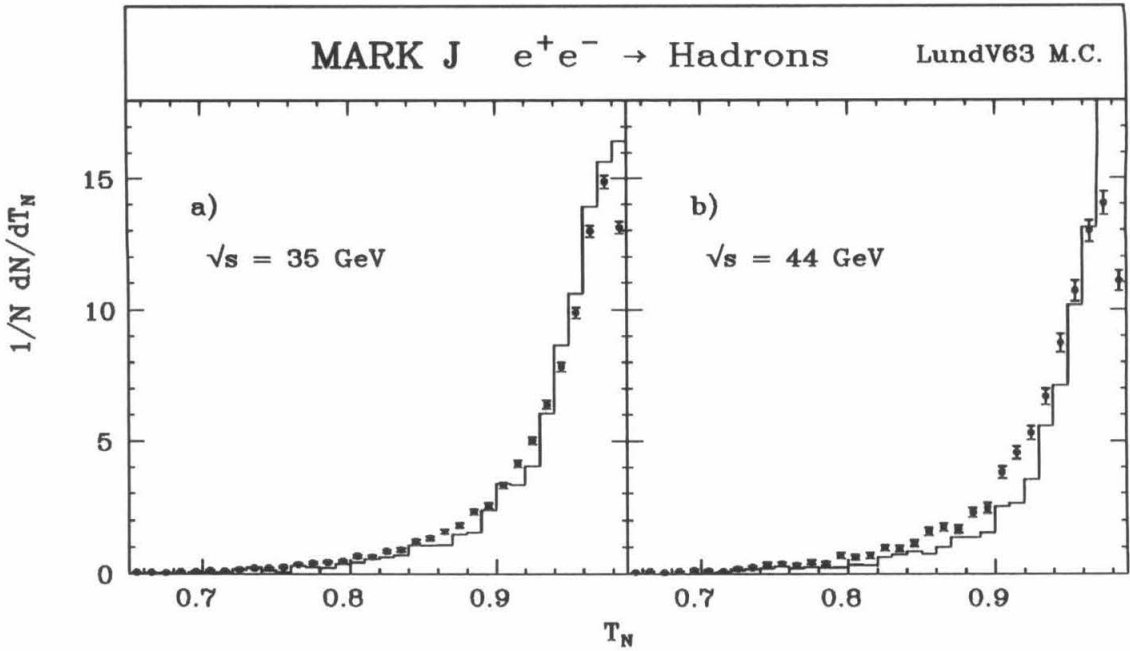


Figure C.3 The LundV6.3 model predictions for T_N compared to the data at 35 GeV, a), and 44 GeV, b).

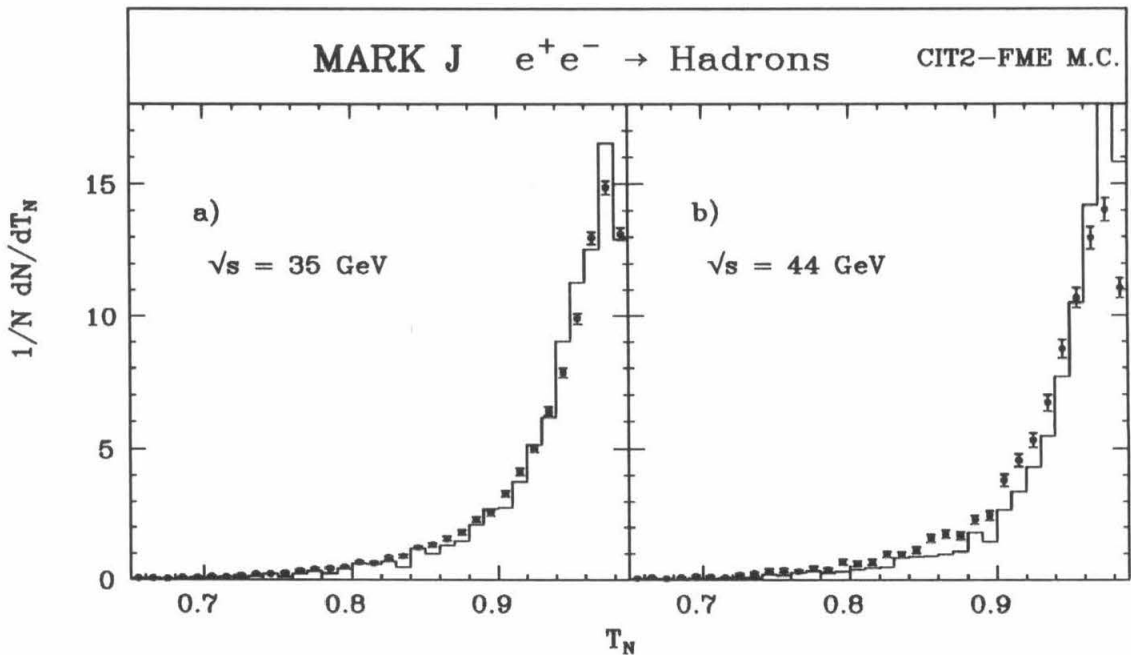


Figure C.4 The CIT2-FME model predictions for T_N compared to the data at 35 GeV, a), and 44 GeV, b).

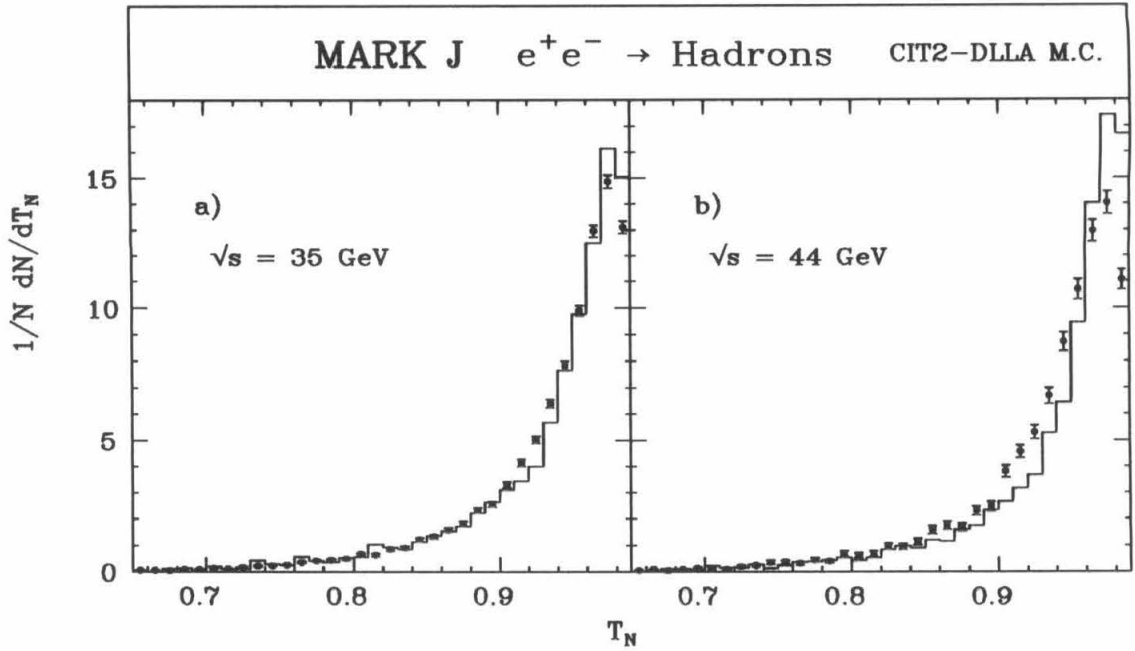


Figure C.5 The CIT2-DLLA model predictions for T_N compared to the data at 35 GeV, a), and 44 GeV, b).

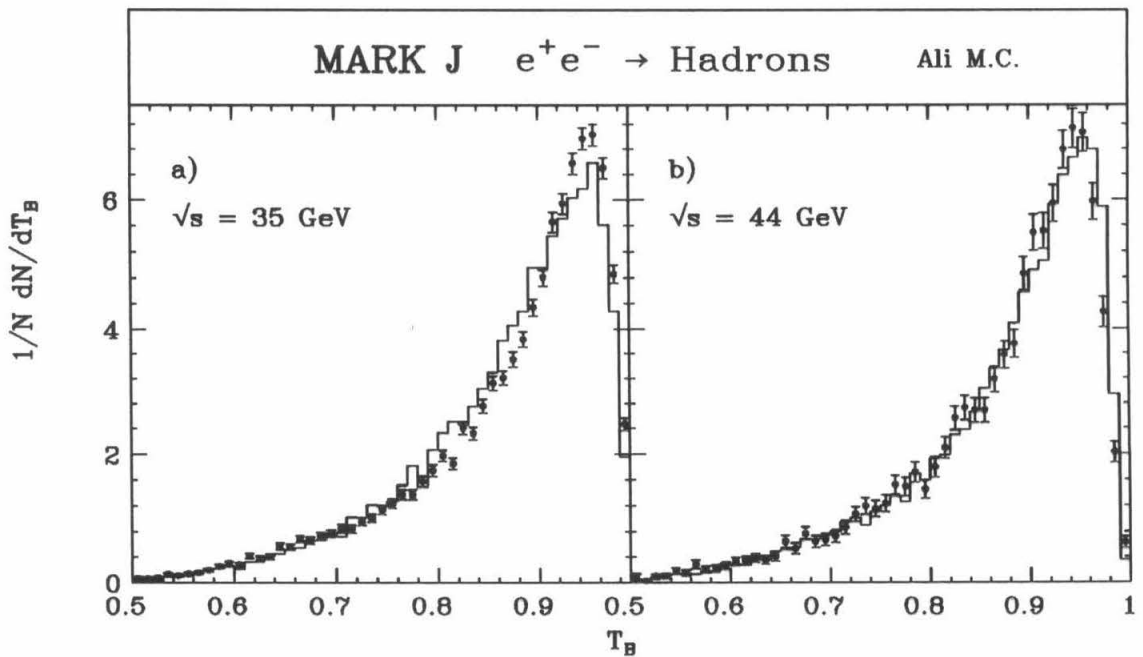


Figure C.6 The Ali model predictions for T_B compared to the data at 35 GeV, a), and 44 GeV, b).

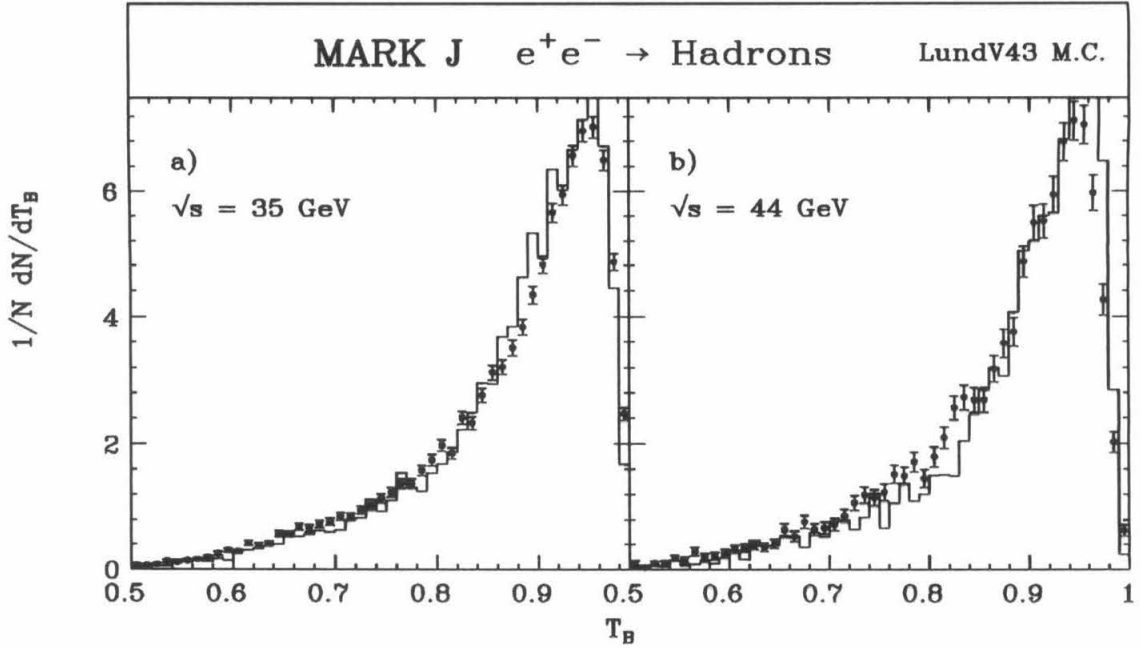


Figure C.7 The LundV4.3 model predictions for T_B compared to the data at 35 GeV, a), and 44 GeV, b).

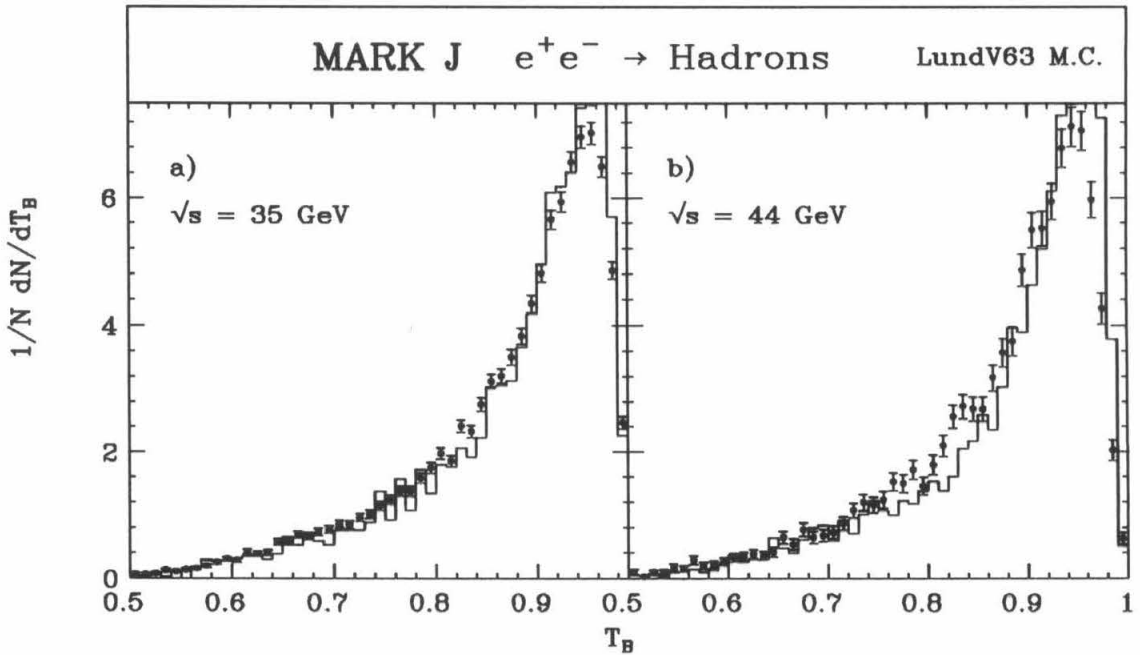


Figure C.8 The LundV6.3 model predictions for T_B compared to the data at 35 GeV, a), and 44 GeV, b).

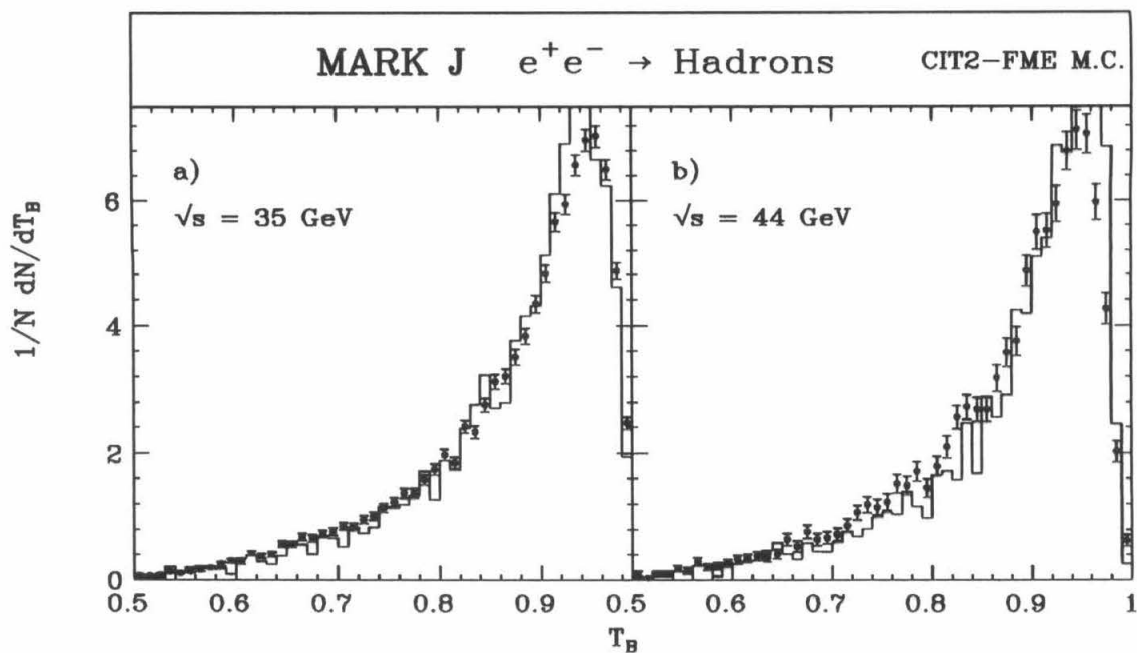


Figure C.9 The CIT2-FME model predictions for T_B compared to the data at 35 GeV, a), and 44 GeV, b).

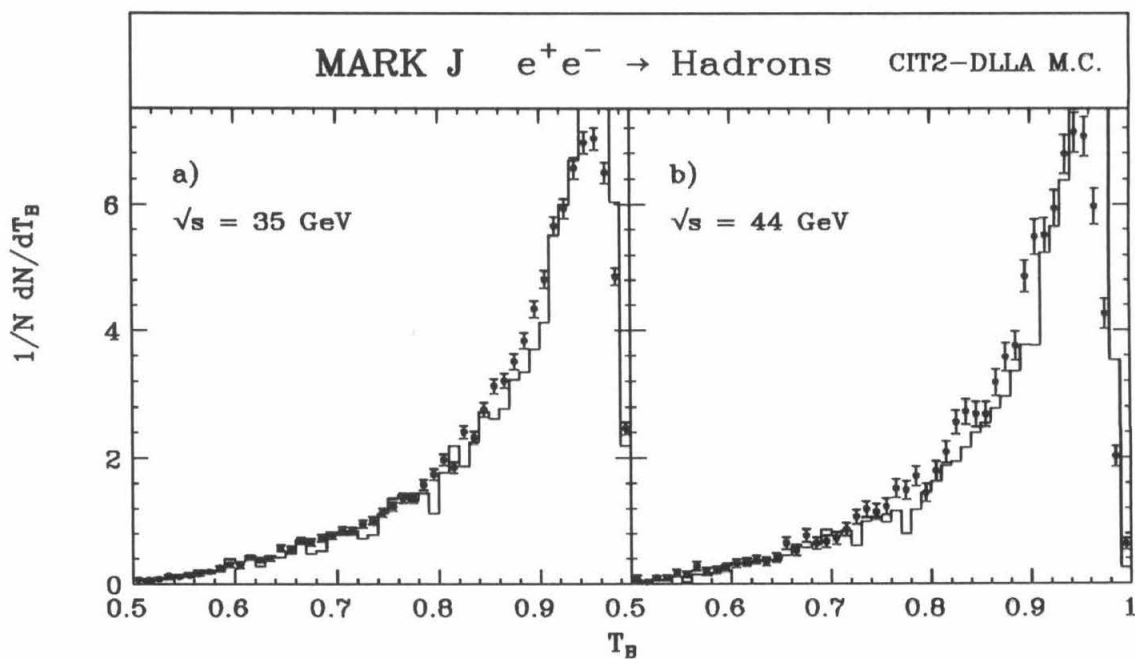


Figure C.10 The CIT2-DLLA model predictions for T_B compared to the data at 35 GeV, a), and 44 GeV, b).

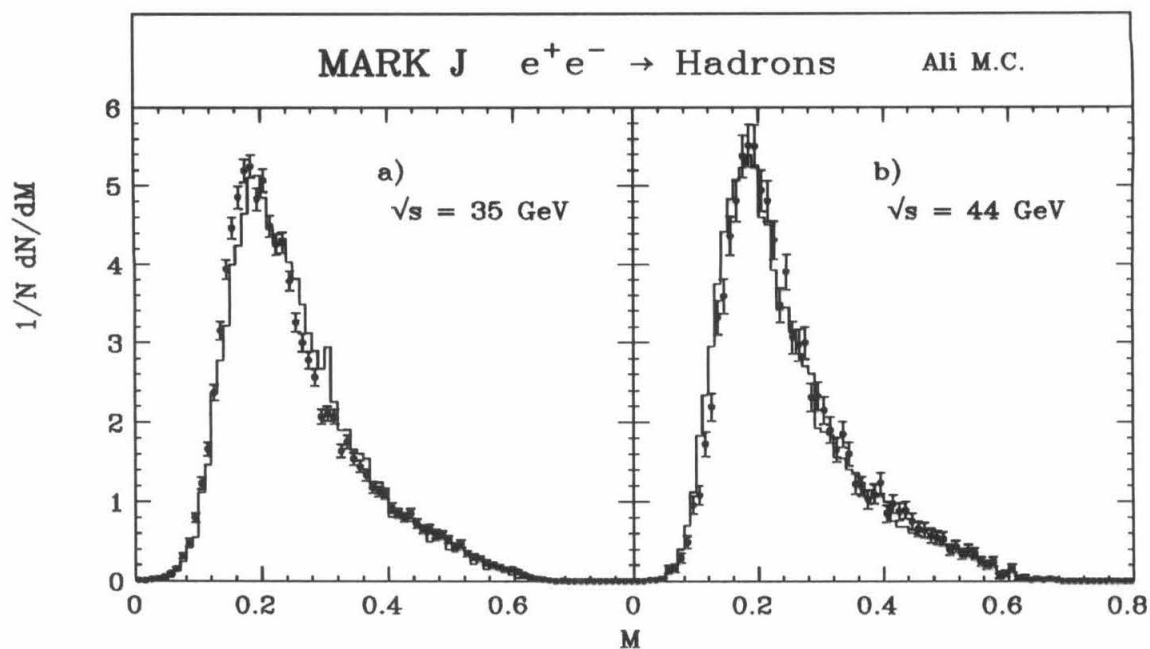


Figure C.11 The Ali model predictions for M compared to the data at 35 GeV, a), and 44 GeV, b).

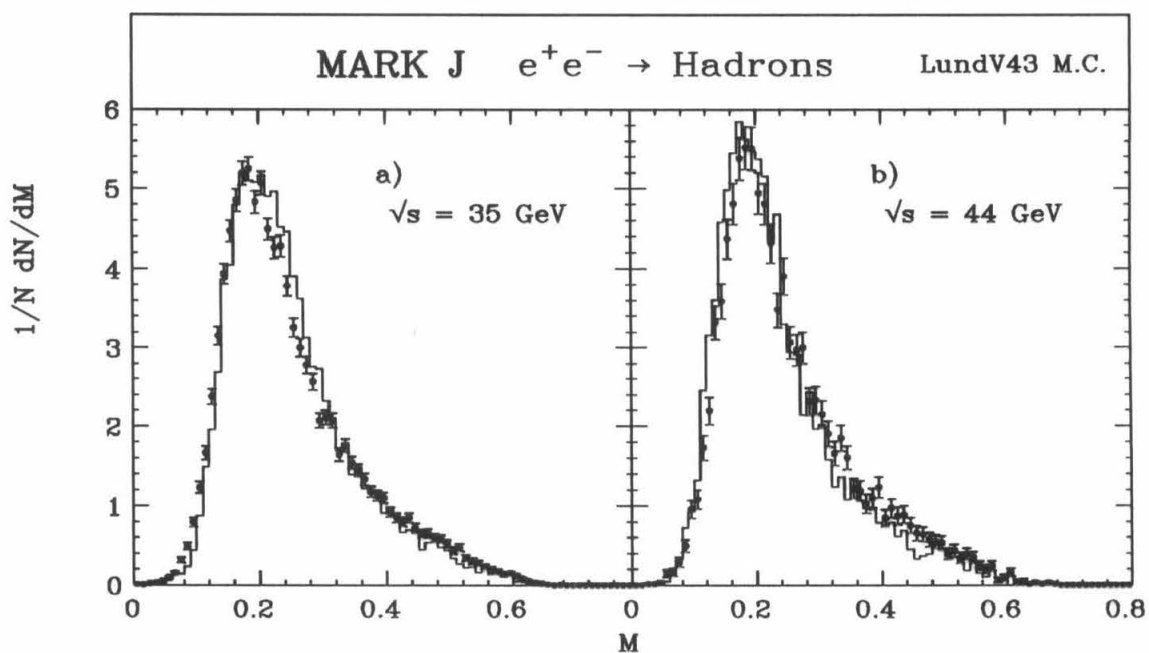


Figure C.12 The LundV4.3 model predictions for M compared to the data at 35 GeV, a), and 44 GeV, b).

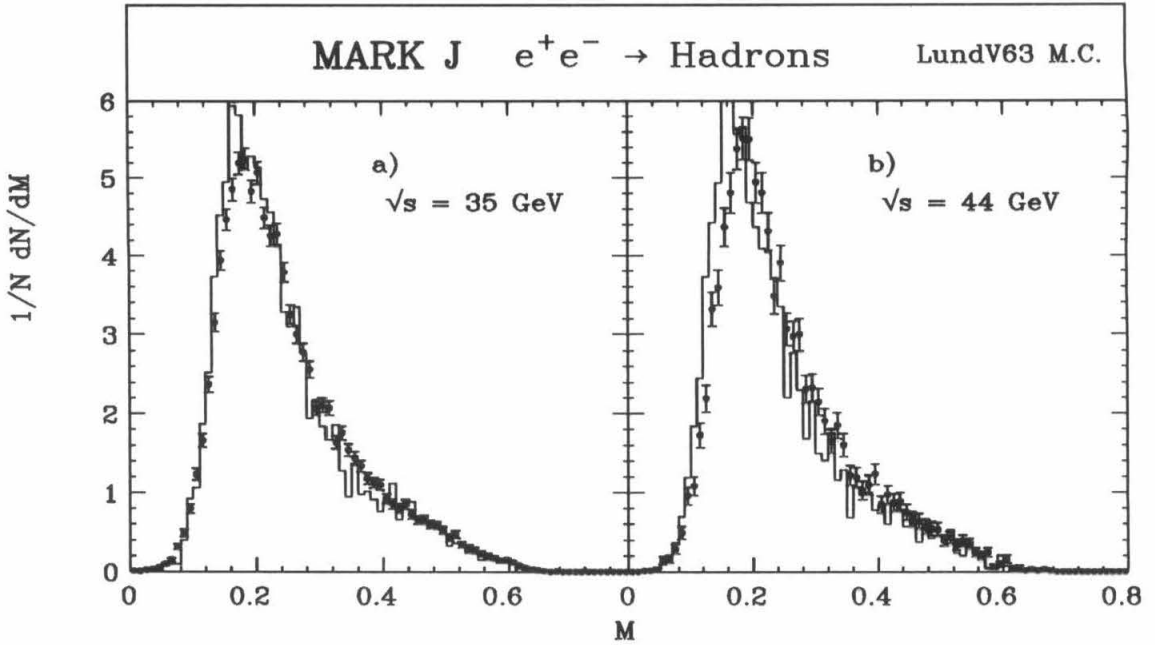


Figure C.13 The LundV6.3 model predictions for M compared to the data at 35 GeV, a), and 44 GeV, b).

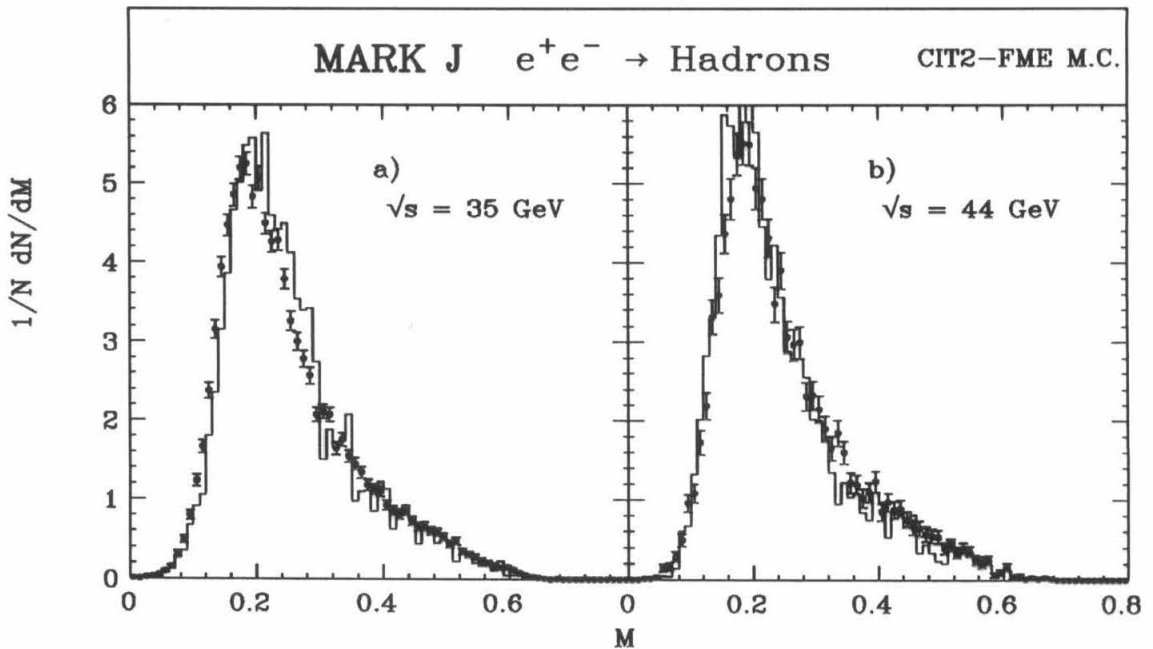


Figure C.14 The CIT2-FME model predictions for M compared to the data at 35 GeV, a), and 44 GeV, b).

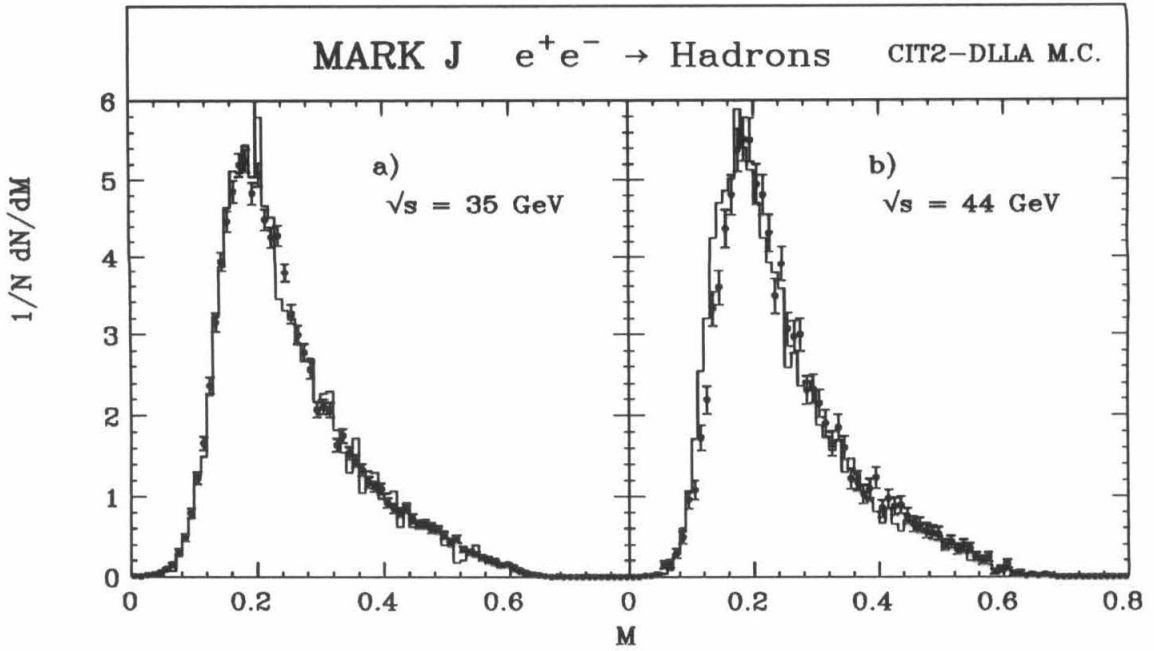


Figure C.15 The CIT2-DLLA model predictions for M compared to the data at 35 GeV, a), and 44 GeV, b).

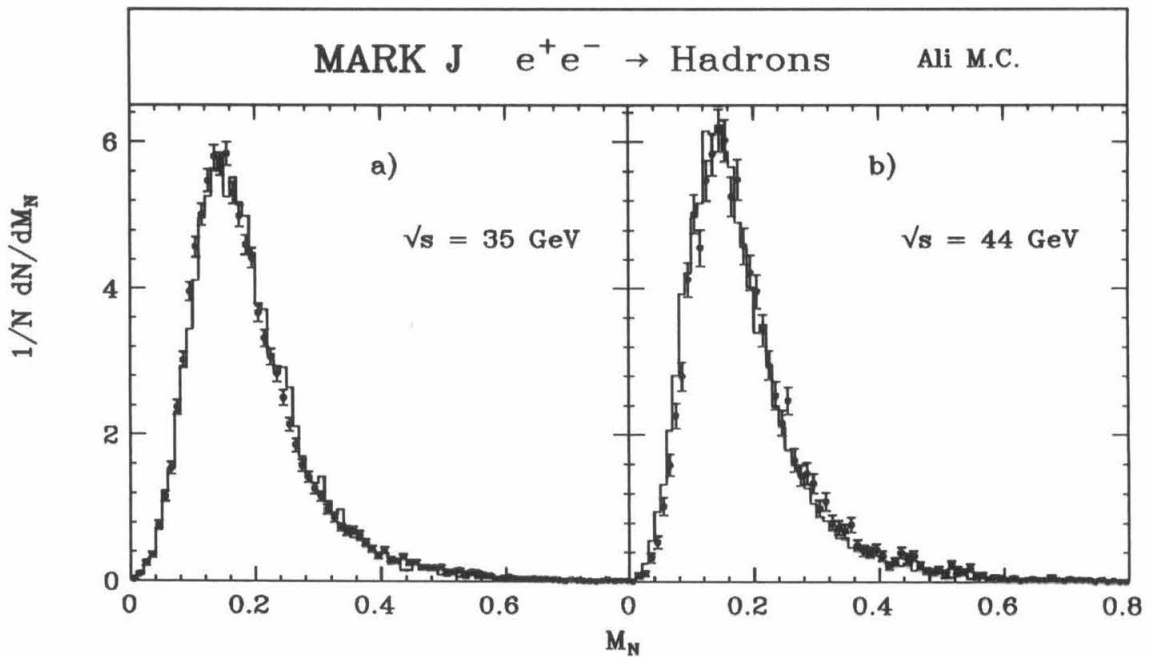


Figure C.16 The Ali model predictions for M_N compared to the data at 35 GeV, a), and 44 GeV, b).

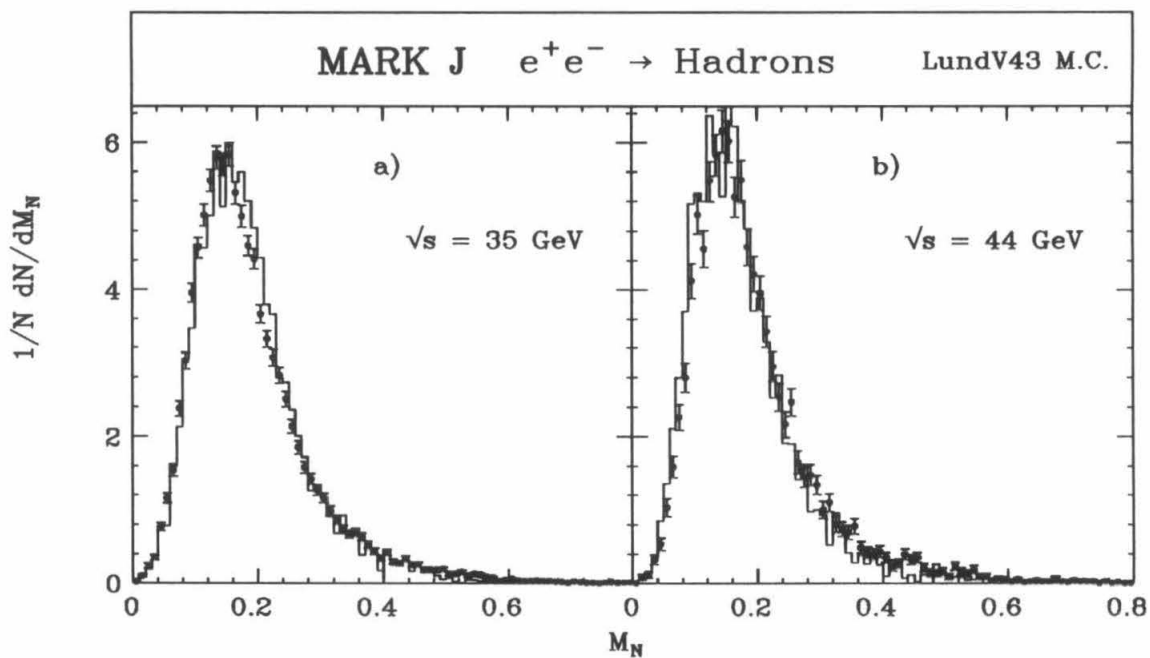


Figure C.17 The LundV4.3 model predictions for M_N compared to the data at 35 GeV, a), and 44 GeV, b).

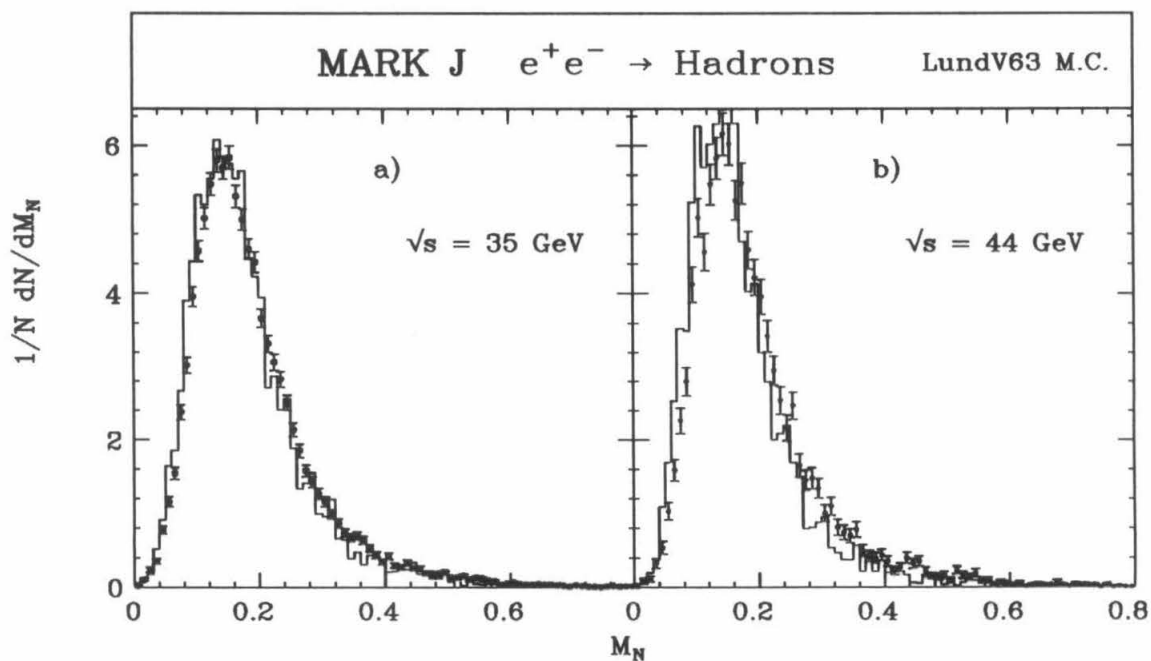


Figure C.18 The LundV6.3 model predictions for M_N compared to the data at 35 GeV, a), and 44 GeV, b).

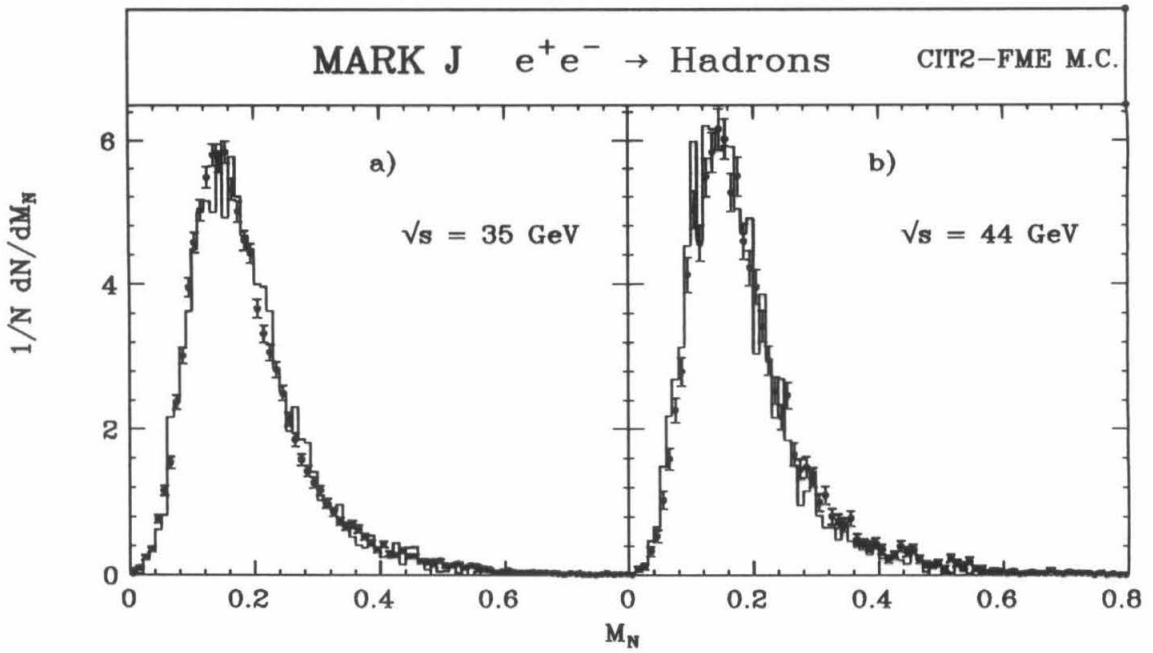


Figure C.19 The CIT2-FME model predictions for M_N compared to the data at 35 GeV, a), and 44 GeV, b).

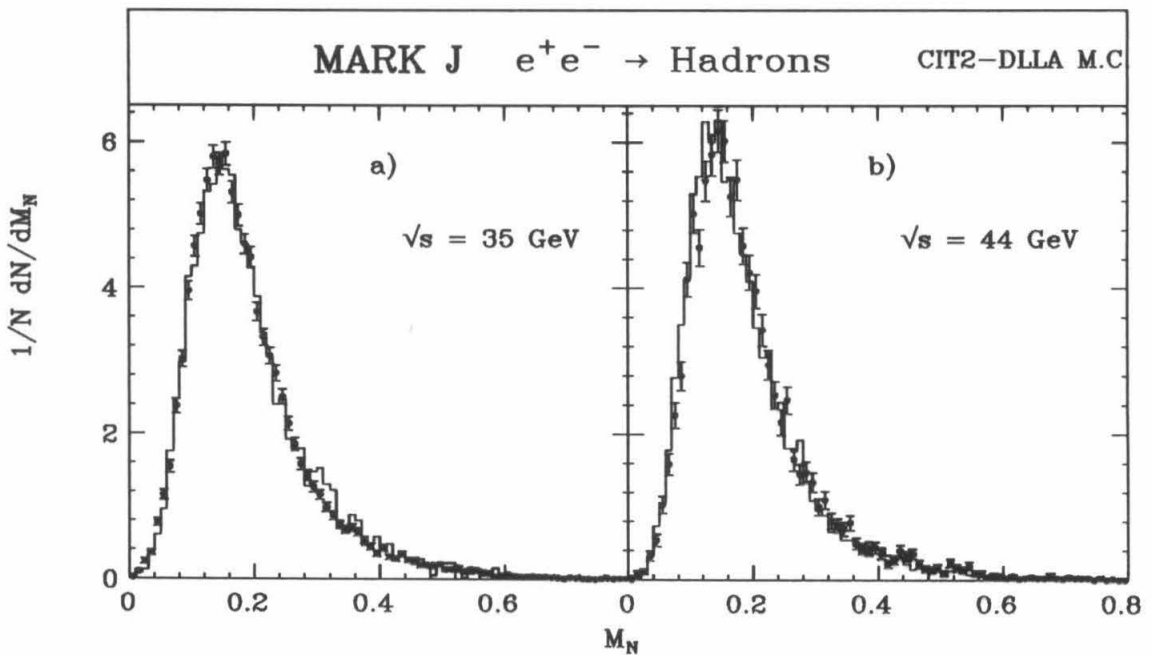


Figure C.20 The CIT2-DLLA model predictions for M_N compared to the data at 35 GeV, a), and 44 GeV, b).

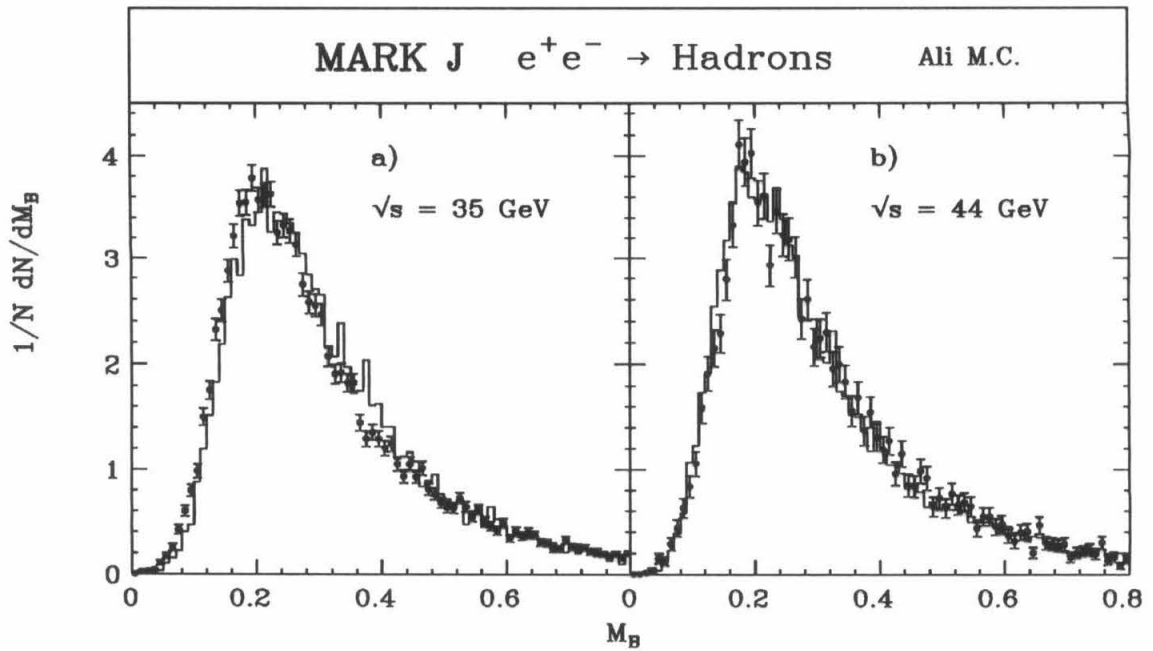


Figure C.21 The Ali model predictions for M_B compared to the data at 35 GeV, a), and 44 GeV, b).

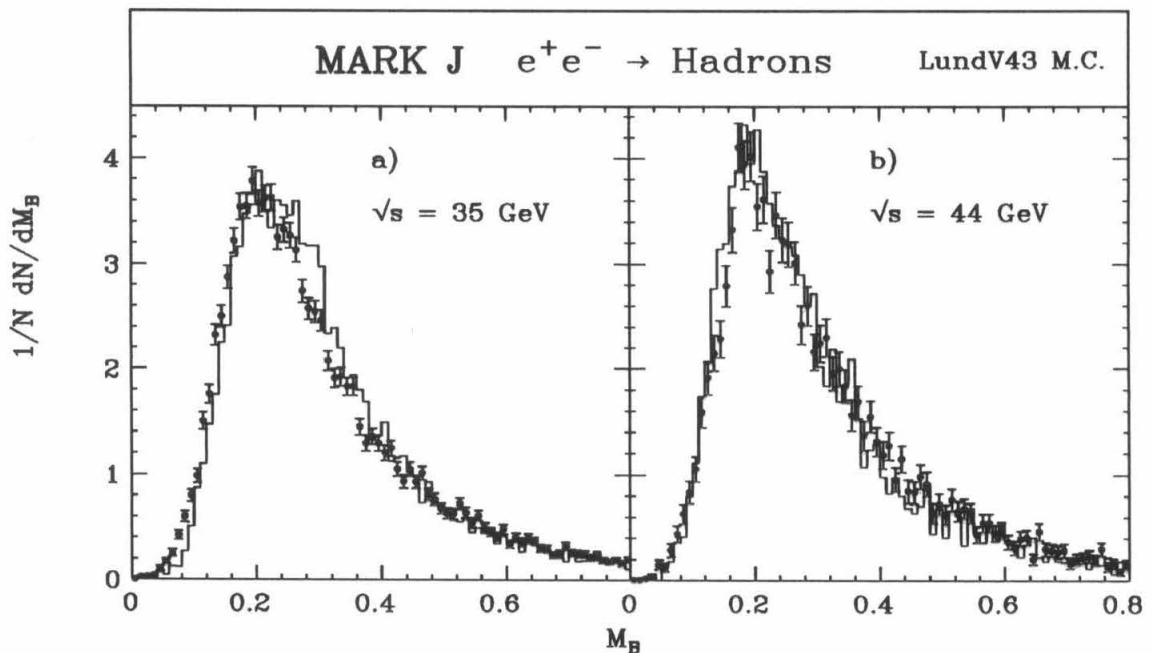


Figure C.22 The LundV4.3 model predictions for M_B compared to the data at 35 GeV, a), and 44 GeV, b).

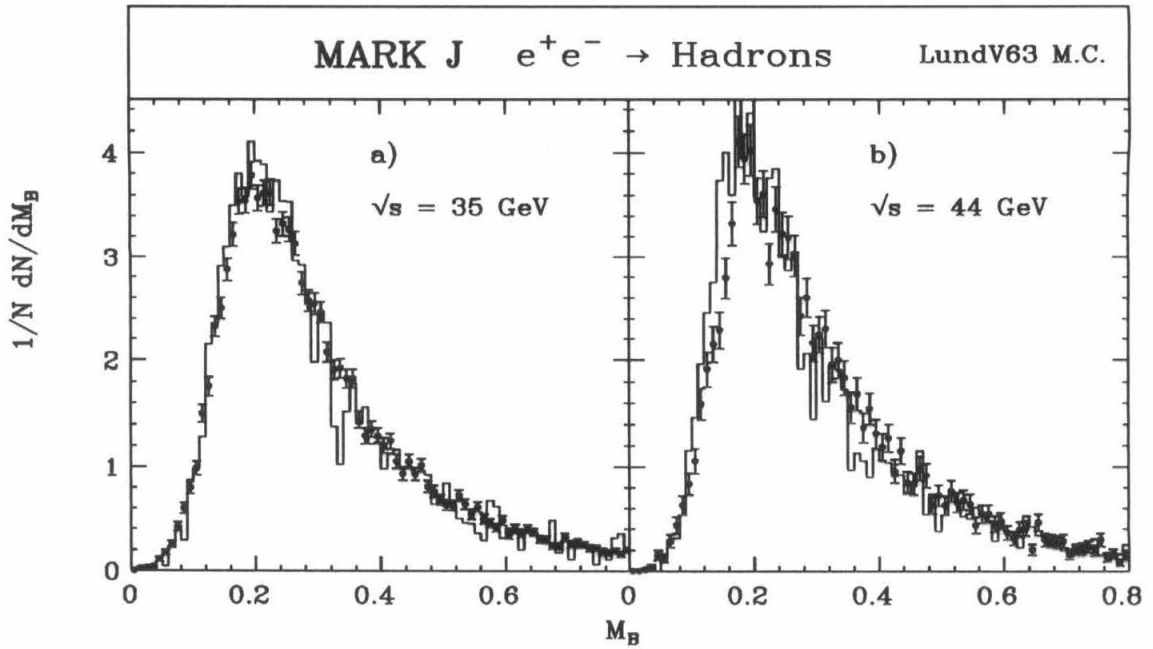


Figure C.23 The LundV6.3 model predictions for M_B compared to the data at 35 GeV, a), and 44 GeV, b).

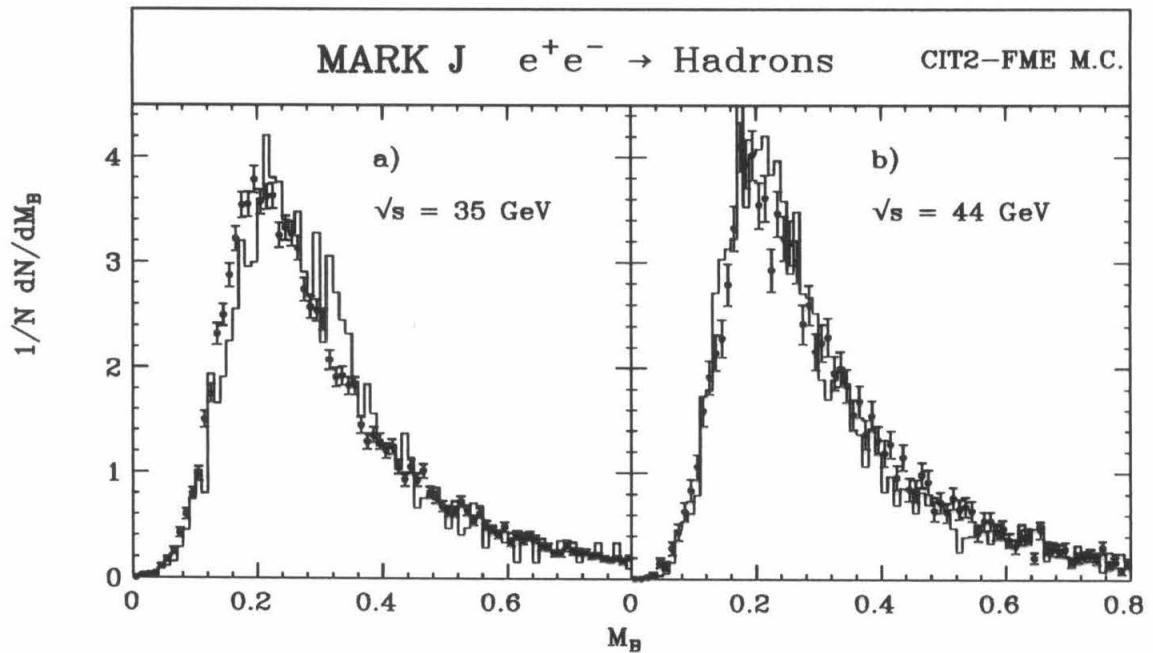


Figure C.24 The CIT2-FME model predictions for M_B compared to the data at 35 GeV, a), and 44 GeV, b).

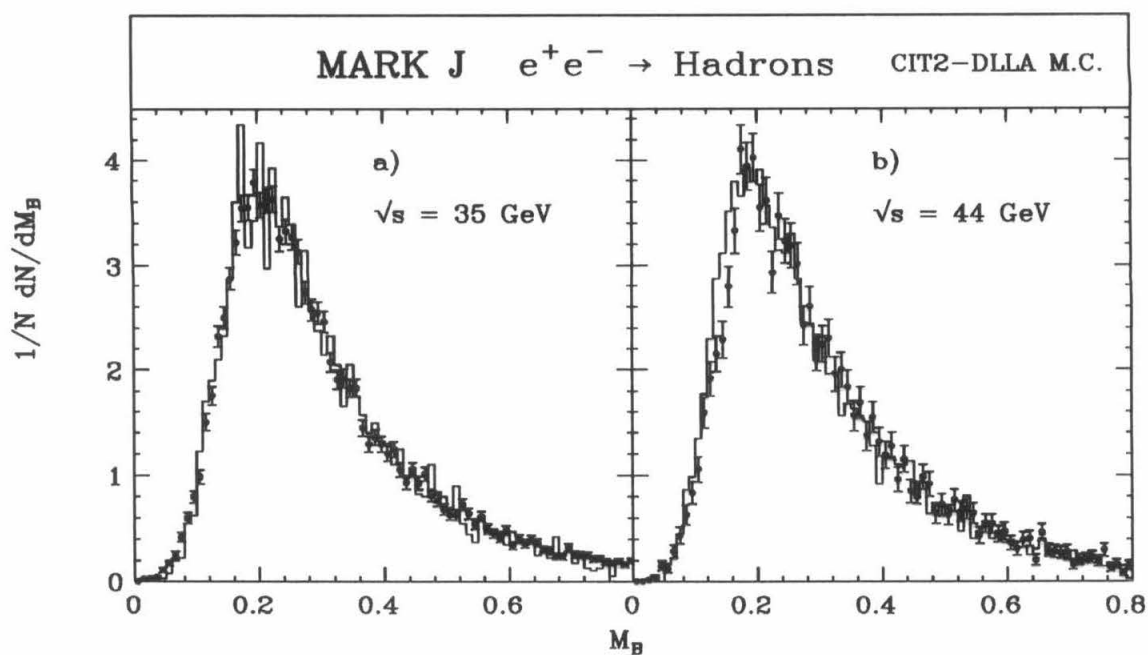


Figure C.25 The CIT2-DLLA model predictions for M_B compared to the data at 35 GeV, a), and 44 GeV, b).

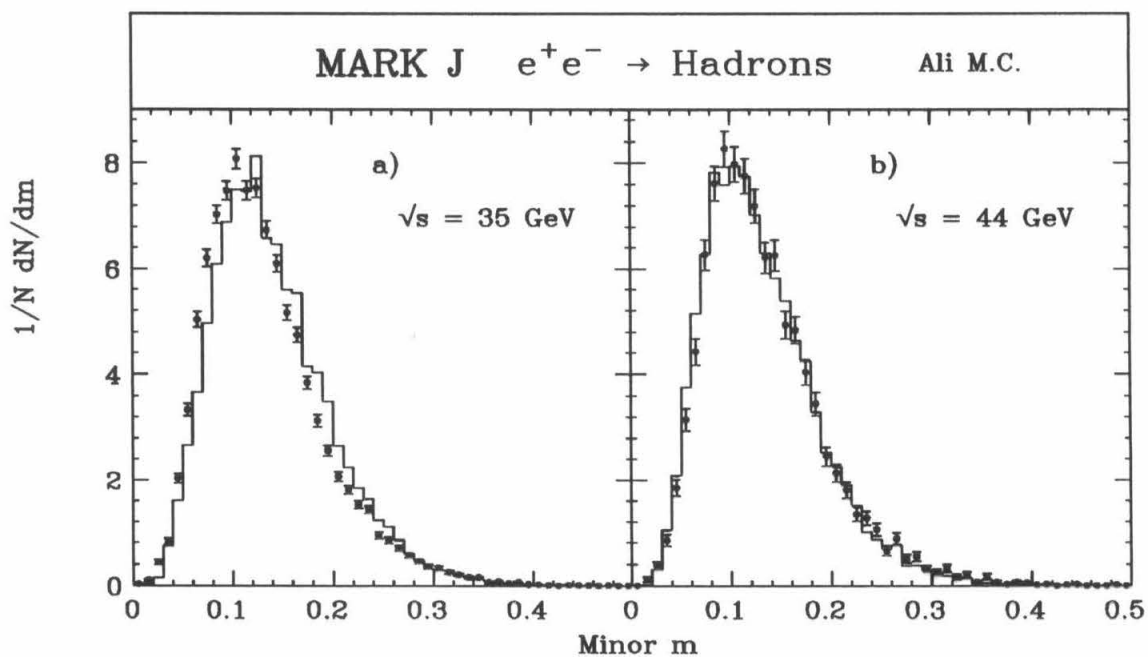


Figure C.26 The Ali model predictions for m compared to the data at 35 GeV, a), and 44 GeV, b).

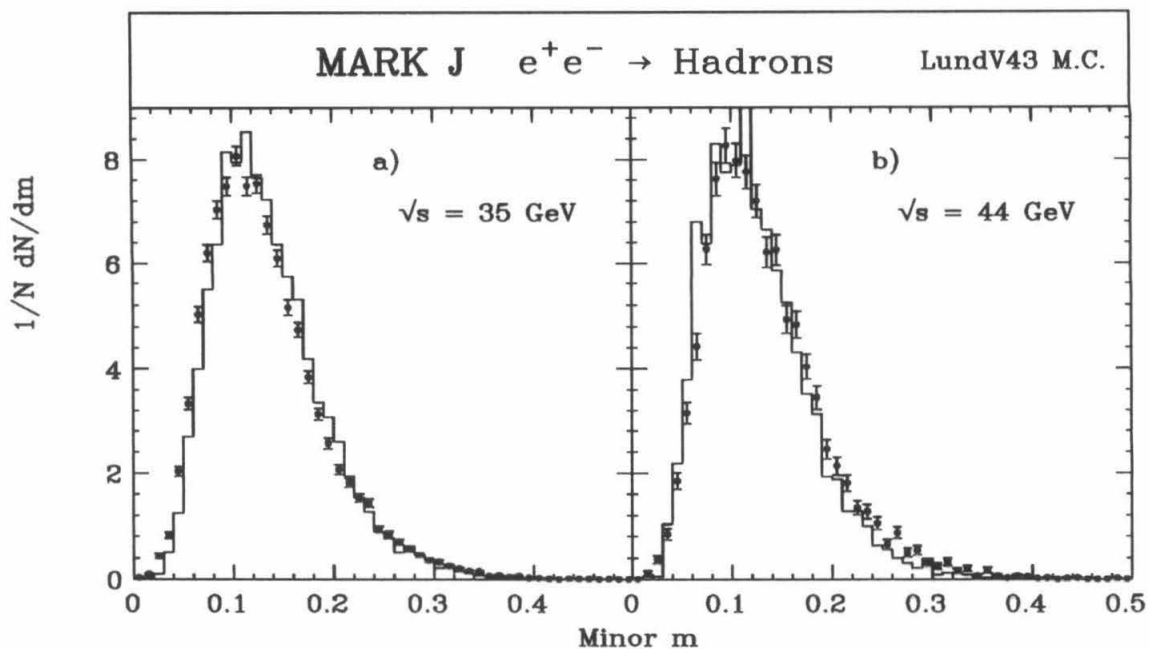


Figure C.27 The LundV4.3 model predictions for m compared to the data at 35 GeV, a), and 44 GeV, b).

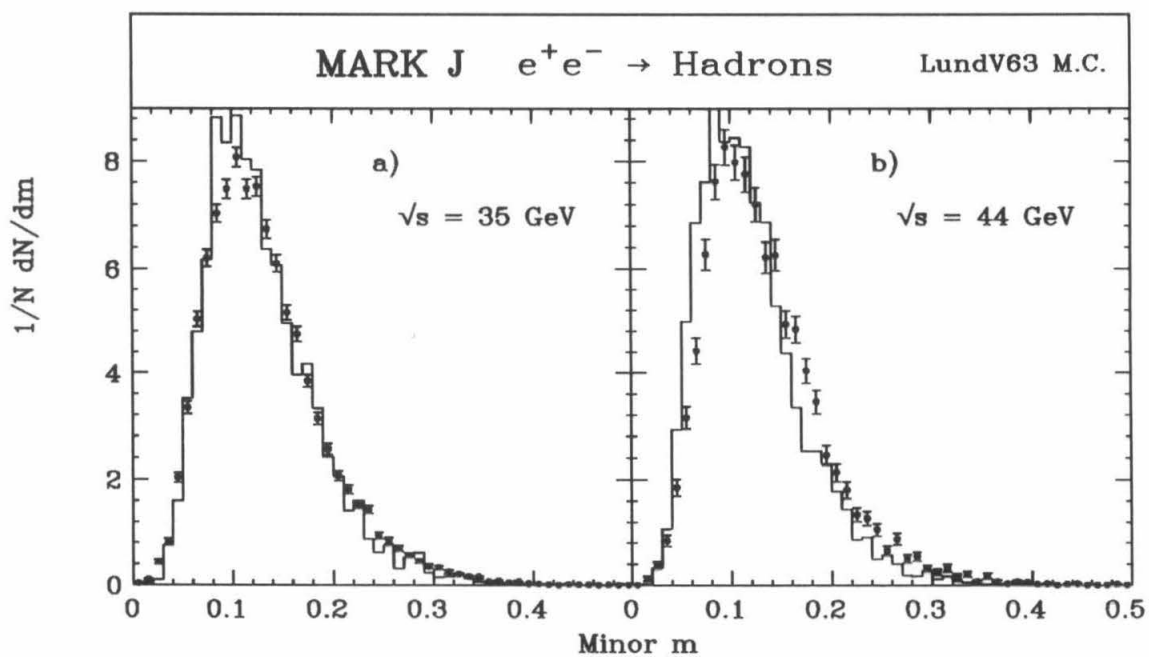


Figure C.28 The LundV6.3 model predictions for m compared to the data at 35 GeV, a), and 44 GeV, b).

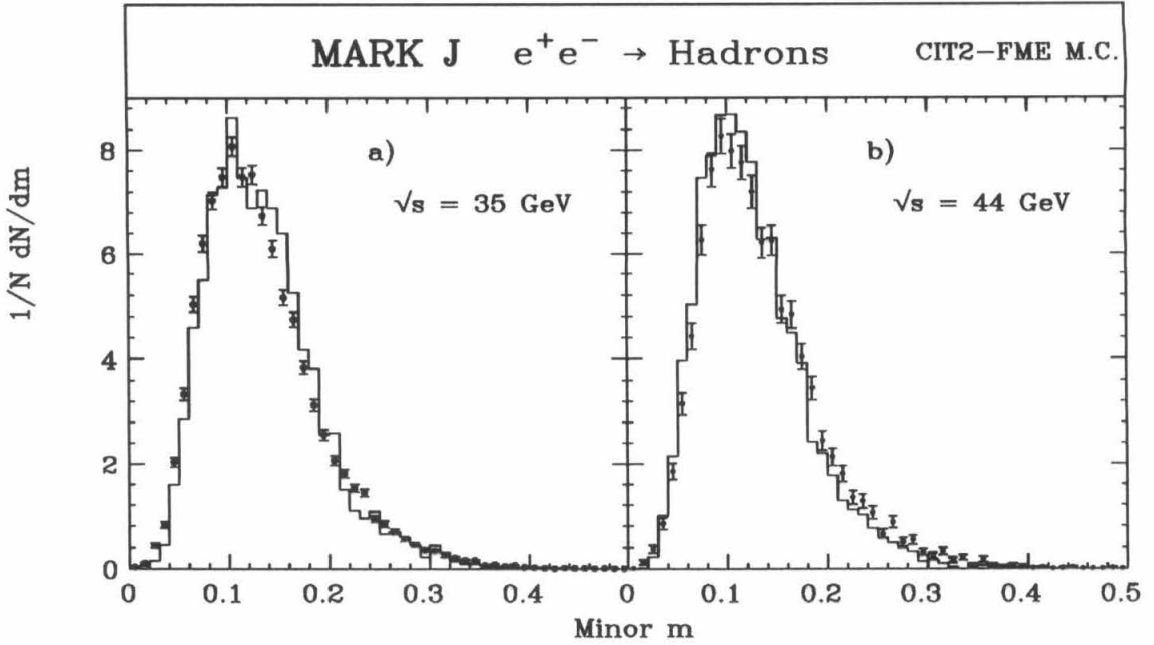


Figure C.29 The CIT2-FME model predictions for m compared to the data at 35 GeV, a), and 44 GeV, b).

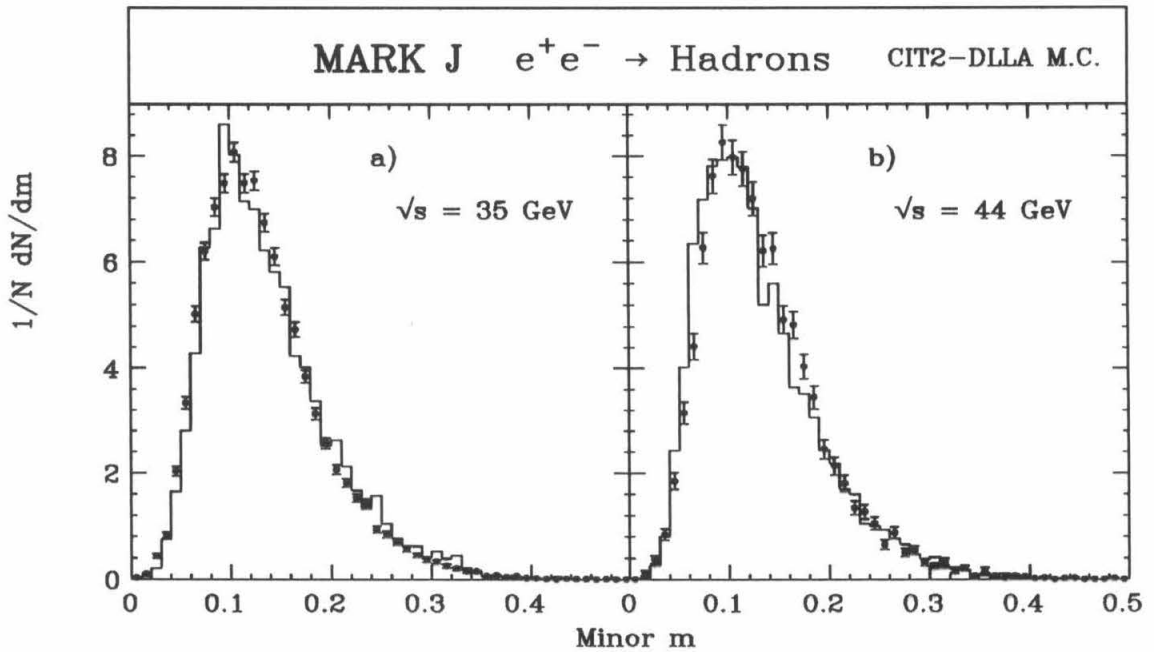


Figure C.30 The CIT2-DLLA model predictions for m compared to the data at 35 GeV, a), and 44 GeV, b).

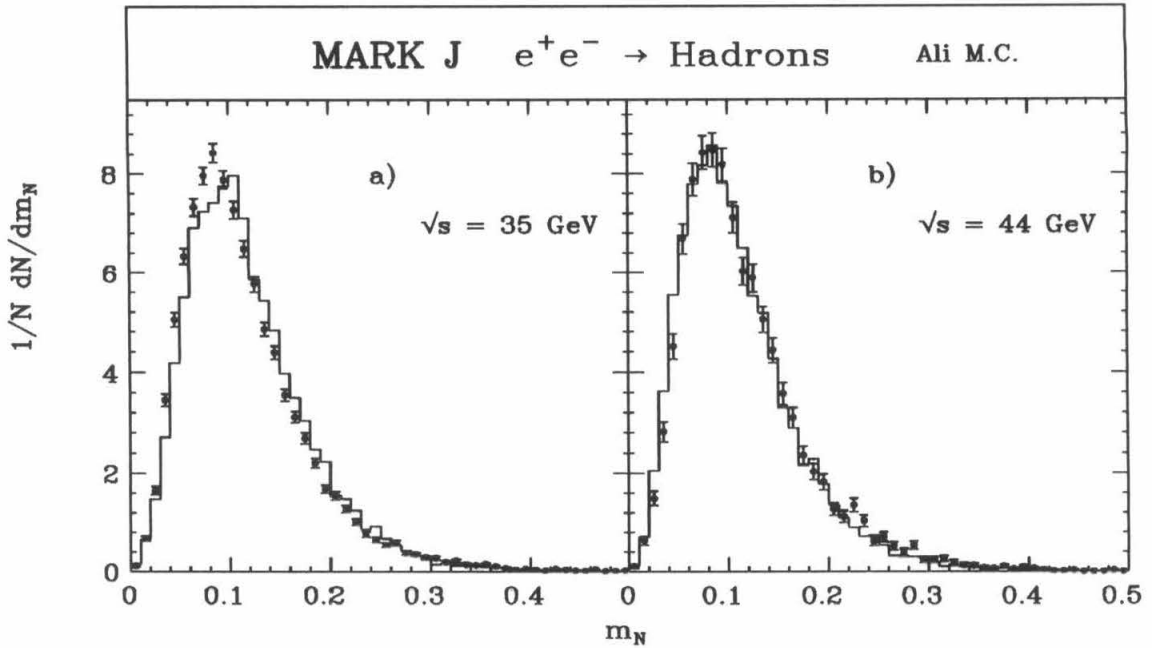


Figure C.31 The Ali model predictions for m_N compared to the data at 35 GeV, a), and 44 GeV, b).

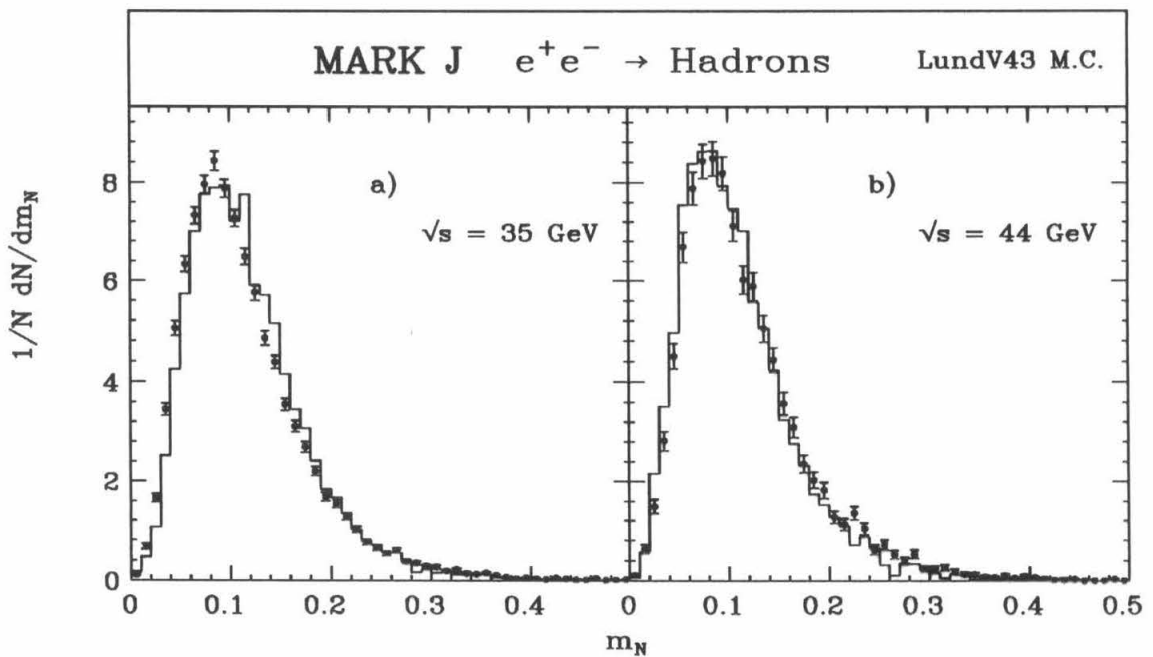


Figure C.32 The LundV4.3 model predictions for m_N compared to the data at 35 GeV, a), and 44 GeV, b).

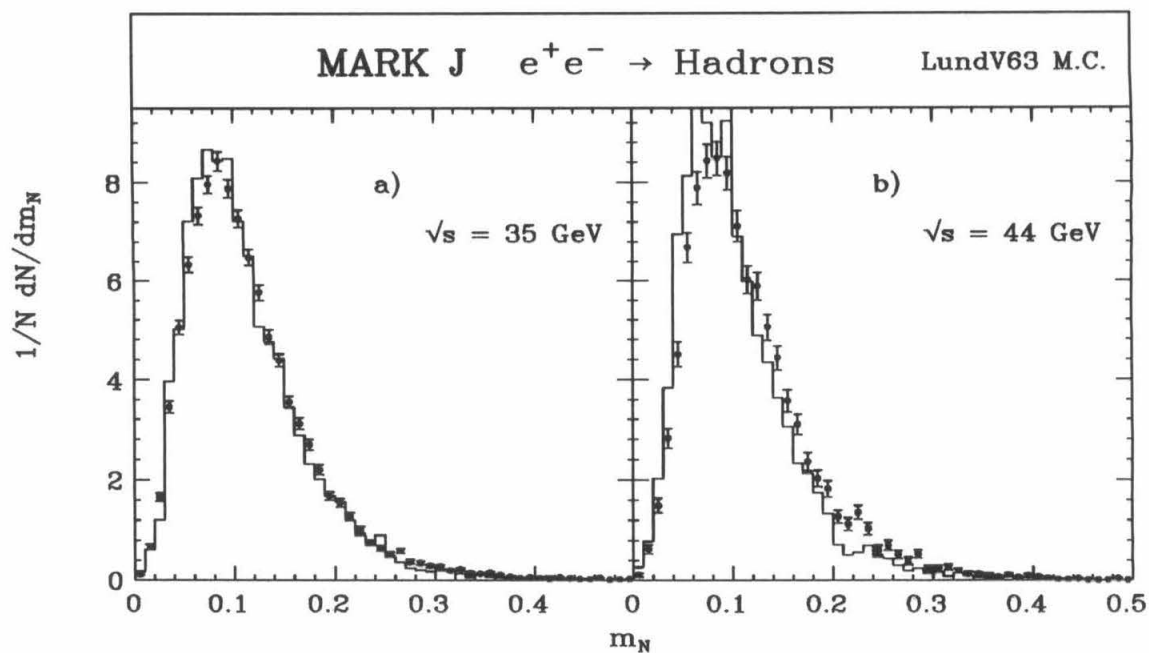


Figure C.33 The LundV6.3 model predictions for m_N compared to the data at 35 GeV, a), and 44 GeV, b).

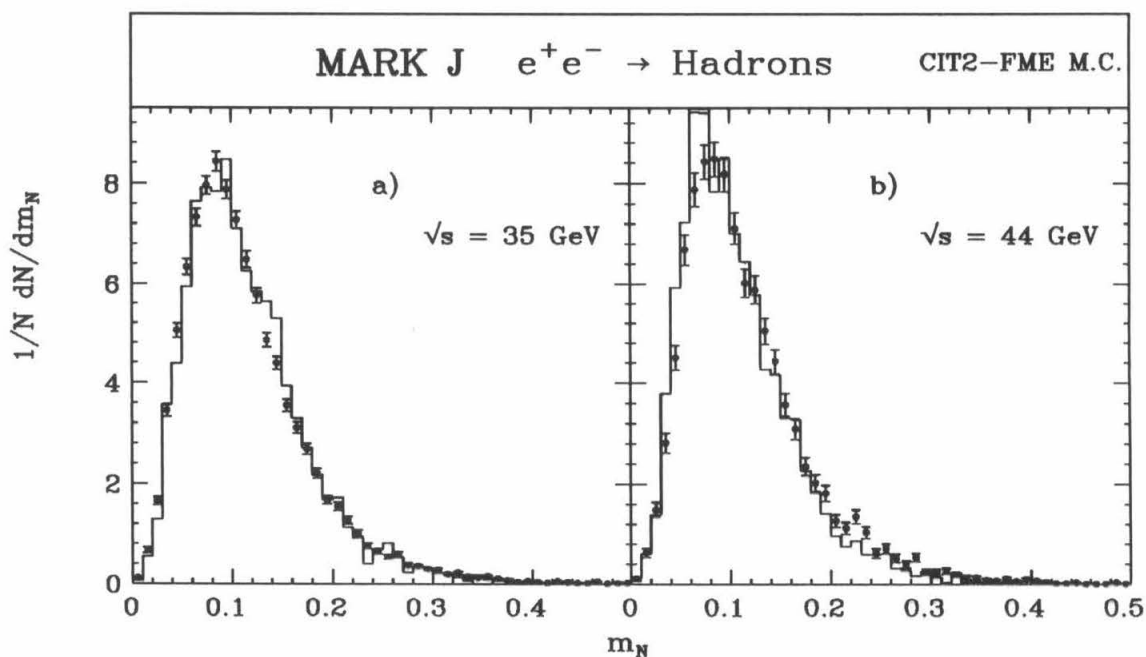


Figure C.34 The CIT2-FME model predictions for m_N compared to the data at 35 GeV, a), and 44 GeV, b).

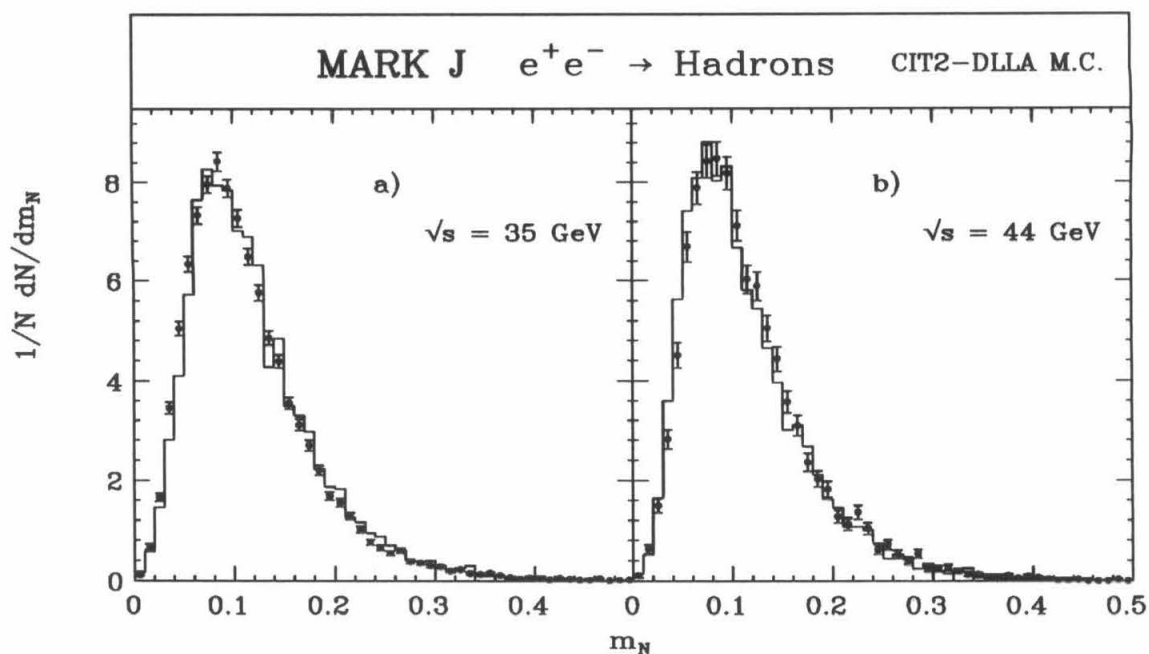


Figure C.35 The CIT2-DLLA model predictions for m_N compared to the data at 35 GeV, a), and 44 GeV, b).

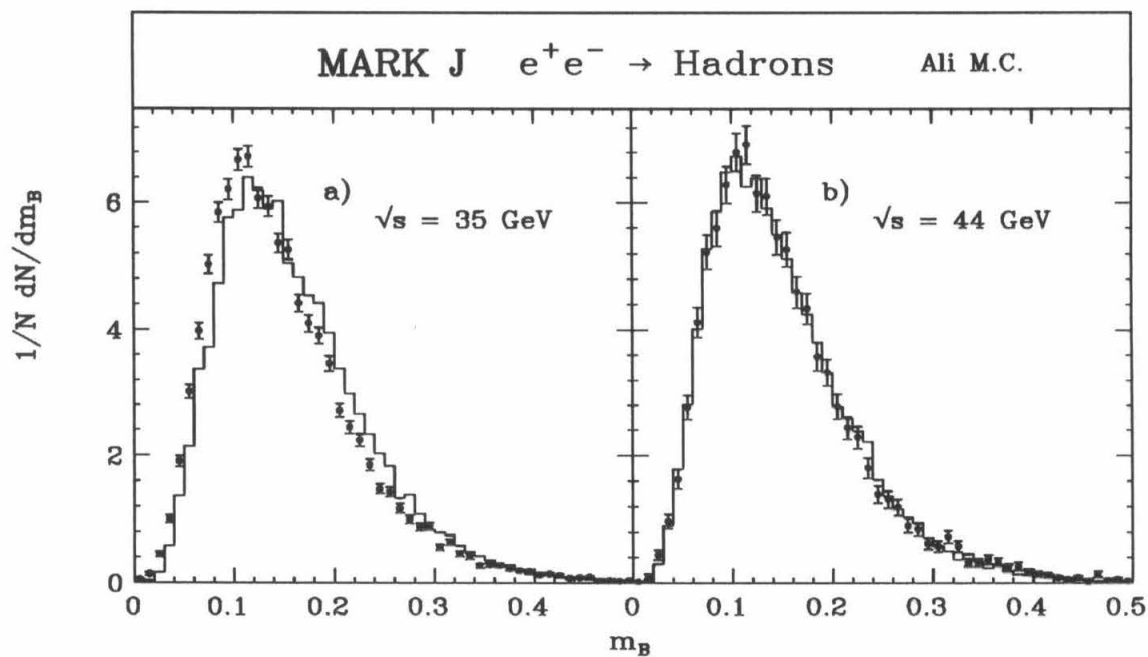


Figure C.36 The Ali model predictions for m_B compared to the data at 35 GeV, a), and 44 GeV, b).

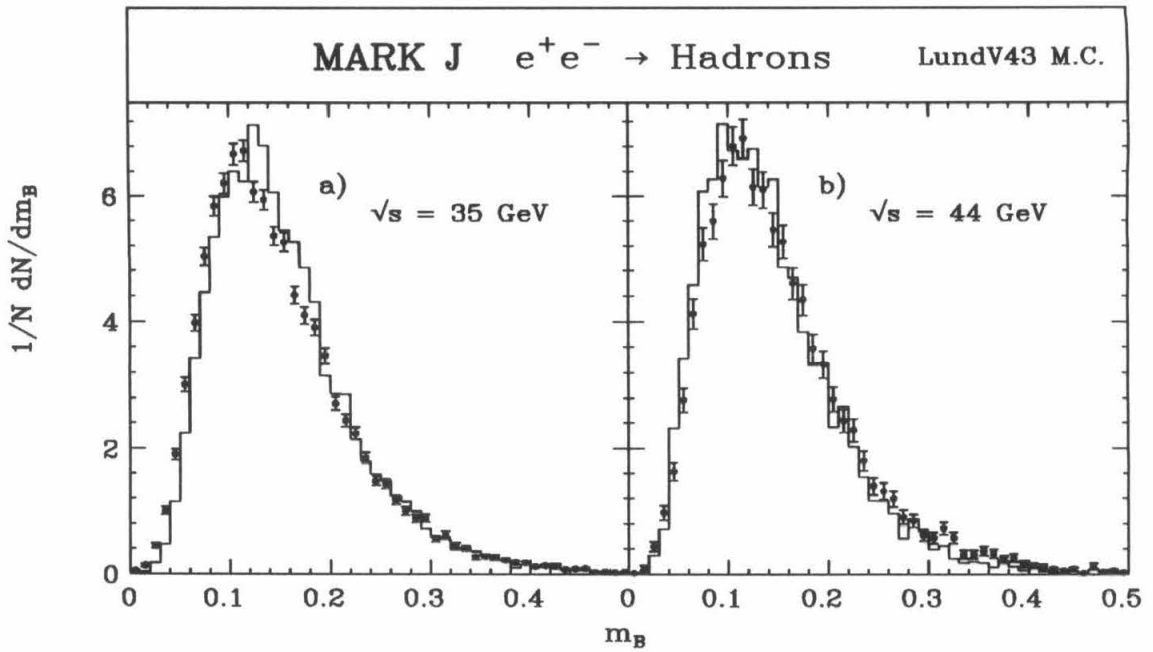


Figure C.37 The LundV4.3 model predictions for m_B compared to the data at 35 GeV, a), and 44 GeV, b).

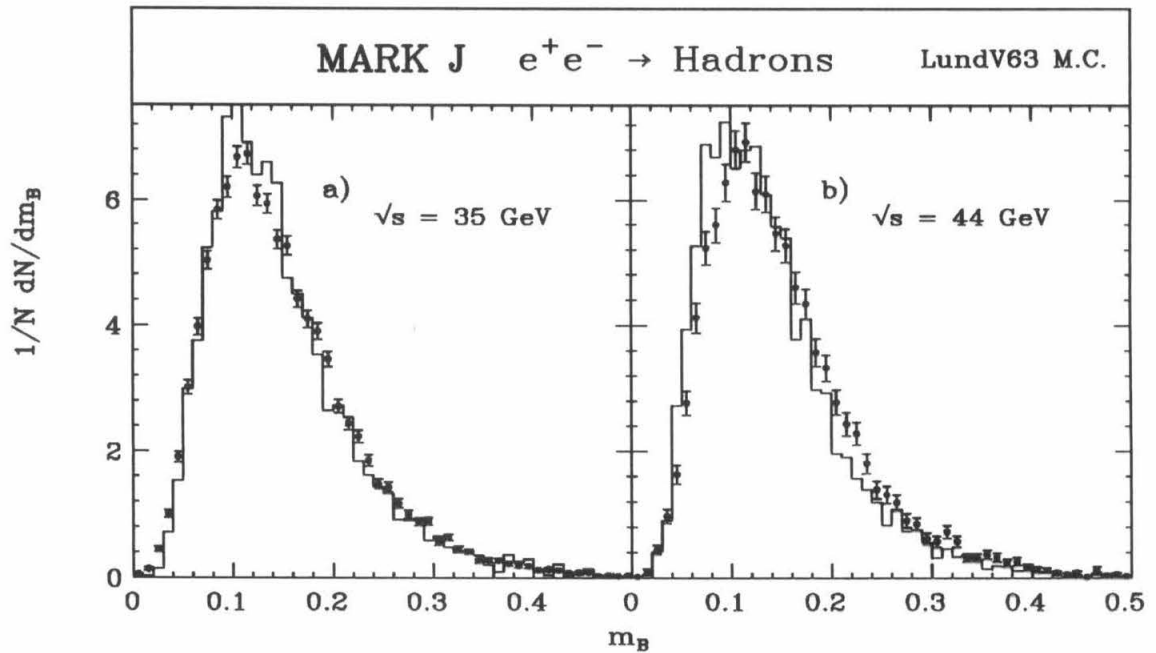


Figure C.38 The LundV6.3 model predictions for m_B compared to the data at 35 GeV, a), and 44 GeV, b).

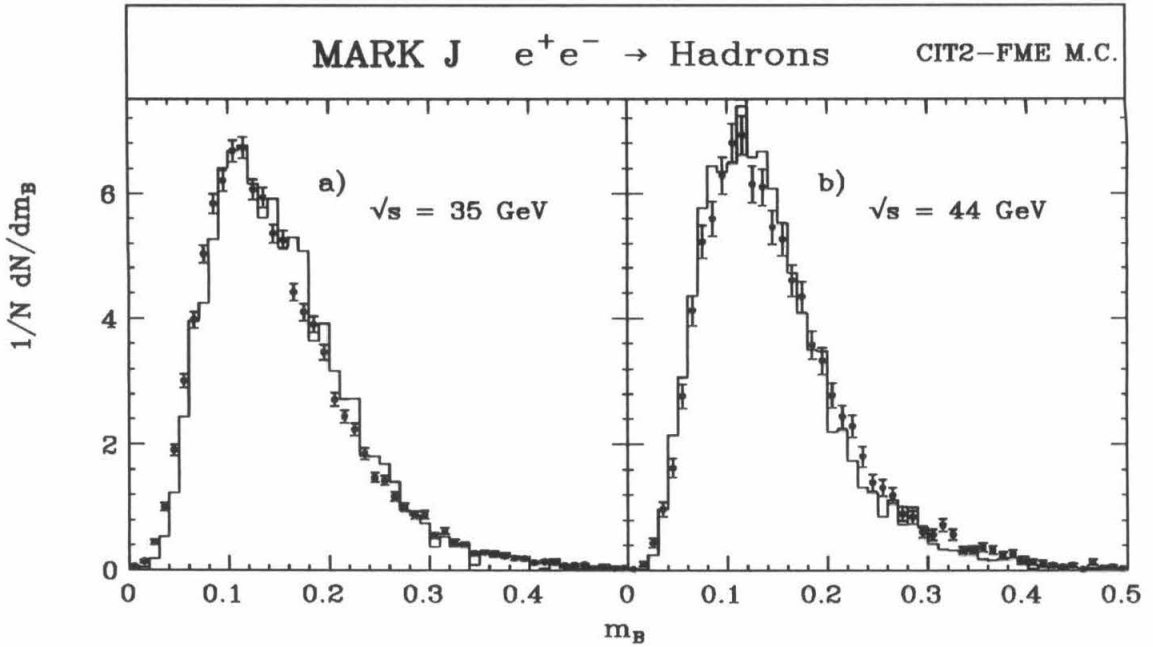


Figure C.39 The CIT2-FME model predictions for m_B compared to the data at 35 GeV, a), and 44 GeV, b).

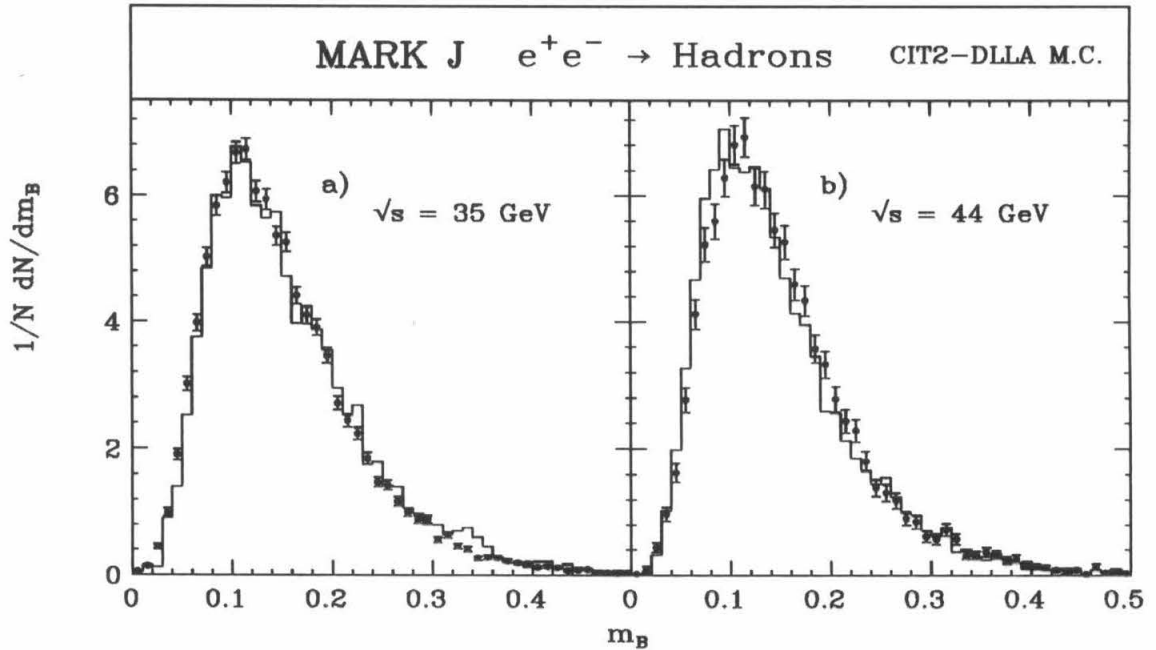


Figure C.40 The CIT2-DLLA model predictions for m_B compared to the data at 35 GeV, a), and 44 GeV, b).

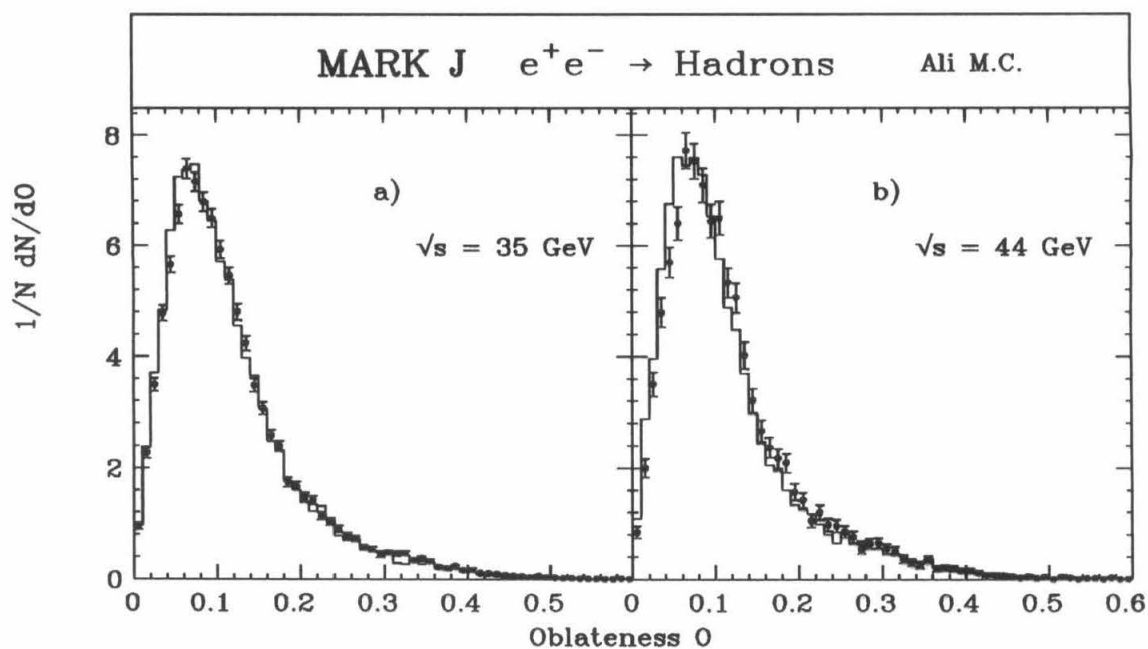


Figure C.41 The Ali model predictions for O compared to the data at 35 GeV, a), and 44 GeV, b).

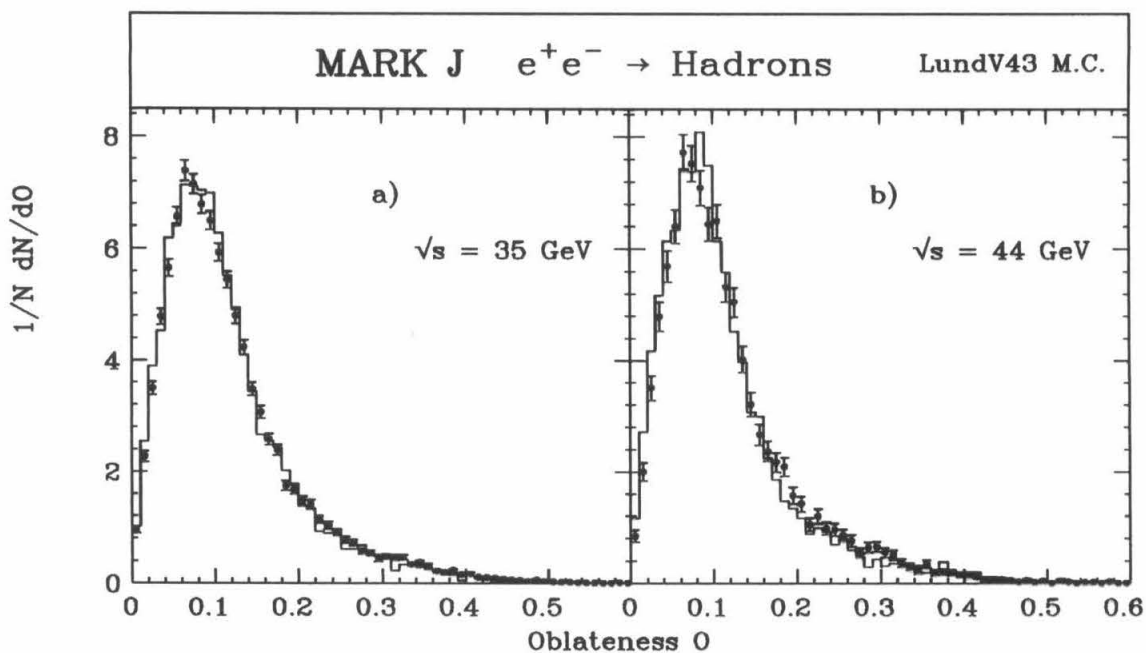


Figure C.42 The LundV4.3 model predictions for O compared to the data at 35 GeV, a), and 44 GeV, b).

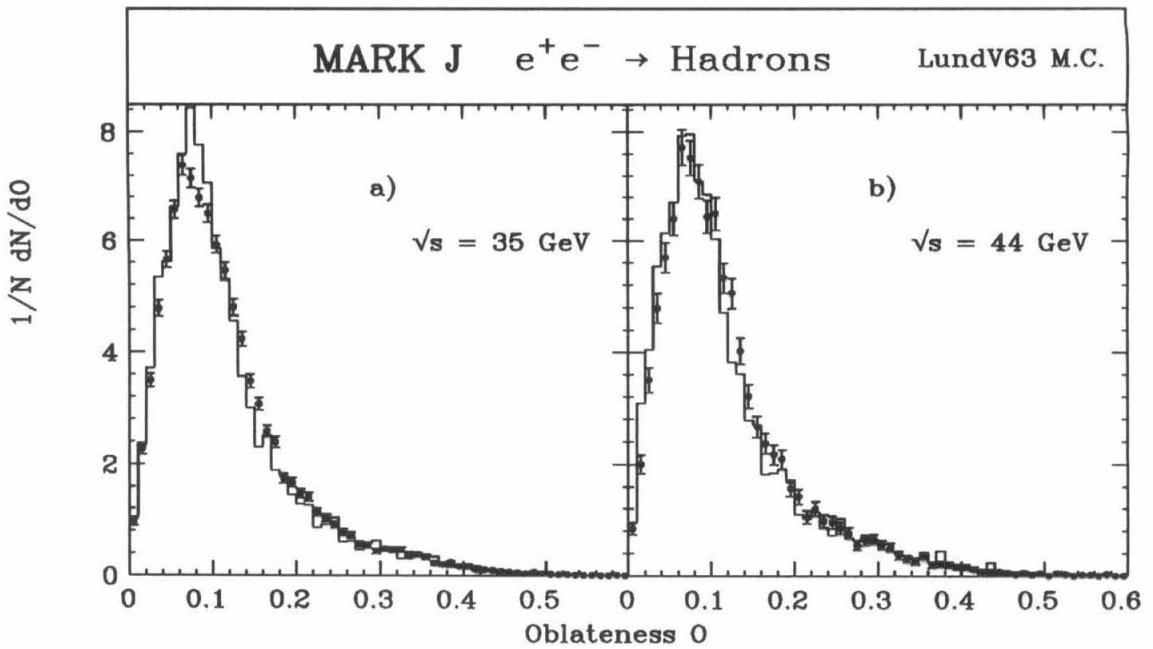


Figure C.43 The LundV6.3 model predictions for O compared to the data at 35 GeV, a), and 44 GeV, b).

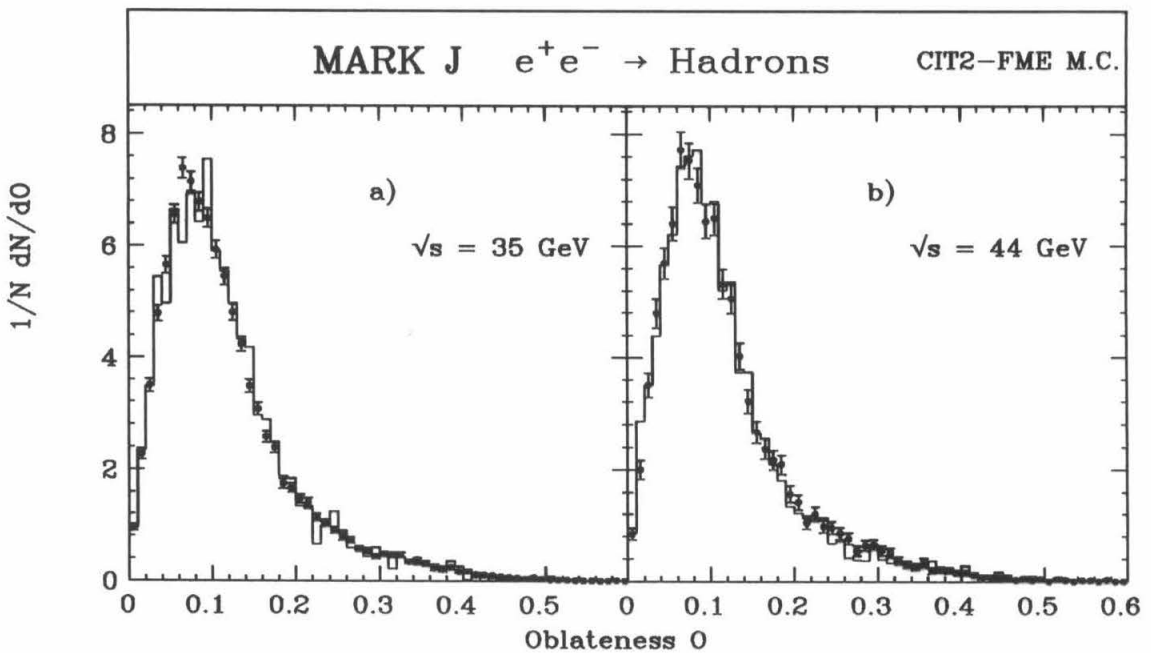


Figure C.44 The CIT2-FME model predictions for O compared to the data at 35 GeV, a), and 44 GeV, b).

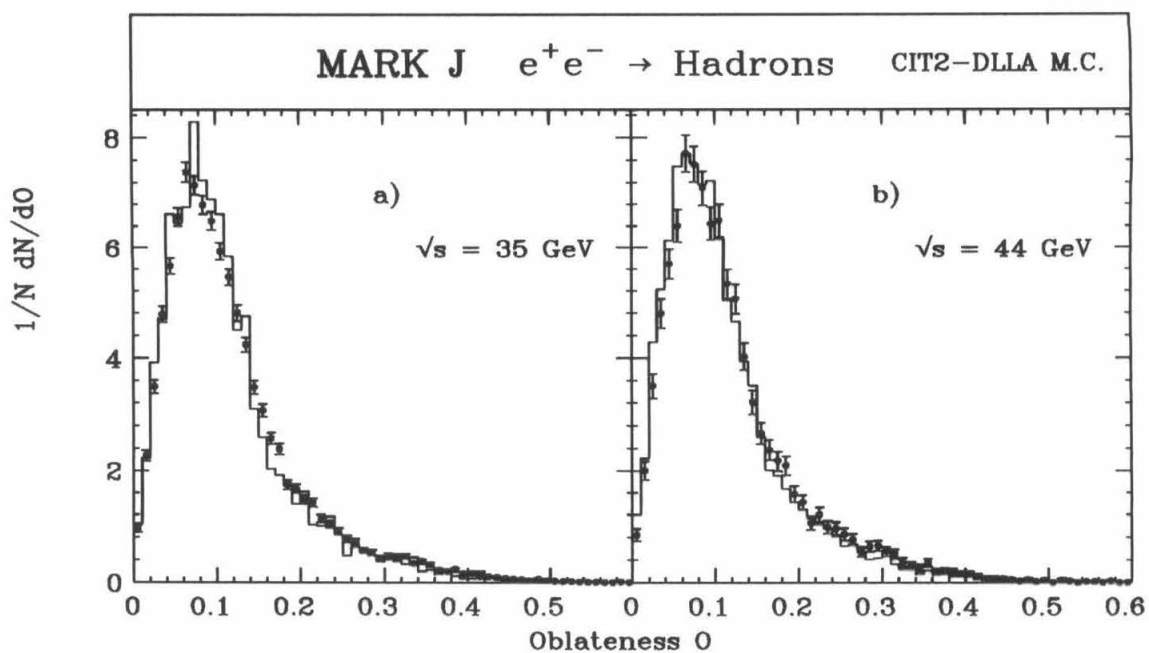


Figure C.45 The CIT2-DLLA model predictions for O compared to the data at 35 GeV, a), and 44 GeV, b).

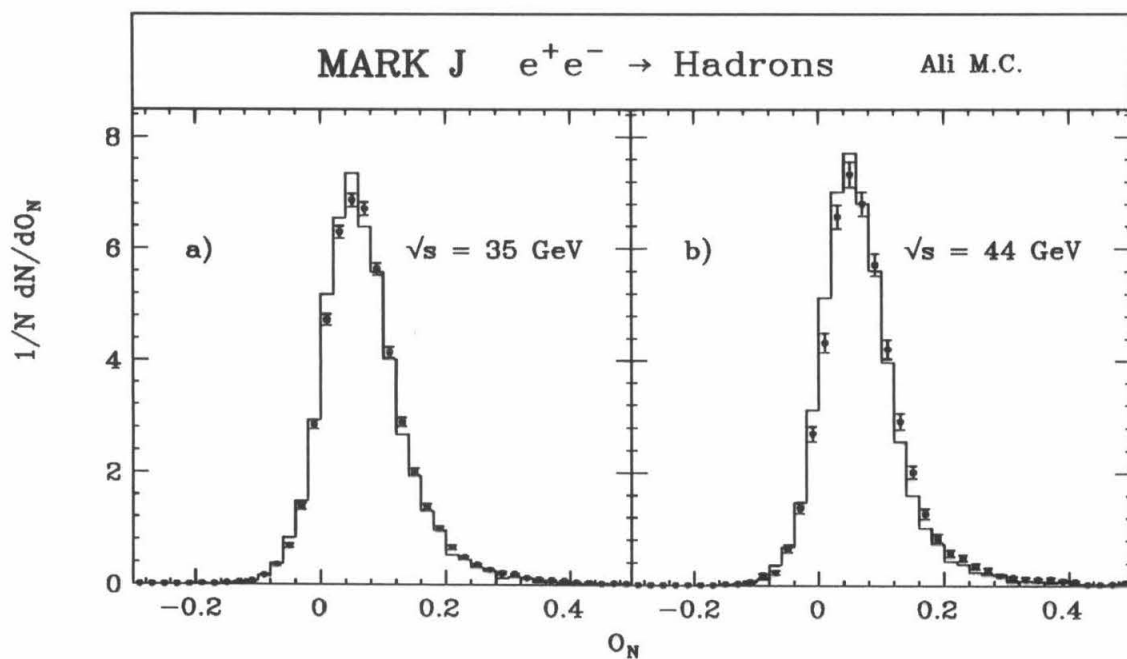


Figure C.46 The Ali model predictions for O_N compared to the data at 35 GeV, a), and 44 GeV, b).

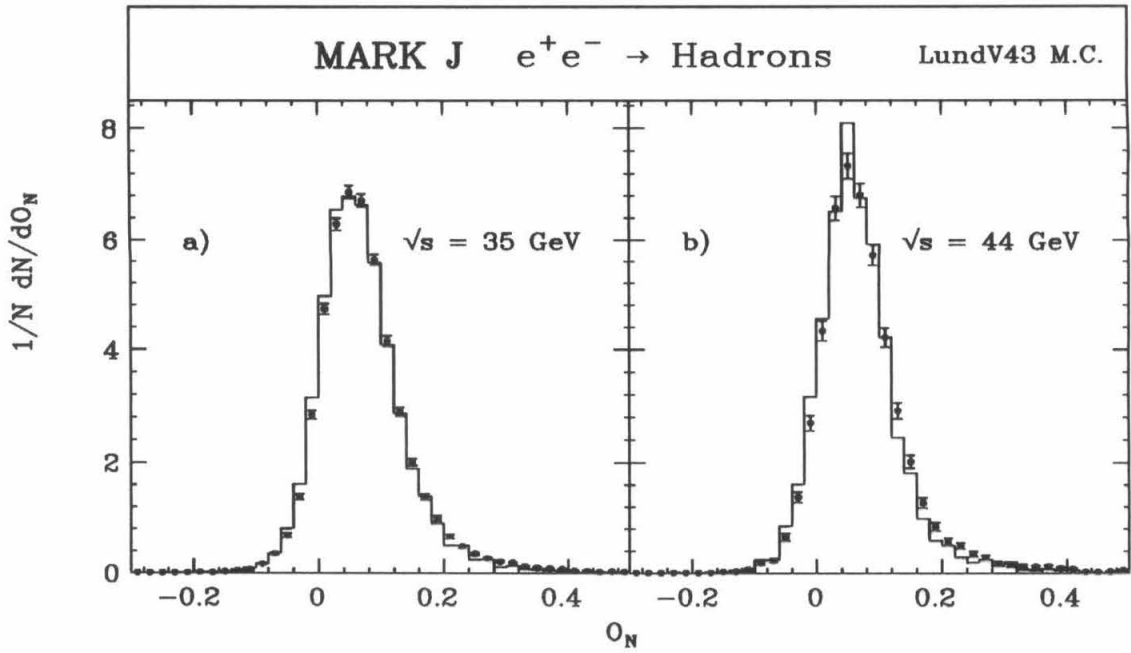


Figure C.47 The LundV4.3 model predictions for O_N compared to the data at 35 GeV, a), and 44 GeV, b).

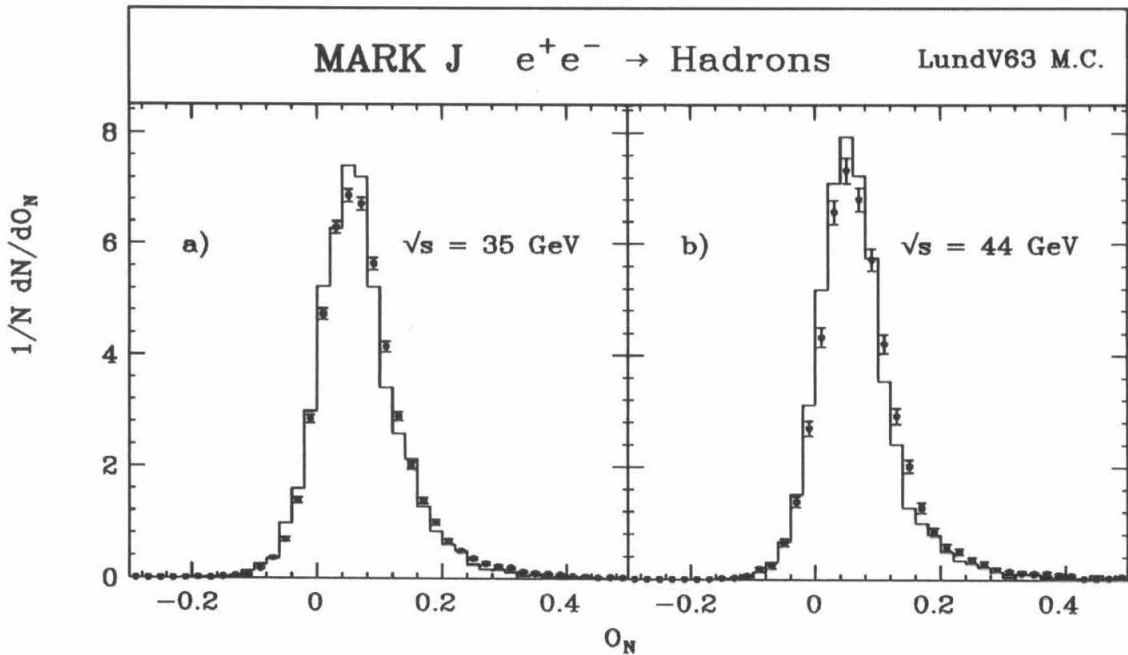


Figure C.48 The LundV6.3 model predictions for O_N compared to the data at 35 GeV, a), and 44 GeV, b).

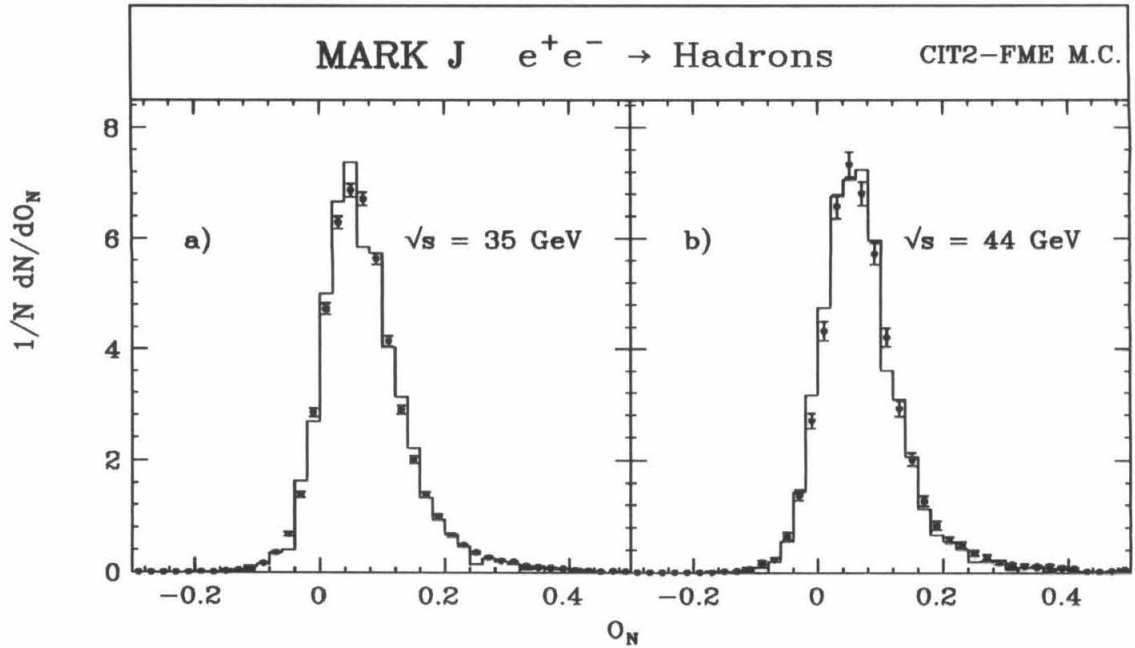


Figure C.49 The CIT2-FME model predictions for O_N compared to the data at 35 GeV, a), and 44 GeV, b).

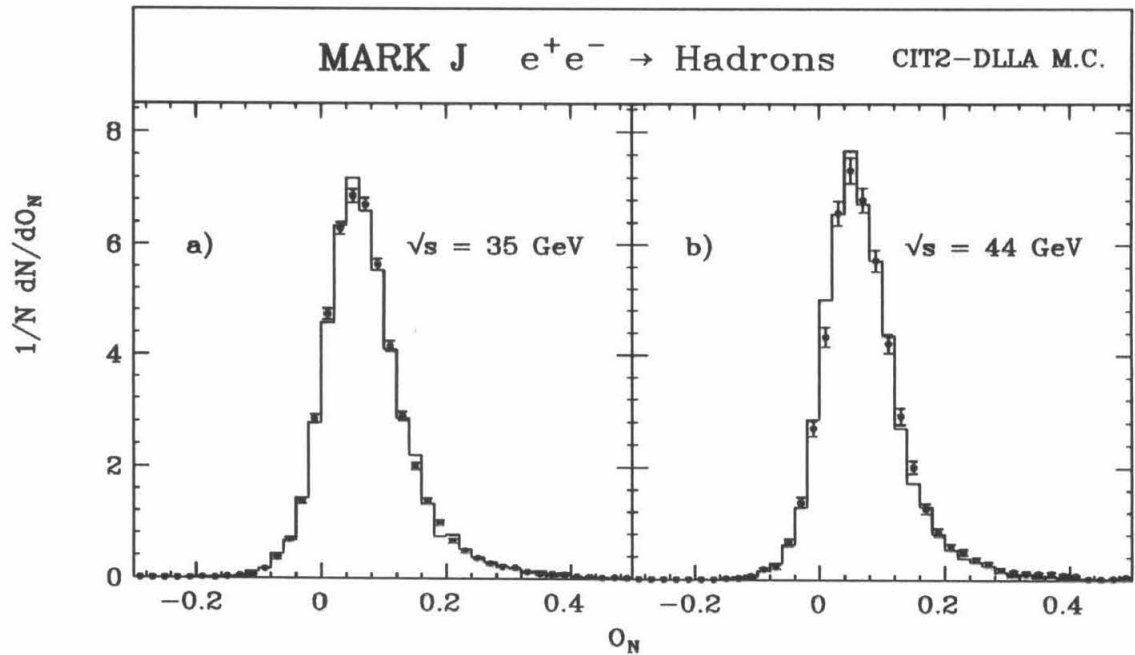


Figure C.50 The CIT2-DLLA model predictions for O_N compared to the data at 35 GeV, a), and 44 GeV, b).

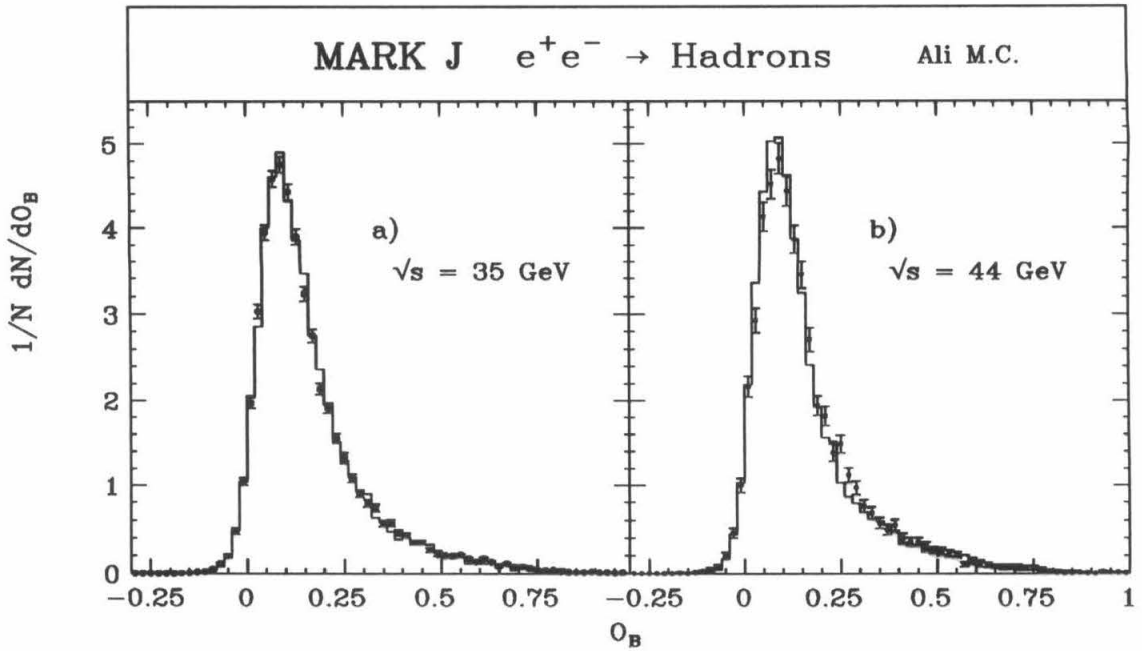


Figure C.51 The Ali model predictions for O_B compared to the data at 35 GeV, a), and 44 GeV, b).

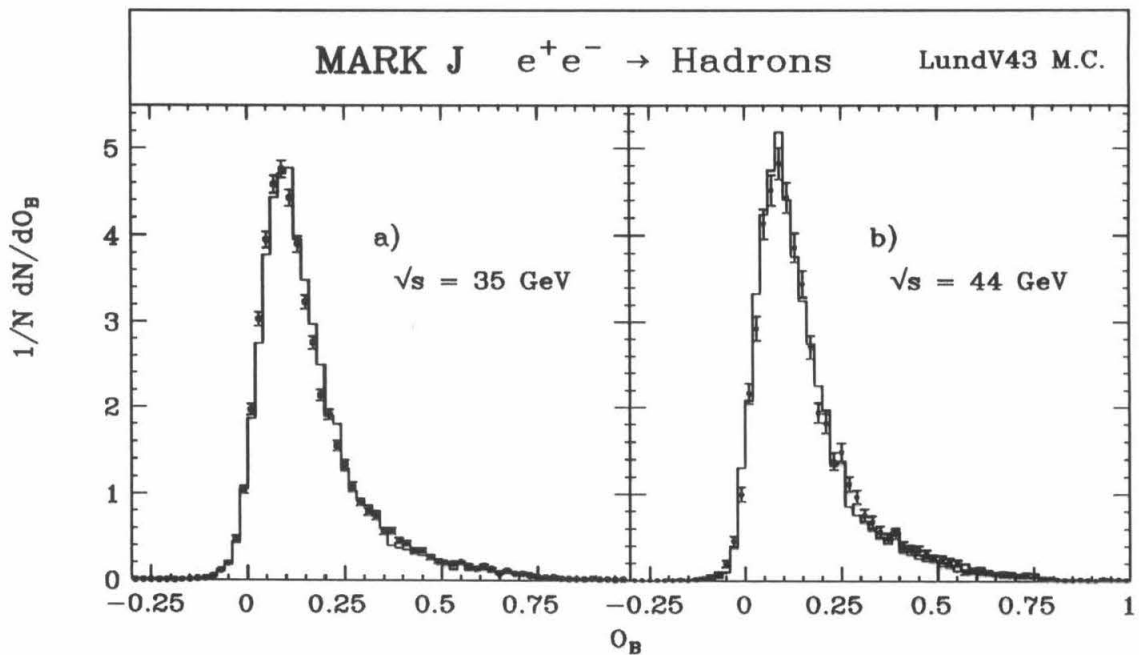


Figure C.52 The LundV4.3 model predictions for O_B compared to the data at 35 GeV, a), and 44 GeV, b).

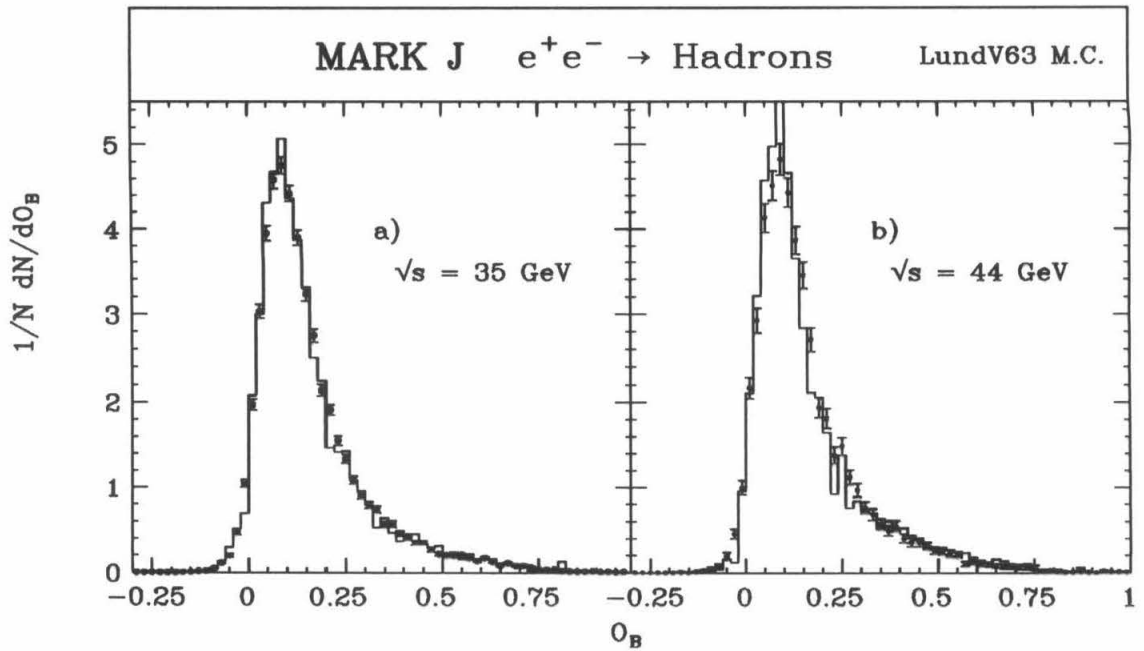


Figure C.53 The LundV6.3 model predictions for O_B compared to the data at 35 GeV, a), and 44 GeV, b).

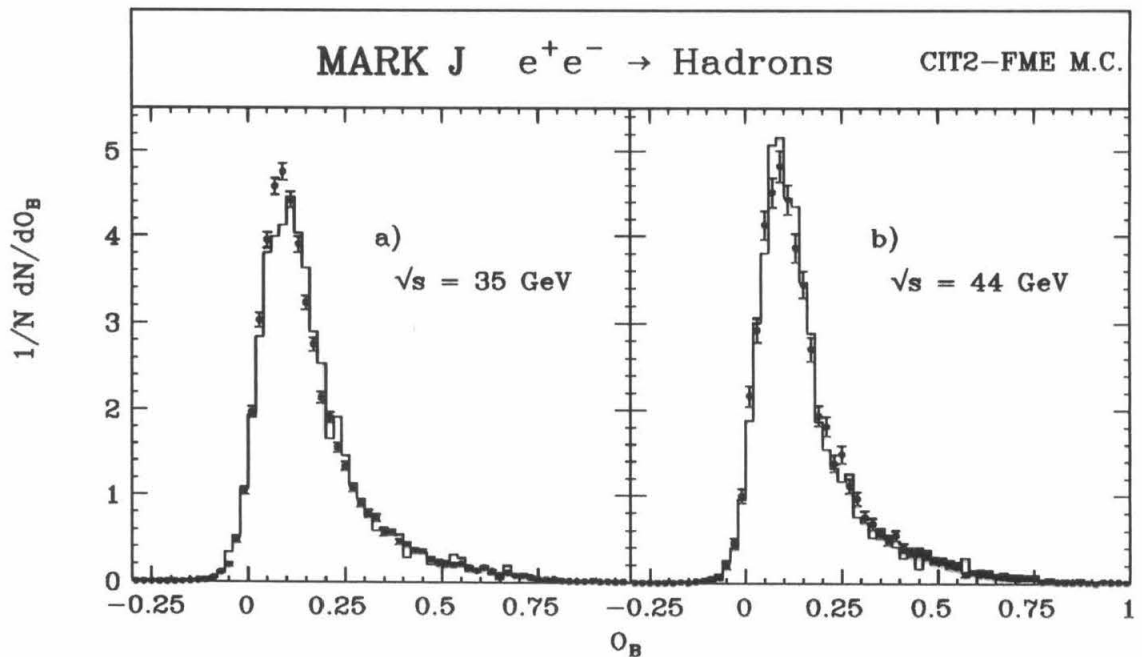


Figure C.54 The CIT2-FME model predictions for O_B compared to the data at 35 GeV, a), and 44 GeV, b).

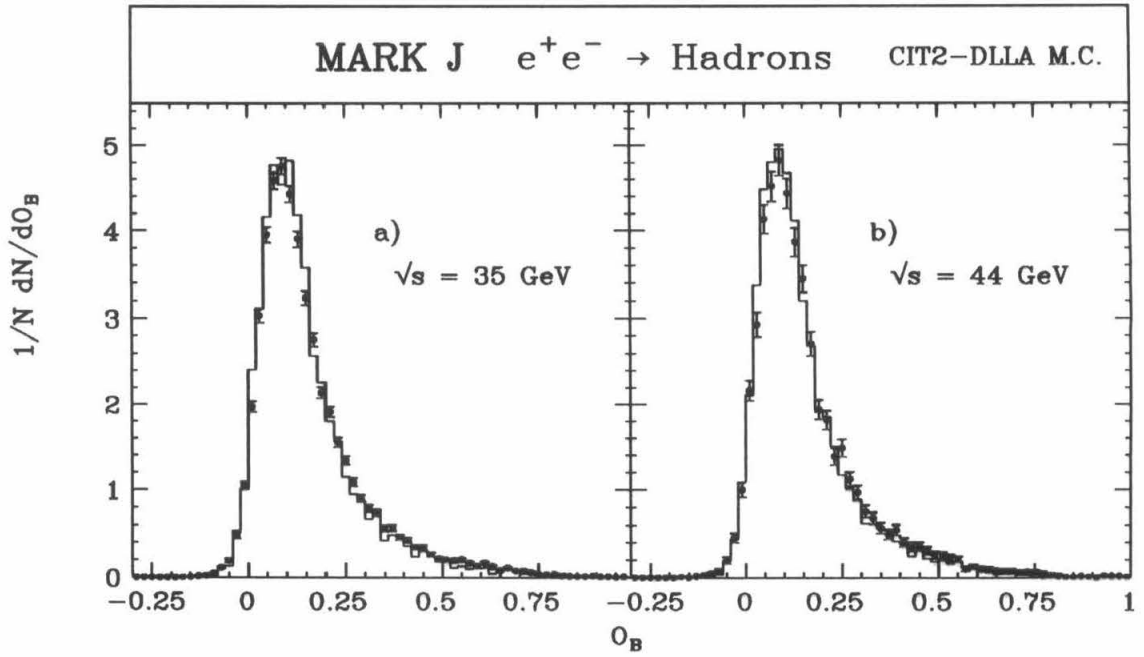


Figure C.55 The CIT2-DLLA model predictions for O_B compared to the data at 35 GeV, a), and 44 GeV, b).

Appendix D

α_s values extracted with the FKSS calculation

In this Appendix α_s values extracted with the use of the FKSS calculation are presented. It should be remarked that the α_s values obtained with the FKSS calculation are systematically larger than those obtained with the ERT calculation. This is due to the incorrect treatment of soft partons within the FKSS calculation.

Group	QCD	Frag.	α_s	$\alpha_s^{Str.}/\alpha_s^{i,j.}$	Ref.	Year
JADE	GKS	Lund	0.165 ± 0.01	1.280 ± 0.013	[23]	84
		I.J	0.11-0.14			
CELLO	GKS	Lund	0.19 ± 0.02	1.280 ± 0.013	[24]	84
		I.J	0.12-0.15			
TASSO	FKSS	Lund	0.19 ± 0.01	1.280 ± 0.013	[21]	84
		Ali	0.11-0.16			
MAC	GKS	Lund	0.185 ± 0.013	1.215 ± 0.019	[158]	87
		Ali	0.105 ± 0.014			

Table D.1 Summary of α_s values obtained in e^+e^- annihilation near center-of-mass energies of 35 GeV with the FKSS calculation.

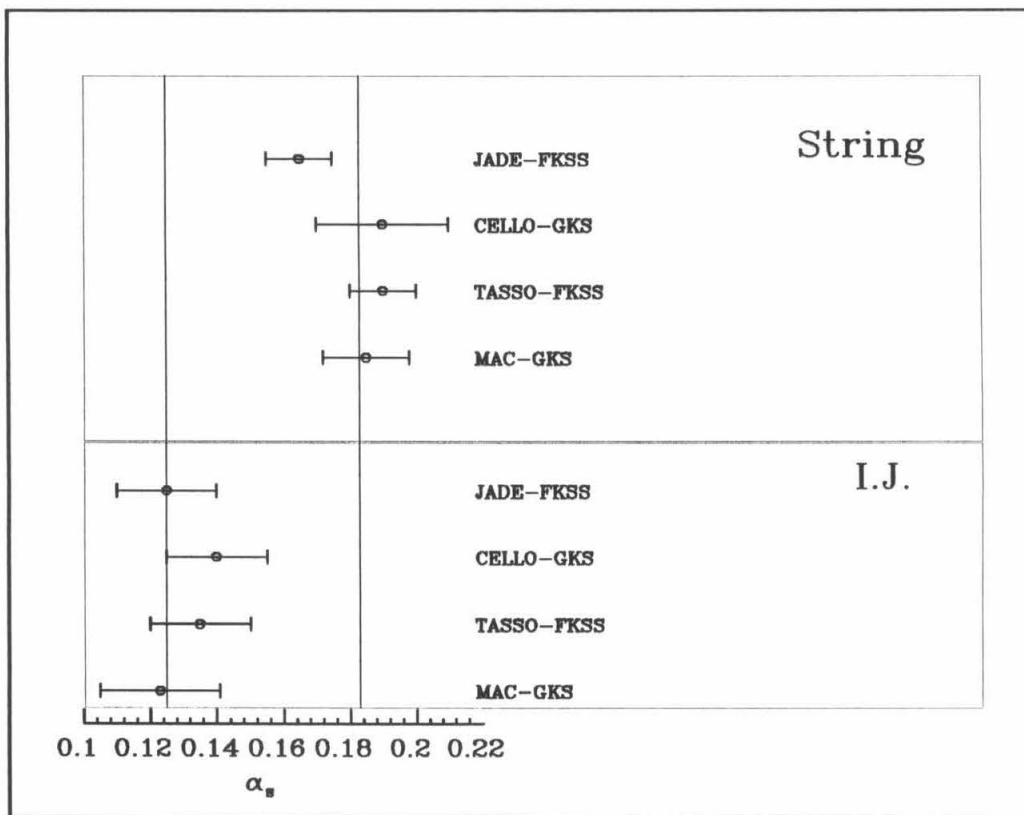


Figure D.1 Comparison of α_s values obtained in e^+e^- annihilations. These values were all obtained from the asymmetry in the Energy-Energy Correlation function. The values shown were obtained with the aid of the FKSS calculation.

References

- [1] D. Barber *et al.* (MARK J), Physics with high energy electron-positron colliding beams with the MARK J detector, *Phys. Rep.* **63C** (1980) 339.
- [2] B. Adeva *et al.* (MARK J), A summary of experimental results from MARK J: high energy e^+e^- collisions at PETRA, *Phys. Rep.* **109C** (1984) 133.
- [3] G. Hanson *et al.* (SPEAR), Evidence for jet structure in hadron production by e^+e^- annihilation, *Phys. Rev. Lett.* **35** (1975).
- [4] G. Hanson *et al.* (SPEAR), Hadron production by e^+e^- annihilation at center-of-mass energies between 2.6 and 7.8 GeV, *Phys. Rev.* **D26** (1982) 991.
- [5] D. Barber *et al.* (MARK J), Study of electron-positron collisions at center-of-mass energies of 27.4 and 27.7 GeV at PETRA, *Phys. Rev. Lett.* **43** (1979) 463.
- [6] D. Barber *et al.* (MARK J), Study of electron-positron collisions at the highest PETRA energy, *Phys. Lett.* **85B** (1979) 463.
- [7] Ch. Berger *et al.* (PLUTO), First observation of hadron production in e^+e^- collisions at 13 GeV and 17 GeV CMS energy with the PLUTO detector at PETRA, *Phys. Lett.* **81B** (1979) 410.
- [8] H.A. Berends *et al.* (CELLO), Topology of hadronic e^+e^- annihilation events at 22 GeV and 34 GeV CM energy, *Phys. Lett.* **110B** (1982) 329.

- [9] R. Brandelik *et al.* (TASSO), Properties of hadron final states in e^+e^- annihilation at 13 GeV and 17 GeV center of mass energies, *Phys. Lett.* **83B** (1979) 261.
- [10] D. Barber *et al.* (MARK J), Discovery of three-jet events and a test of quantum chromodynamics at PETRA, *Phys. Rev. Lett.* **43** (1979) 830.
- [11] R. Brandelik *et al.* (TASSO), Evidence for planar events in e^+e^- annihilation at high energies, *Phys. Lett.* **86B** (1979) 243.
- [12] Ch. Berger *et al.* (PLUTO), Evidence for gluon bremsstrahlung in e^+e^- annihilations at high energies, *Phys. Lett.* **86B** (1979) 418.
- [13] W. Bartel *et al.* (JADE), Observation of planar three-jet events in e^+e^- annihilation and evidence for gluon bremsstrahlung, *Phys. Lett.* **91B** (1980) 152.
- [14] W. Bartel *et al.* (JADE), Observation of four-jet structure in e^+e^- annihilation at $\sqrt{s} = 33$ GeV, *Phys. Lett.* **115B** (1982) 338.
- [15] M. Althoff *et al.* (TASSO), Jet production and fragmentation in e^+e^- annihilation at 12-43 GeV, *Z. Phys.* **C22** (1984) 307.
- [16] D.W. Duke and R.G. Roberts, Determinations of the QCD strong coupling α_s and the scale Λ_{QCD} , *Phys. Rep.* **120C** (1985) 275.
- [17] R.Y. Zhu, *Status of α_s determination in e^+e^- annihilation*, Caltech Preprint CALT-68-1306 1986.
- [18] D.P. Barber *et al.* (MARK J), A model independent second order determination of the strong coupling constant α_s , *Phys. Rep. Lett.* **54** (1983) 443.

- [19] C. Berger *et al.* (PLUTO), A study of energy-energy correlations in e^+e^- annihilations at $\sqrt{s} = 34.6$ GeV, *Z. Phys.* **C28** (1985) 365.
- [20] Min Chen, A short history of measuring the strong coupling constant, α_s , to complete second order, *Int. J. Mod. Phys.* **A1** (1986) 669.
- [21] M. Althoff *et al.* (TASSO), Determination of α_s in first and second order QCD from e^+e^- annihilation into hadrons, *Z. Phys.* **C26** (1984) 157.
- [22] H.A. Berends *et al.* (CELLO), An analysis of the charged and neutral energy flow in e^+e^- hadronic annihilation at 34-GeV, and a determination of the QCD effective coupling, *Phys. Lett.* **113B** (1982) 427.
- [23] W. Bartel *et al.* (JADE), Measurements of energy correlations in $e^+e^- \rightarrow$ hadrons, *Z. Phys.* **C25** (1985) 231.
- [24] H.A. Berends *et al.* (CELLO), On the model dependence of the determination of the strong coupling constant in second order QCD from e^+e^- annihilation into hadrons, *Phys. Lett.* **138B** (1984) 311.
- [25] T. Sjöstrand, Some comments on jet fragmentation models and α_s determinations, *Z. Phys.* **C26** (1984) 93.
- [26] P. Soeding, Rappatuer talk, In *Proceedings of the International Europhysics Conference on High Energy Physics, Brighton U.K., 1983*.
- [27] R.Y. Zhu, *Determination of the Strong Coupling Constant up to Complete Second Order in QCD*, PhD thesis Massachusetts Institute of Technology 1983.
- [28] T.D. Gottschalk and M.P. Shatz, *Clarification of disagreements in the $O(\alpha_s^2)$ dressed 3-jet cross-section for e^+e^- Annihilation*, Caltech preprint CALT-68-1173 1984.

- [29] T.D. Gottschalk and M.P. Shatz, A reassessment of the $O(\alpha_s^2)$ three jet cross-section for e^+e^- annihilation, *Phys. Lett.* **105B** (1985) 451.
- [30] R.D. Field and R.P. Feynman, A parameterization of the properties of quark jets, *Nucl. Phys.* **B136** (1978) 1.
- [31] A. Ali *et al.*, A QCD analysis of the high energy e^+e^- data from PETRA, *Phys. Lett.* **93B** (1980) 155.
- [32] P. Hoyer, P. Osland, H.G. Sander, T.F. Walsh, and P.M. Zerwas, Quantum chromodynamics and jets in e^+e^- annihilation, *Nucl. Phys.* **B161** (1979) 349.
- [33] R. Odorico (COJETS), Simulation of QCD in hard hadronic processes including gluon radiation effects, *Nucl. Phys.* **B228** (1983) 381.
- [34] T. Sjöstrand, The LUND Monte Carlo for jet fragmentation, *Comput. Phys. Commun.* **27** (1982) 243.
- [35] T. Sjöstrand, The LUND Monte Carlo for e^+e^- jet physics, *Comput. Phys. Commun.* **28** (1982) 229.
- [36] T.D. Gottschalk, A simple phenomenological model for hadron production from low mass clusters, *Nucl. Phys.* **B239** (1984) 325.
- [37] T.D. Gottschalk, An improved description of hadronization in the QCD cluster model for e^+e^- annihilation, *Nucl. Phys.* **B239** (1984) 349.
- [38] B.R. Webber, A QCD model for jet fragmentation including soft gluon interference, *Nucl. Phys.* **B238** (1984) 492.
- [39] T.D. Gottschalk and D.A. Morris, *A New Model for Hadronization and e^+e^- Annihilation*, Caltech preprint CALT-68-1365 1986.

- [40] T. Sjöstrand, The LUND Monte Carlo for jet fragmentation and e^+e^- physics — JETSET version 6.2, *Comput. Phys. Commun.* **39** (1986) 347.
- [41] W. Bartel *et al.* (JADE), Particle distribution in 3-jet events produced by e^+e^- annihilation, *Z. Phys.* **C21** (1983) 37.
- [42] W. Bartel *et al.* (JADE), Test of fragmentation models by comparison with three-jet events produced in e^+e^- annihilation, *Phys. Lett.* **134B** (1984) 275.
- [43] W. Bartel *et al.* (JADE), Comparison of three-jet events with QCD shower models, *Phys. Lett.* **157B** (1985) 340.
- [44] H. Aihara *et al.* (TPC), Tests of models for parton fragmentation by means of three-jet events in e^+e^- annihilation at $\sqrt{s} = 29$ GeV, *Phys. Rev. Lett.* **54** (1985) 270.
- [45] H. Aihara *et al.* (TPC), Tests of models for quark and gluon fragmentation in e^+e^- annihilation at $\sqrt{s} = 29$ GeV, *Z. Phys.* **C28** (1985) 31.
- [46] J.W. Gary, *Tests of Models for Parton Fragmentation in e^+e^- Annihilation*, PhD thesis Berkeley 1985, LBL-20638.
- [47] A. Peterson *et al.* (MARK II), Inclusive charged-particle distribution in nearly threefold-symmetric three-jet events at $E_{\text{CM}} = 29$ GeV, *Phys. Rev. Lett.* **55** (1985) 1954.
- [48] T.D. Gottschalk and M.P. Shatz, *Analytic formulae for the $O(\alpha_s^2)$ dressed 3-jet e^+e^- Annihilation cross section*, Caltech preprint CALT-68-1172 1986.
- [49] J. Vermaseren *et al.*, Perturbative QCD calculation of jet cross sections in e^+e^- annihilation, *Nucl. Phys.* **B187** (1981) 301.

- [50] R.K. Ellis *et al.*, The perturbative calculation of jet structure in e^+e^- annihilation, *Nucl. Phys.* **B178** (1981) 421.
- [51] M. Capell, *A study of hadronic final states from e^+e^- annihilation as a function of center of mass energy*, PhD thesis Massachusetts Institute of Technology 1986.
- [52] B. Adeva *et al.* (MARK J), Study of hadron production and inclusive muon production from electron-positron annihilation at $39.79 < \sqrt{s} \leq 46.78$ GeV, *Phys. Rev.* **34D** (1986) 1750.
- [53] W. Bartel *et al.* (JADE), *Hadronic events with low thrust containing isolated leptons*, DESY REPORT DESY-86/052 1986.
- [54] U. Becker *et al.*, Drift-tube arrays for high spatial resolution, *N.I.M.* **180** (1981) 61.
- [55] U. Becker *et al.*, A comparison of drift chambers, *N.I.M.* **128** (1975) 593.
- [56] H. Meng-Chia, *The Trigger and Data Taking System of The MARK J Detector*, PhD thesis NIKHEF 1983.
- [57] S. Glashow, Partial-symmetries of weak interactions, *Nucl. Phys.* **22** (1961) 579.
- [58] S. Glashow, Weak interactions with lepton-hadron symmetry, *Phys. Rev.* **D2** (1970) 1285.
- [59] S. Weinberg, A model of leptons, *Phys. Rev. Lett.* **19** (1967) 1264.
- [60] A. Salam, Renormalizability of gauge theories, *Phys. Rev.* **127** (1962) 331.
- [61] S. Glashow, Towards a unified theory: threads in a tapestry, *Rev. Mod. Phys.* **52** (1980) 539.

- [62] S. Weinberg, Conceptual foundations of the unified theory of weak and electromagnetic interactions, *Rev. Mod. Phys.* **52** (1980) 515.
- [63] A. Salam, Gauge invariance of fundamental forces, *Rev. Mod. Phys.* **52** (1980) 525.
- [64] R.K. Ellis *et al.*, Factorization and the parton model in QCD, *Phys. Lett.* **78B** (1978) 281.
- [65] H.A. Berends *et al.* (CELLO), Hard photon contributions for Bhabha scattering, *Nucl. Phys.* **B68** (1974) 541.
- [66] F.A. Berends *et al.*, Distributions in the process $e^+e^- \rightarrow \mu^+\mu^-(\gamma)$, *Nucl. Phys.* **B177** (1981) 237.
- [67] F.A. Berends *et al.*, Initial state radiation for e^+e^- annihilation into jets, *Nucl. Phys.* **B178** (1981) 141.
- [68] H. Politzer, Asymptotic freedom: an approach to strong interactions, *Phys. Repts.* **14C** (1974) 129.
- [69] S. Coleman and E. Weinberg, Radiative corrections as the origin of spontaneous symmetry breaking, *Phys. Rev.* **D7** (1973) 1888.
- [70] W. Caswell, Asymptotic behaviour of Non-Abelian gauge theories to two-loop order, *Phys. Rev. Lett.* **33** (1974) 244.
- [71] R.K. Ellis *et al.*, Perturbation theory and the parton model in QCD, *Nucl. Phys.* **B152** (1979) 285.
- [72] T. Kinoshita, Mass singularities of Feynman amplitudes, *J. Math Phys.* **3** (1960) 650.

- [73] T.D Lee and M. Nauenberg, Degenerate systems and mass singularities, *Phys. Rev.* **133** (1966) 1549.
- [74] M. Dine and J. Sapirstein, Higher order quantum chromodynamic corrections to e^+e^- annihilation, *Phys. Rev. Lett.* **43** (1979) 668.
- [75] K. G. Chetyrkin *et al.*, Higher order corrections to $\sigma_{tot}(e^+e^- \rightarrow \text{Hadrons})$ in quantum chromodynamics, *Phys. Lett.* **85B** (1979) 277.
- [76] G. Kramer and B. Lampe, $O(\alpha_s^2)$ two jet cross section in e^+e^- annihilation, *Prog. Theor. Phys.* **76** (1986) 1340.
- [77] K. Fabricius *et al.*, Higher order perturbative QCD calculation of jet cross-sections in e^+e^- annihilation, *Z. Phys.* **C11** (1982).
- [78] A. Ali *et al.*, QCD predictions for four-jet final states in e^+e^- annihilation, *Nucl. Phys.* **B167** (1980) 454.
- [79] G. Sterman and S. Weinberg, Jets from quantum chromodynamics, *Phys. Rev. Lett.* **39** (1977) 1436.
- [80] A. Bassetto *et al.*, Jet structure and infrared sensitive quantities in perturbative QCD, *Phys. Repts.* **C100** (1983) 201.
- [81] J. Schwinger, Gauge invariance and mass, *Phys. Rev.* **125** (1962) 397.
- [82] J. Schwinger, Gauge invariance and mass II, *Phys. Rev.* **128** (1962) 2425.
- [83] A. Casher *et. al.*, Vacuum polarization and the absence of free quarks, *Phys. Rev.* **D10** (1974) 732.
- [84] A. Casher *et. al.*, Chromoelectric-flux-tube model of particle production, *Phys. Rev.* **D20** (1979) 179.

- [85] T.D. Gottschalk, A new model for coherent final state parton showers, In H-U Bengtsson, C. Buchanan, T.D. Gottschalk, and A. Soni, editors, *Observable Standard Model Physics at the SSC: Monte Carlo Simulation and Detector Capabilities* page 122 1986.
- [86] M. Althoff *et al.* (TASSO), A detailed study of strange particle production in e^+e^- annihilation at high energy, *Z. Phys.* **C27** (1985) 27.
- [87] M. Althoff *et al.* (TASSO), Experimental test of the flavor independence of the quark-gluon coupling constant, *Phys. Lett.* **138B** (1984) 317.
- [88] M. Althoff *et al.* (TASSO), Properties of charm jets in e^+e^- annihilation near 34 gev., *Phys. Lett.* **135B** (1984) 243.
- [89] X. Artru and G. Mennessier, String model and multiproduction, *Nucl. Phys.* **B70** (1974) 93.
- [90] X. Artru, Classical string phenomenology. How strings work, *Phys. Reports* **97** (1983) 147.
- [91] T.D. Gottschalk, *Pictures of Hadronization*, Caltech preprint CALT-68-1413 1986.
- [92] R.Y. Zhu, *Determination of the strong coupling constant upto complete second order in QCD*, PhD thesis M.I.T 1983.
- [93] Y.L. Dokshitzer *et al.*, *Coherence effects in QCD jets*, Leningrad Nuclear Physics Institute report 1051 1985.
- [94] R. Odorico, *Phenomenological irrelevance of coherence effects in QCD cascades*, Univ. di Bologna IFUB 85/14 1985.

- [95] T.A. Gabriel and R.L. Bishop, Calculated hadronic transmission through iron absorbers, *N.I.M.* **155** (1970) 81.
- [96] H. Aihara *et al.* (TPC), Comparison of the particle flow in $q\bar{q}g$ and $q\bar{q}\gamma$ events in e^+e^- annihilation, *Phys. Rev. Lett.* **57** (1986) 945.
- [97] P.D. Sheldon *et al.* (MARK II), A comparison of particle flow in three-jet events and radiative two jet events from e^+e^- annihilation at $e_{c.m.} = 29$ GeV, *Phys. Rev. Lett.* **57** (1986) 1398.
- [98] M. Althoff *et al.* (TASSO), A study of 3-jet events in e^+e^- annihilation into hadrons at 34.6 GeV c.m. energy, *Z. Phys.* **C29** (1985) 29.
- [99] A. Peterson *et al.* (MARK II), *Multihadronic events at $E_{cm} = 29$ GeV and predictions of QCD models from $E_{cm} = 29$ GeV to $E_{cm} = 93$ GeV.*, 1987.
- [100] A. Ali and F. Barreiro, An $O(\alpha_s^2)$ calculation of energy-energy correlation in e^+e^- annihilation and comparison with data, *Phys. Lett.* **118B** (1982) 155.
- [101] D.G. Richards *et al.*, Second-order corrections to the energy-energy correlation function in quantum chromodynamics, *Phys. Lett.* **119B** (1982) 193.
- [102] D.G. Richards *et al.*, Energy-energy correlations to second order in quantum chromodynamics, *Nucl. Phys.* **B229** (1983) 317.
- [103] H.N. Schneider, G. Kramer, and G. Schierholz, Higher order QCD corrections to the energy-energy correlation function, *Z. Phys.* **C22** (1984) 201.
- [104] Lluís Garrido and Min Chen, Determination of α_s using the planar triple energy correlation and the energy correlation asymmetry, *Int. J. Mod. Phys.* **A1** (1986) 321.

- [105] B. Adeva et al. (MARK J), A measurement of the strong coupling α_s to second order for $14 < \sqrt{s} < 46.78$ GeV, *Phys. Rep.* **109C** (1984) 133.
- [106] S.L. Wu, Talk presented at the Hamburg conference, (Aug 1987) .
- [107] Chris. Hawkes, Private communication, .
- [108] A. Boehm, In , editor, *Proceedings of the XXth Rencontre de Moriond, Les Arcs* page 559 1985.
- [109] G.C. Fox and S. Wolfram, Tests for planar events in e^+e^- annihilation, *Phys. Lett.* **82B** (1979) 134.
- [110] G.C. Fox and S. Wolfram, Event shapes in e^+e^- annihilation, *Nucl. Phys.* **B149** (1979) 413.
- [111] J. R. Cudell et al., *Is a low-mass top quark ruled out ?*, University of Wisconsin report MAD/PH/353 1987.
- [112] F.A. Berends et al., Radiative corrections to muon pair and quark pair production in electron-positron collisions in the Z^0 region, *Nucl. Phys.* **B202** (1982) 63.
- [113] S. Gusken et al., Toponium production in e^+e^- collisions, *Nucl. Phys.* **B262** (1985) 393.
- [114] J.H. Kuhn et al., Z decays to top quarks, *Nucl. Phys.* **B272** (1986) 560.
- [115] P. Lutz, *How to recognize the hard elementary process in hadronic events at LEP energies*, College de France preprint LPC 84-26 1984.
- [116] M. Gell-Mann, Symmetries of baryons and mesons, *Phys. Rev.* **125(3)** (1962) 1067.

- [117] Zweig, CERN Report 8419/TH.412 and 8182/TH.401 1964.
- [118] Y. Ne'eman, Derivation of strong interactions from a gauge invariance, *Nucl. Phys.* **26B** (1961) 222.
- [119] M. Gell-Mann, A schematic model of baryons and mesons, *Phys. Lett.* **8** (1964) 214.
- [120] V. E. Barnes *et al.*, Observation of a hyperon with strangeness minus three, *Phys. Rev. Lett.* **12** (1964) 204.
- [121] E. D. Bloom *et al.*, High energy inelastic e-p scattering at 6° and 10° , *Phys. Rev. Lett.* **23** (1969) 930.
- [122] J. D. Bjorken and E. A. Paschos, Inelastic electron-proton and γ -proton scattering and the structure of the nucleon, *Phys. Rev.* **185** (1969) 1975.
- [123] J.I. Friedman and H.W. Kendall, Deep inelastic electron scattering, *Phys. Lett.* **22** (1972) 203.
- [124] M. Breidenbach *et al.*, Observed behaviour of highly inelastic electron-proton scattering, *Phys. Rev. Lett.* **23** (1969) 1969.
- [125] R.P. Feynman, *Photon-Hadron interactions*, 1972.
- [126] J. D. Bjorken, Asymptotic sum rules at infinite momentum, *Phys. Rev.* **179** (1969) 1547.
- [127] G. Miller *et al.*, Inelastic electron-proton scattering at large momentum transfers and the inelastic structure functions of the proton, *Phys. Rev.* **D5** (1972) 528.
- [128] T. Eichten *et al.*, Measurement of the neutrino-nucleon and antineutrino-nucleon total cross sections, *Phys. Lett.* **46B** (1973) 274.

- [129] H. Deden *et al.*, Experimental study of structure functions and sum rules in charge-changing interactions of neutrinos and antineutrinos on nucleons, *Nucl. Phys.* **B85** (1975) 269.
- [130] F.E. Close, *An introduction to quarks and leptons*, Academic press 1981.
- [131] H. Abramowicz *et al.*, Determination of the gluon distribution in the nucleon from deep inelastic neutrino scattering, *Zeit. Phys. C.* **12** (1982) 289.
- [132] J. Christenson *et al.*, Observation of massive muon pairs in hadron collisions, *Phys. Rev. Lett.* **25** (1970) 1523.
- [133] J. Christenson *et al.*, Observation of muon pairs in high-energy hadron collisions, *Phys. Rev.* **D8** (1974) 2016.
- [134] F. Buser *et al.*, Observation of π^0 mesons with large transverse momentum in high-energy proton-proton collisions, *Phys. Lett.* **46B** (1973) 471.
- [135] J.J. Aubert *et al.*, Experimental observation of a heavy particle J, *Phys. Rev. Lett.* **33** (1974) 1404.
- [136] J.-E. Augustin *et al.*, Discovery of a narrow resonance in e^+e^- annihilation, *Phys. Rev. Lett.* **33** (1974) 1406.
- [137] C. Bacci *et al.*, Preliminary result of Frascati(ADONE) on the nature of a new 3.1 GeV particle produced in e^+e^- annihilation, *Phys. Rev. Lett.* **33** (1974) 1408.
- [138] E. Bloom and C. Peck, Physics with the crystal ball detector, *Ann. Rev. Nucl. Sci.* **33** (1983) 143.
- [139] J. Richards *et al.*, The heavy quark potential and the Υ , J/ψ systems, *Phys. Lett.* **82B** (1979) 272.

- [140] E. Eichten *et al.*, Spectrum of charmed quark-antiquark bound states, *Phys. Rev. Lett.* **34** (1975) 369.
- [141] E. Eichten *et al.*, Interplay of confinement and decay in the spectrum of charmonium, *Phys. Rev. Lett.* **36** (1976) 500.
- [142] T. Appelquist and H. Politzer, Heavy quarks and e^+e^- annihilation, *Phys. Rev. Lett.* **34** (1975) 43.
- [143] A. De Rújula and S. Glashow, Is bound charm found ?, *Phys. Rev. Lett.* **34** (1975) 46.
- [144] J. Gaiser *et al.*, χ_b states in radiative decay of the $\Upsilon(2S)$, *Phys. Rev.* **34** (1986) 2611.
- [145] S. Herb *et al.*, Observation of a dimuon resonance at 9.5 GeV in 400 GeV proton-nucleus collisions, *Phys. Rev. Lett.* **39** (1977) 252.
- [146] H.J. Lipkin, Quarks for pedestrians, *Phys. Repts.* **8C** (1973) 174.
- [147] J. Kogut and L Susskind, The parton picture of elementary particles, *Phys. Repts.* **8C** (1973) 78.
- [148] A. Pickering, *Constructing quarks*, University of Chicago press 1984.
- [149] O.W. Greenberg, Spin and unitary-spin independence in a paraquark model of baryons and mesons, *Phys. Rev. Lett.* **13** (1964) 598.
- [150] O.W. Greenberg and C.A. Nelson, Color models of hadrons, *Phys. Repts.* **32C** (1977) 71.
- [151] A. De Rújula and H. Georgi, Counting quarks in e^+e^- annihilation, *Phys. Rev.* **13D** (1976) 1296.

- [152] S.L. Adler, Axial-vector vertex in spinor electrodynamics, *Phys. Rev.* **177** (1969) 2426.
- [153] J. Calmet *et al.*, The anomalous magnetic moment of the muon: A review of the theoretical contributions, *Rev. Mod. Phys.* **49** (1977) 21.
- [154] J. Bailey *et al.*, Final report of the CERN muon storage ring including the anomalous magnetic moment and the electric dipole moment of the muon, and a direct test of relativistic time dilation, *Nucl. Phys.* **B150** (1979) 1.
- [155] W. Marciano and H. Pagels, Quantum chromodynamics, *Phys. Rep.* **36C** (1978) 137.
- [156] S. Coleman and D.J. Gross, Price of asymptotic freedom, *Phys. Rev. Lett.* **31** (1973) 851.
- [157] F. Gutbrod *et al.*, *Recombination dependence of the $O(\alpha_s^2)$ three-jet cross-section for e^+e^- Annihilation*, DESY 87-047 1987.
- [158] E. Fernandez *et al.* (MAC), A measurement of Energy-Energy Correlations in $e^+e^- \rightarrow$ hadrons at $\sqrt{s} = 29$ GeV, *Phys. Rev. D* **31** (1985) 2724.